UNIVERSIDADE FEDERAL DO RIO GRANDE DO SUL
INSTITUTO DE GEOCIÊNCIAS
PROGRAMA DE PÓS-GRADUAÇÃO EM GEOCIÊNCIAS

DEPÓSITOS PIROCLÁSTICOS DE QUEDA (PFDs) COMO FERRAMENTA ESTRATIGRÁFICA. PROVENIÊNCIA, GEOCRONOLOGIA E RECONSTRUÇÃO DAS SEQUÊNCIAS DEPOSICIONAIS DA FORMAÇÃO IRATI

AURÉLIO FAGUNDES SILVA

ORIENTADOR: Prof. Dr. Norberto Dani

CO-ORIENTADOR: Prof. Dr. Marcus Vinícius Dorneles Remus

Porto Alegre

2021

UNIVERSIDADE FEDERAL DO RIO GRANDE DO SUL
INSTITUTO DE GEOCIÊNCIAS
PROGRAMA DE PÓS-GRADUAÇÃO EM GEOCIÊNCIAS

DEPÓSITOS PIROCLÁSTICOS DE QUEDA (PFDs) COMO FERRAMENTA ESTRATIGRÁFICA. PROVENIÊNCIA, GEOCRONOLOGIA E RECONSTRUÇÃO DAS SEQUÊNCIAS DEPOSICIONAIS DA FORMAÇÃO IRATI

AURÉLIO FAGUNDES SILVA

ORIENTADOR: Prof. Dr. Norberto Dani

CO-ORIENTADOR: Prof. Dr. Marcus Vinícius Dorneles Remus

BANCA EXAMINADORA

Prof. Dr. Edison José Milani – Petrobras

Prof. Dr. Ernesto Luiz Correa Lavina – Universidade do Vale do Rio dos Sinos

Prof. Dr. Márcia Elisa Boscato Gomes – Instituto de Geociências, Universidade Federal do Rio Grande do Sul

Tese de Doutorado apresentada como requisito parcial para a obtenção do Título de Doutor em Ciências.

Porto Alegre

2021

CIP - Catalogação na Publicação

Silva, Aurélio
DEPÓSITOS PIROCLÁSTICOS DE QUEDA (PFDs) COMO FERRAMENTA ESTRATIGRÁFICA. PROVENIÊNCIA, GEOCRONOLOGIA E RECONSTRUÇÃO DAS SEQUÊNCIAS DEPOSICIONAIS DA FORMAÇÃO IRATI / Aurélio Silva. -- 2021.
206 f.
Orientador: Norberto Dani.

Coorientador: Marcus Vinícius Dorneles Remus.

Tese (Doutorado) -- Universidade Federal do Rio Grande do Sul, Instituto de Geociências, Programa de Pós-Graduação em Geociências, Porto Alegre, BR-RS, 2021.

1. Formação irati. 2. Depósitos piroclásticos de queda . 3. Métodos estratigráficos. 4. Datação U-Pb por LA-ICP-MS. 5. Argilominerais. I. Dani, Norberto, orient. II. Dorneles Remus, Marcus Vinícius, coorient. III. Título.

Elaborada pelo Sistema de Geração Automática de Ficha Catalográfica da UFRGS com os dados fornecidos pelo(a) autor(a).

DEDICATÓRIA

Dedico esta tese aos meus pais, á todos
que me ajudaram, á toda sociedade
basileira e á toda sociedade geológica.

AGRADECIMENTOS I

Agradeço a minha família, particularmente aos meus pais Afrânio Ferreira da Silva e Luiza Marilia Fagundes Silva que nunca hesitaram em me apoiar, com muito sacrifício, me dando sempre a liberdade para escolher meu próprio caminho.

Agradeço a Universidade Federal do Rio Grande do Sul, pela educação pública, gratuita e de qualidade e por todas as oportunidades. Agradeço tambem aos cidadãos brasileiro que com seus impostos sustenta a educação pública. Á pós-graduação de Geociências (PPGgeo-UFRGS), por garantir condições de estudos e pela infraestrutura de pesquisa disponibilizada para o projeto, e aos técnicos dos laboratórios. Agradeço ainda a todos os meus professores, pelos seus exemplos, bons e ruins, que me inspiraram para a escolha da minha carreira, em especial aos orientadores Dani e Remus, às professora Magot e Lidia e aos professores Claiton, Rualdo, Ruy e Schultz.

Agradeço a todos os amigos que, ao seu momento, compartilharam experiências: Elis, Jonas, Priscilla, Carine, Tai, Klayne, Juliana, Roberta, Yolanda, Francesco, Clarice, Rosana, Maya, Mariana, Marina, Pabline, Kalil, Georgius, Nágila, Laisa, Franciela, Jéssica, Ameli, Amanda, Lucas, Kel, Solana, Isa, Sara, Marciéli, Ingred, Marcely, Natalia, Pedro, Sandro, Veridiana, Betina, Dani, Mônica, Alessandra, Adriano, Ricardo, Joãozinho, Barbosinha, Clara, Piqui, Renata, Mari, Simon, Ana, Felípe, Sissa, pessoal da APG, do grupo dos estrangeiros, do grupo do FLEC, entre tantos outros.

Agradeço ao Conselho Nacional de Desenvolvimento Científico e Tecnológico (CNPq) por ter garantido a bolsas de doutorado e ao ao Serviço Geológico Brasileiro (Companhia de Pesquisa de Recursos Minerais - CPRM), por ter permitindo acesso na litoteca de Caçapava do Sul – RS e a descrição de poços e coleta de materiais para os estudos.

"A ciência é feita ao ver algo que todos veem, e então pensar o que ninguém pensou." Albert St Georce (bioquímico)

"A ciência cresce a partir de modelos mentais imaginários, é aguçada por medições que verifiquem o ajuste dos modelos com a realidade. Atualmente, grande parte da ciência carece de integridade de cisão, divididas em dialetos isolados de especialidades reducionistas." (Lovelock, 2005)

RESUMO

A presente tese estudou registros de depósitos piroclásticos de queda (PFDs) em pacotes sedimentares. Os tipos principais estudados foram uma amostra de tephra in situ (cinza vulcânica) e duas amostras de tufos (bentonita e tonstein). Essas amostras foram caracterizadas em diferentes técnicas analíticas (descrição faciológica, petrografia descritiva, MEV, DRX, IR e FRX). A integração das diferentes respostas analíticas possibilitou análises descritivas integradas dos dados, descrevendo uma possível gênese para a estrutura cristaloquímica para cada PFD. As estruturas cristaloquímicas foram comparadas entre si para estimar os processos das alterações pós-deposicionais, com o PFD de cinza vulcânica, representando o produto inicial das fácies e os PFDs tufos (bentonita e tonstein), sinalizando a alteração pós-deposicional final entre as trocas com o ambiente sedimentado. Em um segundo estudo relacionando à análise estratigráfica da Formação Irati, foram identificados, coletados e analisados pelo método U/Pb por LA-ICP-MS em zircões três níveis de PFDs ao longo do furo de sondagem HV-44-RS, localizado na porção Sul da Bacia do Paraná. As análises obtiveram idades numéricas de 284.1± 3.5 (2σ; MSWD = 1.14, n=4), 280.8 ± 1,4 Ma (2σ; MSWD = 0.85, n=13) e 274.2 ± 2.8 (2σ; MSWD=0.87, n=4). As idades numéricas foram posicionadas no perfil estratigráfico, possibilitando estimar o período cronoestratigráfico, que depositou a Formação Irati. Combinando-a com ciclos estratigráficos, obteve-se diferentes taxas de deposição dos pacotes, estimativas durações de cada ciclo e idade de deposição de um horizonte fossilífero. Os resultados permitiram calibrar a seção para uma subsequente reconstrução paleoambiental, em que o ecossistema lacustre do Mar Irati-Whitehill se desenvolveu num clima que variou entre condições interglaciais e de aridificação.

Palavras-Chave: Modelos de fácies; Datação U-Pb por LA-ICP-MS; Métodos estratigráficos; Tefrocronologia; Argilominerais; Geoquímica exógena; Bentonita; Tonstein.

ABSTRACT

The present thesis studied records of pyroclastic fall deposits (PFDs) in sedimentary packages. The main types studied were a sample of tephra in situ (volcanic ash) and two samples of tufts (bentonite and tonstein). These samples were characterized by different analytical techniques (faciologic description, descriptive petrography, SEM, XRD, IR and XRF). The integration of the different analytical responses enabled integrated descriptive analyses of the data, describing a possible genesis for crystallochemical structure for each PFD. The crystallochemical structures were compared with each other to estimate the post-depositional alteration processes, with the volcanic ash PFD representing the initial facies product and the tuff PFDs (bentoinite and tonstein) signaling the final post-depositional alteration between exchanges with the sedimentary environment. In a second study relating the stratigraphic analysis of the Irati Formation, three levels of PFDs were identified, collected and analyzed by U/Pb method by LA-ICP-MS in zircons along drill core HV-44-RS, located in the southern portion of the Paraná Basin. The analyzes obtained numerical ages of 284.1 ± 3.5 (2s; MSWD = 1.14, n = 4), 280.8 ± 1.4 Ma (2s; MSWD = 0.85, n = 13) and 274.2 ± 2.8 (2s; MSWD = 0.87, n = 4). The numerical ages were positioned on the stratigraphic profile, making it possible to estimate the chronostratigraphic period that deposited the Irati Formation. Combining it with stratigraphic cycles, we obtained different rates of deposition of the packages, estimated durations of each cycle and age of deposition of a fossiliferous horizon. The results allowed to calibrate the section for subsequent paleoenvironmental reconstruction, where the lake ecosystem of the Irati-Whitehill Sea developed in a climate ranging from interglacial to aridification conditions.

Keywords: Facies Models; LA-ICP-MS U-Pb dating; Stratigraphic Methods; Tephrochronology; Clay Minerals; Exogenous geochemistry; Bentonite; Tonstein.

LISTA DE FIGURAS

LISTA DE TABELAS

SUMÁRIO

ESTRUTURA DA TESE

Esta tese de doutorado está estruturada na forma de três artigos submetidos em periódicos classificados nos estratos Qualis-CAPES, de acordo com a Norma 118. A sua estruturação está dividida em duas partes. Uma parte corresponde a fundamentação da tese e outra parte apresenta os três artigos.

O capítulo I de fundamentação da Tese apresenta o quadro sintético da pesquisa através de um texto integrador, no qual se faz a introdução e as hipóteses da investigação, os objetivos da pesquisa, contexto geológico do objeto de estudo, o estado da arte do tema da pesquisa, materiais e métodos utilizados para a materialização do trabalho, resumo dos principais resultados obtidos e discussões, e conclusões finalizarão esta primeira seção.

O capítulo II da Tese é dedicado a apresentar os três artigos, como autor principal, enviados às revistas científicas e as cartas comprovantes de submissão.

1. Chemical Geology (Elsevier), QUALIS Capes A1 (ISSN -0009-2541). Título: *Pyroclastic fall deposits (PFD) from Irati Formation: characterization and chronostratigraphy reconstruction based on high-resolution geochronology*.

2. Sedimentary Geology (Elsevier), QUALIS Capes A2 (ISSN -0037-0738). Título: *Evolution and transformations of Pyroclastic fall deposits (PFDs) of Permian Paraná Basin (Bentonite and tonstein) and tephras from Salta. Contributions to provenance in sedimentary sequences*.

3. Gondwana Research (Elsevier), QUALIS Capes A1 (ISSN -1342-937X). Título: *Chronostratigraphy of Cisuralian (early Permian) Irati Formation. Depositional sequence, paleogeographic and paleoenvironmental reconstruction of Western Gondwana*.

O capítulo II apresenta também dois artigos de co-autoria que já se encontra publicados.

CAPITULO 1 - FUNDAMENTAÇÃO DA TESE

1.1. Introdução

A presente pesquisa é uma continuidade dos estudos desenvolvidos durante o Mestrado. Nesse estágio, foram caracterizados de forma sistemática alguns níveis de argilominerais contidos na formação Irati, expostos, na época, por recente corte para a construção de açudes numa fazenda em Aceguá-RS. Os níveis foram coletados em campo e, posteriormente, foram realizados estudos laboratoriais (Difratometria de Raios-X - DRX, Microscópico Eletrônico de Varredura - MEV, Fluorescência de Raios-X - FRX) e identificação de assembleia de minerais magmáticos, o que revelou excelentes resultados e comprovando serem tufos, fácies estratigráficas correspondentes a depósitos piroclásticos de queda (Pyroclastic fall deposits - PFDs).

No Doutorado, buscou-se uma melhor compreensão da distribuição desses níveis nas sucessões de fácies da formação Irati e do uso como ferramentas para estudos geocronológicos, correlações cronoestratigráficas e tefrocronológicas, e reconstruções paleoambientais. Com este objetivo, a pesquisa buscou identificar novos níveis em toda a seção da Formação Irati, descrevendo alguns dos testemunhos de sondagem presentes na Litoteca Regional de Caçapava do Sul, da Companhia de Pesquisa e Recursos Minerais (LIR- CPRM, Caçapava do Sul, RS, Brasil).

Foram coletados sistematicamente no poço HV-44-RS níveis de argilitos cujas características aparentavam evidências de serem bentonitas evoluídas a partir de tufos, para posteriores confirmações em laboratório. Comprovados, em diferentes níveis, foram coletados zircões vulcanogênicos para a datação por U/Pb pelo método *laser-ablation inductively coupled plasma mass spectrometry* (LA-ICP-MS). Os dados foram satisfatórios, gerando a idade aproximada com as idades existentes na parte norte da formação (Santos et al., 2006; Rocha Campos et al., 2019).

Durante a caracterização, identificou-se a deficiente informação bibliográfica sob a relação entre PFDs em depósitos sedimentares, motivando assim outro estudo de caracterização de três diferentes níveis de PFDs. Assim, para este trabalho, utilizaram-se metodologias aplicadas para a identificação de cinza vulcânica, bentonitas e tonsteins, caracterizando pelos métodos de descrição faciológica, petrográfica, DRX, MEV, FRX e assembleia de minerais resistatos. Para isto, foram

utilizados amostras de cinzas vulcânicas oriundas de três situações: nível de cinzas vulcânicas da Quebrada de las Conchas, Salta- Argentina, coletada durante a atividade de campo da disciplina de Geologia dos Andes Centrais; nível de bentonita identificado na Formação Irati; e nível de tonsteins coletados pela pesquisadora Margot Guerra-Sommers.

Esses estudos constituíram a base para os artigos.

1.1.1. *Definições*

O PFD (depósito piroclástico de queda) representa uma unidade geológica de muitos usos técnicos, podendo acarretar confusão. A presente Tese segue a definição de nomenclatura de PFDs de Lowe (2008) (Figura 1). Os PFDs podem estar preservados em depósitos sedimentares na forma in situ e serem também chamados de Tephras, e podem estar alterados e serem chamados de Tufo. Tufos engloba outras nomenclaturas relacionadas ao contexto genético de alteração, podendo também ser chamado de Bentonita, Tonstein ou k-bentonita.

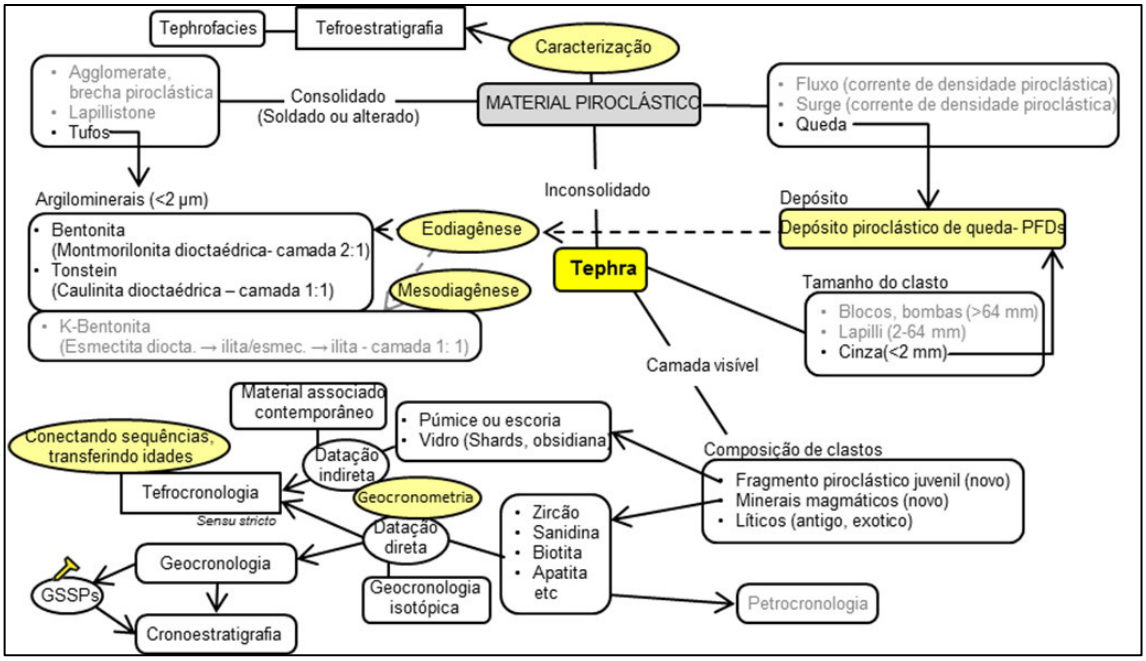

Figura 1- Nomenclatura de tephra, termos derivados e suas relações entre si (modificado de Lowe, 2008).

1.1.1. *Hipóteses de investigação*

As hipóteses deste estudo podem ser sintetizadas nos itens seguintes:

- Tephras de PFD in situ são bons indicadores das características química do magma, momentos antes da extrusão, e sua organização mineralógica representa o seu resfriamento para o estado sólido.
- Tufos de PFDs preservados em ambiente aquoso (marinho ou lacustre), como o da Formação Irati, são propícios a apresentarem uma evolução para uma composição mineralógica monominerálica de constituição montmorilonita.
- Tufos de PFDs preservados em ambientes paludal, como o da Formação Rio Bonito, deverão apresentar composição mineralógica monominerálica de constituição caulinítica.
- As observações mineralógicas e químicas em PFD, mesmo quando alterados, trarão respostas à influência dos diferentes ambientes durante os processos pós-deposicionais.
- Dentre os minerais magmáticos presentes em PFDs, os zircões possuem uma assinatura ígnea e podem ser considerados contemporâneos à deposição dos sedimentos, podendo ser utilizados como minerais balizadores da cronoestratigrafia para a Formação/Membro.
- As idades numéricas obtidas por datação geocronológica pelo método LA-MC-ICP-MS, em zircões vulcanogênicos, podem ser usadas como ferramenta estratigráfica geocronológica para o estudo em cronoestratigrafia.
- Tendo-se as idades numéricas de dois ou mais PFDs posicionados em perfil estratigráfico, é possível estabelecer a taxa de deposição para o pacote.
- Técnicas tefrocronológicas constituem uma ferramenta de correlação cronoestratigráfica entre bacias sedimentares.
- A descrição geocronológica das sucessões de ambientes sedimentares contribuem para aprimorar o entendimento da história evolutiva da bacia. Este entendimento é consistente para ser usado *como* proxies secundário nas definições cronoestratigráficas internacionais.

1.2. Objetivos da pesquisa

Este projeto de tese faz parte dos estudos de caracterização de PFDs em sequências sedimentares. Teve como objetivo aplicar aos diferentes PFDs, técnicas integradas de análise para proveniência, obtendo em cada técnica determinada informação, tais como as apresentadas na Tabela 1. Para tal realização, foram utilizadas amostras de cinzas vulcânicas sub-atuais da região andina e níveis Permianos de tonstein e de bentonita. Um dos objetivos específicos é comparar três diferentes níveis de PFDs, um composto por cinza vulcânica, outro por cinza transformada para bentonita e outro para tonstein, discutindo as alterações pós-deposicionais e as transformações para argilominerais em diferentes ambientes.

Outro objetivo foi o estudo em detalhe da sequência deposicional da Formação Irati ao longo do poço HV-44-RS, no qual identificaram-se oito níveis de PFDs evoluídos para bentonitas. Desses foram coletadas as amostras, caracterizadas e realizadas datações isotópicas U-Pb em zircões vulcanogênicos separados de cinco níveis de bentonitas, obtendo resultados satisfatórios em três níveis. Com os dados obtidos foi possível posicionar os níveis ao longo do perfil estratigráfico, determinar a cronoestratigrafia da Formação Irati e obter a taxa de deposição para todo o pacote do poço HV-44-RS. Correlações tefrocronológica com outros PFDs com idades semelhantes, a partir de uma sistemática consulta a publicações da Formação Irati e unidades cronoestratigráficas correlatas, permitindo interpretações paleogeográficas, paleoclimáticas e paleoambientais mais precisas.

Tabela 1 - Técnicas analíticas para estudos de proveniência em Bentonitas. Relações entre as diferentes escalas de estudos (modificado de Meunier, 2005).

Escala de observação			
	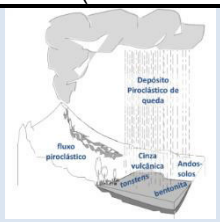	Método Revisão bibliográfica Técnica analítica Revisão bibliográfica sistemática Informação esperada Processo de formação de gênese. Paleogeografia contemporânea ao ambiente deposicional, possíveis eventos vulcânicos e relações entre sistemas. Informação geológica regional da bacia. Importância da camada no contexto geológico.	Análise de fácies sedimentares, e análise de relações entre minerais
	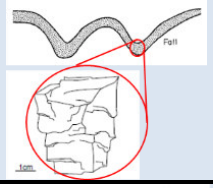	Método Descrição de campo e de amostra Técnica analítica Levantamento estratigráfico; Descrição faciológica. Informação esperada Identificação de fácies. Análise e descrição de fácies (e.g. cor, textura). Correlações entre sucessão de fácies	
	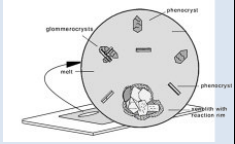	Método Microscópio petrográfico Técnica analítica Descrição petrografia qualitativa Informação esperada Identificação de minerais e relações de contato entre eles. Tamanho do mineral, relações de alterações e microestruturas.	
		Método Microscópio Eletrônico de Varredura (MEV) e Microscópio Eletrônico de Transmissão (MET) Técnica analítica Análise morfológica do mineral Informação esperada Identificação textural, visão 3D do mineral de argila e relações de contato entre eles. Obtenção do espaçamento entre as camadas	
	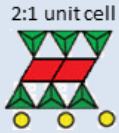	Método Difratometria de Raio X (DRX) e Infravermelho (IR) Técnica analítica DRX (Análise de rocha total, fração argila (<2µm) (N,G,C) e saturação): IR (Análise de rocha total no modo absorbance na faixa 4000 cm^{-1}- 400 cm^{-1} Wavenumbers (infravermelho médio)) Informação esperada Ferramenta básica para estudos mineralógicos e cristaloquímicos de rocha total e em diferentes frações. Mostra as distâncias interplanares e tipos de ligações químicas.	Análise elementares
	$(Si_{3.83}\ Al_{0.7})(Al_{1.32}\ Fe_{0.30}\ Mg_{0.38})(Ca_{0.43}\ K_{0.05}\ Mg_{0.03})O_{10}(OH)_2.nH_2O$	Método Fluorescência de Raios-X (FRX) Técnica analítica Análise de rocha total para elementos maiores (SiO_2; Al_2O_3; Fe_2O_3; MnO; K_2O; Na_2O; MgO; CaO; TiO_2; P_2O_5) e menores (Y; Pb; Ni; Cu; Sr; Zr; Zn; Nb; Rb; Cr; Ba). Informação esperada Composição química da rocha total para identificação da estrutura atômica. Fórmula química.	
	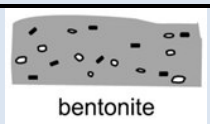	Método Concentração de minerais resistatos Técnica analítica Concentração de minerais resistatos em peneira 500 Mesh; Análise mineralógica em Lupa e em MEV. Informação esperada Identificação de assembleia de minerais magmáticos. Proveniência e Informações geológicas de gênese	Análise de assembleia mieral, quimica mineral e isotópica,
		Método Análise isotópica Técnica analítica LA-ICP-MS; CA-TIMS Informação esperada Razão de decaimento Isótopos $^{238}U/^{206}Pb$ e Idade geológica de cristalização. Outras diversas possibilidades de refinar a proveniência.	

1.3. Contexto geológico do objeto de estudo

Ocorrem PFDs em muitos eventos de erupções vulcânicas (Figura 2A). No entanto, a geração de grande volume e a maior capacidade de espalhamento está relacionada aos tipos de magma mais ácidos (rico em sílica), com viscosidade e poder explosivo. A energia das erupções vulcânicas destes eventos pode lançar material vulcânico a distâncias consideráveis, sendo que as cinzas são lançadas em grandes altitudes que, dependendo das condições climáticas, normalmente são carregadas através de correntes de ar atmosférico e percorrem centenas a milhares de quilômetros de distância a partir da fonte vulcânica até a sua deposição (e.g. Figura 2B). Dependendo do tamanho das partículas de cinza, o transporte aerodinâmico pode durar de dias a meses com capacidade para ultrapassar as barreiras fisiográficas do terreno e cobrir instantaneamente (na escala de tempo geológico) grandes superfícies do terreno (Figura 2C), num ambiente terrestre ou aquático. Geralmente, a transição dos PFDs com depósitos vulcânicos intermediários são perdidos pela erosão (Lajoie & Stix, 1992; Jerram e Petford, 2014).

Ambientes favoráveis à deposição e preservação da camada de cinzas na coluna geológica são corpos aquosos caracterizados por uma baixa energia de fluxo, como estuários, lagos, lagoas, paludal (pântanos), fundos de vale, marinho raso e o fundo do mar. Também podem ser encontrados em depósitos glaciais e desertos (Grim & Güven, 1978; Fisher & Schmincke, 1984; Formoso et al., 1997; Meunier, 2005; Huff, 2016). Quando preservados, PFDs formam camadas alogênicas que diferem quanto a aparência e composição na coluna estratigráfica, na maioria das vezes formando uma camada delgada e contínua com espessuras centimétricas, raramente podendo atingir a escala métrica e com um arranjo interno maciço a plano-paralelo. Os PFDs são compostos por material de origem vulcânica com granulação fina (Figura 2D), predominantemente cinzas vulcânicas com ou sem a participação de uma fração detrítica, e com contatos nítidos com as litologias adjacentes (Zuffa 1980; 1985; Bohor & Triplehorn, 1993).

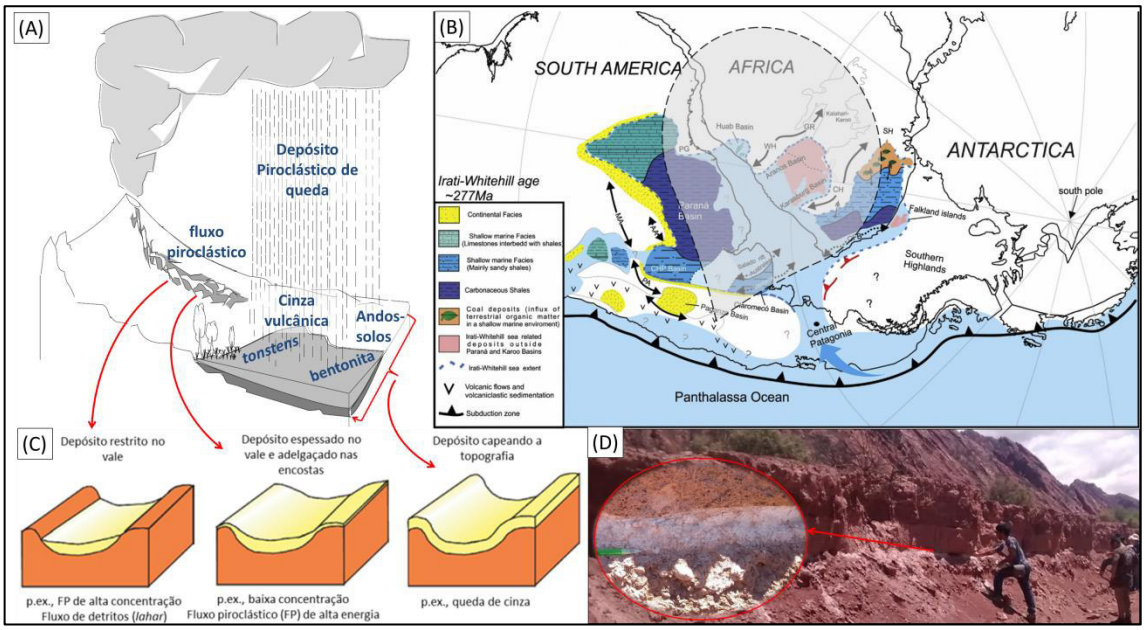

Figura 2 - Característica dos depósitos piroclásticos de queda em função da topografia (modificado de Meunier, 2005). Em (B) a reconstrução paleogeográfica e paleoambiental do Gondwana Ocidental durante o Cisuraliano (modificado de Bastos et al., 2021), e ao centro uma reconstrução de transportes de cinzas vulcânicas de um evento de erupção vulcânica explosiva que poderia corresponder a um nível de bentonita. Em (C) diferentes modelos de arquitetura deposicional formados por depósitos vulcânicos (modificado de Jerram e Petford, 2014). O PFD corresponde ao terceiro modelo. Em (D) PFD em Salta, Argentina.

Sendo a deposição dos PFDs considerada como um evento instantâneo no tempo geológico, a sua identificação numa seção sedimentar agrega um significado temporal, tornando-se marcadores cronoestratigráficos eficientes em sequências sedimentares. Os PFDs sendo formados a partir de material vulcânico contêm quantidades variáveis de fragmentos de vidro vulcânico associado com minerais cristalizados na câmara magmática, estes normalmente em quantidades subordinadas. São os minerais magmáticos que geram a possibilidade de aplicação de técnicas de datação geocronológica e obtenção da idade numérica da época de deposição, fornecendo informações adicionais que irão contribuir, por vezes decisivamente, para o entendimento da estratigrafia e geodinâmica da bacia sedimentar (Huff et al., 1997; Huff, 2016).

Como as cinzas são originalmente um material inconsolidado e de fácil erosão, quando incorporadas em ambientes terrestres e aquáticos de alta energia tendem a ser retrabalhadas formando camadas epiclásticas ou de arenitos-híbridos (Zuffa 1980; 1985). Em certas situações os PFDs podem conter duplicações de uma única erupção, com a parte superior da camada concentrando fragmentos epiclásticos de ambientes adjacentes. No entanto, as alterações pós-deposicionais mascaram a duplicação e, apesar de tais complicações, para a maioria dos fins estratigráficos, a idade da cinza retrabalhada pode ser considerada como a mesma

da camada de cinza original. Deste modo a estratigrafia de uma área pode ser reconstituída e a extensão lateral da camada original determinada (Fisher & Schmincke, 1984; Meunier, 2005; Jerram & Petford, 2014).

As cinzas vulcânicas contidas em PFDs in situ, quando se transformam para tufos, tendem a apresentar uma constituição final formada por argilominerais (Figura 2A), em que se destacam os minerais do grupo da esmectita. A variedade mais comum é a montmorilonita, um alumínio-silicato hidratado, que contém como cátions interfoliar o Na^{+}, Ca^{2+} e/ou Mg^{2+} (Grim & Güven, 1978. Formoso et al., 1997). Tonsteins e K-bentonita são também rochas geradas pela alteração de cinzas vulcânicas, sendo que as diferenças com a bentonita devem-se à mineralogia. Nos tonsteins, a argila principal é a caulinita e a K-bentonita (meta-bentonita) é composta por argilominerais de camadas mistas tipo ilita/esmectita (I/S) (Figura 3) (Grim & Güven, 1978; Formoso et al., 1997; Meunier, 2005; Huff, 2016).

No estudo da proveniência, consideram-se os minerais contidos na rocha sedimentar contêm o registro de informações microscópicas do mosaico geológico da área de origem e dos processos sob os quais os grãos que os constituem foram submetidos (intemperismo, transporte, diagênese) (e.g. Zuffa et al., 1995). No estudo dos PFDs utiliza-se a caracterização pelo modelo de proveniência genética. Na sistemática proposta, Zuffa (1985; 1987; 1991) estabelece uma classificação qualitativa dos constituintes. Sua classificação leva em conta, além das características composicionais (carbonáticos ou não carbonáticos), classificações temporais (contemporâneos ou não contemporâneos) e espaciais (intrabasinal ou extrabasinal) (Figura 4). Os tipos de constituintes não carbonáticos são sedimentos terrígenos, sedimentar químico, plutônico, vulcânico, vegetal e de modificações diagenéticas (envolvendo modificações mineralógicas e texturais, que tendem a ofuscar as características primárias dos grãos). Grãos contemporâneos são os depositados dentro do primeiro ciclo de sedimentação, e grãos não contemporâneos são reciclados de depósitos sedimentares erodidos. Os grãos extrabaciais têm sua origem de formação fora do ambiente de deposição da bacia, como os grãos gerados por atividades vulcânicas, e os grãos intrabaciais têm sua origem de formação dentro da bacia de deposição.

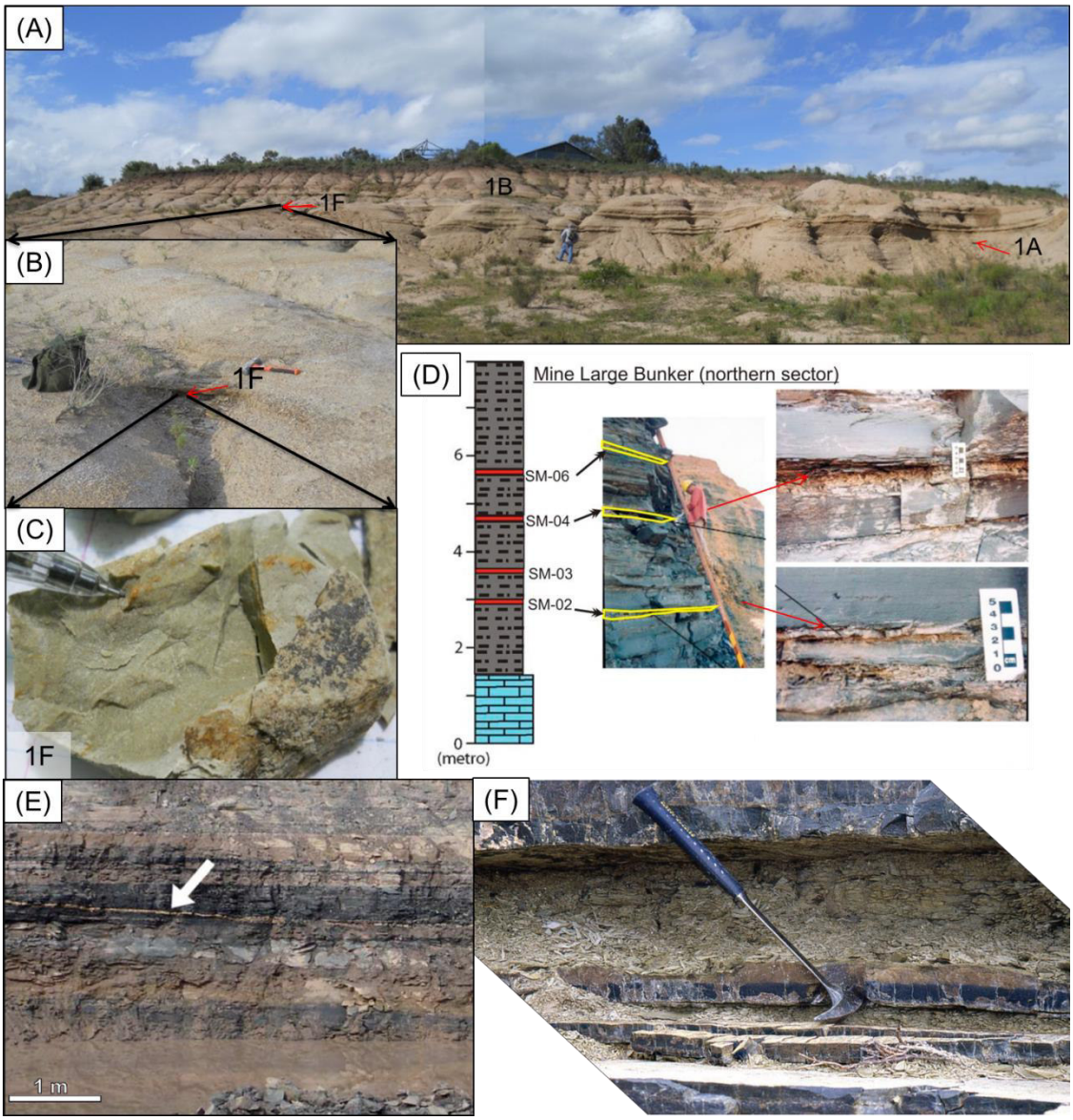

Figura 3 - Níveis alterados de PFDs identificados em levantamentos estratigráficos. Em (A, B, C) apresentam a visão geral do afloramento e respectiva aproximações da camada de bentonita e nível de bentonita da formação Irati. Em (D) apresentam na Mina PetroSix outros níveis de bentonita da Formação Irati (Costa, 2016). Em (E) apresenta um nível de tonstein em depósito permiano da Formação Rio Bonito (Simas, *et al*., 2013). Em (F) apresenta um nível em k-bentonita em depósito permiano da Formação Collingham (Huff, 2016).

A identificação de grãos vulcânicos contribui com importantes informações sobre o contexto geodinâmico. Em teoria, grãos vulcânicos contemporâneos a sedimentação podem chegar na bacia sedimentar de três maneiras diferentes: 1) por ejeção explosiva como queda de cinza, fluxo piroclástico ou pela erosão de depósito vulcânico penecontemporâneo ao ambiente sedimentar (epiclástico singenético); 2) pelo vulcanismo submarino intrabasinal; e 3) por ejeção explosiva localizada fora da província geotectônica da bacia (Zuffa, 1980).

Zuffa (1985) busca diferenciar as partículas vulcânicas, encontrando quatro grupos de estrutura principais (Figura 5). A diferenciação propicia implicações para

uma determinação das configurações da área de origem e da bacia deposicional. A primeira subdivisão relaciona-se à contextualização espacial, podendo ser produzida dentro da bacia ou fora dela; a segunda subdivisão relaciona-se à contextualização temporal, podendo ser fragmentos formados contemporaneamente ao momento da sedimentação (neo vulcânico) ou fragmentos providos da erosão.

Na classificação, o modelo com código NCEc (Não-Carbonático Extrabacial contemporâneo) enquadra os PFDs nos seguintes subtipos:

- NCE_{cV3} – proveniente de vulcanismo explosivo localizado fora da província geotectônica da bacia e transportado pelo vento.
- NCE_{cV2b} – proveniente de vulcanismo ativo contemporâneo à bacia e contido dentro da província geotectônica da bacia e transportado pelo vento.
- NCE_{cV2c} – proveniente de vulcanismo ativo contemporâneo à bacia e contido dentro da província geotectônica da bacia e transportado pela água.

Para a distinção entre estas classificações, Zuffa (1985; 1987) propõe etapas de análise da camada em campo integrado com informações específicas da reconstrução paleogeográfica da época. A distinção de PFDs em análise de campo leva em conta a observação dos minerais constituintes, grau de selecão e estrutura interna da unidade sedimentar. Numa primeira análise, deve-se distinguir se a unidade sedimentar apresenta constituição majoritária por grãos vulcânicos ou se há uma mistura com outros grãos siliciclásticos. Nesta distinção, unidades sedimentares constituídas majoritariamente por grãos vulcânicos podem representar depósitos contemporâneos (NCE_{cV2b}, NCE_{cV3} ou NCE_{cV4}) (Figura 5 e Figura 6), enquanto as unidades sedimentares mistas podem representar ou uma mistura de grãos antigos e contemporâneos ou apenas grãos antigos (NCE_{cV2a}, NCE_{cV2c}, NCE_{cV1} e NCE_{cv4}). Este modelo de classificação dos constituintes da rocha, além de fornecer informações do tipo de rocha da área fonte, permite obter uma melhor informação genética dos constituintes da rocha, como a dinâmica ocorrida na bacia na época da deposição e os controles estratigráficos e tectônicos atuantes na sedimentação.

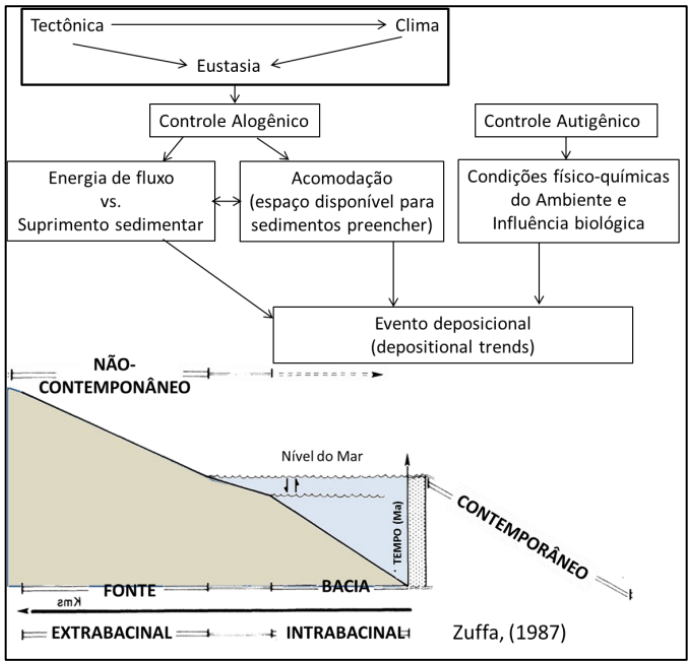

Figura 4 – Ilustração esquemática de características temporais e espaciais de partículas de areia siliciclástica em relação à área fonte dos sedimentos e bacia sedimentar (modificado de Zuffa, 1987).

CRITÉRIOS	TEMPORAL	ESPACIAL	COMPOSICIONAL	TIPOS DE GRÃOS FRAÇÃO AREIA	CÓDIGO DE IDENTIFICAÇÃO
TIPOS DE GÃOS	Conteporâneos (c)	Extrabacial (E)	Corbonato (C)	oólitos	CEc
				bioclastos	
				caliches	
				travertino	
			Não-carbonato (NC)	**VULCÂNICOS (V2a, V2b, V2c, V3)**	NCEc
				particulas de vegetais	
		Intrabacial (I)	Corbonato (C)	OÓLITOS	CIc
				BIOCLASTOS	
				INTRACÁSTOS	
				PELÓIDES	
			Não-carbonato (NC)	Glauconita	NCIc
				oxido de ferro	
				anidrita	
				fosfatos	
				clastos *rip-up*	
				VULCÂNICOS (V4)	
	Não conteporâneos (nc)	Extrabacial (E)	Corbonato (C)	CALCÁRIOS	CEnc
				DOLOMITOS	
			Não-carbonato (NC)	SILICICLÁSTICOS	NCEnc
				VULCANOCLÁSTICOS (V1b)	
		Intrabacial (I)	Corbonato (C)	calcáreos	CInc
				dolomitos	
			Não-carbonato (NC)	siliciclásticos	NCInc
				VULCANOCLÁSTICOS (V1a)	

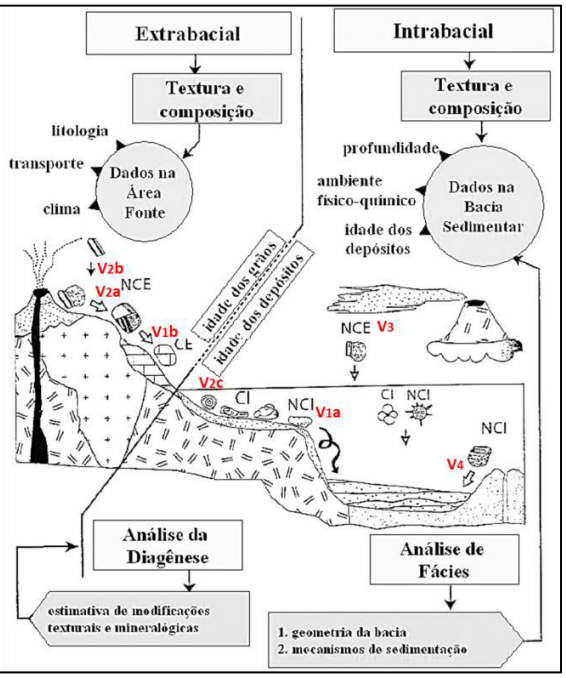

Figura 5 – Modelo representando as diferentes origens genéticas de grãos para bacias sedimentares, separando suas distribuições temporais (contemporâneos ou não contemporâneos), espaciais (intrabasinal ou extrabasinal) e composicionais. Os grãos assinalados em vermelho representam os diferentes tipos de gênese de grãos vulcânicos em uma bacia sedimentar (modificado de Zuffa 1985).

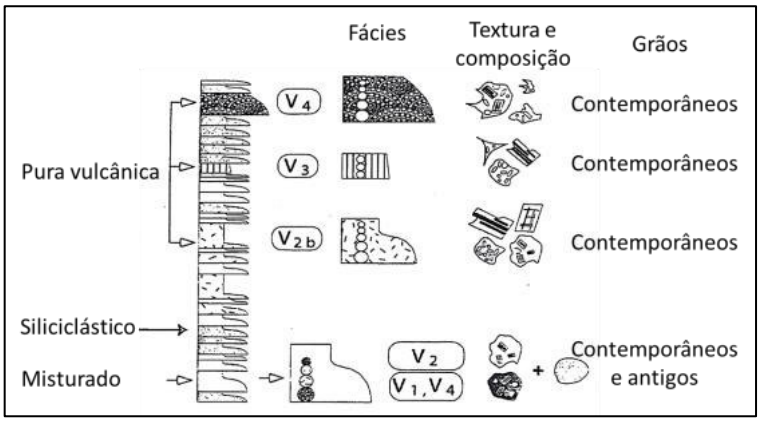

Figura 6 – Modelo de descrição em campo, comparando características faciológicas, mineralógicas e a interpretação prévia da gênese da camada (Modificado de Zuffa, 1985;1987).

A evidência de queda de cinzas contemporâneas (NCE_{cV2b} ou NCE_{cV3}) pode ser representada pela abundância de detritos vulcânicos morfologicamente imaturos (Figura 6), seleção de grão de moderada à alta, geralmente inalterados, e composições com tendência unimodais enriquecidas em fragmentos vulcânicos (pomes e partículas vítricas). Critérios comprobatórios são a presença de cristais magmáticos euédricos, minerais instáveis e fragmentos de rocha.

Já a distinção de vulcões explosivos localizados na área tectônica da bacia deposicional (NCE_{cV2b}) ou em domínios geotectônicos distintos (NCE_{cV3}), não diretamente relacionados ao sistema deposicional da bacia, geralmente apresenta dificuldades (Zuffa, 1987). Para isso, é importante a reconstrução paleogeográfica e suas configurações geotectônicas, em associação a um bom conhecimento da geologia e da estratigrafia regionais, para poder inferir a área-fonte e as reconstruções dos trajetos até a bacia deposicional e sua preservação.

Por exemplo, os estudos de Hermanns et al. (2000; 2008) identificaram que a camada de PFD encontrada nos depósitos quaternários de Salta tinha como origem o evento vulcânico *Alemanía Ash*. Este foi um magmatismo local, portanto, o PFD representa o tipo NCE_{cV2b}. Já os PFDs encontrados nos depósitos permianos foram reconhecidos através da reconstrução paleogeográfica, que obteve evidências que a região de vulcanismo se localizava na borda da placa litosférica, há quilômetros de distância, sendo, portanto, uma NCE_{cV3}. Estes PFDs, por terem os seus constituintes lábeis alterados e modificados pela diagênese somente podem ser classificados através do estudo dos minerais magmáticos resistatos.

1.4. Estado da arte do tema da pesquisa

O planeta Terra é um reator atômico, cuja reatividade no seu núcleo transfere por convecção calor e matéria para o manto. As correntes de convecção no manto superior promovem fusão e geração de magmas e a consequente movimentação das placas litosféricas sobrejacentes. A movimentação das placas promove, através dos ciclos tectônicos, modificações e evoluções constantes na litosfera (Faustinoni and Carneiro, 2015; Brito-Neves, 2020). Assim, a Teoria da Tectônica de Placas estabelece dois grandes tipos de mecanismos de trocas entre elementos químicos no interior e na superfície do planeta, o endógeno e o exógeno, separando-os e combinando-os segundo complexos processos de entropia e afinidades químicas, numa busca de novos equilíbrios termodinâmicos (Gill, 2014). Os processos endógenos ocorrem na crosta e no manto por eventos vulcânicos e metamórficos, produzindo conjuntos minerais magmáticos e ígneos. Os processos exógenos ocorrem na camada superficial da Terra, sendo resultantes da interação entre as rochas (litosfera e geosfera), o ar (atmosfera), a água (hidrosfera) e os organismos (biosfera), compondo o produto desta interação registrado principalmente nos pacotes sedimentares.

Especificamente, as manifestações de atividades vulcânicas representam manifestações de massa e calor do interior para o exterior do planeta, e podem ocorrer em diferentes escalas de tempo (desde horas, meses até milhões de anos). O **artigo 1** da presente Tese busca descrever o processos endógenos que levaram a formação dos minerais de zircão até o momento de sua extrusão. Já o **artigo 2** busca descrever o processo endógeno da lava e seu resfriamento para o estado sólido durante o evento vulcânico extrusivo, formando diversos fragmentos (minerais, rocha, constituintes amorfos).

As alterações da crosta terrestre causadas pela ciclos tectônicos interferem nas relações de transferência de calor e massa em toda a superfície terrestre. A depender da característica predominante do regime tectônico, de compressão ou distensão, os movimentos das placas propiciam compensações isostáticas da crosta terrestre (litosfera). Ocorrem portanto, processos de soerguimento com a formação de cadeias de montanhas (ex. orogênese), ou processos de subsidência e geração de depressões (ex. tafrogênese), propiciando o estabelecimento de áreas soerguidas e deprimidas. As áreas soerguidas e acima do nível de base (nível médio

dos mares) ficam expostas aos agentes exógenos (fatores climáticos e bióticos) que modificam as rochas e seus constituintes pelo intemperismo e erosão. As áreas deprimidas (bacias), por sua vez, recebem a transferência de massa gerada pela erosão dos produtos de intemperismo das áreas soerguidas, que gradativamente vão preenchendo com sedimentos as bacias (Faustinoni and Carneiro, 2015; Brito-Neves, 2020).

Na superfície terrestre, a água é o principal agente responsável pelos processos exógenos, atuando nas interações rocha-solução (processos químicos), fluido-partícula e fluido-substrato (processos físicos) e organismos-ambiente-substrato rochoso (processos biológicos). As reações físico-químicas de intemperismo em minerais em ambiente de baixa pressão e temperatura dependem da presença da água. Os minerais formados em ambientes endógenos são estruturas em desequilíbrio com as condições vigentes na superfície terrestre, e o intemperismo é um conjunto de reações que transformam as fases endógenas instáveis em estruturas estáveis nas condições físico-químicas superficiais. Os argilominerais são um conjunto de fases em equilíbrio com as condições reinantes em superfície e sua formação depende da composição do fluido presente no ambiente e da diferença entre as taxas de reação química e lixiviação (Curtis, 1977; Chamley, 1989; Worden & Burley, 2003; Meunier, 2005; Gill, 2014).

Em superfície, as cinzas e produtos vulcânicos são metaestáveis e facilmente sofrem influência dos processos exógenos. O **artigo 2** descreve os processos físico-químicos de fragmentos vulcânicos, promovendo transformações em fase sólida e sua neoformação para minerais de argilas (bentonita e tonstein), de acordo com dois ambientes sedimentares distintos, ambiente marinho e paludal. O **artigo 3** descreve alguns processos exógenos (biogeoquímicos e físico-químicos) que podem ter ocorrido em ambiente marinho de plataforma durante a vigência do Sistema Irati na Época Cisuraliana.

1.4.1. ***Estratigrafia***

A Estratigrafia, do Latim *stratum* + *graphia* do grego, é a ciência do ramo da Geologia responsável pela descrição de todos os corpos rochosos que formam a crosta terrestre e sua organização sistemática em unidades distintas, úteis e mapeáveis, a fim de estabelecer sua distribuição geográfica, sua sucessão cronológica e interpretar a história geológica. Ela divide os corpos rochosos, com base em suas propriedades ou atributos inerentes, em duas principais hierarquias distinguindo a Unidade Litodêmica, compondo as ígneas e metamórficas, e a Unidade Litostratigrafia, compondo as rochas sedimentares(Murphy & Salvador, 1999; NACSN, 2005).

As Unidades Litodêmicas classificam rochas ígneas e metamórficas, cuja distribuição espacial e temporal é controlada principalmente pelos eventos tectônicos, originando diferentes províncias geológicas.

Já as Unidades Litoestratigráficas estudam e decodificam os registros dos depósitos estratificados, decodificando a sucessão original dos registros das escrituras geológicas e ordenando-os. Os depósitos sedimentares são em grande parte estratificados no registro geológico (Figura 7) e seguem leis fundamentais: I) Lei da superposição de camadas; II) Lei do Princípio da Sucessão Faunística; III) Lei do Princípio do atualismo e evolucionismo; e IV) Lei de Correlação de Fácies.

Além das unidades hierarquias da Estratigrafia baseada em rochas, há outras diferentes unidades da Estratigrafia, muitas das quais se correlacionam com as Unidades Litoestratigráficas, baseada em: fósseis (Bioestratigráfica, Biocronologia e bioestratigrafia quantitativa), ciclos deposicionais (Estratigrafia de sequências), variações geoquímicas (Quimioestratigráfica), decaimento de radioisótopos (Geocronológica, Geocronométrica), inversões de polaridade magnética (Magnetoestratigráfica), ciclos astronômicos (Cicloestratigráfica) e rocha-tempo geológico isócrono (Cronoestratigráficas), entre outros (Gradstein et al., 2012; Ogg et al., 2016; Gradstein et al., 2020).Hoje sabemos que as principais informações da evolução da Terra estão materializadas, principalmente nos estratos rochosos preservados em bacias sedimentares (desde que ausente de deformações tectônicas), embora as regiões cratônicas também forneçam informações indiretas. As diferentes unidades estratigráficas são as ferramentas para decifrar e

compreender a história do nosso planeta, fornecendo uma base para a ordenação sistemática das mudanças dinâmicas terrestres, e estabelecer uma estrutura evolutiva para a discussão da história geológica. Os códigos de nomenclatura estratigráfica foram criados com a finalidade de apresentar formalização apropriada a diferentes unidades estratigráficas, usando terminologia e procedimentos para classificar e nomear, e para as comunicações científicas aceitáveis internacionalmente (Murphy & Salvador, 1999; NACSN, 2005).

Mas a questão não é tão simples quanto ler um livro. A leitura da “grafia” é normalmente apresentada de forma complexa e há alguns fatores complicadores. Aurell & Bádenas (1997) apresentam uma analogia interessante de pensar a Estratigrafia como um livro:

- O livro está escrito em uma língua geológica, contado por eventos geológicos. Suas anotações estão na matéria, estrutura e em suas relações de contatos;
- O livro está incompleto, faltam várias páginas e a maioria delas nunca foi escrita;
- As páginas estão espalhadas e desordenadas;
- A escrita, com o passar do tempo, fica borrada e se altera devido a processos pós-deposicionais e tectônicos;
- Algumas escritas são apagadas devido às rochas serem erodidas, dobradas, fraturadas e recicladas, podendo haver desconexão física entre os registros escritos;
- A maioria das páginas está enterrada.

Precisa-se assim de geocientistas que tem uma atuação comparável com a do bibliotecário, classificando, organizando e agrupando as páginas individuais (Figura 7). Somente assim poderão as informações da história contidas nesses livros serem lidas de forma sistemática e ordenada.

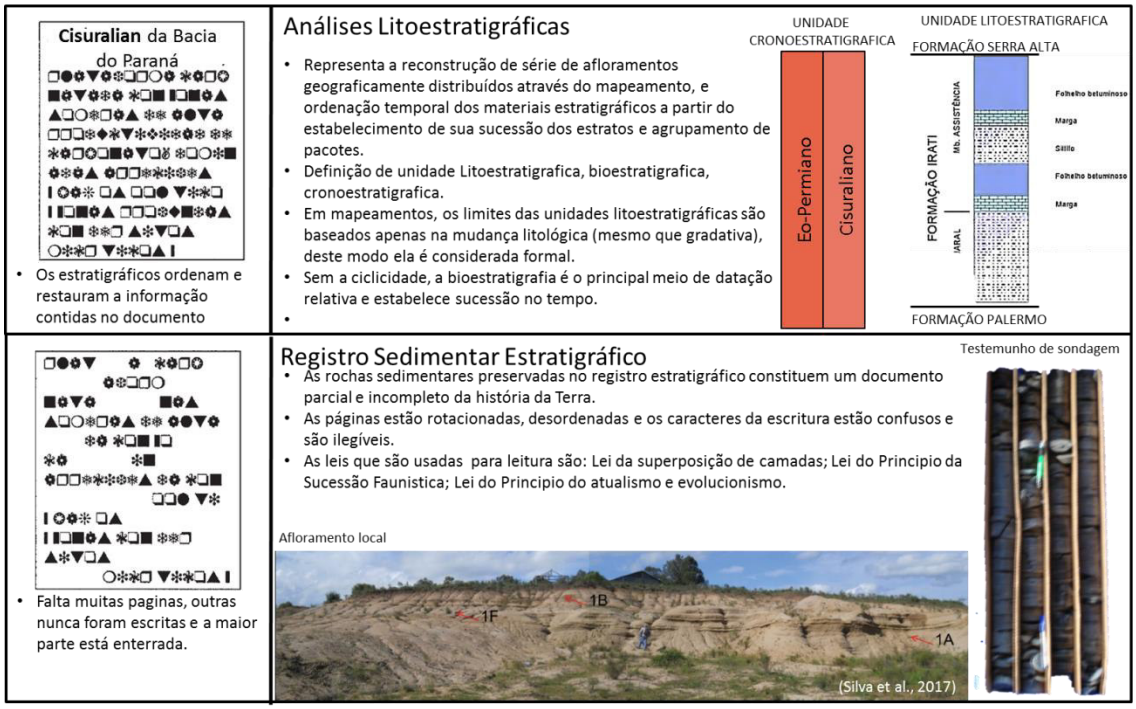

Figura 7 - Estudos desenvolvidos na tese e analogia do registro estratigráfico e análise litoestratigráfica com as tarefas de coleta de dados na preparação de um livro (Modificado de Aurell & Bádenas, 1997).

Análise Litoestratigráfica

Sobre a superfície terrestre, as interações fluido-partícula e fluido-substrato da água atuam em ciclos de intemperismo, erosão e transporte dos materiais terrígenos para deposição em bacias sedimentares. Tal ação tenderia transformar a superfície da Terra em uma grande área aplainada, porém este clímax não é alcançado devido a ação das forças endógenas que movimentam as placas tectônicas. A interação da tectônica, eustasia e clima (Figura 4 e Figura 8) são as principais forças geológicas motrizes influenciadoras do processo de sedimentação. Elas constituem os controles alogênicos, configurando as modificações das áreas fontes até e nas bacias sedimentares ao longo do tempo (Amorosi & Zuffa, 2011), originando muitas vezes ciclicidades nos processos sedimentares.

Os processos sedimentares trativos (fluido-substrato) geram diversidades de leitos durante a deposição (ex: Figura 9), preservando estruturas em pacotes sedimentares. Já os processos sedimentares em suspensão (fluido-partícula) geram depósitos em grande parte, constituindo estruturas plano-paralelas. Os estudos destas estruturas propiciam entendimento de processos deposicionais distintivos, caracterizando fácies, como sendo uma combinação particular de litologia, estruturas físicas e biológicas de diferentes corpos de rocha acima, abaixo e

lateralmente adjacentes (Reading, 1996; James & Dalrymple, 2010). As sucessões de fácies podem preservar registros dos processos deposicionais que ocorreram no momento da formação, podendo evidenciar outras configurações por mudanças composicionais e texturais de fácies sedimentares.

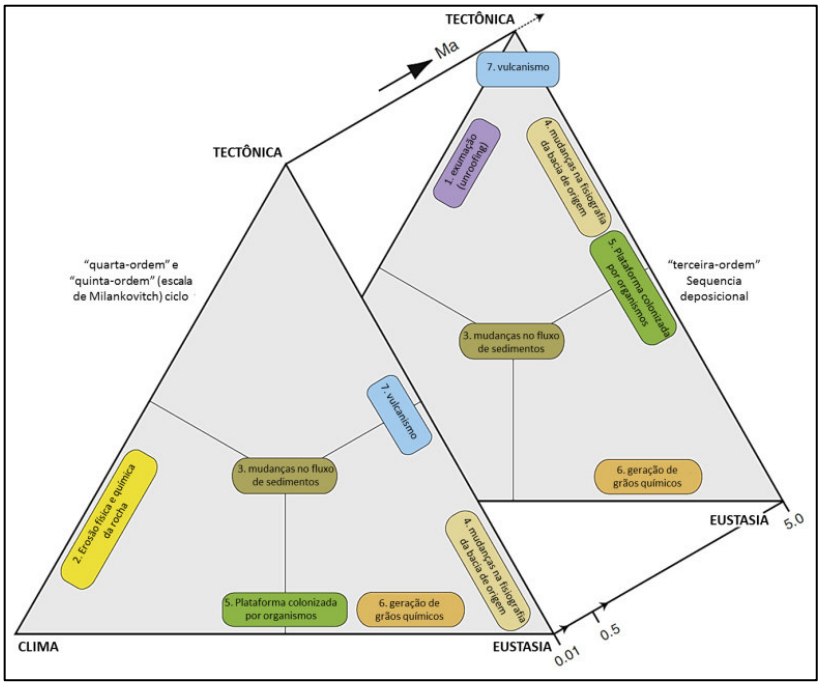

Figura 8- Fatores alogênicos controladores de mudanças composicionais do arenito, classificados de acordo com a influência relativa da tectônica, do clima e da eustasia. Os triângulos não incluem fatores autogênicos, nem fatores que controlam mudanças petrofácies (Modificado de Amorosi & Zuffa, 2011).

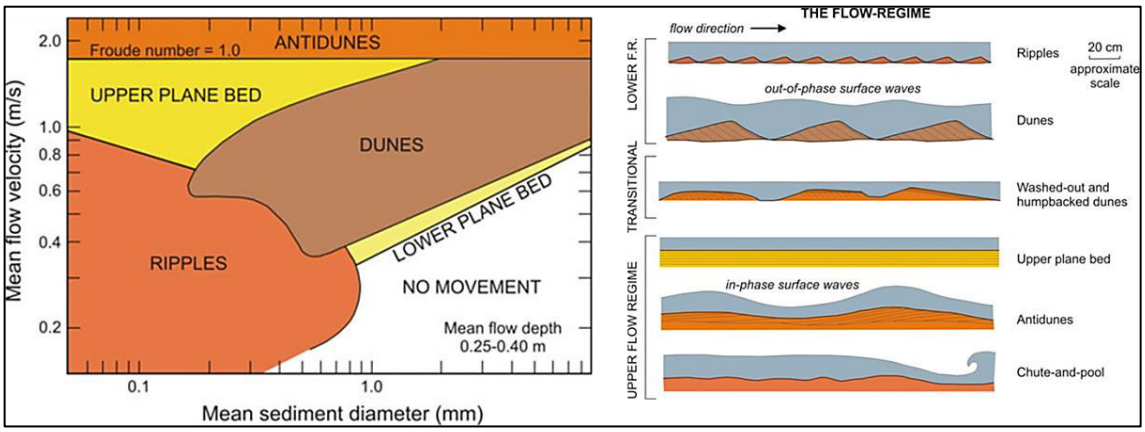

Figura 9 - Campos de estabilidade de formas de leito em areia e lodo em uma profundidade de fluxo de 25–40 cm e as diferentes formas de leito que se desenvolve com o aumento da velocidade do fluxo (Modificado de Miall, 2016).

A Formação Irati, foco da tese, é constituída em grande parte por estruturas plano-paralelas, com poucas fácies representativas de estruturas trativas. Já os PFDs estão relacionados com processos sedimentares distintos, pois seu agente de

transporte foi aerodinâmico e a deposição ocorreu por queda das cinzas vulcânicas, preservando assim estruturas maciças ou plano-paralelas.

Os registros dos processos deposicionais ao longo da sucessão faciológica evidenciam mudanças ambientais nas bacias sedimentares, registrando parcialmente os processos superficiais da Terra nos preenchimentos estratais, distribui formando arranjos arquiteturais. Assim, seus eventos (pequenos e grandes) e intervalos (curtos e longos) são os principais arquivos para o estudo da história geológica da Terra, particularmente em sucessões estratigráficas e pelos vários sinais guardados, onde evidencia a importância da Cronoestratigrafia (Gradstein et al., 2012; Ogg et al., 2016; Gradstein et al., 2020). No entanto, devido aos eventos tectônicos e a atuação do intemperismo estarem continuamente alterando os pacotes sedimentares, e a vida ter diversificado durante o Éon Fanerozóico, os registros em bacias sedimentares documentam principalmente a história geológica e a evolução durante o Éon Fanerozóico (Figura 10).

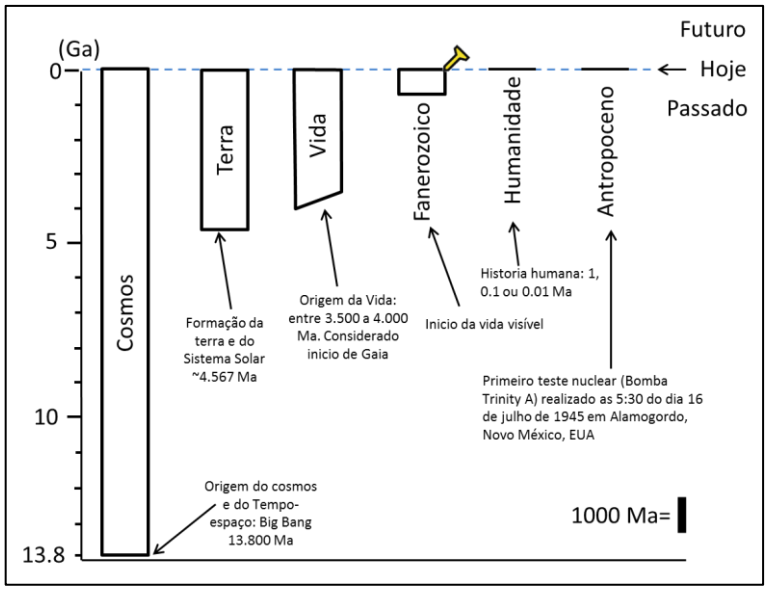

Figura 10 – Escala do tempo Cósmico. A história da Terra começa após 2/3 do início do Cosmos. Os registros em rochas de vida microscópica surgem logo depois. A vida visível surge após 540 Ma, dando início ao Éon Fanerozóico. A história do homem, seja considerada começando 1.000.000, 100.000 ou 10.000 anos atrás, representa não mais do que uma linha tênue no diagrama. O Antropoceno é uma unidade Geológica ainda informal, cujo GSSP foi definido no ano de 1945, 76 anos atrás.

Neste entendimento, o **artigo 3** busca descrever a história geológica vigente durante o Éon Fanerozóico, descrevendo os processos de preenchimento da bacia do Paraná durante a formação do sistema Irati, durante o Cisuraliano.

Estratigrafia de sequência

A estratigrafia de sequência é uma ferramenta metodológica aplicada para análise e interpretação do arcabouço dos pacotes sedimentares. Trabalha sob o viés de estratos repetitivos e geneticamente relacionados, limitados por superfícies de erosão, não deposição, ou suas conformidades correlativas. O objetivo principal é reconstruir o ambiente sedimentar e a sucessão de eventos que levaram ao preenchimento dos espaços de uma bacia ao longo do tempo (registro cronoestratigráfico) (Figura 11).

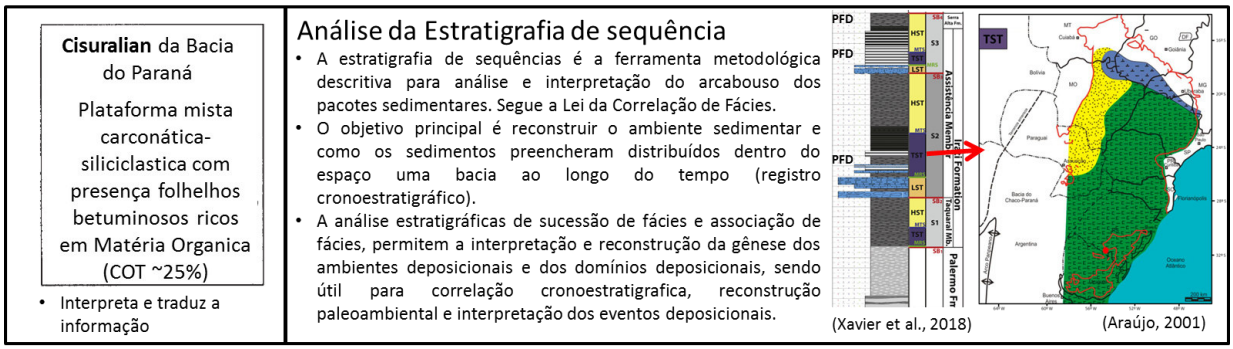

Figura 11 - Estudos desenvolvidos na tese e analogia da análise por estratigrafia de sequência com as tarefas de coleta de dados para a preparação de um livro.

Seu princípio estrutural é a Lei de Correlação de Fácies, a qual reconhece que as fácies que ocorrem em uma sequência vertical concordante guardam relações genéticas entre si dentro de um contexto deposicional, desde que registradas em registro estratigráfico físico sequencial e não separadas por “discordâncias”. Mudanças no ambiente, como variações eustáticas provocam alterações do cenário deposicional, gerando movimentações de fácies que coexistem lateralmente, apresentando, então, numa sucessão vertical de fácies geneticamente relacionadas no ambiente sedimentar. No entanto, a dedução dos ambientes deposicionais mais prováveis, nos quais os processos deposicionais inferidos podem ter operado, tornam a análise e correlação de fácies um conceito abstrato.

Para desenvolver a leitura de pacotes sedimentares, através da Estratigrafia de Sequências, há muitas definições organizadas em hierarquia de ordens de sequência (e.g. Reading, 1996; Walker & James, 1992; Catuneanu, 2006; James & Dalrymple, 2010; Boggs, 2014; Miall, 2016), listadas na tabela abaixo (Tabela 2):

Tabela 2 – Definições de conceitos interpretativos da Estratigrafia de Sequência.

Facies: *a body of rock characterized by a particular combination of lithology and physical and biological structures that bestow an aspect ("facies") that is different from the bodies of rock above, below and laterally adjacent. The characteristics used to define facies are generally those that have genetic significance (James & Dalrymple, 2010).*
Facies Succession: *a vertical succession of facies characterized by a progressive change in one or more parameters such as the abundance of sand, grain size, sedimentary structures, bed thickness or faunal composition (James & Dalrymple, 2010).*
Facies Association: *groups of facies genetically related to one another and which have some environmental significance (Collinson, 1969, p. 207).*
Depositional Environment: *geographic and/or geomorphic area characterized by a distinct assemblage of depositional processes (James & Dalrymple, 2010).*
Depositional System: *three dimensional assemblage of lithofacies, genetically linked by active or inferred processes and environments (Posamentier et al., 1988). It embraces depositional environments and the processes acting therein over a specific interval of time. The deposits of contemporaneous depositional systems form systems tracts.*
Parasequence: *is a relatively conformable succession of genetically related beds or bedsets bounded by marine-flooding surfaces and their correlative surfaces (Van Wagoner, 1985). A relatively conformable succession of genetically related beds or bedsets bounded by marine flooding surfaces and their correlative surfaces (Posamentier et al., 1988).*
Systems Tract: *a linkage of contemporaneous depositional systems (Posamentier et al., 1988), forming the subdivision of a sequence. Systems tracts consist of conformable strata that were deposited during a particular segment of an accommodation (or base-level) cycle. Up to four systems tracts can be identified within a sequence: highstand systems tract (HST), falling-stage systems tract (FSST), lowstand systems tract (LST) and transgressive systems tract (TST).*
Sequence: *a relatively conformable succession of genetically related strata bounded at its top and base by unconformities and their correlative conformities... it is composed of a succession of systems tracts and is interpreted to be deposited between eustatic fall inflection points (Posamentier et al., 1988). A succession of strata deposited during a full cycle of change in accommodation or sediment supply (Catuneanu et al., 2009). Such cycles can range in duration for a few thousand years to many millions of years. Usually, they are taken to be bounded by unconformities and their correlative conformities (James e Dalrymple, 2010).*
Sequence Boundary (SB): *the surface separating two sequences. Different workers place this surface at different locations within a depositional cycle (Catuneanu et al., 2009). It is most commonly placed at the subaerial erosion surface and at the correlative conformity that occurs in the area seaward of the lowstand shoreline. When defined in this way, the sequence boundary falls close to the lowest point in the relative sea-level cycle.*
Correlative Conformity (CC): *the conformable surface within the basin that is temporally equivalent with the tip of the subaerial unconformity (James & Dalrymple, 2010).*
Unconforniity: *A surface separating younger from older strata, along which there is evidence of subaerial erosional truncation... or subaerial exposure, with a significant hiatus indicated" (Posamentier et al., 1988). A surface at which there is a 'significant' gap in time, caused by a combination of non-deposition and erosion. Most such surfaces are formed in subaerial settings during a relative lowstand of sea level. However, they can form in other ways, such as by non-deposition (with or without erosion) in distal marine environments. Subaerial unconformity surfaces and their correlative conformities are used as sequence boundaries. In this context, 'significant' necessitates that the temporal gap is a substantial fraction of a cycle of base-level change (James & Dalrymple, 2010).*

Ao contrário de outras ferramentas que apresentam como unidade fundamental a menor unidade estudada (ex. geoquímica tem o elemento químico como unidade fundamental; a geocronologia isotópica tem a data como unidade fundamental), a estratigrafia de sequências tem como sua unidade fundamental não as fácies, mas a sequência, o que pode gerar confusão de interpretação espacial. Definindo isso, é possível a reorganização do modelo de arranjo das hierarquias realizada por Walker & James (1992), para um modelo que represente as diferentes definições dentro de uma unidade fundamental de sequência (Figura 12).

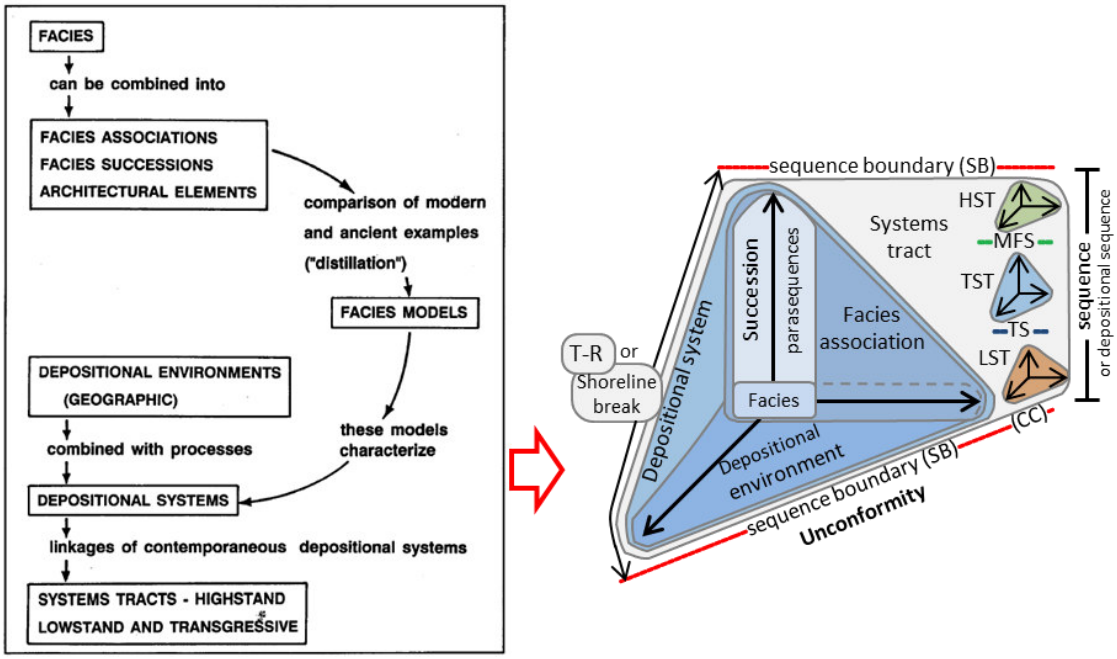

Figura 12 - Modelo do arranjo das hierarquias das unidades da estratigrafia de sequência (Walker & James, 1992) e modelo do arranjo das hierarquias dentro de uma unidade fundamental.

A sequência é limitada por superfícies de inconformidades (*sequence boundary* - SB) e suas conformidades correlativas (*correlative conformities* - CC), ao longo da qual há evidências de exposição erosional subaéreo (e, em algumas áreas, erosão submarina correlativa), indicando um hiato deposicional significativo (Mitchum, 1977). Em função da existência de vários tipos de contatos estratais (nítido, erosivo, gradacional etc.), o contato entre as fácies assume uma vital importância para a interpretação das relações de fácies (interpretação dedutiva). Entre dois limites de sequência, essa é composta por estratos geneticamente relacionados nos quais são interpretadas as fácies e suas inter-correlações (fácies, sucessão de fácies, associação de fácies, ambiente deposicional, sistema deposicional) (Figura 12).

A análise de sucessão de fácies, em conjunto com a associação de fácies, possibilita analisar os processos sedimentares e ter uma melhor compreensão das relações espaciais dos sedimentos em uma sequência formada num tempo relativamente definido, de uma maneira que não é possível usando simples correlações litoestratigráficas. Permite, assim, interpretar o cenário de sedimentação do ambiente deposicional, isto é, um compartimento geomorfológico da superfície da Terra.

O **artigo 1 e 3** utilizam as interpretações de três ciclos deposicionais na Formação Irati observadas no poço HV-44-RS, interpretados sob o viés da estratigrafia de sequência e descrito em Xavier et al. (2018). Estes três ciclos

deposicionais foram estendidos por correlações tefrocronológicas para outras áreas da bacia, possibilitando associações de fácies e interpretações dos diferentes ambientes deposicionais.

Para ajudar na análise e correlação de fácies e utilizando-se dos princípios do atualismo, foram desenvolvidos concomitantemente os modelos de fácies para uso como analogia (ex: Figura 12). Os modelos de fácies representam um conjunto harmônico de fácies existentes em determinados ambientes, obtidos das interpretações ambientais em: I) ambientes de sedimentação atuais; II) sucessões de fácies, associações de fácies e elementos arquiteturais e depósitos sedimentares; e III) ensaios de simulação laboratorial. Usa-se destas abordagens interativas para compor a "bíblia" de Modelos de fácies (ex: Walker and James, 1992; James & Dalrymple, 2010; Boggs, 2014; Miall, 2016), que são usados para previsões em novas análises de fácies, constituindo assim uma maneira sofisticada de chegar a interpretações ambientais em depósitos sedimentares (Figura 13) (James & Dalrymple, 2010; Miall, 2016).

Há duas vertentes conceituais do uso de modelos de fácies (Borghi, 2000):

- Modelo de fácies generalistas (ex: Walker & James, 1992; James & Dalrymple, 2010; Miall, 2016): é uma simplificação idealizada de determinado sistema deposicional, devendo representar um sumário geral das relações faciológicas representativas de um ambiente de sedimentação. Este modelo, *stricto sensu*, deveria conjugar o maior número possível de casos de estudo, despindo-se da(s) fácies (ou das relações entre fácies) que, específicas a certos casos considerados particulares, representam um ruído à sua comunicação global. Deve ser usado como: (i) norma para propostas de comparação; (ii) guia para outras observações; (iii) previsor de novas situações; e (iv) base integrada para a interpretação paleoambiental.
- Modelos de fácies locais (ex: Xavier et al., 2018), em contrapartida, julgam importante estabelecer exatamente as relações particulares, locais, de um caso de estudo.

O trabalho de Xavier et al. (2018) descreve um modelo de fácies local para a Formação Irati, descrito no **artigo 3** para correlacionar com outros modelos parecidos da bibliografia. Assim, foram utilizados para as reconstruções

paleoambientais de domínios deposicionais em diferentes tratos de sistemas, desenvolvidos por Araújo (2001).

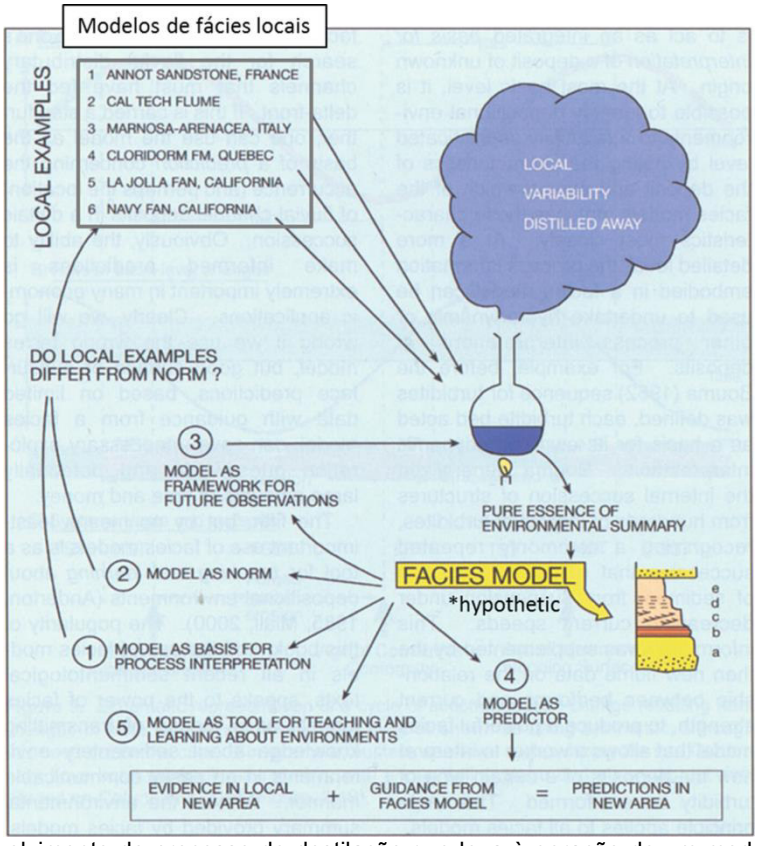

Figura 13 - O desenvolvimento do processo de destilação que leva à geração de um modelo de fácies, usando como exemplo depósitos em leque submarino (modificado de James & Dalrymple, 2010).

Correlações cronoestratigraficas

No entanto, nem todos os processos deposicionais são cíclicos, condicionados estritamente pela variação da eustasia ou linha de costa da bacia. Os registros dos eventos de transgressões e regressões estão misturados com registros de outros eventos deposicionais singulares, contribuindo para certo caráter caótico (caos determinístico) nas relações entre fácies. Os eventos deposicionais singulares podem ser muitas vezes “catastróficos”, formados em curto espaço de tempo, ou gerados por processos alocíclicos (governados por mecanismos exógenos ao ambiente deposicional), os quais podem provocar mudanças ambientais da bacia. Os pacotes sedimentares comportam diversos tipos de registros (Einsele & Seilacher 1982; Einsele et al., 1996; Boggs, 2014; Miall, 2016):

- Mudanças estratigráficas que possam ser reconhecidas na litologia, como: eventos estratigráficos (ex: transgressão-regressão do nível de base, mudança

na linha de costa, anoxia marinha; inunditos; impactos de astroblemas, etc.), proveniência sedimentar (ex: mudança na taxa de aporte sedimentar, mudança de proveniência sedimentar do paleo-embasamento, variação tectônica) e vulcânicos (ex: depósitos vulcânicos, como: lava, fluxo piroclástico e PFDs);

- Mudanças biológicas taxonomicamente reconhecidas nos fósseis (ex: surgimento, evoluções ou extinções de parcela da flora e fauna da época);
- Mudanças climáticas (ex: depósitos glaciais, evaporitos, pacotes de sedimentos vermelhos, depósitos de carvão etc.); e/ou
- Mudanças isotópicas ambientais registradas como proxies (ex: irídio procedente de astroblema, $\delta^{18}O$, $\delta^{34}S$, $\delta^{13}C$, $pCO_{2\ atm}$).

Esses eventos deposicionais, constituindo-se em unidade estratigráfica material mensurável, podem ser interpretados como registro da história geológica da Terra (Murphy & Salvador, 1999). Exemplos de coexistência entre depósitos cíclicos e de eventos deposicionais em pacote sedimentar, são apresentados por Boggs (2014) (Figura 14).

Deve-se buscar também correlacionar os depósitos gerados por eventos singulares com os registros cronoestratigráficos locais, regionais e/ou globais, em rochas estratificadas ou não estratificadas (ex: fases orogênicas e LIPs). Havendo alguma correlação, esses depósitos podem se tornar um marco cronoestratigráfico, passíveis de correlação (Figura 15).

Os três artigos discutem a gênese extrabacial de PFDs depositados em bacias sedimentares, correlacionados a províncias vulcânicas, como as que existiram no Permiano durante a Fase Orogênica San-Rafaélica. Como discutido no artigo 2, os PFDs podem interagir com o ambiente sedimentar; no entanto, geralmente, não geram alteração no registro sedimentar. O Artigo 3 discute outros **eventos deposicionais** singulares de fatores extrabaciais, que podem ter influenciado no ambiente e na deposição da Formação Irati. Alguns desses eventos foram as transgressões e regressões oceânicas do Pantalassa, evento de depósitos evaporíticos, associando a regressão e eventos climáticos globais, eventos de anoxia do substrato associando a transgressão, subsidência por flexura crustal provocada pela orogenia na borda do continente Gondwana, evento de queda de bólido e formação de *bonebeds,* contendo fósseis de *mesosaurídeos.*

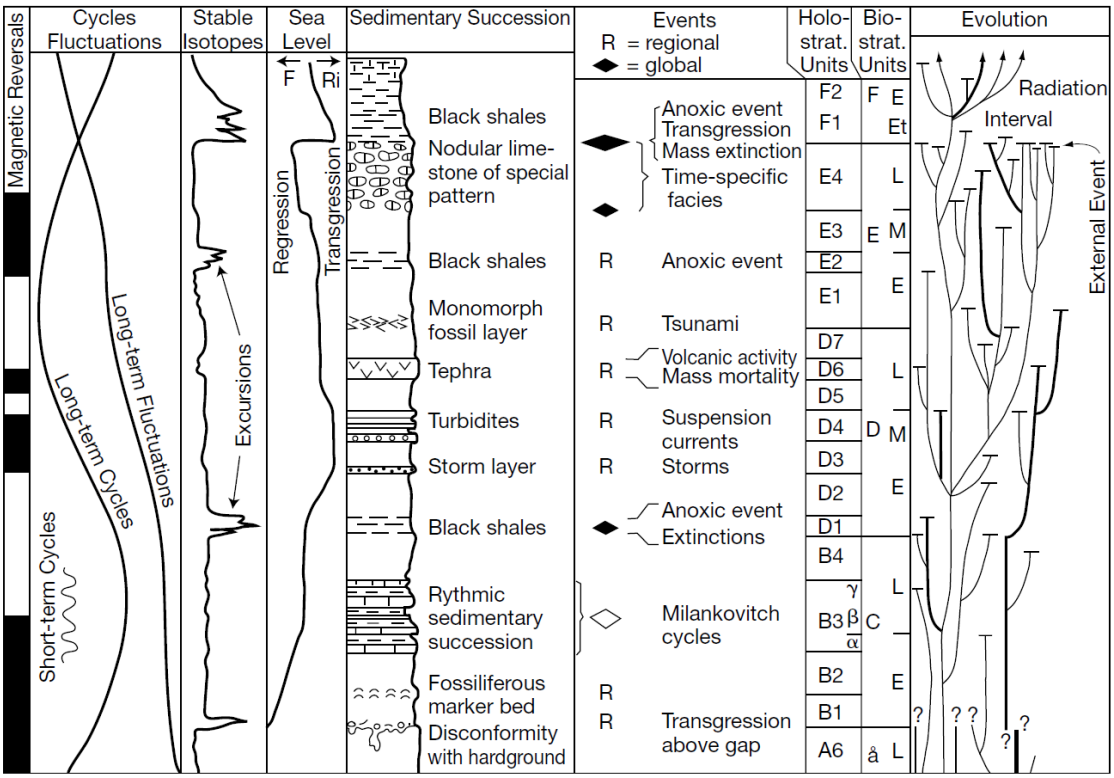

Figura 14 - Ilustração esquemática de depósitos e eventos que são úteis na correlação cronoestratigráfica. Nível do mar da coluna: F = queda, Ri = elevação (Boggs, 2014). Na figura, o PFD corresponde à camada de tephra.

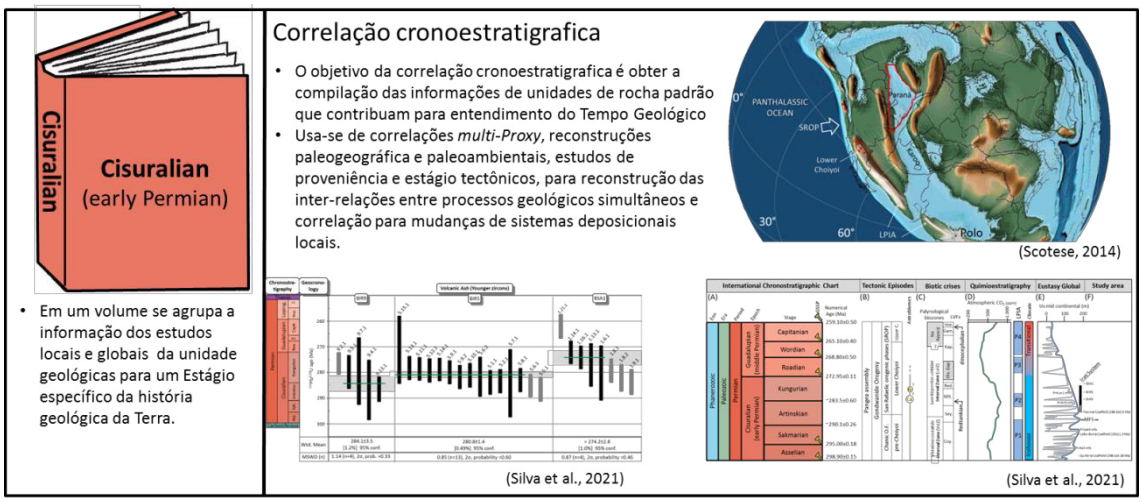

Figura 15 - Analogia entre os estudos estratigráficos desenvolvidos na tese envolvendo correlações cronoestratigráficas e as tarefas de coleta de dados na preparação de um livro.

Uma das questões importantes na estratigrafia é o entendimento de como são datados os depósitos sedimentares. A calibração da cronoestratigrafia, com dados de geocronometria, promove um aumento na resolução temporal. O principal mecanismo é através de unidades de origem vulcânica em meio aos pacotes sedimentares, como os PFDs e podem ser considerados como a principal unidade litoestratigráfica para obtenção de dados de Geocronologia radioisotópica e passíveis de uso em geocronometria.

Possivelmente, esses depósitos contêm minerais magmáticos cristalinos, que preservaram elementos radioativos durante sua formação. Depois de cristalizados, funcionam como um sistema fechado, preservando o isótopo radiogênico pai e ao longo do decaimento o isótopo filho, tendo na razão do decaimento radioativo o foco para obtenção da idade numérica. O principal mineral para este fim é o zircão (Figura 16) com uma temperatura de fechamento ou de cristalização da ordem de 800º a partir da qual é mantido o registro da razão $^{206}Pb/^{238}U$. Corfu et al. (2003), Alan (2018) e Reiners et al. (2018) apresentam caracterizações sob as diferentes gêneses de zircões, que podem influenciar em sua heterogeneidade e no uso do método analítico.

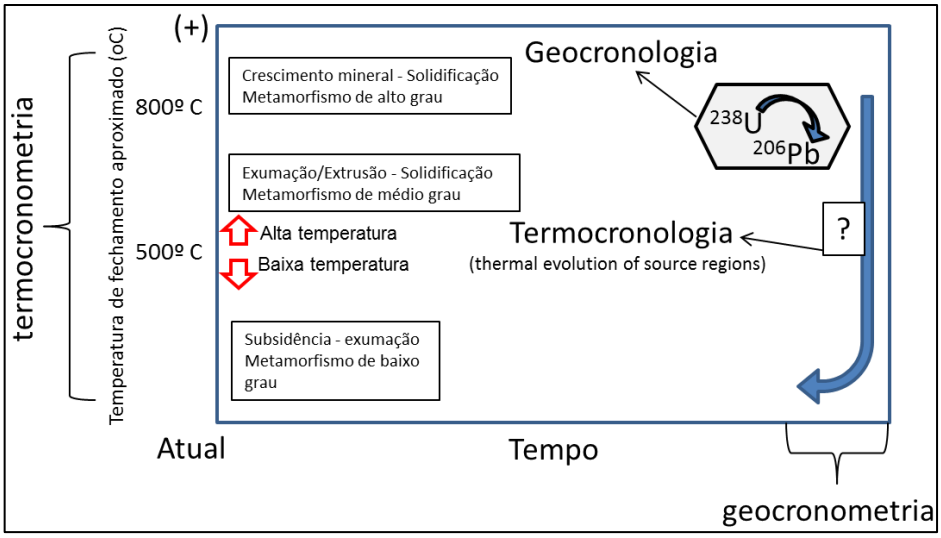

Figura 16 – Gráfico de termocronometria para Minerais Magmáticos contidos em PFDs. O gráfico demonstra a fase de fechamento do zircão por volta de 800º C. A idade geocronométrica entre o zircão e outros minerais magmáticos, com diferente termocronológica, será muito próxima devido a terem se formado pelo rápido resfriamento.

No vulcanismo, no momento da erupção, o zircão tem seu sistema cristalino fechado, dando início ao registro do decaimento radioativo (Figura 16) e imediatamente após os PFDs são depositados em superfície e preservados junto aos sedimentos nas bacias adjacentes. Assim, a idade numérica de PFDs representa o momento isócrono da deposição sedimentar. Um nível de PFD com idade numérica é utilizado como ferramenta geocronológica para calibrações cronostratigráfica dos depósitos sedimentares. Com duas ou mais idades numéricas de diferentes níveis de PFDs, torna-se favorável a possibilidade de calibração do balanço de massa dos depósitos sedimentares (isto é, taxa sedimentar: volume de sedimento por unidade de tempo).

A abordagem possibilita no depósito sedimentar um controle geocronológico com resolução, precisão e exatidão e o refinamento dos estágios cronoestratigráficos. Esse mesmo método é utilizado na biocronologia para estabelecer FADs (first appearance datum) de grupo fóssil (Boggs, 2014; Miall, 2016).

O **artigo 1** descreve o método de obtenção de idade numérica por Geocronometria do tempo-geológico, sendo o PFD a principal unidade sedimentar usada para a obtenção geocronológica para a reconstrução cronoestratigráfica de depósitos do Fanerozóico. No artigo é apresentado o estudo de três níveis de PFDs do poço HV-44-RS como proxies da Formação Irati, calibrando-a na cronoestratigráfica e avaliando a sua taxa deposicional. A correlação tefroestratigráfica e os PFDs identificados na mina PetroSix confirmaram a extensão deposicional da Formação Irati.

A informação de mudanças climáticas é registrado em várias unidades litoestratigráficas específicas, como carbonatos, fósseis, microfósseis, evaporitos, folhelhos, entre outros, tornando-os arquivos naturais. O uso *multi-Proxy* da estratigrafia isotópica contribuiu com informações climáticas relevantes para a determinação das condições biogeoquímicas do passado (ex: Qie et al., 2019). Gráficos de estratigrafia isotópica (ex: $\delta^{18}O$, $\delta^{34}S$, $\delta^{13}C$, $pCO_{2\ atm}$) são gerados pela compilação de dados de análise isotópica em unidades sedimentares de equivalência cronoestratigráfica (e.g. Gradstein et al., 2012; Ogg et al., 2016; Gradstein et al., 2020). Trata-se de um volume com texto aberto, trabalhando de forma retroalimentar (*feedback*) e melhorado à medida que novos dados vão sendo obtidos em diferentes depósitos sedimentares.

O uso de mapas de reconstrução paleogeográfica (ex: Scotese, 2014), paleoclimática (ex: Boucot et al., 2013) e paleoambiental (Araújo, 2001), possibilita que a correlação cronoestratigráfica seja feita sob uma organização espacial, obtendo base para informações da proveniência sedimentar, estágios tectônicos, outros sistemas locais/regionais e globais atuantes, e as condições climáticas operantes.

Todas essas ferramentas de correlações cronoestratigráficas, incluindo também bioestratigrafia (fósseis marinho-marinhos, fósseis terrestres, palioestratigrafia, paleoecologia e paleobiologia), biomarcadores geoquímicos,

eustasia fanerozóica, magnetoestratigrafia, astroblemas, astrocronologia, evolução da vida, entre outros, elevam significativamente o estudo da Geologia histórica (Figura 17).

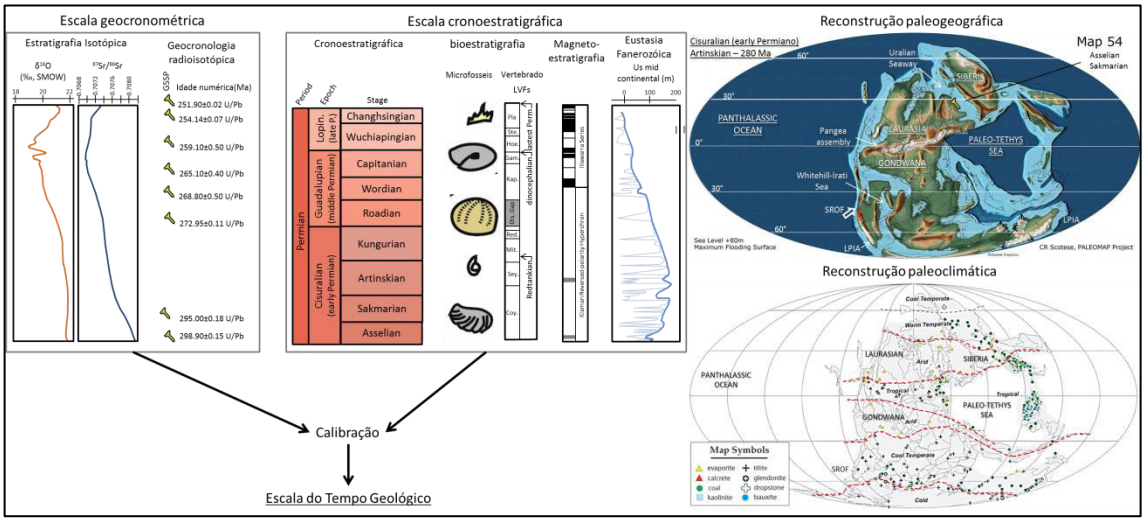

Figura 17 - A construção de uma escala de tempo geológico é a fusão da escala cronométrica (medida em anos) e da escala cronoestratigráfica (definições formalizadas de estágios geológicos, unidades de zoneamento bioestratigráfico, zonas de polaridade magnética e outras subdivisões do registro rochoso). A identificação precisa de sua localização na reconstrução do passado permite melhores estudos da Geologia histórica.

O **artigo 3** contribui para a reconstrução Cronoestratigráfica da Época Cisuraliana, sendo utilizados *multi-Proxy* da Formação Irati complementado por dados obtidos a partir da revisão bibliográfica sistemática em trabalhos publicados. Foram discutidos os isótopos estratigráficos de carbono ($\delta^{13}C$), oxigênio ($\delta^{18}O$), enxofre ($\delta^{34}S$), nitrogênio ($\delta^{15}N$) e biomarcadores geoquímicos. O estudo correlacionou a formação dos depósitos com os ciclos glacio-eustático e eventos climáticos do Fanerozóico. A correlação tefroestratigráfica dos PFDs do poço HV-44-RS com PFDs de outras bacias possibilitou a expansão cronoestratigráfica da área estudada. Somado às correlações como episódios tectônicos, crises bióticas, dados do CO_{2atm} globais, fases glaciais e eutasia global do Fanerozoico que geraram associações regionais para processos geológicos ocorridos na bacia. O modelo paleogeográfico de Scotese (Map 54; 2014) serviu de base para a reconstituição tectônica da margem Gondwana Ocidental, durante o Cisuraliano, estudo de proveniência e de subsidência regional. As influências paleoclimáticas do Permiano estão baseadas na reconstrução paleoclimática de Boucot et al. (2013).

Geologia Histórica

O longo dos 4,6 bilhões de anos da Terra, o estudo da geologia histórica é um estudo da Terra comportando-se como um sistema semi-fechado, possibilitando interpretar ações e reações de mudanças tectônicas e ambientais no globo, que podem ser usadas para elaborar proposta para explicar, de forma ordenada, os eventos e o processo histórico-geológico, que se sucederam na evolução da Terra, e para ajudar a compreender melhor o sistema da Terra e para o entendimento dos problemas ambientais atuais. O estudo da cronostratigrafia começa efetivamente no Arqueano, ca. 3.8 Ma, desde sua individualização como planeta até o presente (Figura 10). Em sua superfície, a Terra funciona em como um sistema termodinamicamente aberto, havendo trocas entre a biota, a atmosfera, a hidrosfera (oceano, gelo, água doce) e litosfera que interagem com os processos de superfície. No entanto, a superfície em si, se comporta como um sistema semi-fechado (Figura 18), havendo a interação sinergética de todos (litosfera, hidrosfera, biosfera e atmosfera) e contribuições de matéria e energia do manto (vulcanismo) e do sistema solar (energia solar e queda de bólido). Está constantemente aprimorando o conhecimento dessa história, incluindo as relações entre a evolução da vida, as tendências e oscilações climáticas e geoquímicas, as trangressões e transgressões ao nível do mar, as placas tectônicas, os principais distúrbios vulcânicos, entre outros.

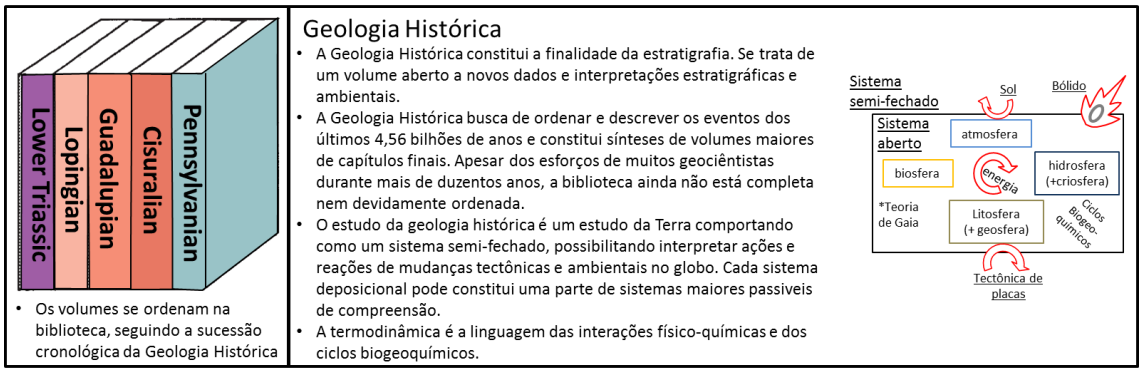

Figura 18 - Estudos estratigráficos desenvolvidos na Tese e analogia da reconstruções paleogeográficas e as tarefas de coleta de dados na preparação de uma biblioteca.

A movimentação das placas tectônicas favorece mudanças e a superfície terrestre permanece em desequilíbrio de massa e entropia, possibilitando, assim, uma troca energética. Os registros fossilizados da biosfera, principalmente extinções, são usados também para identificar eventos específicos e nortear

momentos de mudança dos sistemas e assim estabelecer seus períodos geológicos. No entanto, o seu surgimento e evolução manteve-se em co-evolução com o ambiente físico-químico. A biosfera, representada pelo conjunto dos ecossistemas reinante nas épocas geológicas, influenciou os ciclos biogeoquímicos (principalmente do C, O, H, S e N) ao ponto de partir dos organismos fotossintetizantes, mudar a química da atmosfera e influenciando substancialmente a evolução da litosfera (ex: Hazen et al., 2008).

Uma teoria que apresenta uma visão de sistema integrado é a Teoria de Gaia (ou Geia do grego, Mãe-Terra) (Lovelock & Margulis, 1974). Ela diz que a biosfera interage em sinergia com fatores geológicos, hidrológicos e geoquímicos, na perspectiva que a evolução biológica e a evolução do ambiente físico-químico não são dois processos independentes, mas, antes, duas facetas do mesmo processo. A biosfera exerce a função de controle adaptativo, mantendo uma série de variáveis ambientais constantes numa escala global (por exemplo, temperatura, composição química atmosférica, pH e salinidade dos oceanos etc.), ou seja, uma homeostase planetária que conservaria condições biogeoquímicas do planeta Terra relativamente constantes, mantendo-as dentro dos limites de habitabilidades adequadas para a vida.

A regulação de tais variáveis ambientais é entendida como uma propriedade emergente do sistema Gaia, resultante das interações complexas de organismos e subsistemas físico-químicos num conjunto de alças de retroalimentação positiva e negativa. De fato, durante o Permiano, as Florestas boreais constituídas de Glosopteris regularam o clima regional de modo parecido com a analogia do ‘Mundo das Margaridas’ descrita em Lovelock (2005).

Escala cronoestratigráfica global

Uma escala de tempo geológica padronizada é a estrutura para decifrar e entender a longa e complexa história do planeta Terra. Ela apresenta o objetivo de estabelecer uma hierarquia de unidades cronoestratigráficas estável que possa servir como uma referência padrão para correlações entre rochas de todo mundo (Boggs, 2014).

A Escala Cronoestratigráfica global vem sendo desenvolvida há várias décadas, evoluindo ao longo do tempo com aprimoramentos de novas ciências,

como a geocronologia. Atualmente, a escala cronoestratigráfica global é baseada em GSSP (*Global Stratotype Section and Point*) (Figura 19), utilizada para a calibração em idades numéricas para a definição de limites cronológicos de Idades, Épocas e Períodos em depósitos sedimentares (Remane et al., 1996), chamados de estratótipos. Os GSSPs são estabelecidos pela chamada Comissão Internacional de Estratigrafia (ICS), da União Internacional de Ciências Geológicas (IUGS), ramificando-se em várias subcomissões, cada qual dedicada a uma parte específica da escala cronoestratigráfica, geralmente a um Sistema/Período (*por exemplo: Subcommission on Permian Stratigraphy* – SPS) (https://permian.stratigraphy.org/).

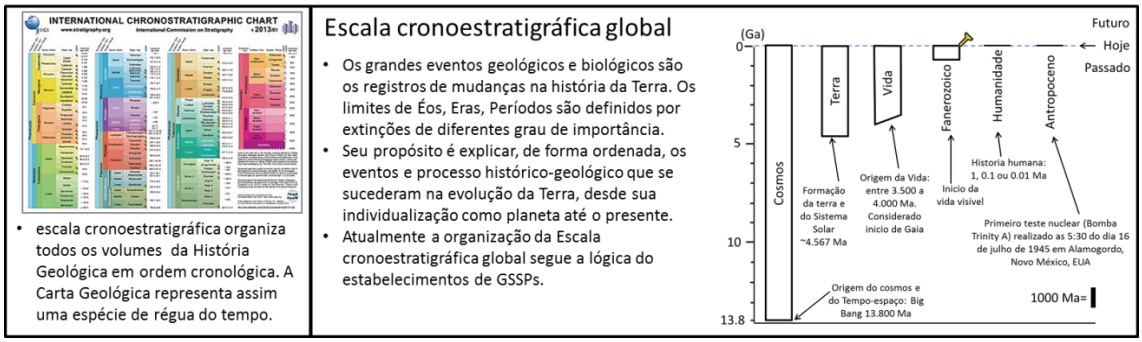

Figura 19 – Estudos estratigráficos desenvolvidos na tese e sua analogia da escala cronoestratigráfica global como uma biblioteca da História Geológica da Terra.

A Escala Cronoestratigráfica Global também é uma ciência e está em constante modificação. Lucas (2018) sugere que a permanência da Escala Cronoestratigráfica global como ciência dependerá do retorno aos conceitos de Cronoestratigrafia natural, mais informativa possível, com base em técnicas modernas e metodologias consistentes. Esta adaptação permite a atualização com aumento de precisão e descrição, produzindo assim uma geologia histórica mais informativa possível.

Possivelmente, a estratigrafia de sequência é parte fundamental neste retorno. A questão de tornar a estratigrafia de sequência uma ferramenta formal no código estratigráfico deve passar por identificar os depósitos sedimentares singulares em meio aos depósitos sedimentares cíclicos, correlacioná-los em reconstruções paleogeográficas, paleoclimáticas, *multi-Proxy* e, quando possível, com as variações eustáticas ocorridas durante o Fanerozóico. Por exemplo, isso foi realizado no artigo 3 para descrever o Gondwana Ocidental durante o Cisuraliano.

1.5. Materiais e métodos utilizados na aquisição de dados

O presente projeto de tese escolheu como metodologia o uso conjunto de trabalhos de campo e técnicas laboratoriais. As amostras utilizadas foram coletadas em:

- Amostra de cinza vulcânica (Figura 20A) proveniente de corte ao longo da rota 68 na Quebrada De Las Conchas (Lat 25°42′S/Long 65°42′W), Sul de Salta, Argentina. Foi obtido durante o campo da cadeira “Geologia dos Andes Centrais”.
- Amostra de bentonita (Figura 20B) proveniente de afloramentos na região da cidade de Aceguá-RS (Lat 31°53’602”S/Long 54°00’125”W) (Silva et al., 2017).
- Amostra de tonstein (Figura 20C) da mina de carvão Faxinal (Simas et al., 2013), a 25 km ao Sul da cidade de Arroio dos Ratos-RS (Lat 30°15′58.22″S/Long 51°42′13.36″W). Amostra de acervo no Instituto de Geociências cedida para a pesquisa pela Profa. Dra. Margot Guerra-Sommer.
- Amostras de níveis de bentonita contidas na sondagem HV-44-RS, perfurados pelo Serviço Geológico do Brasil (CPRM,) no final de 1982, no município de Herval-RS (Lat 31°56'42.90"S/ Long 53°53'18.85"O). Armazenada na litoteca da CPRM na cidade de Caçapava do Sul.

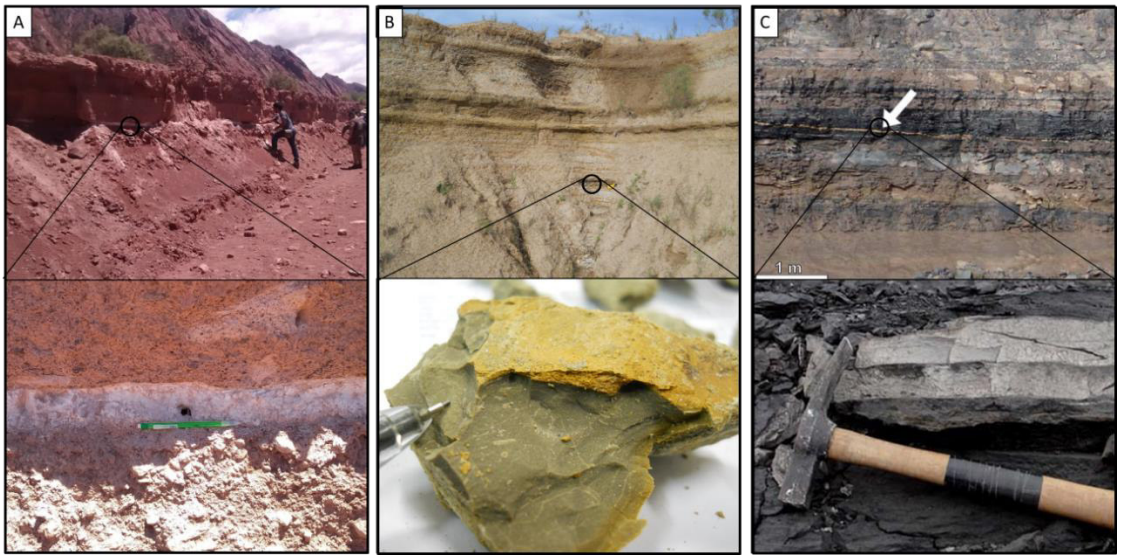

Figura 20 - Afloramento no qual foram coletadas as amostras de PFDs utilizadas neste trabalho. Em (A), apresenta-se o perfil estratigráfico na qual foi coletada a amostra de cinza vulcânica. Em (B), apresenta-se o perfil estratigráfico no qual a amostra de bentonita foi coletada (Silva et al., 2017). Em (C,) apresenta-se o perfil

estratigráfico no qual foi coletada a amostra de tonstein (Simas et al., 2013). No perfil A e C, pode-se observar a continuidade da camada de PFD.

As técnicas laboratoriais envolveram (Tabela 1) uma preliminar revisão bibliográfica sob diversos temas da pesquisa, identificação e descrições de campo, descrições petrográficas, análise em Microscópio Eletrônico de Varredura (MEV), identificação cristalo-química por Difração de Raios-X (DRX) e Infravermelho (IR), identificação química de elementos maiores e menores por Fluorescência de Raios-X (FRX), concentração e caracterização de minerais magmáticos de bentonita, e análise isotópica por LA-ICP-MS em minerais de zircões vulcânicos.

1.5.1. ***Descrição de campo***

No doutorado ocorreram quatro visitas à litoteca da CPRM em Caçapava do Sul – RS (Figura 21A, B e C). Foram duas visitas para a descrição de testemunho em 2016, totalizando oito dias, uma visita em 2017 para descrição de testemunho e coleta de amostras, totalizando 11 dias. Uma em 2020 para coleta de amostras, totalizando 6 dias.

I) 04 a 08 de julho de 2016;
II) 11 a 15 de setembro de 2016;
III) 10 a 21 de abril de 2017; e
IV) 02 a 08 de fevereiro de 2020.

A sucessão de fácies foi levantada na escala 1:50 (Figura 21D) para o intervalo completo da Formação Irati em 12 poços, incluindo-se o furo HV-44-RS, adotando-se a metodologia de Dalrymple (2010) (ex: Figura 22). Os resultados obtidos com o levantamento da sucessão faciológica do intervalo completo da Formação Irati foi publicado em Xavier et al. (2018).

Figura 21 – Etapa de descrição de testemunho na litoteca da CPRM em Caçapava do Sul – RS. Em (A), observa-se uma visão geral da litoteca sob dois pontos de vista. Em (B), tem-se a quantidade de caixa de cada poço, contendo aproximadamente 60 metros de rochas da Formação Irati. Em (C), são reveladas as caixas organizadas para a descrição e em (D) é mostrada a metodologia de levantamento de sucessão faciológica, utilizando tanto a luz natural quanto luminárias.

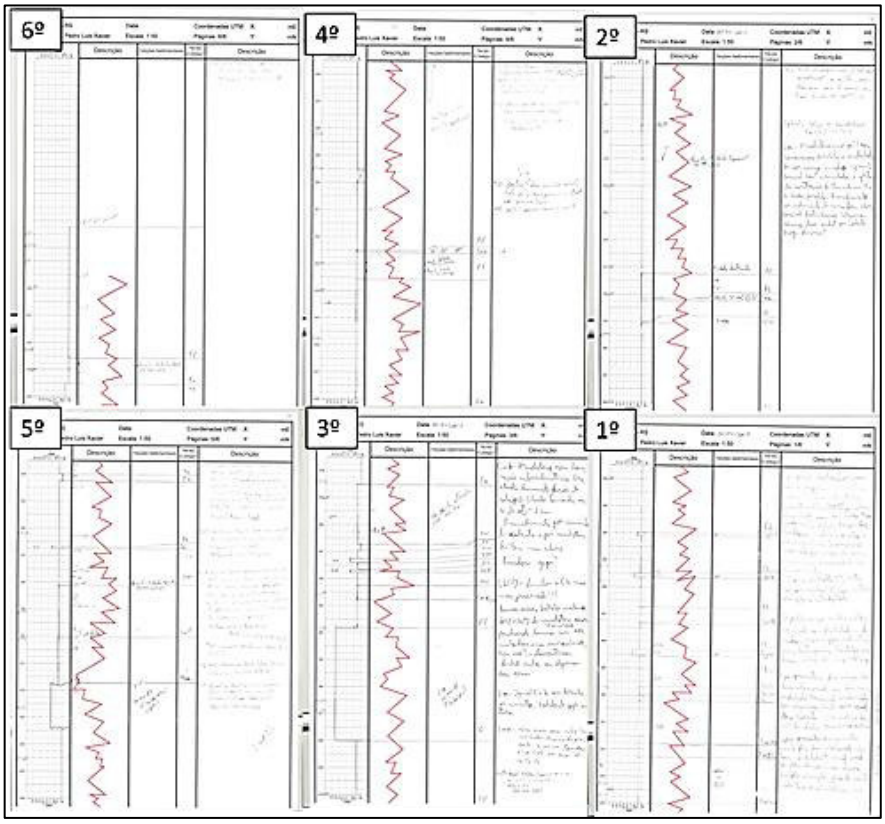

Figura 22 - Perfil 1:50 descrito do poço HV-44-RS. A numeração corresponde à ordem de descrição, da base para o topo, correspondendo, assim, a 66 metros de testemunho descrito em cada poço.

Foram identificados os níveis de argilitos com características macroscópicas de serem bentonitas (e.g. Costa, 2016; Huff, 2016; Silva et al., 2017). As fácies

destes níveis são, costumeiramente, muito particulares, a partir da quais se destacam (Figura 23) as seguintes características:

- Litologia constituída por minerais de argila, apresentando textura sedosa;
- Espessura do nível é pequena, entre 1 a 12 cm, média 4 cm;
- Tonalidades da fácies diferentes das outras fácies adjacentes, geralmente formadas por cores claras, como: castanho, verde, amarelo, marrom, rosa e branco, entre outras;
- Maciças, na grande maioria das vezes;
- Falta de assinatura sedimentar causada pela alteração;
- Seus contatos são, predominantemente, abruptos com as litologias adjacentes, podendo haver contato gradacional no topo da fácies;
- Apresenta contraste perante os processos que formaram as estruturas das fácies adjacentes;
- Grandes extensões laterais, que excedem centenas de quilômetros;

Complementando a descrição faciológica, a confirmação da proveniência a partir de material vulcânico, passa necessariamente por um estudo mineralógico e da composição química dos prováveis níveis de PFDs (e.g. Bohor & Triplehorn, 1993; Meunier, 2005). Assim, devido ao diâmetro do furo e as limitações para a coleta de amostra para assegurar a preservação do furo na litoteca, foram extraídas amostras de alguns poucos gramas de fragmentos de cada nível de argilito. A amostragem somente foi autorizada pela CPRM na terceira etapa de descrição dos furos (10 a 21 de abril de 2017). O furo escolhido foi o HV-44-RS, pela possibilidade de integração com outros estudos (Araújo, 2001; Xavier et al., 2018). A metodologia escolhida para a coleta foi a sistemática dos níveis de argilitos identificados no perfil da Formação Irati ao longo do furo HV-44-RS, na forma de pequenas amostras de acordo com as determinações da litoteca da CPRM e a própria natureza do níveis, geralmente com pequenas espessuras. Foram um total de oito amostras de argilitos maciços, que variaram entre um máximo de 30 gramas e um mínimo de 0,7 gramas (Figura 24). Em laboratório, as amostras foram secas em estufa e, inicialmente, procedeu-se à descrição macroscópica com o auxílio de lupa binocular.

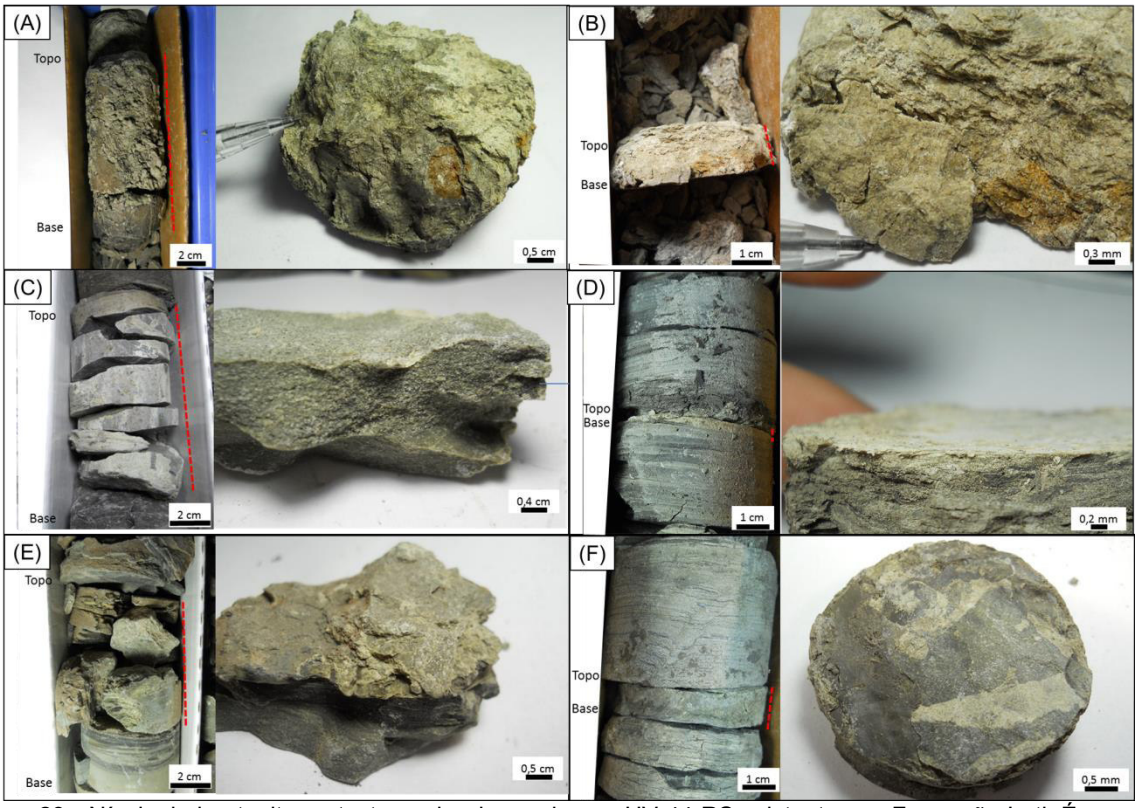

Figura 23 - Níveis de bentonita no testemunho de sondagem HV-44-RS existentes na Formação Irati. É possível observar as diferentes espessuras, normalmente na ordem de 1 cm, podendo atingir excepcionalmente até doze centímetros, e tonalidades entre verde, amarela, cinza e marrom.

Figura 24 - Amostras de bentonita coletadas do poço HV-44-RS. Em (A) nível BSA1 (antigo BIR8); em (B) nível BIR5; e em (C) BIR9.

A preparação de amostras e o uso de alguns dos equipamentos adotados para o trabalho foram realizados nos laboratórios do instituto (IGEO) da Universidade Federal do Rio Grande do Sul (UFRGS) – Brasil. Especificamente, nos laboratórios do Centro de Pesquisas em Geoquímica (CPGq), do Centro de Estudos de Geologia

Costeira (CECO), e do Laboratório de Geologia Isotópica (LGI). Foram feitas as seguintes análises: Difração de Raios-X (DRX), Fluorescência de Raios-X (FRX), concentração de minerais resistatos, separação por líquidos densos, análise de minerais em lupas, Microscopia Eletrônica de Varredura (MEV) e Energy Dispersive X-ray Spectroscopy (EDS). Análises complementares de infravermelho (IR) foram realizadas com apoio da Central Analítica (CA-IQ) do Instituto de Química da UFRGS e as análises do Laser Ablation-Inductively Coupled Plasma-Mass Spectrometry (LA-ICP-MS) foram feitas no Isotopic Geochemistry Laboratory da Universidade Federal de Ouro Preto (IGL-UFOP).

1.5.2. ***Difratometria de raio X (DRX)***

A Difratometria de Raios-X (DRX) permite determinar os planos dos materiais cristalinos que são característicos de cada mineral e devido a dimensão pequena dos argilominerais se constitui numa técnica básica para o seu estudo, sendo uma ferramenta básica para sua identificação. O equipamento utilizado foi o difratômetro Siemens D5000 com unidade geradora Pw 1010 e painel registrador Pw 1050 (radiação CuKα, filtro de níquel e condições de energia de 40 mA e 25 kV). Conforme a composição cristalina das amostras, o produto da análise são difratogramas com uma série de picos principais e secundários que se destacam em relação a uma linha de base (background) correspondente a difração em fase dos planos cristalinos, cuja intensidade (eixo dos Y) é normalmente apresentada em contagem por segundo (cps) em relação ao ângulo 2 *theta* de varredura do goniômetro (eixo dos X). Através da Lei de Bragg os ângulos 2 theta dos picos são transformados em espaçamento em angstrons (Å) relacionados com parâmetros da célula unitária e planos cristalinos dos minerais. Os difratogramas obtidos foram manipulados e interpretados através da rotina *MacDiff 4.2.5*.

Para análise da mineralogia foram utilizadas técnicas diferenciadas de preparação e análise das amostras para a identificação de duas frações: I) análise por DRX da amostra total ou rocha total (RT) através da forma desorientada dos grãos, e II) análises por DRX das frações granulometricas correspondente a argila (3 a 28º 2θ, com *step size* de 0,02º e *step time* de 1s) (e.g. Meunier, 2005).

A preparação para a análise total da rocha é obtida pela moagem e peneiramento em 200 mesh (0,074 mm) (Figura 25A). O material moído é depositado sob um suporte para uma análise na forma de pó. O intervalo angular adotado para a varredura das amostras não orientadas foram de 2 a 50°2θ, com *step size* de 0,02º e *step time* de 1s.

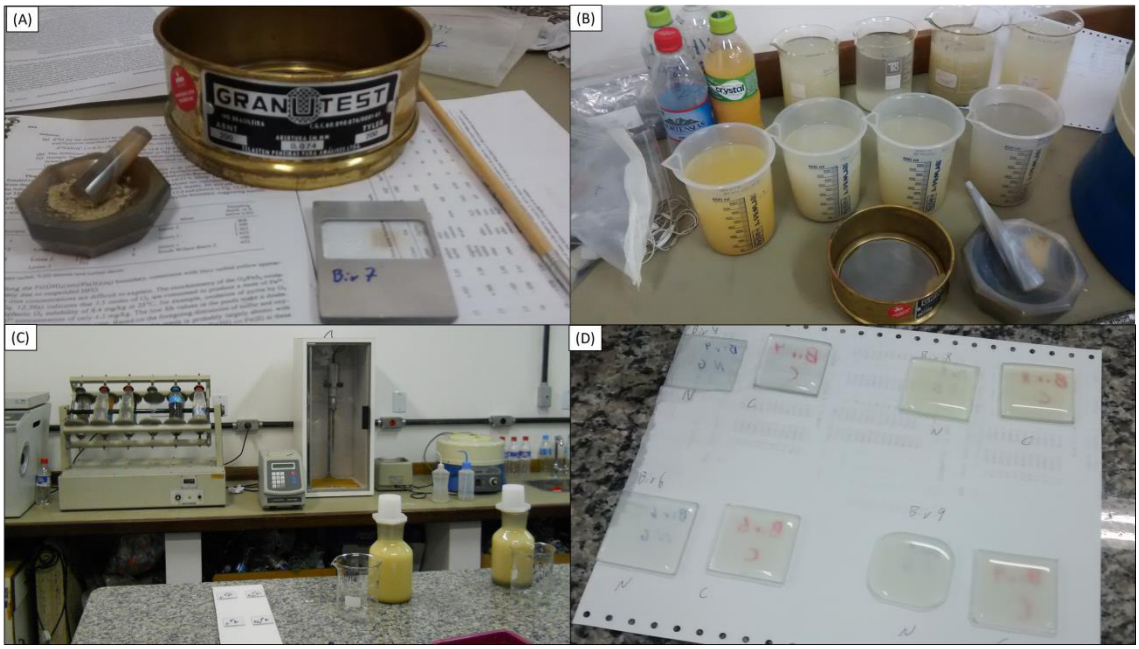

Figura 25 – Processo de preparação de amostras desorientada e orientada em DRX. Em (A) é indicada a etapa de preparação de amostra de rocha total para uma análise desorientada. Em (B) a preparação das amostras para análise orientada. Em (C) são expostas, em primeiro plano, as amostras em solução. Na bancada junto à parede aparece à direita o equipamento de ultrassom de ponteira e à esquerda o orbitador. Na imagem (D) a fração argila é depositada na lâmina de vidro que após serão submetidas ao DRX para obtenção dos difratogramas.

Para a preparação da fração fina e orientada, desagregaram-se as amostras num grau de ágata seguido de peneiramento em 200 mesh (0,074 mm) (Figura 25B). A fração passante na peneira foi depositada em frascos com água deionizada e levada ao ultrassom para uma maior dispersão. Ao final transferiu-se o líquido e a amostra para um frasco fechado onde permaneceu sob agitação num orbitador por um período de 14 horas para implementar a desagregação dos minerais (Figura 25C). Após esta etapa, as amostras foram postas para decantação, segundo um tempo definido pela Lei de Stokes necessário para a separação de partículas de acordo com o diâmetro de interesse.

O cálculo do tempo de decantação pela Lei de Stokes foi feito com o programa *Sedtools 1.1.2*. Este programa possibilita a entrada de variáveis como a temperatura

do líquido (ºC), densidade média das partículas (g/cm^3) (usado 2,5 g/cm3 como padrão), diâmetro das partículas em mícrons (µm) a serem concentradas (4µm e 2µm), e a altura em centímetros da coluna do líquido para a coletada (Settling Height). Definido o tempo, as frações de interesse foram separadas e uma alíquota foi colocada com uma pipeta sobre duas lâminas de vidro em superfície plana (Figura 25D).

Após a secagem natural (amostra orientada), as lâminas foram submetidas à análise por DRX. A identificação dos minerais presentes na fração argila deu-se a partir do modo orientado da fração fina, que abrange os componentes da amostra com dimensão inferior a 2µm. Três conjuntos de dados foram usados para a identificação de minerais de argila com propriedades expansivas: I) amostra orientada após secagem ao ar (N); II) amostra solvatada com etileno glicol (EG); e III) amostra aquecida a 540º C por 2h (C).

a) (N): observação do comportamento do argilomineral sem tratamento ou natural;
b) (G): observação do comportamento do argilomineral após tratamento com etileno glicol ou glicolado;
c) (C): observação do comportamento do argilomineral após tratamento térmico;

O intervalo angular adotado para a varredura das amostras orientadas foram de 2 a 38°2θ, com *step size* de 0,02º e *step time* de 1s. Para estas técnicas foram usadas frações menores que 4 µm na amostra de cinza vulcânica e frações menores que 2 µm nas amostras de bentonita e tonstein.

Na amostra de bentonita foram utilizadas duas técnicas analíticas complementares em DRX. Uma técnica apresentou o objetivo de identificar o parâmetro-b e a outra foi para o estudo dos cátions interfoliares na argila, mediante a saturação com cátions interfoliares.

A técnica de identificação do parâmetro-b seguiu o mesmo método de preparação por pó de rocha total desorientada. Neste método busca-se identificar a estrutura octaédrica (di- ou tri-) interfoliar, observada pelo pico 060. O intervalo angular adotado para a varredura das amostras foram de 61° a 64° 2θ, com *step size* de 0,01º e *step time* de 10s.

A técnica de troca de catiônica é utilizada para homogeneizar o espaçamento interfoliar das argilas que causam interferência na identificação dos picos de cristalização identificados pela difração. A metodologia seguiu procedimento parecido com o descrito por Christidis (2007). A amostra de bentonita foi moída suavemente e dispersa em água deionizada e após em ultrassom. Sua fração fina (<2 μm) foi coletada após o tempo de decantação (Figura 26A).

Figura 26 – Processo de saturação das amostras para análise em DRX. Em (A) são reveladas as amostras em solução. Em (B) é mostrado o momento do teste com $AgNO_3$. Em (C), são indicadas as amostras no tubo usado na centrifugação e em (D) são expostos os tubos no centrifugador.

Após separada, a amostra foi saturada por soluções de 1 ml de $CaCl_2$ 1N. Ao saturar, misturou-se com bastão de vidro e deixou-se em contato durante uma hora. Após o tempo de interação, centrifugou-se a 20' e 4000 rotações/min. Foram feitas posteriormente cinco lavagens com água deionizada para eliminar o excesso de cátions em solução, seguida de nova centrifugação. Após a quinta lavagem, fez-se um teste com $AgNO_3$ na água da lavagem para verificar a ausência do cátion em solução usado para saturação (Figura 26B). Observando-se a não formação de um precipitado branco coletou-se parcela do líquido para a confecção da amostra orientada em lâmina de vidro e análise por DRX no modo N e G (3 a 38° 2θ 0,02º/1s).A amostra restante em solução seguiu para um novo processo de saturação (Figura 26C e D), uutilizando-se 1 ml de KCl 1N e depois novamente por 1 ml de $CaCl_2$ 1N.

1.5.3. *Petrografia*

Foram feitas duas lâminas delgadas no Laboratório de Preparação de Amostras do IGEO-UFRGS. Na amostra de tonstein, foi feita uma preparação convencional da lâmina petrográfica; já na amostra de bentonita foi realizada uma preparação especial (i.e. utilizando óleo mineral evitando-se o uso de água para a laminação petrográfica). As amostras foram impregnadas com resina epóxi e todas as seções delgadas foram desgastadas até uma espessura de aproximadamente 0,03 mm. Na análise petrográfica buscou-se identificar: mineralogia, microestruturas, alterações, tipos de grãos existentes na rocha e o seu tamanho (e.g. Ddani, et al., 2005).

1.5.4. *Infravermelho (IR)*

A preparação de pastilha prensada para análise em infravermelho foi feita no CPGq/UFRGS, utilizando-se 100 mg (0,1 g) de KBr (Brometo de potássio) e 1,5 mg (0,0015 g) de amostra pulverizada da amostra que foram homogeneizados num cadinho de ágata (Figura 27A). A mistura é colocada na prensa (Figura 27B), seguindo sucessões de pressões para garantir a compactação. A relação de pressão *versus* tempo utilizado foi: 15 kgf por 4 min, seguido por 20 kgf por 3 min e finalizado por 30 kgf por 3 min (Figura 27C). Finalizado o processo a pastilha é removida do pastilhador (Figura 27D), e levada para uma estufa a 100º C por 12h.

Retirada da estufa, as pastilhas foram levadas para a CA-IQ-UFRGS para a análise em IR (Figura 28A). A obtenção do espectro foi feita através do espectrômetro IRPrestige-21, operando na região infravermelho médio (faixa 4000 - 400 cm^{-1} Wavenumbers) no modo absorbance (Figura 28B). Os resultados foram avaliados na região de alta energia entre 4000 a 3000 cm^{-1}, e baixa energia entre 1300 a 400 cm^{-1} (e.g. Madejová and Kornadel, 2005).

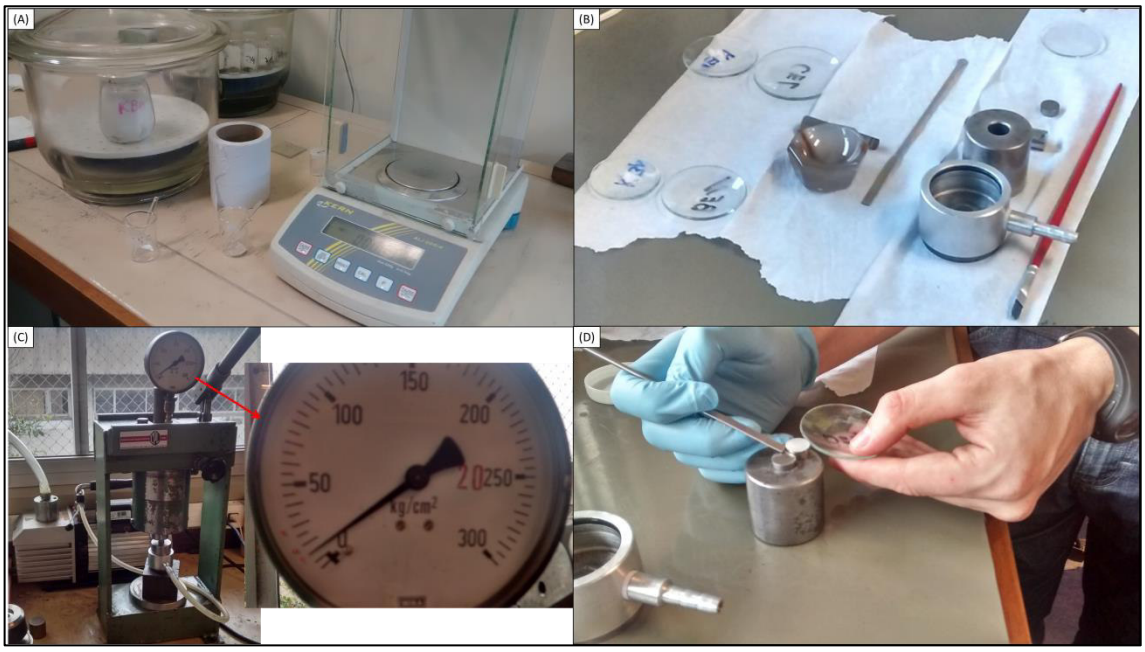

Figura 27 – Processo de preparação de pastilha para o IR. Em (A) é mostrado o procedimento de pesagem e mistura da amostra e do KBr. Em (B) é mostrado o processo de limpeza do suporte da prensa usado para a confecção da partilha. Em (C) é mostrada a prensa e no detalhe as três pressões usadas. Em (D) é exposta a remoção da pastilha prensada.

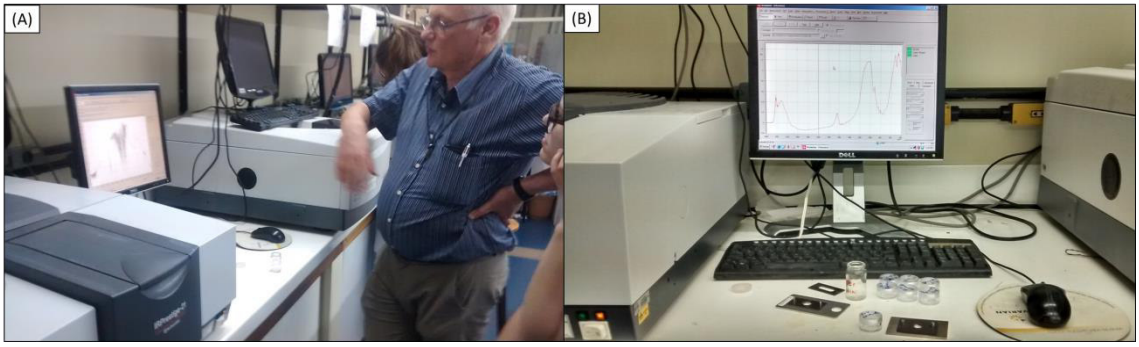

Figura 28 – Processo de análise em IR. Em (A) é mostrado o momento da obtenção dos dados de infravermelho e na parte inferior da imagem o espectrômetro IRPrestige-21. Em (B) é mostrado o dado coletado no modo absorbance.

1.5.5. *Fluorescência de* Raios X (FRX)

A preparação de pastilhas e as análises na Espectrometria de Fluorescência de Raios-X (FRX) foram feitas no CPGq/UFRGS. A técnica utilizada consistiu da moagem da amostra em grau de ágata e de peneiramento em peneira de 200 mesh (menores 0,074 mm) (Figura 29A), necessitando-se num modo convencional de 10 g de material moído para a preparação das pastilhas (Figura 29B). Foram preparadas pastilhas ditas fundidas para a quantificação da concentração dos elementos maiores (na forma de óxidos e a perda ao fogo-LOI) (Figura 29C) e prensadas para análise dos elementos menores e traços (ABNT, 1985). A determinação da

composição química dos elementos óxidos maiores e menores foi feita no espectrômetro de FRX Rigaku RIX2000 em funcionamento no CPGQ (Figura 29D) a partir de curvas de calibração construídas a partir de um conjunto de padrões internacionais de rocha (Govindaraju, 1994).

Figura 29 – Processo de preparação de amostras para FRX. Em (A) é mostrado o processo de peneiramento para análise química e em (B) a amostra pulverizada para a confecção de pastilha prensada e fundida. Em C, o forno para a confecção das pastilhas fundidas. Em (D) o espectrômetro de fluorescência de Raios-X Rigaku RIX2000 em processo de análise.

1.5.6. ***Concentração de minerais resistatos***

A concentração de minerais resistatos foi feita no CPGq/UFRGS. O método de concentração de minerais resistatos teve a intenção de obter a partir de cada amostra a separação de duas frações por densidade. O processamento é semelhante à metodologia apresentada por Bohor & Triplehorn (1993) e Reiners et al. (2018). Nesta metodologia utilizou-se uma peneira de 500 mesh (0,025 mm) (Tabela 3 e Figura 30), visando a ampliar a faixa de retenção de minerais com possível origem vulcânica primária nos níveis de PFDs.

Nesta etapa, a parcela da rocha é desagregada em grau de ágata em meio aquoso (Figura 30A). Numa primeira etapa procede-se o peneiramento a 200 Mesh com lavagem a úmido. A parcela da amostra passante é retida e armazenada para

decantar. A parcela retida na peneira volta novamente ao cadinho para nova moagem e repetição do processo (Figura 30B).

Um segundo peneiramento em 500 mesh foi feito no laboratório do CECO-UFRGS. A lavagem é feita com cuidado, controlando a pressão do jato d'água, buscando retirar os fragmentos menores de 0,025 mm (Figura 30C). Este processo de lavagem elimina a maior parte da fração argila e silte, restando um concentrado. Após a lavagem, a amostra é armazenada num recipiente devidamente etiquetado e levado para secagem numa estufa (Figura 30D).

Figura 30 - Etapas do processo de separação dos minerais resistatos. Na imagem, (a) mostra a balança na qual se começa o processo, pesando as amostras. Em (b) mostram-se os materiais usados para a separação (à esquerda) e as amostras geradas na separação (à direita). Em (c) é mostrada a atividade de lavagem e separação em curso. Na imagem (d), é mostrada a peneira de 500 Mesh utilizada para lavar as frações menores que 80 Mesh passadas no método (b), e seis amostras de níveis diferentes à esquerda.

1.5.1. *Líquidos densos*

Para evitar a contaminação do líquido Bromofórmio, que altera sua densidade, a amostra submetida aos líquidos densos não deve possuir argila e fragmentos de frações menores que a capacidade de retenção do filtro. Assim, antes da passagem, a amostra deve ser analisada em lupa (aumento 80x), para identificar fragmentos menores que 0,025 mm. Caso ainda persistam fragmentos, a amostra deve ser novamente lavada na peneira de 500 Mesh (0,0025 mm).

Tabela 3 - Tabela de granulometria da ASTM (mesh) e abertura (mm) das peneiras, em comparação com a granulometria de grãos sedimentares e tamanho dos minerais.

ASTM	Tyler	Aperture (mm)	Granulometry		Magmatic minerals
70	65 mesh	0,212	Fine sand	Sand / Sandstone	250 µm // 0. 25 mm
80	80 mesh	0,180			
100	100 mesh	0,150			
120	115 mesh	0,125	Very fine sand		
140	150 mesh	0,106			
170	170 mesh	0,090			
200	200 mesh	0,075			
230	250 mesh	0,063			
270	270 mesh	0,053	Coarse Sill	Mud / Mudock	
325	325 mesh	0,045			
400	400 mesh	0,038	Medium Sill		
450	450 mesh	0,032			
500	500 mesh	0,025			30 µm // 0.03 mm

A separação por líquidos densos é feita no laboratório de Núcleo de Preparação de Amostras CPGq/UFRGS. Como preparo inicial, monta-se dentro de uma capela um suporte que se acoplará a um balão de decantação, um funil para o filtro de papel e um copo de Becker ao final (Figura 31A). Para cada concentrado de amostra houve dois filtros de papel devidamente etiquetados a lápis com o nome da amostra e qual densidade foi filtrado: um para os minerais pesados e outro para os minerais leves (Figura 31B). O balão de decantação foi preenchido por Bromofórmio (densidade aproximada de 2,86 g/cm³) e, em seguida, depositou-se o concentrado de amostra. Fizeram-se pequenos movimentos circulares com o balão, de modo a misturar o líquido com a amostra, deixando em repouso por 15 minutos para os minerais mais densos decantarem (Figura 31C).

Para a coleta do minerais pesados, como zircão (4.55-4.65 g / cm^3) e apatitas (3.1-3.3 g / cm^3), abriu-se a torneira do balão de decantação por alguns segundos para o escoamento da fração pesada, que foi retida no filtro de papel. Logo após a passagem desta fração fechou-se novamente a torneira. O filtro reteve os minerais pesados enquanto o bromofórmio migrou para o becker. Em seguida, após toda a passagem do Bromofórmio pelo filtro, trocou-se de filtro de papel para a coleta agora da fração inferior a 2,8 g/cm³ e repetiu-se o processo (Figura 31D). Após a passagem de todo Bromofórmio pelo filtro, trocou-se o becker por um vazio e foram lavados o balão, os filtros e a amostra com álcool. A mistura de álcool e Bromofórmio, contida no becker, foi armazenada para um futuro descarte correto. Após a lavagem, os filtros foram levados para secar em forno a 60ºC por 24h. Após a secagem, os minerais foram transferidos do filtro para um recipiente devidamente

etiquetado com a identificação da amostra, a fração e a densidade dos minerais (minerais pesados e minerais leves).

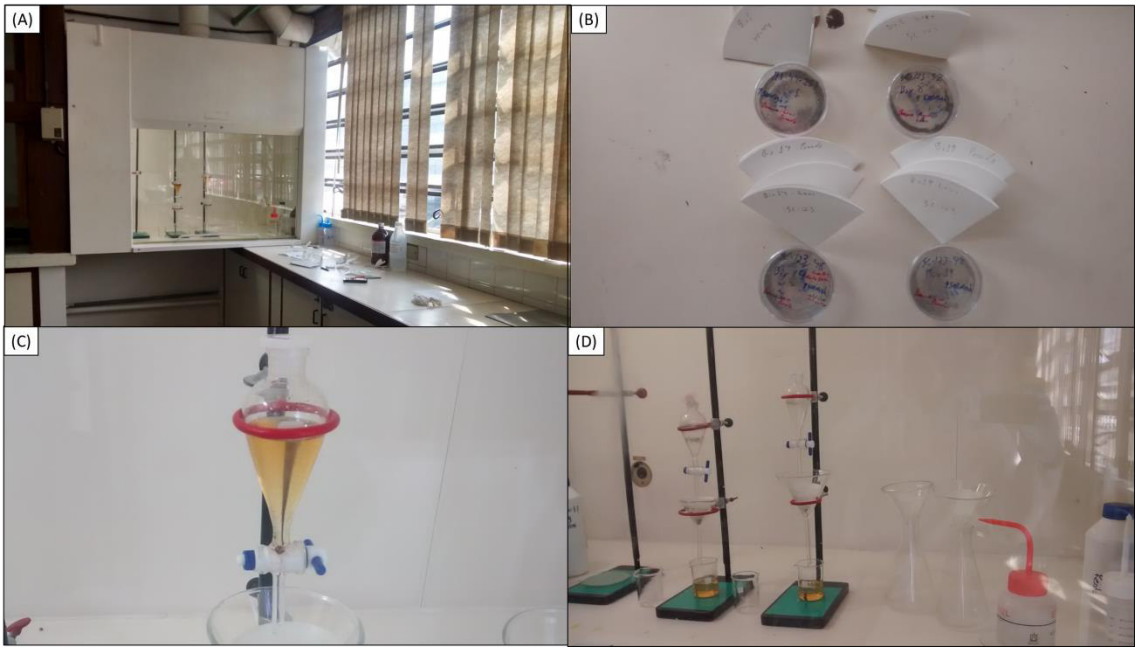

Figura 31 - Processo de separação das frações dos minerais nos líquidos densos. Em (A) pode-se observar toda a estrutura usada dentro da estufa, e em (B) as amostras preparadas para a passagem no líquido e seus respectivos filtros de retenção. Em (C) pode-se observar o processo de separação em que os minerais pesados afundam e os leves flutuam. Em (D) parte final de todo o processo.

1.5.2. *Catação em lupa e Microscópio Eletrônico de Varredura (MEV)*

As frações leves e pesadas foram analisadas em lupa binocular (lupa da marca Laica S8AP0, de até 80 vezes de aumento) (Figura 32A). Os minerais de zircões, apatitas, biotitas e ilmenita foram cuidadosamente catados na fração de minerais pesados através do uso de uma agulha e transferidos para outro recipiente com álcool, para o armazenamento (Figura 32B).

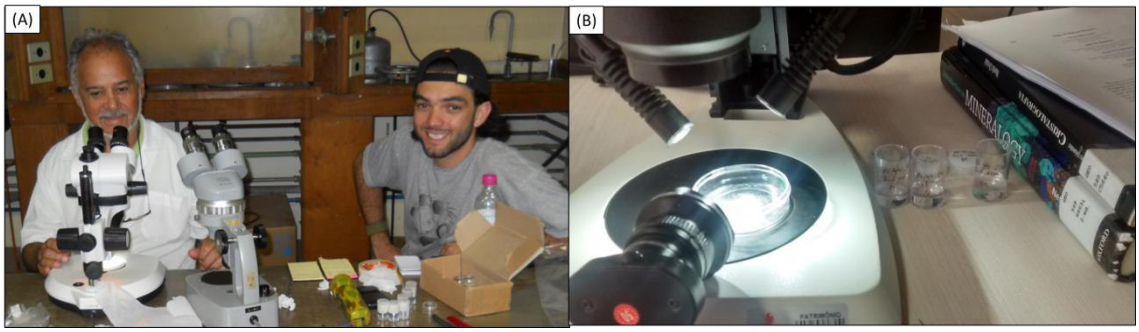

Figura 32 - Processo de separação de minerais. Em (A) mostra o momento de identificação de minerais em lupa, e em (B) mostra o momento de separação de minerais.

Para as análises no MEV, a preparação do material consistiu de colagem de pequenos fragmentos de rocha e mineral em uma lâmina, contendo fita dupla-face. Sobre a fita foram colados de forma ordenada os minerais e/ou a rocha de interesse, com o respectivo mapa de localização na lâmina. Os minerais escolhidos para a análise foram os euédricos, prismáticos e/ou aciculares, que apresentaram dúvidas na classificação na observação pela lupa binocular ou eram até desconhecidos. Foram registradas imagens da lâmina para a produção do mapa de localização dos fragmentos e minerais (Figura 33), utilizando-se para isso uma lupa com câmera acoplada (*Leica Application Suite – LAS-EZ, Version 1.6.0*, câmera *Leica EC3,ICC50*).

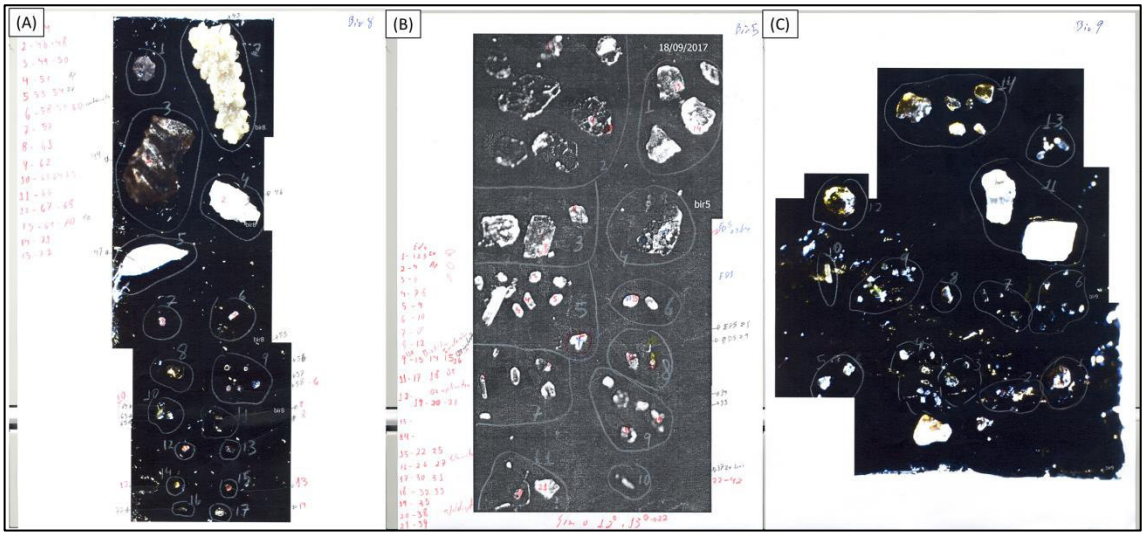

Figura 33 – Mapa usado para a identificação de minerais e fragmentos em MEV. Em (A) o mapa da amostra BSA1, em (B) o mapa da amostra BIR5, e em (C) o mapa da amostra BIR9.

No dia anterior à análise, a lâmina foi levada ao forno para retirar a água adsorvida, ficando na temperatura de 40º C durante 12h. Após, a lâmina foi levada à metalização por carbono e ouro (Figura 34A e B) no Laboratório de Geologia

Isotópica (IG-UFRGS). Após a metalização, ela é analisada no MEV do Laboratório de Geologia Isotópica (IG-UFRGS), marca *JEOL – JSM-6610LV* (Figura 34C). Foram realizadas três sessões.

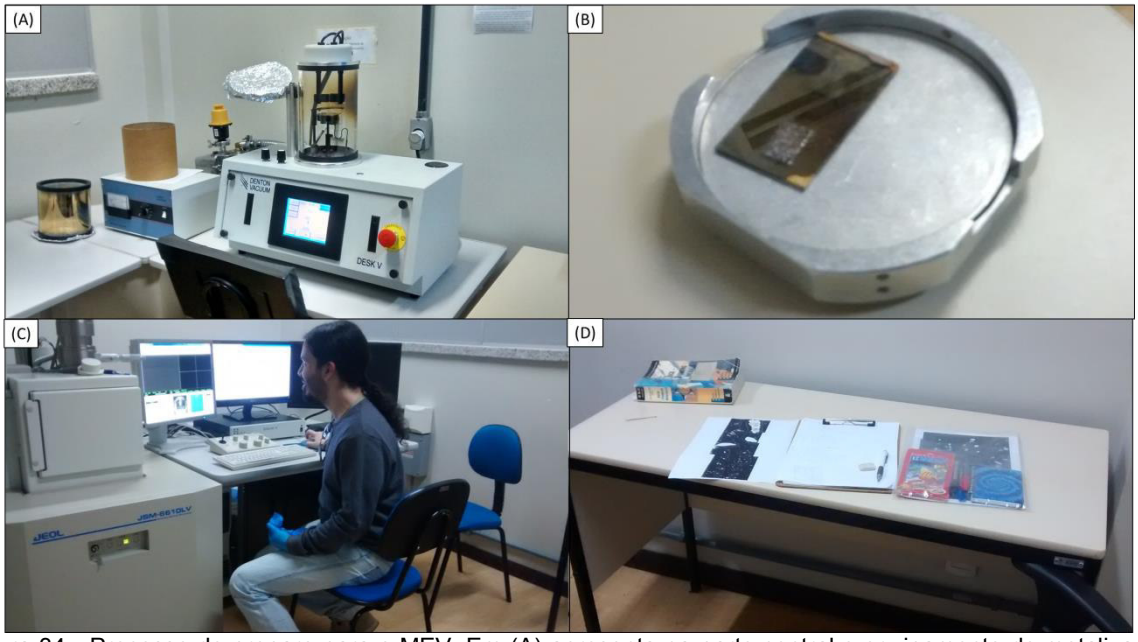

Figura 34 - Processo de preparo para o MEV. Em (A) apresenta na parte central o equipamento de metalização do IG-UFRGS. Em (B) mostra a lâmina metalizada e em (C) o equipamento MEV. Em (D) apresenta o mapa da lâmina utilizado durante o procedimento no MEV.

O MEV auxiliou na identificação textural dos argilominerais e na morfologia dos minerais. As identificações dos minerais vulcânicos primários (Figura 35) permitiram a comprovação que os níveis analisados são de origem vulcânica. Acoplado ao MEV, o Espectrômetro de Energia Dispersiva de Raios X (EDS), da marca *Bruker Nano X Flash Detector 5030*, possibilitou uma análise rápida e eficiente para a determinação da composição química qualitativa dos minerais de interesse.

Os exemplos são cristais de zircão (Figura 36A) que, sob a lupa, apresentam-se hialinos a alaranjados, predominando a morfologia euédrica, prismas tetragonais alongados, com 200-50µm de comprimento e com terminações bipiramidais tetragonais, juntamente com inclusões fluidas de forma irregular. Ao MEV sua morfologia euédrica foi novamente evidenciada (Figura 36B) e em EDS confirmam através das concentrações de zircônio e sílica (Figura 36C).

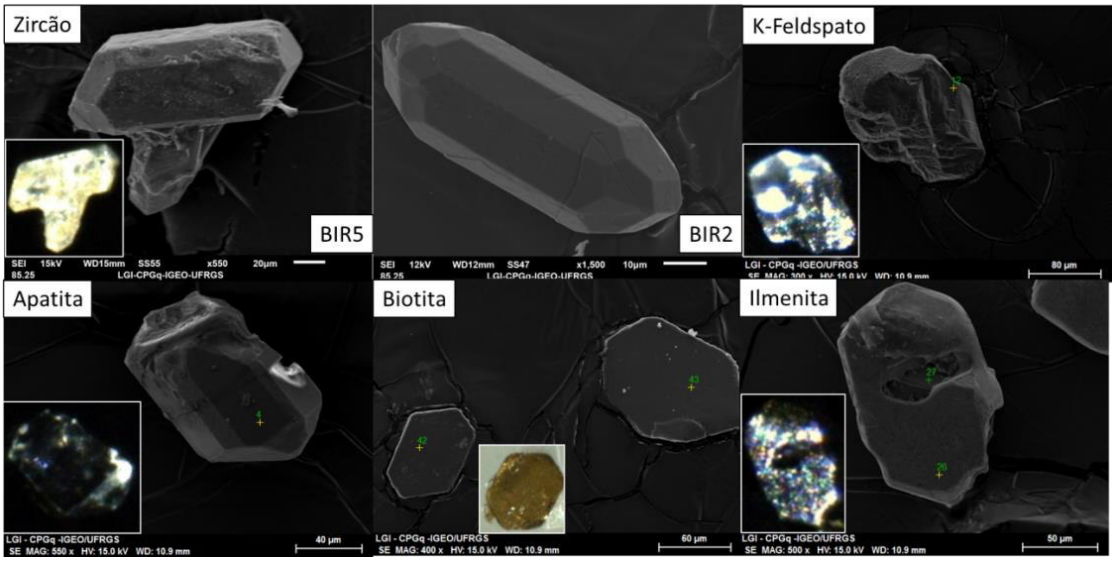

Figura 35 - Diferentes minerais magmáticos encontrados nos níveis de bentonita.

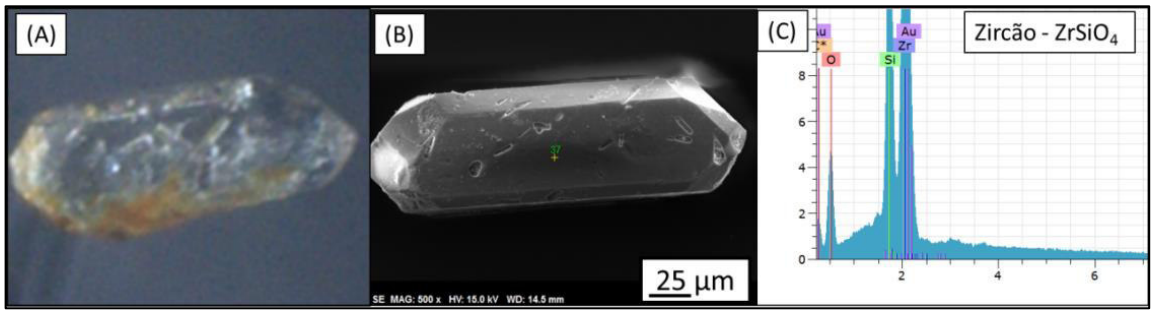

Figura 36 - Imagem de um zircão em (A) lupa binocular e em (B) MEV, com sua respectiva (C) análise química por EDS.

1.5.3. *Análise Isotópica- Laser Ablation (LA-MC-ICP-MS)*

Os concentrados de minerais pesados dos níveis BIR9, BIR2, BIR4, BIR5 e BSA1 apresentaram populações consideráveis de zircões. Assim, em cada nível, foram coletados entre 20 a 50 grãos de zircões euédricos e fixados em uma lâmina com fita dupla face de forma agrupada por níveis, sendo estes mapeados. A escolha de 20 a 50 grãos é uma amostragem representativa e leva em consideração a possível perda ou não exposição de cristais na fase de preparação da pastilha. Esta quantidade é a recomendada para a determinação das idades (e.g. Santos, et al., 2006; Schaltegger et al., 2015).

Durante a preparação da pastilha (*mount*) para a datação (Figura 37A), foi posto sobre a lâmina um disco de diâmetro de 2,5 cm (Figura 37B), preenchendo com resina epóxi (Temora y 91500) sobre os zircões até atingir 1 cm de altura. Após a secagem, a pastilha foi polida com pasta diamantada de até 20 µ (Figura 37C),

sendo acompanhado de checagem constante em lupa até a melhor exposição de seções transversais dos zircões (Figura 37D).

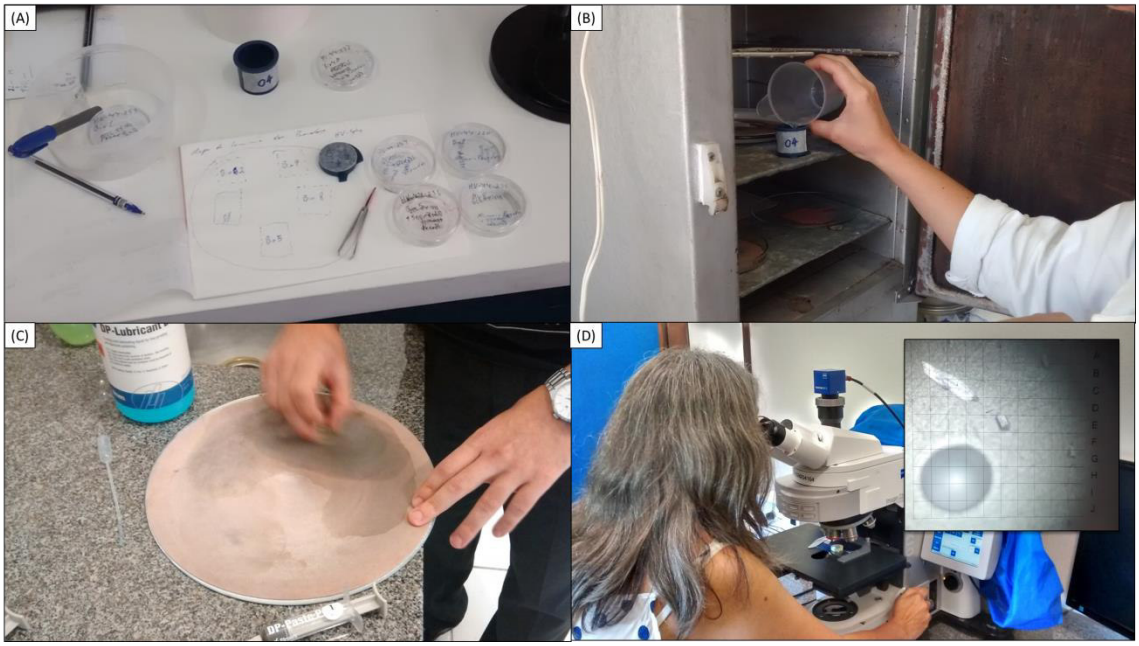

Figura 37- Processo de preparo de pastilha para datação em LA-MC-ICPMS. Em (A) apresenta o mapa das localizações dos agrupamentos dos níveis de PFDs. Em (B) mostra o momento de preenchimento por resina epóxi do disco sobre a lâmina. Em (C) revela o polimento da pastilha e em (D) a checagem das exposições dos zircões.

O mapeamento dos minerais foi feito em lupa com luz refletida e catodoluminescência (CL) para determinar o zoneamento interno (tipicamente oscilatório). A metalização e a CL foram feitas no Isotopic Geochemistry Laboratory (IGL) do Instituto de Geociências da Universidade Federal de Ouro (UFOP), com equipamento JEOL 6510.

As imagens ópticas de luz transmitida e CL foram importantes para orientar a seleção de locais durante a ablação a laser (Figura 38) e em estudos posteriores de interpretação dos dados. As imagens ópticas de luz refletida foram úteis para visualizar e evitar fraturas, contaminação e inclusões. As imagens de CL auxiliaram na avalização das texturas magmáticas de zoneamento oscilatório.

Os minerais da pastilha foram analisados por Laser Ablation-Inductively Coupled *Plasma-Mass Spectrometry* (LA-ICP-MS) no IGL-UFOP (Figura 39A e B). Foi utilizado o *Thermo Scientific Element 2* sector field (SF) ICP-MS acoplado ao sistema de laser CETAC LSX-213 G2 + (Figura 39C). O equipamento funcionou no modo de alta sensibilidade padrão (STDS), usando tamanho de diâmetro de ponto de 20µm, energia do laser de 15%, frequência de disparo do laser de 10 Hz e atraso

do obturador de 15 s. Os padrões usados para calibração incluíram zircão GJ-1, BB e Plešovice. Na obtenção das datas analíticas foi utilizada a constante de decaimento radioisotópica de 137.88, estabelecida da razão $^{238}U/^{235}U_{zircon}$ por Jaffey et al. (1971) e Steiger & Jager (1977). Ao final, as pastilhas foram guardadas (Figura 39D).

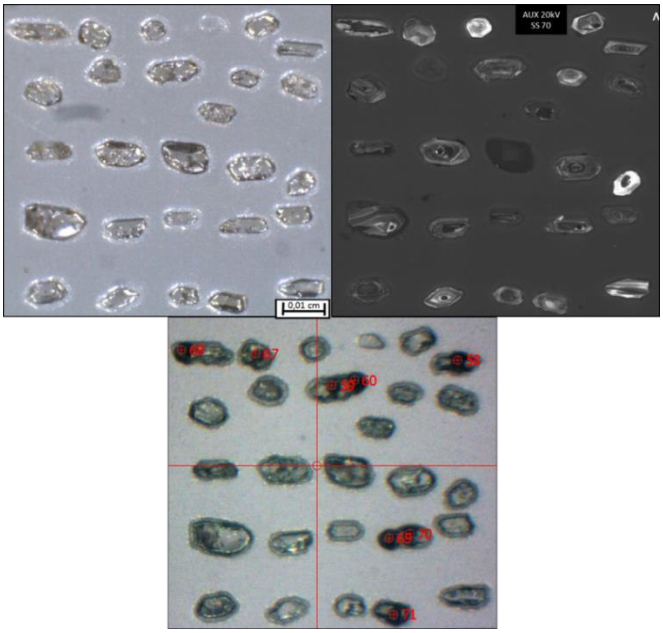

Figura 38- Exemplo de mapa em imagem de luz refletida e em CL do nível BSA1, utilizados para seleção de ponto de ablação a laser.

Figura 39 – Departamento de análise isotópica da IGL-UFOP em (A) e (B). Em (C) equipamento de ICP-MS *Thermo Scientific Element 2*. Em (D) as pastilhas que contêm os zircões analisados.

Os spots foram realizados, preferencialmente em zonações paralelas e perto das bordas dos grãos, evitando as interfaces núcleo/borda, inclusões ou áreas heterogêneas. Foram analisados em cada nível (Figura 40): BIR9 (n = 50 cristais, 15 análises), BIR2 (n = 31 cristais, 8 análise), BIR4 (n = 28 cristais, 8 análise), BIR5 (n = 56 cristais, 22 análises) e BSA1 (n = 25 cristais, 27 análises).

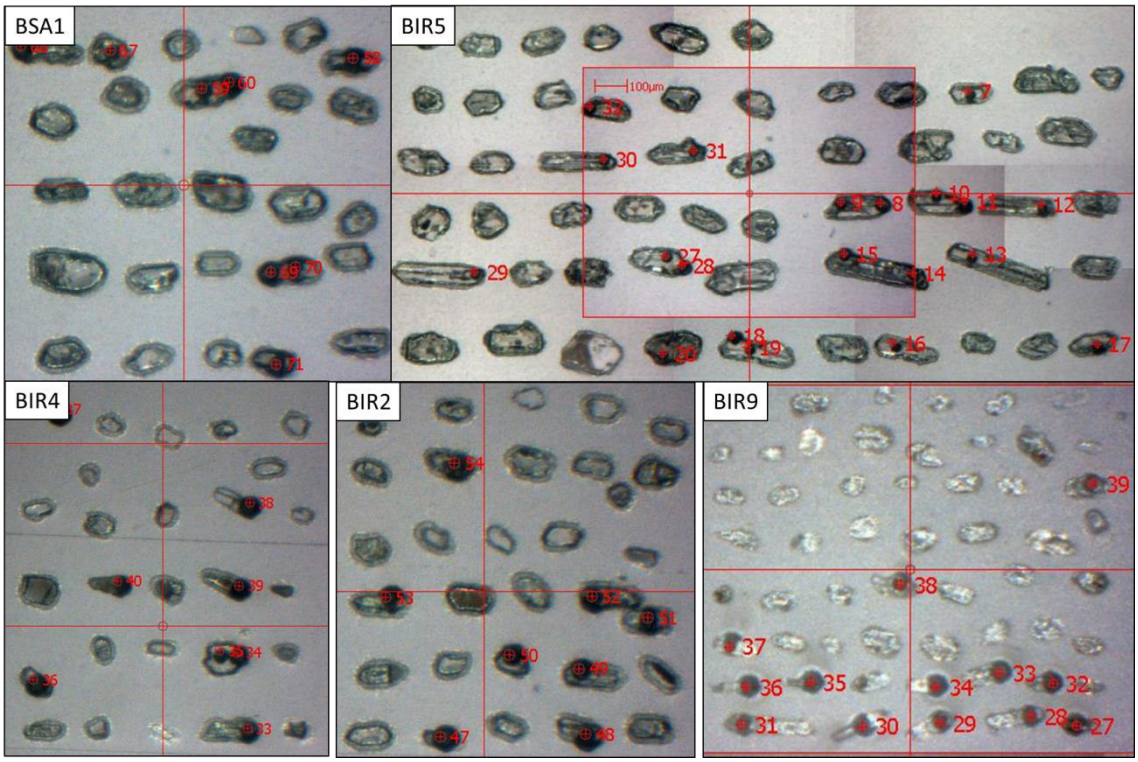

Figura 40 - Imagem do mapa de datação por LA-ICP-MS dos zircões de cinco níveis de PFDs da Formação Irati.

As análises dos dados analíticos dos spots utilizáveis para obtenção de idade numérica foram feitas em combinação com as imagens de CL e de luz refletida (ex: Reiners et al., 2018). A localização do spot no grão permitiu o reconhecimento do domínio textural do cristal analisado (Tabela 4), garantindo a avaliação de incerteza composicional e estrutural relacionadas às datas.

Nos dados analíticos foram avaliadas as seguintes colunas de cada spot:

- % conc – valores entre 95%-105%. Esta coluna demonstra quanto concordante estão os dados analisados.
- f206c – valores menores que 1. Esta coluna representa o Pb comum, devendo ser menor que 1.

- U_{ppm} – Valores entre 10 a 1000 (10> U <1000). Valores menores que 10 apresentaram baixa resolução analítica e valores maiores que 1000 tendem a provocar metamictização no cristal de zircão.
- $^{206}Pb/^{204}Pb_c$ – valores maiores que 20. A razão de Pb para grãos ígneos tende a ser maior que 20.
- Th/U – valores menores que 0.1. Esta razão tende a ser menor que 0.1 para grãos magmáticos.
- $^{207}Pb/^{206}Pb$ – valores menores que 0.06.

Tabela 4 - Tabela de síntese das principais características morfológicas em imageamento qualitativo em luz refletida e em CL, e suas interpretações (modificado de Silva, 2006).

	Feições	**interpretações**
Morfologia externa	morfologia subédrica a euédrica, tamanho entre 20 e 300 µm ao longo do eixo-C e sem evidencias de retrabalhamento sedimentar	Indica preservação das características magmáticas
Morfologia interna	Zoneamentos oscilatórios	Indica evolução magmática
Forma do núcleo	Idiomórfico	ígneo (restito ou xenocristal) ou metamórfico (xenocristal)
	Arredondado	Corrosão magmática (restrito ou xenocristal); corrosão metamórfica (xenocristal) ou abrasão (xenocristal detrítico)
	Contorno fraturado	Xenocristal detrítico
	Contorno irregular	Corrosão magmática ou metamórfica
Variações nas taxas de luminescência	Tonalidades cinza-médio uniforme	Origem magmática
	Tonalidades cinza-claro e branco (alta luminescência)	Baixos conteúdos em U (e Th), baixas razões Th/U, (< 0.1): domínios metamórficos de fácies anfibolito alta a eclogito
	Tonalidades cinza-escuro a preto (baixa luminescência)	Alto conteúdos de U (> 1000 ppm) domínios magmáticos metamitizados

Segundo Schaltegger et al. (2015), são necessárias de 10 a 20 análises em LA-ICP-MS para interpretar uma população complexa com confiança suficiente para serem aplicadas como uma ferramenta cronoestratigráfica em uma sucessão sedimentar. Dentre os cincos níveis de PFDs datados (Figura 40), três níveis obtiveram resultados satisfatórios, correspondendo ao BIR9, BIR5 e BSA1.

- Entre os dados adquiridos do nível BIR8, quatorze spots obtiveram resultados satisfatórios. Os outros spots foram descartados por motivos diferentes: uma análise foi rejeitada por conter alto teor de ^{204}Pb comum; oito análises foram interpretadas como tendo sofrido perda de $Pb_{radiogênico}$; sete análise foram rejeitadas por serem cristais herdados.
- Entre os dados adquiridos do nível BIR5, quatorze spots obtiveram resultados satisfatórios. Os outros spots foram descartados por motivos diferentes: duas

análises foram rejeitadas por conter alto teor de ^{204}Pb comum; cinco análises foram interpretadas como tendo sofrido perda de Pb $_{radiogênico}$; uma análise foi rejeitada por ser de cristal herdado.

- Entre os dados adquiridos do nível BSA1, nove spots obtiveram resultados satisfatórios. Os outros spots foram descartados por motivos diferentes: quatro análises apresentaram alto teor de ^{204}Pb comum; duas análises apresentaram baixo teor de U e uma alto teor de U; onze análises foram interpretadas como tendo sofrido perda de Pb $_{radiogênico}$; e quatro análises foram interpretadas como sendo cristais herdados.

O cálculo das ages em milhões de anos antes do presente (Ma) foram determinadas através de plotagem em diagramas de distribuição normal univariada da razão $^{206}Pb/^{238}U$, utilizando o software IsoplotEx 4.15 (Ludwig, 2012). Foram escolhidos ±σ2 (2 desvios padrão da média) como variável aleatória gaussiana para representar a incerteza analítica na plotagem, estabelecendo um intervalo de confiança de 95.4%.

Para a representação de uma boa calibração de idade numérica, buscou-se o agrupamento de datas da razão $^{206}Pb/^{238}U$ concordantes e a obtenção de valores de *Mean Square Weighted Deviation* (MSWD) próximo a 1 (NACSN, 2005; Reiners et al., 2018). A apresentação dos dados geocronológicos de U/Pb segue as formatações recomendadas pela PlasmAge website (www.Plasmage.org), integrado ao EARTHTIME.

1.5.4. ***Disciplinas assistidas***

Tabela 5 - Disciplinas do candidato cursadas no decorrer da Pós-graduação.

		Período	Código	Disciplina	Professor (a)	Créd.	Conc.
Mestrado acadêmico	1 ano	2014/01	GEB00046	Análise estratigráfica	Claiton M.S.S.	6	A
		2014/01	GEB00044	Estratigrafia Avançada	Claiton M.S.S.	4	C
		2014/01	GEB00045	Fácies e Sistemas Deposicionais	Claiton M.S.S.	5	B
		2014/01	GEB00101	Proveniência de Arenitos	L.F.De Ros e M. V. Remus	3	C
		2014/02	GEP00033	Geologia do Quaternário Costeiro do Rio Grande do Sul	L.J. Tomazelli	5	A
		2014/02	GEP92-56	T.E. em Geoquímica: Técnicas Analíticas Aplicadas a Geologia do Petróleo	Marleni	2	A
		2014/02	GEB00047	Tectônica de Bacias Sedimentares	Farid C.J.	6	A
	2 ano	2015/01	GEB00125	Argilominerais Sedimentares	N. Dani	4	A
		2015/01	GPG00020	Processos de dinâmica superficial e riscos naturais associados	Robaina L.E.S.	6	A
						36	Total
Doutorado	1 ano	2016/01	GEB00105	Análise de fácies em sequências vulcânicas	C. A. Sommer	4	A
		2016/01	GEB00052	Geologia Estrutural de rochas intrusivas - estrut. magmáticas e subsolid	M. Fatima B.	5	A
		2016/01	GEP92-43	T.E. em Geoq: Estruturas e texturas de rochas vulcânicas efusivas e vulc	-	2	A
		2016/02	GEB00065	Geoquímica isotópica aplicada a depósitos minerais	M. V. Remus	5	A
		2016/02	GEP92-60	T. E. em Geoquímca: Geopolítica do petróleo - aspectos políticos e econômica	-	2	A
	2 ano	2017/01	GEB00121	Paleoclimatologia	K. Goldberg	3	B
		2017/02		Estágio Docência: Princípios de geoestatística	-	2	A
		2017/02	GEB00128	Redação e submissão de artigo científico	L.A. Hartmann	5	D
		2017/02	GEP19-41	T.E. em Geologia Sedimentar: Microbialitos - Distribuição no tempo-espaço	-	2	A
		2017/02		Exame de Qualificação (Tema: Registro de quedas de cinzas vulcânicas em sequências sedimentares, proveniência e aspectos genéticos)	-	-	Aprv.
	3 ano	2018/01	GEB00106	Termocronologia: Técnicas, aplicações e interpretação	Jelinek A. R.	3	A
		2018/02	GEB00135	Biomarcadores na geoquímica do petróleo	Tais F. da S.	4	A
		2018/02	GEB00139	Geologia dos Andes centrais	Carla P. e Marcia G.	5	A
		2018/02	GEB00132	Geologia dos argilominerais	Marcia G.	5	A
	4 ano	2019/01	GEB00100	Diagênese das rochas sedimentares clásticas	L.F.De Ros	3	C
		2019/02	GEB00142	Análise exploratória	J. Kuchle	4	A
	5	2020/01	Aprov. Externo	GEO734 - Geocronologia	Cristiano de C. Lana	3	A
						52	Total

1.6. Resumo dos principais resultados obtidos e discussões

Partes das interpretações desenvolvidas nos artigos estão explicadas no tópico “Estado da arte do tema da pesquisa” da presente tese.

O Artigo 1 está direcionado para a geocronologia, apresentando dados inéditos de datação U-Pb por LA-ICP-MS e três novas idades numéricas obtidas para os PFDs na parte sul da Bacia do Paraná. No estudo, os PFDs foram posicionados no perfil estratigráfico, distribuídos ao longo de toda Formação Irati na coluna cronoestratigráfica e obtendo informações de taxa deposicional da unidade.

O Artigo 2 está direcionado para a mineralogia e geoquímica, utilizando-se seis diferentes técnicas analíticas para caracterização de três diferentes PFDs, uma cinza vulcânica, uma bentonita e um tonstein. No estudo, os dados de cada PFD foram utilizados para definição das características mineralógicas. A partir do ambiente deposicional de cada PFD, da estrutura cristaloquímica e da correlação entre elas, interpretou-se os processos de alteração pós-deposicional de esmectitização em ambiente marinho e de caulinização em ambiente paludal.

O Artigo 3 está direcionado para a cronoestratigrafia, desenvolvendo a reconstrução do desenvolvimento paleoambiental do Mar Irati-Whitehill durante a Época Cisuraliano. Para tal, utilizou-se o posicionando da Formação Irati na coluna cronoestratigráfica do Artigo 1, em conjunto com estudos de tefrocronologia de PFDs para correlações isócronas com outras bacias, reconstruções cronoestratigráficas das condições globais, tectônicas, climáticas e quimio-estratigráficas. Reconstruções paleogeográficas para posicionamento espacial da bacia do Paraná sobre o Gondwana, correlações regionais com outras bacias e reconstruções tectônicas a partir de mapas paleoclimáticos e da revisão sistemática de trabalhos publicados da Formação Irati, interpretando multi-Proxy de isótopos estratigráficos de carbono ($\delta^{13}C$), oxigênio ($\delta^{18}O$), enxofre ($\delta^{34}S$) e nitrogênio ($\delta^{15}N$), biomarcadores geoquímicos e argilominerais sedimentares.

1.7. Conclusões

Os estudos permitiram estabelecer as seguintes conclusões gerais:

1. O uso de metodologias e técnicas analíticas em três PFDs: uma tephra sub atual (cinza vulcânica); bentonita da Formação Irati; tonstein da Formação Rio Bonito. Em termos termodinâmicos, as tephras contidas no PFD de cinza vulcânica preservam os minerais primários do magma, “congelados” devido a perda brusca de temperatura. Já as estruturas cristaloquimicas dos PFDs alterados para tufos,representam o produto final entre as trocas pós-deposicionais das tephras com os ambientes depositados. O estudo dos arranjos cristaloquimicos destes PFDs possibilitaram, em conjunto com cada contexto geológico, possibilitaram interpretações de suas gêneses, sendo descritos os processos pós-deposicionais, embasado na segunda teoria da termodinâmica (entropia).

2. Apesar do pequeno tamanho dos cristais de argilominerais, sua forma, tamanho e defeitos representam resultados da nucleação (nascimento) de sua cristalização e das condições físico-químicas prevalecentes no ambiente durante o crescimento.

3. As reações pós-deposicionais, havendo transferência de massa (não estequiométricas), possibilitam interpretações de influências que PFDs podem exercer nos ambientes depositados.

4. A partir de PFDs identificados no furo de sondagem HV-44-RS, em meio ao pacote sedimentar do Grupo Passa Dois da Bacia do Paraná, especificamente das Formações Irati e Serra Alta, foram obtidos por LA-ICP-MS em zircão vulcanogênico três novos *datum* geocronológicos a partir de zircões separados de níveis de PFDs, denominados: BIR9 (284.1 ± 3.5 Ma; 2s; MSWD = 1.14, n=4), BIR5 (280.8±1.4 Ma; 2s; MSWD = 0.85, n=13) e BSA1 (274.2 ± 2.8 Ma; 2s; MSWD=0.87, n=4).

5. A comprovação de proveniência genética dos PFDs são apresentadas com base na descrição faciológica, mineralogia dominante composta de montmorilonita dioctaédrica, presença de assembléias de minerais magmáticos, datas de $^{206}Pb/^{238}U$ concordantes, idades numéricas estimada com MSWD próximo a 1, correlações tefrocronológicas isócronas e geocronológica-estratigráfica (diminuição das idades numéricas de acordo com a deposição).

6. As comprovações de PFDs reforçam a hipótese de proveniência a partir da Província Magmática Choiyoi, tendo sido identificadas nas cinzas vulcânicas dos PFDs mudanças composicionais do magma entre um vulcanismo ácido e intermediário.

7. As novas idades numéricas dos níveis de PFDs foram posicionados na estratigrafia do poço HV-44-RS, possibilitando a integração com a

litoestratigrafia, sequências estratigraficas, bioestratigrafia, quimioestratigrafia e correlações tefrocronológicas regionais. As idades numéricas obtidas mostram o período de aproximadamente 12 Myr (entre 286 Ma a 274.5 Ma) para o Sistema Irati do Sul do Brasil, o que possibilitou estabelecer novas contribuições para a cronoestratigrafia do Cisuraliano (298-272 Ma, inicial Permiano). Foram identificadas também, nos pacotes sedimentares da Formação Irati no poço HV-44-RS, taxas de deposição dos diferentes ciclos sedimentares, dois períodos de eventos de anoxia com intervalos de duração bastante diferenciados de 1.2 Myr e 6 Myr, estimativa do estabelecimento de LST na Bacia do Paraná durante 284.5 Ma e 281.2 Ma.

8. As descrições do poço HV-44-RS foram associadas a uma revisão bibliográfica da sistemática Formação irati, permitindo o endossamento de informações ambientais publicadas da Formação Irati (biomarcadores geoquímicos orgânicos, proveniência sedimentar e quimioestratigrafia isotópica de elementos estáveis). Estes dados foram interpretados em conjunto com mapas paleogeográficos e paleoclimáticos da Época, permitindo a reconstrução deposicional da Bacia do Paraná durante a deposição da Formação Irati. As correlações tefroestratigráficas possibilitam estender fatores que levaram à criação do Sistema Mar Irati-Whitehill na Época Cisuraliano. Os resultados são importantes para o avanço do conhecimento paleogeográfico, paleoclimático, paleoambiental e para a cronoestratigrafia global (e.g. Qie et al., 2019).

9. As idades obtidas contribuem para o ajuste cronoestratigráfico da Supersequência Gondwana I e para o entendimento de eventos observados ao longo da seção estratigráfica estudada. A correlação tefrocronológica com PFDs estudados no setor Norte da bacia (mina PetroSix, 276 Ma, Santos et al., 2006), distanciada por 757 Km, destaca a Formação Irati como marcador estratigráfico de abrangência em toda a Bacia do Paraná. Já a correlação tefrocronológica regional possibilitou a reconstrução paleogeográfica mais confiante entre as bacias Permianas do Gondwana Ocidental, melhorando a discussão dos fatores que levaram a criar as condições observadas no Sistema Irati-Whitehill Sea na Época Cisuraliana.

10. Os estudos evidenciaram que existiu uma estreita relação entre o desenvolvimento da Bacia do Paraná no interior continental e o regime tectônico Gondwanides. A instalação do mar Irati-Whitehill deveu-se à confluência de fatores tectônicos da SROP e glacio-estáticos da LPIA, iniciados por volta de 286 Ma.

11. Possivelmente, devido à transgressão glacio-eustática, a Bacia do Paraná foi ligada à Bacia do Parnaíba através da Bacia Sanfranciscana. O fim da conexão possivelmente foi devido a uma regressão marinha e corroborou com o surgimento do Mar Irati-Whitehill, coincidindo com o surgimento do Membro Assistência na Bacia do Paraná e Ecca Group na Bacia do Karoo.

12. A arquitetura estratal da formação Irati foi controlada por condições deposicionais (estilo de bacias), ciclos eustáticos globais e variações climáticas da época. A litosfera do Gondwana Ocidental pode ter reagido por flexura, sob as tensões geradas ao longo das Gondwanides, e isso forneceu um mecanismo eficaz para criar um espaço deposicional *'intracratônico'* dentro do Gondwana, à medida que o soerguimento de suas bordas restringia a Circulação com o Paleo-oceano Panthalassa. Enquanto isto, os terrenos continentais expostos, deglaciação e cinzas vulcânicas forneceram sedimentos alóctones à bacia. Em conjunto, as variações eustáticas, mudanças climáticas e biogeoquímicas marinhas criaram condições para a formação de material autóctone, como argilominerais autigênicos, carbonatos, evaporitos, fósseis, matéria orgânica e glauconita.

13. A partir da análise de estratigrafia de sequência, observou-se que os mesossaurídeos são registrados na S3 da Formação Irati, enquanto que as correlações tefrocronológicas associam este ciclo com a Formação Mangrullo (Uruguai) e a Formação Whitehill (Bacia do Karoo), ambas também contendo fósseis de mesossaurídeos. Deste modo, é possível estabelecer que eles viveram durante o Kungurian (por volta de 281 a 273 Ma) em um cenário de extenso mar epicontinental Irati-Whitehill e condições climáticas mais áridas.

14. Estimou-se que a camada de *mesosaurid bonebed* tenha ocorrido em aproximadamente 280.6 Ma, associando ao evento *Redtankian* de extinção dos vertebrados. Os dois eventos foram correlacionados ao evento de queda de bólido na bacia do Parnaíba, onde formou-se o astroblema Serra da Cangalha.

Os PFDs são produtos de poderosas erupções, como a do tipo pliniana e freatomagmática (e.g. Reading, 1996), e formam, paradoxalmente, finas fácies que parecem insignificantes no registro sedimentar geológico. Espera-se que a descrição analítica e genética dos três diferentes tipos de PFDs descritos possam servir como guia importante para estratígrafos em novos reconhecimentos faciológicos em sequências sedimentares (e.g. Zuffa, 1987). A identificação de novos PFDs proporciona que seus minerais magmáticos sejam analisados através da geocronologia de isótopos radiogênicos (ou datação radiométrica) e sirvam, através da geocronometría, para descobertas de novas *data* cronoestratigraficas (Figura 1).

De modo parecido, espera-se que os dois modelos descritos de mudança do material de cinza vulcânica para argilominerais possam servir de leitura para quem tenha interesse no estudo dos mecanismos da organização e da formação desses minerais nos processos de alterações superficiais.

O PFD é um dos poucos tipos de rochas que oferecem oportunidades para este estudo termodinâmico em baixa temperatura, pois a camada de constituição majoritária de tephras metaestáveis proporciona uma completa alteração das argilominerais. Os processos de intemperismo químico (desordem) superficial envolvem interações numa condição de sistema aberto, de materiais metaestáveis (alta entropia) com os fluidos do ambiente deposicional, coordenados por reações cinéticas em baixa temperatura por hidratação, hidrólise, oxidação e/ou ataques com ácidos. A constituição final dependerá das taxas de intemperismo químico e taxa de lixiviação e providenciará neoformações por equilíbrio termodinâmico (ordem) em baixa temperatura (~25º C), pressão atmosférica (P = 1 a 5 bar). Deste modo, este estudo contribui para quem busca compreender processos termodinâmicos em baixa temperatura, sem, no entanto, conseguir predizer o tempo que ocorreu desde a deposição das cinzas vulcânicas até a transformação em bentonita ou tonstein.

A Formação Irati constitui um registro sedimentar singular nos registros sedimentares do Planeta Terra, preservando tanto carbonatos quanto folhelhos betuminosos com até ¼ de matéria orgânica (por volta de 25%). Seu estudo serve, dentre outras coisas, para compreender os processos que conduziram um ambiente sedimentar a se tornar um reservatório de carbono, sendo capaz de reduzir seus índices atmosféricos globais. Deste modo, na Formação Irati, o passado pode ser a chave para o presente.

Referências

Alan, P.D., 2018. Radiogenic Isotope Geology, 3 ed. United Kingdom: Cambridge University Press, p. 99-133. DOI: 10.1017/9781316163009

Amorosi, A. & Zuffa, G.G., 2011. Sand composition changes across key boundaries of siliciclastic and hybrid depositional sequences. Sedimentary Geology, 236, p.153-163.

Araújo, L.M., 2001. Análise da expressão estratigráfica dos parâmetros de geoquímica orgânica e inorgânica nas sequências deposicionais Irati. PhD Thesis, Instituto de Geociências, Universidade Federal do Rio Grande do Sul, 2 v., 307 pp.

Associação Brasileira de Normas Técnicas (ABNT). (1985). NBR 8828: material refratário - análise química de materiais refratários sílico-aluminosos. 20 p.

Aurell, M., & Bádenas, B., 1997. Didáctica de Las Ciencias Estratigráficas. Enseñanza de las Ciencias de la Tierra, 5(3), 195-199.

Bastos, L.P.H., Rodrigues, R., Pereira, E., Bergamaschi, S., Alferes, C.L.F., Augland, L.E., Domeier, M., Planke, S. & Svensen, H.H., 2021. The birth and demise of the vast epicontinental Permian Irati-Whitehill sea: Evidence from organic geochemistry, geochronology, and paleogeography. Palaeogeography, Palaeoclimatology, Palaeoecology 562, p.13, 110103. https://doi.org/10.1016/j.palaeo.2020.110103.

Boggs, S.Jr., 2014. Principles of Sedimentology and Stratigraphy. British Library Cataloguing-in-Publication Data. 5th Ed.,p. 434-474.

Bohor, B,F. & Triplehorn, D.M., 1993. Tonsteins: altered volcanic-ash layers in coal-bearing sequences. Geological Society of America Special Paper. v. 285, p. 1-44.

Borghi L., 2000. Visão geral da análise de fácies sedimentares do ponto de vista da arquitetura deposicional. Boletim do Museu Nacional, Nova Série, 53, p.1-26.

Boucot, A.J., Chen, X. & Scotese, C.R., 2013. Phanerozoic Paleoclimate: An Atlas of Lithologic Indicators of Climate. SEPM, Concepts in Sedimentology and Paleontology, 11, 478p.

Brito-Neves, B.B. de., 2020. Tectônica de Placas, 50 anos: os adendos científicos e as teorias complementares.Terræ Didatica, 16, 1-24, e020044. doi: 10.20396/ td.v16i0.8662073

Catuneanu, 0., 2006. Principles of Sequence Stratigraphy: Amsterdam , Elsevier, 375p.

Catuneanu, 0., Abreu, V., Bhattacharya, J.P., Blum, M.D., Dalrymple, R.W., Eriksson, P.G., Fielding, C.R., Fisher, W.L., Gallow W.E., Gibli M.R., Giles, K.A., Holbrook, J.M., Jordan, R., Kendall, C.G.St.C., Macurda, B., Martinsen, O.J., Miall, A. D., Neal, J.E., Nummedal, D., Pomar, L., Posamentier, H.W., Pratt, B.R., Sarg, J.F., Shanley, K.W., Steel, R.J., Strasser, A., Tucker , M.E. & Winker C., 2009. Towards the standardization of sequence stratigraphy: Earth-Science Reviews, v. 92, p 1-33

Chamley, H., 1989. Clay sedimentology. Springer, Berlin Heidelberg New York, 623 p..

Christidis, G., 2007. Layer Charge and Charge Distribution of Smectites: a Parameter Which Controls Important Physical Properties of Bentonites. Bulletin of the Geological Society of Greece, 40(2), 690-699. doi:http://dx.doi.org/10.12681/bgsg.16357.

Collinson, J.D., 1969. The sedimentology of the Grindslow Shales and the Kinderscout Grit: a deltaic complex in the Namurian of northern England: Journal of Sedimentary Petrology, v 39, p. 194-221.

Corfu, F., Hanchar, J.M., Hoskin, P.W.O. & Kinny, P., 2003. Atlas of zircon textures, in: Hanchar, J.M. and Hoskin, P.W.O. (Eds.), Zircon, Reviews in Mineralogy and Geochemistry, 53. Mineralogical Society of America, Washington, DC, USA, p. 468– 500.

Costa, L.S., 2016. A proveniência dos sedimentos e cinzas vulcânicas dos sedimentos Permianos da Bacia do Paraná: implicações para a história geológica do sul-sudoeste de Gondwana. Tese (Doutorado). Brasília: Universidade de Brasília – UnB.

Ddani, M., Meunier, A., Zahraoui, M., Beaufort, D.E.L., Wartiti, M., Fontaine, C., Boukili, B., E.L. & Mahi, B., 2005. Clay mineralogy and chemical composition of bentonites from the Gourougou volcanic massif (northeast Morocco). Clays and clay minerals, 53, p. 250-267.

Einsele, G. & Seilacher, A. (Ed.), 1982. Cyclic and Event Stratification. Springer-Verlag, Berlin, 536 pp.

Einsele, G., Chough, S.K., Shiki, T., 1996. Depositional events and their records-an introduction. Sedimentary Geology. 104, p.1-9.

Faustinoni, J.M. & Carneiro, C.D.R., 2015 Movimentos da crosta e relações entre Tectônica e dinâmica atmosférica. Terræ Didatica, 11(3), 173-181. <http://www. ige.unicamp.br/terraedidatica/>.

Fisher, R.V. & Schmincke, H.U., 1984. Pyroclastic Rocks. Springer–Verlag, Berlin. 472 pp.

Formoso, M.L.L., Calarge, L.M., Garcia, A.J.V., Alves, D.B., Gomes, M.B. & Misusaki, A.M., 1997. Permian tonsteins from the Paraná Basin, Rio Grande do Sul, Brazil. 11th Clay Conference, Otawa: Proceedings, pp. 613–621.

Gill, R., 2015. Chemical Fundamentals of Geology and Environmental Geoscience. Ed.3., Wiley, hichester-UK, p.267.

Govindaraju, K., 1994. Compilation of working values and sample description for 383 geostandards. Geostandards Newsletter, 18, 1-158.

Gradstein, F.M., Ogg, J.G., Schmitz, M.D., Ogg, G.M., (Eds.). 2020. The Geologic Time Scale 2020. 2´v. Boston, Elsevier, pp.1400. DOI:https://doi.org/10.1016/C2020-1-02369-3.

Gradstein, F.M., Ogg, J.G., Schmitz, M.D., Ogg, G.M., 2012. The Geologic Time Scale 2012. Amsterdam: Elsevier, 1176 pp.

Grim, R.E. & Güven, N., 1978. Bentonites - geology, mineralogy, properties, and uses. Developments in Sedimentology, n.24, Earth-Science Reviews. p.256.

Hazen, R.M., Papineau, D., Bleeker, W., Downs, R.T., Ferry, F., McCoy, T., Sverjensky, D., Yang, H., 2008. Mineral evolution. American Mineralogist, 93,1693-1720

Hermanns, R.L. & Schellenberge, A., 2008. Quaternary tephrochronology helps define conditioning factors and triggering mechanisms of rock avalanches in NW Argentina. Quaternary International, 178, 261–275.

Hermanns, R.L., Trauth, M.H., Niedermann, S., McWilliams, M. & Strecker, M.R., 2000. Tephrochronologic constraints on temporal distribution of large landslides in northwest Argentina. Journal of Geology, 108, 35–52.

Huff, W. D., Bergstro, S. M., Kolata, D. R., Sun, H. (1997). The Lower Silurian Osmundsberg K-bentonite. Part II: mineralogy, geochemistry, chemostratigraphy and tectonomagmatic significance. Geological Magazine, 135, 15-26.

Huff, W.D., 2016. K-bentonites: A review. American Mineralogist, 101, 43–70.

Jaffey, A.H., Flynn, K.F., Glendenin, L.E., Bentley, W.C. & Essling, A.M., 1971. Precision Measurement of Half-Lives and Specific Activities of ^{235}U and ^{238}U. Phys Rev. C.,4, 1889-1906. https://doi.org/10.1103/PhysRevC.4.1889.

James, N.P. & Dalrymple R.W., (Ed.), 2010. Facies Models 4. GEOtext 6. Geological Association of Canada. p.3-18.

Jerram, D. & Petford, N., 2014. Descrição de rochas ígneas: Guia geológico de campo. 2. ed. Trad.: Ana Maria

Lajoie, J. & Stix, J., 1992. Volcaniclastic Rocks. In: Facies Models: Response to Sea-level Change (Ed. by Walker R.G. and James N.P.), Geological Association of Canada., Waterloo, Ontario. pp. 101-118.

Lovelock, L.E., & Margulis, L., 1974. Atmosphere homeostasis by and for the biosphere: the Gaia hypothesis. Tellus, 26, 2-10.

Lovelock, J., 2005. Gaia: Medicine for an ailing planet. London: Gaia Books.

Lowe, D.J., 2008. Globalization of tephrochronology: new views from Australasia. Progress in Physical Geography, 32(3), 311–335. Doi: 10.1177/0309133308091949

Lucas, S.G., 2018. The GSSP Method of Chronostratigraphy: A Critical Review. Frontiers Earth Science, 6, p.1-18. doi: 10.3389/feart.2018.00191

Ludwig, K.R., 2012. User's manual for Isoplot 3.75. A geochronological toolkit for Microsoft excel. Berkeley Geochronological Center, Special Publication, 5, p. 75.

Meunier, A., 2005. Clays. Berlin: Springer-verlag, 472p.

Miall, A.D., 2016. Stratigraphy: A Modern Synthesis. University of Toronto, Springer. P.311-370. Doi:10.1007/978-3-319-24304-7.

Mitchum, R.M., Vail, P.R. & Sangree, J.B., 1977. Seismic Stratigraphy and global changes of sea level, Part 6: Stratigraphic interpretation of seismic reflection patterns in depositional sequences. In: Payton, C.H.E. (Ed.), Seismic Stratigraphy - application to hydrocarbon exploration. Tulsa: American Association of Petroleum Geologists. Memoir, v .26, p.117-134.

Murphy, M.A. & Salvador M., 1999. International Stratigraphic Guide — An abridged version. Episodes, v.. 22(4), 255-272.

North American Commission on Stratigraphic Nomenclature (NACSN), 2005, North American Stratigraphic Code American Association of Petroleum Geologists Bulletin, v. 89, p. 1547-1591.

Ogg, J.G., Ogg, G., Gradstein, F.M., 2016. A Concise Geologic Time Scale: 2016. Elsevier, Amsterdam 240 pp.

Pimentel Mizusaki and Rualdo Menegat. Porto Alegre: Bookman, 280 p.

Posamentier, H.W., Jervey, M.T. & Vail, P.R., 1988. Eustatic controls on clastic deposition I - conceptual framework. in: Wilgus, C.K., Hastings, B.S., Kendall, C.G.St.C., Posamentier, H.W., Ross, C.A. and Van Wagoner, J.C., (eds.), Sea Level Changes - An Integrated Approach: SEPM , Special Publication, 42, p. 110-124.

Posamentier, H.W., Jervey, M.T. & Vail, P.R., 1988. Eustatic control on clastic deposition I - conceptual framework. In: Wilgus, C.K., Hastings, B.S., Kendall, C.G.ST.C., Posamentier, H.W., Ross, CH.A. & Van Wagoner, J.C. (Eds.). Sea-level changes - an integrated approach. Tulsa: Society of Economic Paleontologists and Mineralogists. Special Publication, v .42, p.109-124.

Reading, H.G. (Ed.) 1996. Sedimentary environments: processes, facies and Stratigraphy. 3.ed. London: Blackwell Science. 688p.

Reading, H.G., 1996. Sedimentary Environments: Processes, Facies and Stratigraphy. 3rd Edition, Blackwell, Oxford, p. 689.

Reiners, P.W., Carlson, R.W., Renne, P.R., Cooper, K.M., Granger, D.E., McLean, N.M. & Schoene, B., 2018. Geochronology and Thermochronology. John Wiley & Sons. p.39-82. ISBN: 978-1-118-45578-4.

Remane, J., Bassett, M.G., Cowie, J.W., Gohrbandt, K.H., Lane, H.R., Michelsen, O. & Wang, N., 1996. Revised guide-lines for the establishment of global chronostratigraphicstandards by the International Commission on Stratigraphy(ICS). Episodes 19, p. 77-81.

Schaltegger, U., Schmitt, A., & Horstwood, M., 2015, U-Th-Pb zircon geochronology by ID-TIMS, SIMS, and laser ablation ICP-MS: Recipes, interpretations, and opportunities: Chemical Geology, 402, p .89–110. https://doi.org/10.1016/j.chemgeo.2015.02.028.

Scotese, C., 2014. Atlas of Permo-Carboniferous Paleogeographic Maps (Mollweide Projection), Maps 53 – 64, Volumes 4, The Late Paleozoic, PALEOMAP Atlas for ArcGIS, PALEOMAP Project, Evanston, IL.. 10.13140/2.1.1837.8244.

Silva, A. F., Dani, N., Remus, M.V.D., Guerra-Sommer M., Horn, B.L.D., 2017. Bentonitas da Formação Irati no setor sul da Bacia do Paraná. Revista do Instituto de Geociências – USP. Geol. USP, Série científica. 17(1), 75-88.

Silva, L.C., 2006. Geocronologia aplicada ao mapeamento regional, com ênfase na técnica U-Pb SHRIMP e ilustrada com estudos de casos brasileiros. Brasília: Publicações Especiais do Serviço Geológico do Brasil - CPRM, pp.132.

Simas, M.W., Guerra-Sommer, M., Mendonça Filho, J.G., Cazzulo-Klepzig, M., Formoso, M.L.L. & Degani-Schmidt, I., 2013. An accurate record of volcanic ash fall deposition as, characterized by dispersed organic matter in a lower Permian tonstein layer (Faxinal Coalfield, Paraná Basin, Brazil). Geologica Acta , 11(1), 45–57.

Steiger, R.H. & Jager, E., 1977. Subcommission on Geochronology: Convention on the use of decay constants in geochronology and cosmochronology. Earth and Planetary Science Letters. 36, p. 359–62.

Walker, R.G. & James, N.P., 1992. Facies models: response to sea level change. Geological Association of Canada. Canada. p.101–118.

Worden, R.H. & Burley, S.D., 2003. Sandstone diagenesis: the evolution of sand to stone. In: Burley, S.D., Worden, R.H. (Eds.), Clastic Diagenesis: Recent and Ancient. International Association of Sedimentologists, v. 4. Blackwell, Oxford, pp.3–44.

Xavier, P.L.A., Silva, A.F., Soares, M.B., Horn, B.L.D. & Schultz, C.L., 2018. Sequence stratigraphy control on fossil occurrence and concentration in the epeiric mixed carbonate-siliciclastic ramp of the Early Permian Irati Formation of southern Brazil. Journal of South American Earth Sciences, 88, p. 157–178. https://doi.org/10.1016/j.jsames.2018.08.014.

Zuffa, G.G., 1980. Hybrid arenites: their composition and classification. J. Sediment. Petrol. 50,p. 21–29. https://doi.org/10.1306/212F7950-2B24-11D7-8648000102C1865D.

Zuffa, G.G., 1985. Optical analyses of arenites: influence of methodology on compositional results. In: Provenance of Arenites. Springer, Dordrecht, p. 165-189.

Zuffa, G.G., 1987. Unravelling Hinterland and Offshore Palaeogeography from Deep-water Arenites. In: Leggett, J. K.; Zuffa, G. G. Marine Clastic Sedimentology: Concepts and case Studies. Dordrecht: Springer, p. 39-61.

Zuffa, G.G., 1991. On the use of turbidite arenites in provenance studies: critical remarks. Geological Society, London, Special Publications, 57(1), p.23-29. doi:10.1144/gsl.sp.1991.057.01.03

Qie, W., Algeo, T.J., Luo, G. & Herrmann, A., 2019. Global events of the Late Paleozoic (Early Devonian to Middle Permian): A review. Palaeogeography, Palaeoclimatology, Palaeoecology, 531. https://doi.org/10.1016/j.palaeo.2019.109259

CAPITULO 2 - ARTIGOS

Artigo 1 - Pyroclastic fall deposits (PFD) from Irati Formation: characterization and chronostratigraphy reconstruction based on high-resolution geochronology.

Acknowledgement of receipt of your submitted article

Chemical Geology <em@editorialmanager.com>

Qua, 07/04/2021 21:14

Para: Você

Dear Mr. Silva,

Your submission entitled "Pyroclastic fall deposits (PFD) from Irati Formation: characterization and chronostratigraphy reconstruction based on high-resolution geochronology" has been received by Chemical Geology.

Please note that submission of an article is understood to imply that the article is original and is not being considered for publication elsewhere. Submission also implies that all authors have approved the paper for release and are in agreement with its content.

You will be able to check on the progress of your paper by logging on to https://www.editorialmanager.com/chemge/ as Author.

Your manuscript will be given a reference number in due course.

Thank you for submitting your work to this journal.

Kind regards

Editorial Office

Chemical Geology

In compliance with data protection regulations, you may request that we remove your personal registration details at any time. (Use the following URL: https://www.editorialmanager.com/chemge/login.asp?a=r). Please contact the publication office if you have any questions.

Pyroclastic fall deposits (PFD) from Irati Formation: characterization and chronostratigraphy reconstruction based on high-resolution geochronology

Aurélio Fagundes Silva[1]*, Norberto Dani[1], Pedro Luis Ammon Xavier[1], Marcus Vinicius Dorneles Remus[1], Cesar Leandro Schultz[1], Ruy Paulo Philipp[1], Marco António Leandro da Silva[2]

[1]Universidade Federal do Rio Grande do Sul – UFRGS. Instituto de Geociências, Pós-graduação em Geociências, Avenida Bento Gonçalves, 9500, CP 15001, CEP 91501-970, Porto Alegre, RS, Brasil

[2]Universidade Federal Ouro Preto - UFOP. Departamento de Geologia, Escola de Minas, 35400-000 - Ouro Preto, MG, Brasil

E-mails: aureliofagundes@hotmail.com, norberto.dani@ufrgs.br, xavier.pedroluis@gmail.com, marcus.remus@ufrgs.br, cesar.schultz@ufrgs.br, ruy.philipp@ufrgs.br, marcomineral@gmail.com

*Corresponding author.

Abstract

The Carbo-Permian sedimentary sequences that occur on Oriental Gondwana are commonly target of palinostratigraphic studies that aim for regional and worldwide correlations. However, this approach often presents low resolution in terms of geochronology and cronostratography. The startpoint of this paper is a detailed stratigraphic description of portion of the Irati Formation, sampled on a borehole that is located at the southern portion of the Paraná Basin. The identification, description and LA-ICP-MS U/Pb zircon dating of pyroclastic fall deposits (PFDs) were also targeted. The PFDs found occur as thin tabular layers on the Passa Dois Group, comprising the section between the Irati and Serra Alta Formations. The results allowed the calibration of the section for further reconstruction studies of part of the paleogeographic and paleoenvironmental evolution that occurred at the Oriental Gondwana during Cisuralian, when the lacustrine ecosystem of the Irati-Whitehill Sea had sedimented and was developed on a climate that varied between conditions of interglaciation and aridification. The sampling was done on three PFDs levels along the section for detailed studies, which presented zircon LA-ICP-MS U/Pb numerical ages of 284.1± 3.5 (2σ; MSWD = 1.14, n=4), 280.8 ± 1,4 Ma (2σ; MSWD = 0.85, n=13) and 274.2 ± 2.8 (2σ; MSWD=0.87, n=4). These novel data of the southern sector of the Paraná Basin enables stratigraphic and tephrochronological comparison with other sectors of the basin. The PFDs ages combined to stratigraphic informations and observed structures along the profile allowed the evaluation of deposition rate, cycles ages, features (fossiliferous horizons) and geochronological positioning of the beginning and ending of the Irati-Whitehill Sea System implantation, of wide paleoenvironmental importance for the Cisularian Epoch (lower Permian) at the southern sector of the Panará Basin.

Keywords: Bentonite; LA-ICP-MS U-Pb dating; Stratigraphic Methods; Tephrochronology; Sequence Stratigraphy

1. INTRODUCTION

In the Gondwana basins, the global chronostratigraphy of the Permian Period is not perfectly adjusted. One factor is that its adjustment is mainly based on palynology (Vázquez and Césari, 2017; Rocha et al., 2020). These have a low resolution for chronostratigraphy (e.g. Stephenson, 2016; Rocha et al., 2020). Another aggravating factor is that Permo-Carboniferous Global Boundary Stratotype Section and Points (GSSPs) have no palynological basis (e.g. Césari, et al., 2011; Gradstein et al., 2012; Ogg et al., 2016; Stephenson, 2016), hindering the development of palynological biochronology. This requires using other tools to refine the Permo-Carboniferous global chronostratigraphic scale, such as isotopic geochronology as secondary proxies.

The sedimentary lithostratigraphic unit used as a geochronological tool in this Period is the pyroclastic fall deposits (PFD), considered the smallest informal lithostratigraphic unit hierarchy of sedimentary lithostratigraphic units (NACSN, 2005). PFDs in sedimentary sequences are of great importance for studying stratigraphy and chronostratigraphic correlations of a Formation or a Group in Global Chronostratigraphic classification Units. Once identified, PFDs can be used to obtain geochronological data. For representing deposits of relatively instantaneous episodic events for the geological time scale (Einsele and Seilacher 1982, Einsele et al., 1996; Boggs, 2014; Miall, 2016), and for containing minerals favourable for the application and obtaining numerical ages by isotopic geochronology (Alan, 2018; Reiners et al., 2018), when identified in sedimentary sequences are considered a geochronological unit, mainly for Phanerozoic deposits (Jaffey et al., 1971; Mattinson, 2000; Boggs, 2014; Reiners et al., 2018). Examples are the various PFDs used for GSSP establishments of the international chronostratigraphic chart (Gradstein et al., 2012; Boggs, 2014; Ogg et al., 2016; Walker et al., 2018). In the stratigraphic code (NACSN, 2005), PFDs is the smallest informal lithostratigraphic unit hierarchy of sedimentary lithostratigraphic units. PFDs become formal lithostratigraphic units when they have established numerical age, making them geochronological landmarks.In the calculations, for Phanerozoic and Neoproterozoic zircons, it is advised to choose only the $^{206}Pb/^{238}U$ ratio because the radioisotopic dates of $^{204}Pb_{rad}$ have insufficient amount to be evaluated in the concordance curve, loss of Pb or subtle inheritance (Jaffey et al., 1971; Mattinson, 2000; Boggs, 2014; Reiners et al., 2018).

Because they are almost always altered in old deposits, its recognition in these deposits requires other characterizations, such as petrographic, mineralogical, geochronological and/or tefrochronological. When preserved in a marine environment, the volcanic ash fragments tend to change to bentonite (Ddani et al., 2005; Meunier, 2005; Spears, 2012; Boggs, 2014; Huff, 2016; Reiners et al., 2018).

The identification and radiometric dating of PFDs allow the transformation of PDFs into geochronological landmarks, making these levels formal geochronological units (Article 26 - NACSN, 2005). The $^{238}U/^{235}U_{zircon}$ ratio of 137.88 of radioisotopic decay constants established by Jaffey et al. (1971) and Steiger and Jager (1977) for obtaining geochronological numerical ages, or just numerical ages. The EARTHTIME group has recalculated radioisotopic decay constants and established a new value of 137,818 ± 0.045 of the $^{238}U/^{235}U_{zircon}$ ratio (Hiess et al., 2012; Condon et al., 2015; McLean et al., 2015).

In the classification of genetic provenance of Zuffa (1980; 1985; 1987), PFDs are considered Noncarbonate Extrabasinal Coeval Neovolcanic (NCE_c) from volcanic manifestations located in the limits of the geotectonic province of the basin (NCE_{cV2b}), or outside its boundaries (NCE_{cV3}) (Zuffa, 1980; 1985; 1987; De Rosa et al., 1986; Critelli & Ingersoll 1995). Provenance studies in the Gondwanic basins correlate PFDs to explosive magmatic events originating in the Choiyoi Volcanic Province (Milani and De Wit, 2008; Rocha-Campos et al., 2011). They are ashes from volcanic eruptions carried by the atmosphere, which under favourable conditions reached Eastern Gondwana and deposited as tabular layers, generally with a small thickness due to the distal character of the deposits (Llambías et al., 1993; Rocha-Campos et al., 2019; Sato et al., 2015; Griffis et al. 2018; 2019).

Its large area distribution will allow for tephrochronological correlations, thus increasing the accuracy of chronostratigraphic correlations of sedimentary packages (e.g. Sato et al., 2015; Huff, 2016; Rocha-Campos et al., 2019) and assisting other stratigraphic methods such as sequence stratigraphy and palynostratigraphy.

In the Paraná Basin, some Cisuralian Epoch (early Permian) PFDs have already been identified (Sato et al., 2015). Previous studies have identified PFDs in the Irati Formation in the region of São Mateus do Sul (PetroSix mine), Paraná state (Santos et al., 2006; Rocha-Campos et al., 2019; Bastos et al., 2020).

This study's main objective is the chronostratigraphic reconstruction of the geological records of the Irati Formation, deposited during the Cisuralian of West Gondwana. For this purpose, different levels of PFDs were identified in the

sedimentary sequence and its zircons analyzed to obtain numerical ages. For this, a drill core was described (Companhia de Pesquisa de Recursos Minerais - CPRM) from another location in the Paraná Basin in the region of Herval, Rio Grande do Sul state, with the aim to identify the presence of PFDs in the Irati section, so to proceed with geochronological determinations for correlation studies with PFDs at the PetroSix mine. After identifying the PFDs, the studies were oriented to mineralogical characterization and to separate zircon grains for U/Pb dating. The zircons found in PFDs present a non-detritical morphology (primary magmatic origin). The occurrences of PFDs along the drill core were placed in a high-resolution stratigraphic section, from which sedimentological parameters were evaluated, such as the estimation of the depositional rate, probable age of the episodic events that occurred during the sedimentation of the Passa Dois Group and additional information for tephrochronological correlation of the Irati Formation. The results obtained allowed the establishment of tephrochronological correlations with other PFDs of the same formation and the determination of deposition interval of time of the System Irati.

2. GEOLOGICAL SETTING

The intracratonic Paraná Basin is one of the widest geological compartments of the South American continent (Figure 1A), extending for an area of 1.7 x 10^6 km^2, of which a large part (1.1 x 10^6 km^2) is located in the central-south portion of Brazil (Milani et al., 2007). It reaches southeastern Paraguay, northeastern Argentina, and northern Uruguay (Figure 1B). The Paraná Basin is related to other basins that register coeval geological evolution, such as the Chaco-Paraná Basin at south, and the Huab, Kalahari and Karoo basins in Namibia, southern region of Africa (Zalán et al., 1990; Milani, 1997; Faure and Cole, 1999; Milani et al., 1994; 2007; Holz et al. 2010). The Paraná Basin preserves approximately 400 Myr of chronostratigraphic record of the Earth's Phanerozoic geological history, ranging from the Paleozoic to the Mesozoic, between the Neo-Ordovician to the Neo-Cretaceous (450 to 65 Ma) (Milani et al., 2007; Milani and De Wit, 2008).

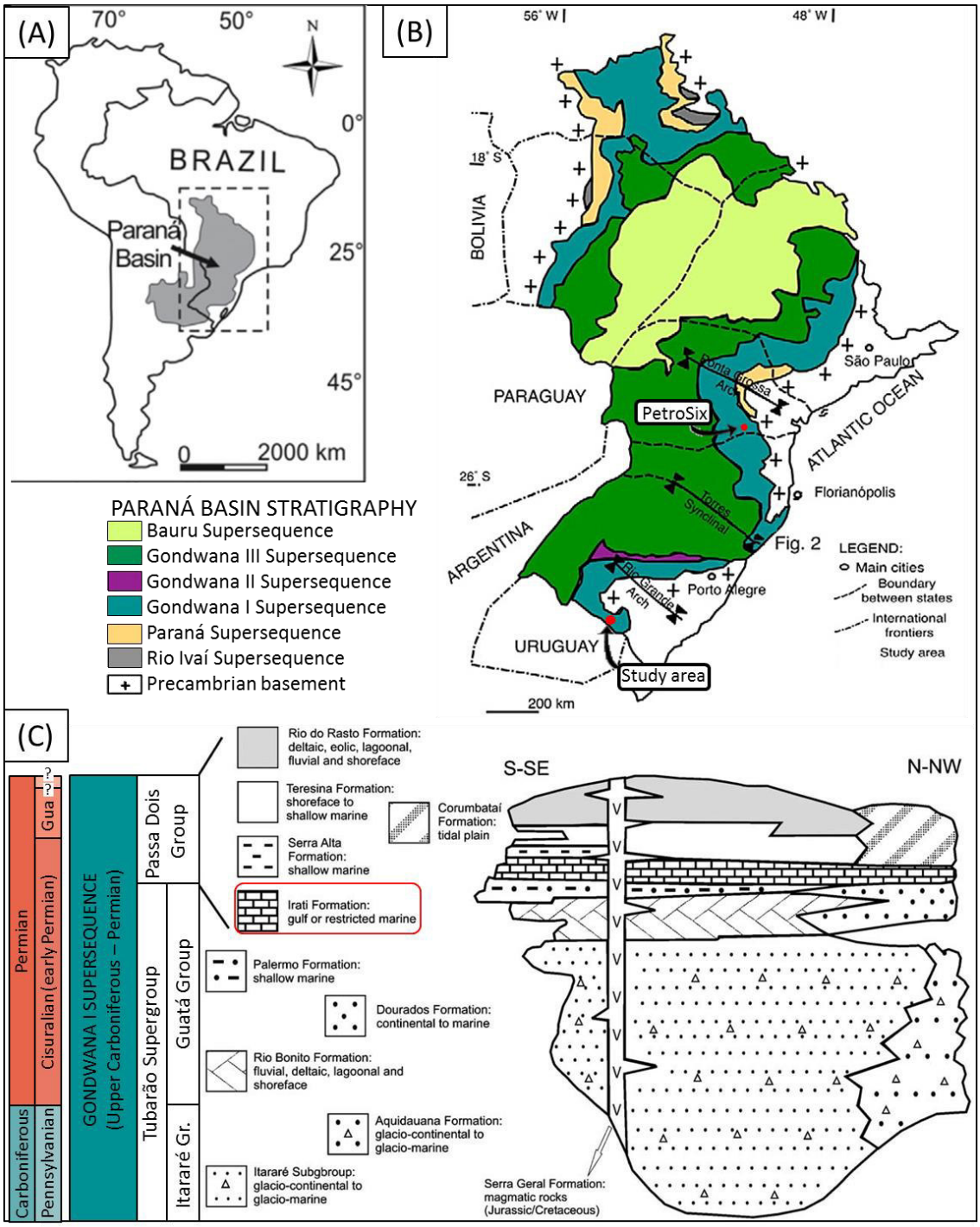

Figure 1- (A) Extension of the Paraná and the Chaco Paraná Basins in South America. (B) Main features and allostratigraphic units of the Paraná Basin in Brazil (modified by Milani et al., 2007) with the location of the study area (survey HV-44 -RS in Herval) and the correlation profile (PetroSix in São Mateus). (C) Stratigraphic chart of Supersequence Gondwana I (Carboniferous-Eotriassic) with the Paraná Basin units' distribution, highlighting the Irati and Serra Alta Formations (modified from Iannuzzi, 2013).

Studies on the lithostratigraphic subdivision of the Paraná Basin and its geological significance began with White (1908), followed by Schneider et al. (1974), Zalán et al. (1990), Milani (1997), Milani and Ramos (1998), Milani and Zalán (1999), Milani et al. (2007), Milani and De Wit (2008), Holz et al. (2010), Iannuzzi et al. (2010), Iannuzzi (2013) and Rocha-Campos et al. (2019). Milani (1997) subdivided the Paraná Basin into six tectonostratigraphic megasequences, being the

Supersequence Gondwana I (Carboniferous-Early Triassic 310-245 Ma) in the time range of interest of this study. The Supersequence Gondwana I is compartmentalized in the following lithostratigraphic units (Figure 1C): Itararé Group (Lagoa Azul, Campo Mourão and Taciba Formations), Guatá Group (Rio Bonito and Palermo Formations) and Passa Dois Group (Irati, Serra Alta, Teresina and Rio do Rastro), followed by the Triassic Sanga do Cabral and Piramboia formations (Holz et al. 2010).

PFDs levels identified as tonsteins and bentonites occur throughout the stratigraphic section of Carboniferous and Permian and are considered geochronological units in the Groups Itararé (Cagliari et al., 2016), Guatá (Rio Bonito Formation) (Griffis et al., 2018) and Passa Dois (Irati and Rio do Rastro Formations) (Santos et al., 2006; Rocha-Campos et al., 2019). Based on lithostratigraphic, biostratigraphic and geochronological studies, it is estimated that the formation interval of the Supersequence Gondwana I is of approximately 58 Myr, ranging from Bashkirian Stage (Carboniferous-Pennsylvanian) to Wachumpingian Stage (Upper Permian) (Holz et al. 2010; Rocha-Campos et al., 2019).

The focus of this study is the Irati Formation, which is the lower unit of the Passa Dois Group (Figure 1C) formed during the Cisuralian Epoch (early Permian) (278.4 ± 2.2 Ma, Santos et al., 2006). The Irati Formation deposition is considered a stratigraphic landmark in the Paraná Basin (Schneider et al. 1974; Lavina, 1991; Araújo, 2001; Araújo et al., 2004; Holz et al., 2010) and it is related to the shallow epicontinental-type sea called Irati-Whitehill Sea (Lavina, 1991; Araújo, 2001; Bastos et al., 2021). This sea was established in southern Gondwana and was extended over a vast area (4×10^6 km^2), settling in central-south region of Brazil, Paraguay, Argentina, Uruguay and Southern Africa (Matos et al., 2017; Bastos et al., 2021). It is an unit of 40-70m thickness and broad regional distribution, composed by horizontal strata, with lithological similarity (e.g. carbonates and bituminous black shales) and fossiliferous identity (mesosaurids). It is correlated to several Formations such as Mangrullo (Uruguay), Tacuary (Paraguay), Chacabuco (Argentina), Huab (Huab Basin), Whitehill (Aranos, Kalahari and Karoo Basins) and Black Rock Member (Falkland Island) (Milani and Zalán, 1999; Araújo, 2001; Matos et al., 2017; Bastos et al., 2021).

In terms of lithostratigraphy, the Irati Formation is divided into a lower portion called the Taquaral Member, that is essentially siliciclastic (siltstones, pelites and dark grey to light grey shales), bioturbated and poor in organic matter, with parallel

lamination as most common sedimentary structure (Xavier et al., 2018). The upper part is called the Assistência Member, composed by siliciclastic rocks (dark grey black shale and bituminous shale) interspersed with carbonates (grey to beige dark limestone, overall dolomitic). It is also noticeable the presence of fish fossils, crustaceans, semi-aquatic reptiles (Matos et al. 2017), fragments of land vegetation (Iannuzzi, 2013) and palynomorphs (Santos et al., 2006; Césari, 2007; Vázquez and Césari, 2017; Rocha et al., 2020) are also present. The reptile fossils present are Mesosaurus (*Progranosauria*), being the most common *Mesosaurus Brasiliensis*, *Stereosternum Tumidum* and *Brazilosaurus* (Santos et al., 2006; Cisneros et al., 2015; Xavier et al., 2018). Palynology analysis exhibits predominance of taenate bisaccate pollen grains (e.g. Stephenson, 2016; Rocha et al., 2020) such as Lueckisporites virkkiae (e.g. Santos et al., 2006) which is placed in the palynological biozone *Lueckisporites virkkiae Zone* (LvZ) (Artinskian a Roadian) (Santos et al., 2006; Vázquez and Césari, 2017; Rocha et al., 2020).

The PFDs levels that belong to the Passa Dois Group were firstly described by Maynard et al. (1996), which identified in the Irati Formation three PFDs levels at PetroSix Mine (Figure 1) located in São Mateus do Sul, Paraná State (coordinates Lat $25^0$48'53" S / Long $50^0$25'42" O) and at 757 km northward of the study area of this work. Successive surveys at PetroSix identified different quantities of PFDs levels, being registered eight levels on Araújo (2001), thirteen on Costa (2016) and one on Bastos et al. (2021). Based on isotopic geochronology, the numerical ages obtained for some of these PFDs were interpreted as the probable time of the volcanic ashes formation/deposition. The most important PFDs on this site are:

- Sample SM-03, zircon U/Pb SHRIMP analysis, $^{206}Pb/^{238}U$ ratio numerical age of 278,4 ± 2,2 Ma, (1σ; MSWD = 1.01, n=7) (Santos et al., 2006);
- Sample SM-01, zircon U/Pb SHRIMP analysis, $^{206}Pb/^{238}U$ ratio numerical age of 280,0 ± 3,0 Ma (1σ; MSWD = 0.9, n=15) (Rocha-Campos et al., 2019);
- Sample Paleosul 05, zircon U/Pb CA-TIMS analysis, $^{206}Pb/^{238}U$ ratio numerical age of 277,22 ± 0,57 Ma (2σ; MSWD = 0.057, n=1) (Bastos et al., 2021).

3. MATERIALS AND METHODS

The study is based on samples collected from the drill core HV-44-RS (Lat 31°56'42.90"S / Long 53°53'18.85"W) at municipality of Herval, in a survey carried out by Geological Survey of Brazil (CPRM) in 1982 (Figure 1; Aborrage and Lopes,

1986). In the studied core in the interval of Irati and Serra Alta Formations (130m to 188m), eight levels of massive claystones were identified and described, all potentially corresponding to PFDs. Sampling was limited to small amounts, between 17 to 28 g of each level. The samples were subjected to mineralogical analysis in the laboratories of the Geosciences Institute of the Universidade Federal do Rio Grande do Sul (UFRGS), specifically at the Centro de Estudos em Petrologia e Geoquímica (CPGq) and at the Centro de Estudos em Geologia Costeira (CECO).

The determination of the mineralogical composition was complemented with X-ray diffractometry analysis (XRD, Siemens D 5000 - CuKα, 40 mA and 25 kV) for clay minerals identification, according to the methodology of Velde (1992) and Meunier (2005). Two fractions were analyzed, one of the whole rock (WR) based on the disoriented alignment of the grains (3° to 50^0 2Θ 0.02^0 / 1s), and another aiming the compositional analysis of fractions smaller than 2μm (3° to 38^0 2Θ 0.02^0 / 1s). In the latter four analytical techniques were applied: I) air-dried oriented sample (N); II) saturated with ethylene glycol (EG); III) calcined at 550^0C for 2h (C); and IV) disoriented preparation for identification of parameter-b (61^0 to 64^0 2Θ 0.01^0/10s).

The mineral separation of heavy minerals followed the methodology of Bohor and Triplehorn (1993) and Reiners et al. (2018), with the use of sieving (500 Mesh) and subsequently heavy liquid (bromoform). By the end of the separation process concentrates of heavy and light minerals of each sample were achieved. Each fraction was analyzed on binocular stereomicroscope for determination of macroscopic properties of grains (colour, external morphology, degree of transparency, presence of inclusions, fractures and alterations). In the heavy minerals fraction special attention was given to the identification and separation of euhedral zircons with dimensions ranging from fine sand to silt (30 to 100 microns). The zircons were analyzed by optical microscopy and by scanning electron microscopy (SEM, JEOL JSM 6060) equipped with an energy-dispersive X-ray spectroscopy detector (EDS, Bruker Nano X Flash Detector 5030) to define the chemical composition.

The isotopic geochronology requires a significant number of zircons, and this is the main criteria used to choose favorable levels for dating along the studied profile. Another criteria used was the distance between the levels, being preferable to achieve a distribution that covered the entire range that corresponded to the Irati Formation in the drill core (e.g. Rossignol et al. 2019). Thus, zircons of three levels of PFDs named BIR9, BIR5 and BSA1 were chosen along the core HV-44-RS to be

subjected to dating. For each level a population 50 grains were chosen, picked and fixed on double-sided tape. Subsequently, the mould with the grains was filled with epoxy resin, and after dry, the resulting tablet was polished with diamond paste to expose the zircon grains.

The polished sections were analyzed at the Isotopic Geochemistry Laboratory (IGL) of the Geosciences Institute of the Universidade Federal de Ouro Preto (UFOP). Firstly, each section was gold and carbon-coating and subjected to cathodoluminescence analysis (CL) in a JEOL 6510 scanning electron microscope (SEM). The objective was to obtain images to assess the mounted grains' integrity and crystallization details such as zonation, all necessary for targeting the laser ablation spots for dating. Then Laser Ablation-Inductively Coupled Plasma-Mass Spectrometry (LA-ICP-MS) U-Pb dating of volcanogenic zircons was performed (n = 131 crystals, 64 analyses) on samples BIR9 (n = 50 crystals, 15 analyses), BIR5 (n = 56 crystals, 22 analyses) and BSA1 (n = 25 crystals, 27 analyses). A ThermoScientific Element 2 sector field (SF) ICP-MS coupled to a CETAC LSX-213 G2 laser system was used for U-Pb isotope analyses of zircons. The equipment ran in standard high-sensitivity mode (STDS), using spot diameter size of 30 μm, laser energy of 15%, laser shot frequency of 10 Hz and shutter delay of 15 s. Detailed description of the method can be found in Gerdes and Zeh (2006) and Lana et al. (2017). The standards used for calibration included GJ-1 zircon (Jackson et al., 2004) and additional BB and Plešovice zircon standards. Glitter Data Reduction Software for laser ablation microprobe was used to reduce data (Van Achterbergh et al., 2001).

The analytical ages were calculated using the radioisotopic decay constant of 137.88, established through the $^{238}U/^{235}U_{zircon}$ zircon ratio by Jaffey et al. (1971) and Steiger and Jager (1977). Considering the ages obtained, those with concordance errors greater than 5% were not considered. The ages were calculated in terms of millions of years before present (Ma) or just numerical ages (NACSN, 2005; Reiners et al., 2018), and their determination was done by plotting on univariate normal distribution diagrams of the $^{206}Pb/^{238}U$ ratio, using Isoplot Ex 4.15 software (Ludwig, 2012). The random Gaussian variable chosen to represent the analytical uncertainty in plotting was ±σ2 (2 standard deviations from the mean), hence establishing a confidence interval of 95.4%. To represent a good numerical age calibration, it was aimed to group the ages of the $^{206}Pb/^{238}U$ rate that were concordant, and to obtain values of Mean Square Weighted Deviation (MSWD) near 1 (NACSN, 2005; Reiners

et al., 2018). The U - Pb geochronological data are presented in the supplementary material, according to the PlasmAge website's format (www.Plasmage.org) integrated to EARTHTIME.

The numerical age obtained and the stratigraphic record was linked to the chronostratigraphic chart version 5.0 of the Geologic Time Scale (GTS2018) by Walker et al. (2018) for data calibration, as indicated by interregional stratigraphic correlations generated using TimeScale Creator (TS-Creator 7.4) (https://www.timescalecreator.org/index/index.php). From the PetroSix Mine the levels SM-03 (Santos et al., 2006), SM-01 (Rocha-Campos et al., 2019), and Paleosul 05 (Bastos et al., 2021) were used for tephrochronological correlation of the Irati Formation.

4. RESULTS

The drill core HV-44-RS consists of grey siltstones, dark to light grey shales, mudstones and claystones. The Irati Formation faciological detailing of the core is available in Xavier et al. (2018). The lower part of the section (Taquaral Member) consists of dark grey siltstones and mudstones, but no PFDs were identified. The upper part (Assistência Member) is composed by a sequence of dark grey shales, bituminous black shales, carbonates and bonebeds, and it is characterized by the presence of PFDs. The Facies association allowed the recognition of three depositional sequences in the Irati Formation called S1, S2 and S3 (Figure 2A) (Xavier et al., 2018).

The levels of PFDs presented distinguishable characteristics to the shales that also occur in the core. The claystones present discrete and thin tabular layers (2 to 12 cm thick), with shades varying from grey, green, brown and/or yellow, abrupt and discordant contact, absence of sedimentary structures and are texturally massive (homogeneous) (Figure 2).

XRD whole rock mineralogical analyses present an intense diffraction line around 15.0 Å (Figure 3), consistent with d_{001} of smectites (Velde, 1992; Meunier, 2005). The presence of expansive minerals was noticed in the glycolate mode (EG - ethylene glycol) analysis of the fine fraction (<2μm), with the modification of the interplanar basal distance close to 17.0 Å, and in heated mode at 550°C (C) with collapse and spacing close to 9.8 Å. Parameter-b presents diffraction line d_{060} of

1.500 Å, which along with the general behavior of the sample on XRD, shows that the PFDs are formed mainly by clay minerals of the smectite group, identified as dioctahedral montmorillonite, with a predominance of Al in octahedral site (e.g. Ddani et al., 2005; Meunier, 2005).

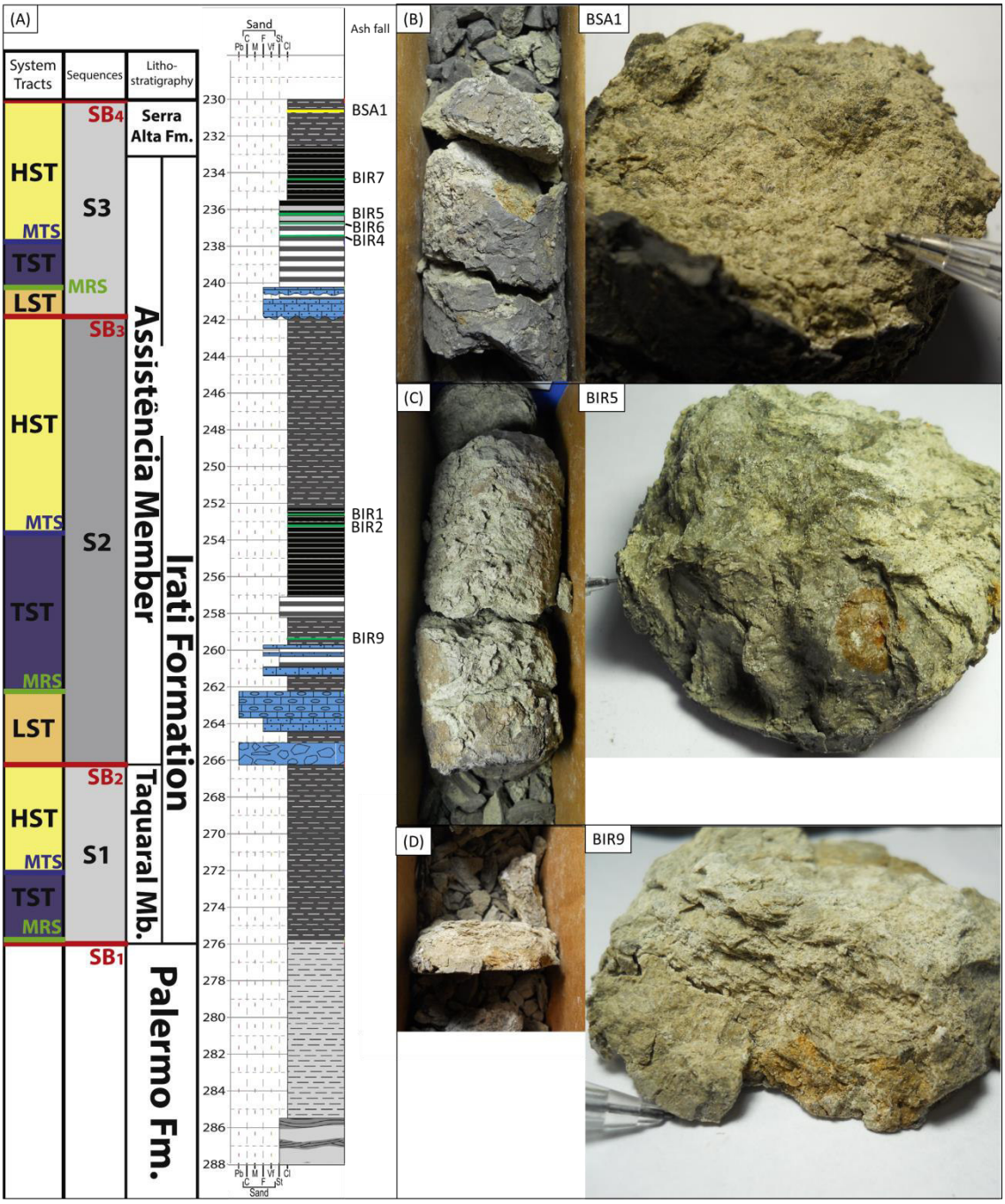

Figure 2 – (A) Facies, sedimentary features and interpretations of HV-44-RS drill core (modified Xavier et al., 2018) and PFDs levels (BSA1, BIR5 and BIR9). In (B), (C) and (D) drilling details of the sampled levels of PFDs (claystones) with respective thickness in the core, considering BSA1 (2 cm), BIR5 (2 cm) and BIR9 (5 cm) (Core width = 5 cm). Detailed photos of the studied fragments BSA1, BIR5 and BIR9 are presented with its macroscopic aspects in evidence.

PFDs BIR9 and BSA1 present clays of the kaolinite group as secondary constituents, identified by the diffraction line in whole-rock (WR) with spacing of 7.1

Å, which disappeared in the calcinated mode (C) of the oriented fine fraction (<2μm). According to Lyons et al. (1994), the PFDs levels of the Irati Formation are classified as bentonite owing to the fact that volcanogenic claystones were formed by more than 50% of clays of smectite group. In the Irati Formation, the levels of PFDs were deposited in marine environment and by post-depositional processes, which transformed most of the labile constituents into clay minerals of the smectite group, through mechanisms such as those established by Fisher and Schmincke (1984), Velde (1992), McKinley et al. (2003), Meunier (2005), Ddani et al. (2005) and Potter et al. (2005).

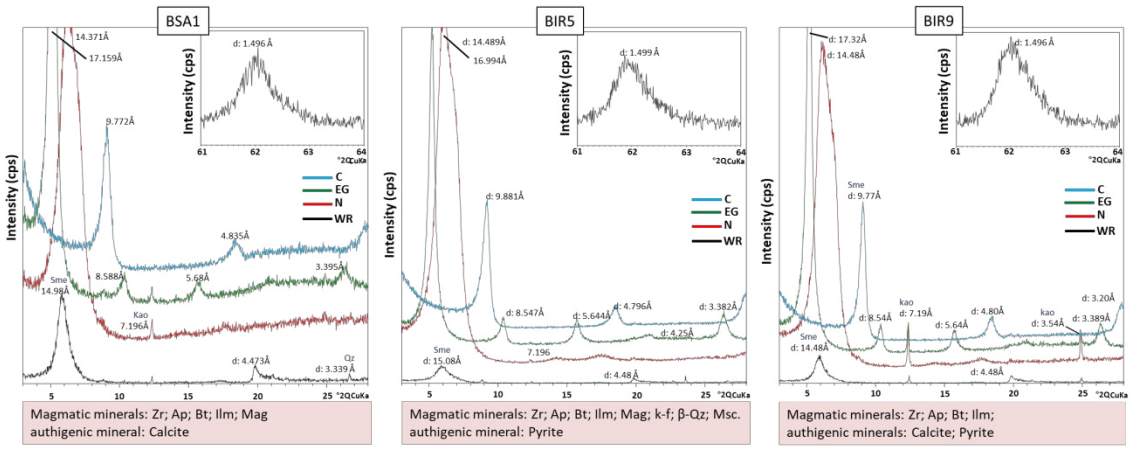

Figure 3 – X-ray diffractograms obtained for the PFDs (BIR5, BIR9, and BSA1) to identify the main components of the claystones. Also presented are the magmatic and authigenic minerals separated by sieving of each level level: Zr (zircon); Ap (apatite); Bt (biotite); Ilm (ilmenite); Mag (magnetite); K-f (K-feldspar); β-Qz (β – quartz); Msc (muscovite); calcite and pyrite.

Besides the clay minerals that are dominant in PFDs, rare minerals are dispersed in the clay matrix (Silva et al., 2017). Such minerals form an assembly of very fine granulometry (30 to 100 microns) of crystals of magmatic origin (Figure 3), that did not present signs of alterations or indications that the grains went through sedimentary transport and reworking processes. These characteristics classify the PFDs in this study as distal volcanic ash, in agreement with previous works performed in other localities (Pupin, 1980; Fisher and Schmincke, 1984; Bohor and Triplehorn, 1993; Spears, 2012). The assembly of volcanic minerals were identified as zircon (Zr), apatite (Ap), biotite (Bt), muscovite (Musc), K-feldspar (Kf), β – quartz (β-Qz), ilmenite (Ilm) and magnetite (Mag) (Figure 3). Authigenic minerals such as framboidal pyrite and calcite were also associated to these deposits (Worden and Burley, 2003).

In this stage, special attention was given to the identification and separation of zircon grains (Figure 4), which is the main mineral for the determination of the

numerical age of this study. The zircon crystals studied (Figure 4) present euhedral morphology, prismatic habit with bipyramids and are elongated in the direction of the c-axis, agreeing with what is observed in crystals of volcanic origin (e.g. Santos et al., 2006; Silva et al., 2017; Rocha-Campos et al., 2019). In BIR9 and BSA1 PFDs, the crystals' length varies between 100-200 μm with length/width (l/w) ratios ranging from 2:1 to 4:1. In PFD BIR5, zircons present elongated prismatic shape, with lengths varying between 140-400 μm and ratios l/w from 4: 1 to 14:1 (with an average of 5:1) and some inclusions and germinations. Under CL analysis, the zircon grains show color variations between white/light grey to dark grey (Figure 4). The majority show oscillatory parallel zoning from the core to the edges, which is sometimes interrupted by posterior overgrowth (Vavra, 1990; Vavra, 1993; Corfu et al., 2003). The spots were selected based on ages values with concordance within the range of 95% and 105% (Table 1), and for the numerical age determination, the ratio $^{206}Pb/^{238}U$ was used (Jaffey et al., 1971; Mattinson, 2000; Boggs, 2014; Reiners et al., 2018). All the analyzed grains presented common lead indicator ($f206_c$) below 1. The U content varied between 231 to 1335 ppm in PFD BIR9, 160 to 615 ppm in PFD BIR5 and 81 to 767 ppm in PFD BSA1. The Th/U ratio varied between 5.77 to 0.59 in PFD BIR9, 2.07 to 0.65 in PFD BIR5, and 3.57 to 0.69 in BSA1 (Table 1).

Following the criteria established by Reiners et al. (2018), as an interpretation of the genesis of minerals and proof of closed U/Pb system, from the fifteen spots analyzed in zircons of PFD BIR9, eight presented satisfactory results (Table 1) and the remaining seven presented low data concordance. To calculate the $^{206}Pb/^{238}U$ weighted mean age, three spots were rejected due to higher ages, and the spot 9.2.1. was discarded because it had signs of Pb_{rad} loss ($^{206}Pb/^{204}Pb$= 12650.53). To obtain the $^{206}Pb/^{238}U$ mean age four analytically concordant results were considered (Figure 5), allowing the determination of an age with three degrees of freedom (Reiners et al., 2018) and $^{206}Pb/^{238}U$ weighted mean age of 284.1±3.5 Ma, with 95% reliability and MSWD = 1.14 (probability = 0.33). This age corresponds to Artinskian Stage, according to GTS2018 of Walker et al. (2018).

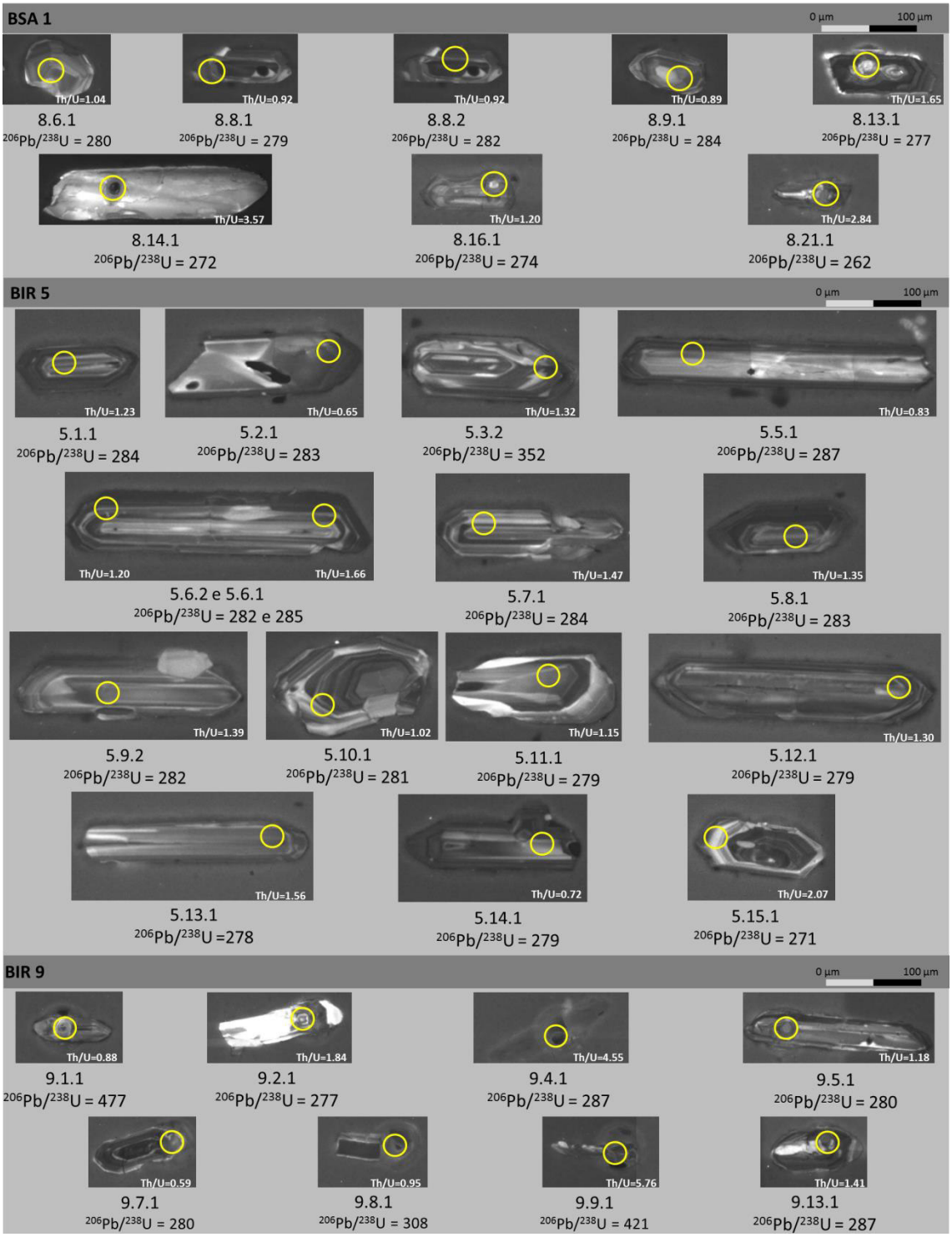

Figure 4 –Cathodoluminescence (CL) images of the zircons from the PFDs. The CL analysis of the zircons studied shows igneous genesis' texture, presenting parallel oscillatory zoning and location of the spot and its number. The yellow circle corresponds to the grain's ablated area, for LA-ICP-MS analysis, with its respective $^{232}Th/^{238}U$ ratios and $^{206}Pb/^{238}U$ ages.

Table 1 - U-Pb zircon data from the Irati Formation PFDs, obtained by LA-ICP-MS.

Spot	$f206_c$	U-Pb geochronological analyses				Isotope ratios							Calculated ages (Ma)						% conc.
		^{207}Pb (CPS)	U (ppm)	$^{206}Pb/^{204}Pb$	$^{232}Th/^{238}U$	$^{207}Pb/^{235}U$	2s (%)	$^{206}Pb/^{238}U$	2s (%)	Rho	$^{207}Pb/^{206}Pb$	2s (%)	$^{206}Pb/^{238}U$	2σ	$^{207}Pb/^{235}U$	2σ	$^{207}Pb/^{206}Pb$	2σ	
BSA 1																			
1.6.1	0.7677	102029	159	13.3	1.04	0.3154	5.07	0.0444	3.87	0.76	0.0515	3.28	280	±10,58	278	±12,39	262	±75,26	100.6
1.8.1	0	159867	250	27.6	0.92	0.3172	2.25	0.0443	1.68	0.74	0.0519	1.50	279	±4,57	279	±5,5	284	±34,34	99.8
1.8.2	0.1848	340836	528	44.4	0.69	0.3206	2.38	0.0447	1.90	0.79	0.052	1.44	282	±5,22	282	±5,87	284	±32,9	99.9
1.9.1	0	112056	173	5830.3	0.89	0.3228	2.18	0.045	1.74	0.8	0.052	1.31	283	±4,81	284	±5,39	287	±29,88	99.9
1.13.1	0.5815	304147	767	18.3	1.65	0.3126	4.01	0.0439	3.06	0.76	0.0516	2.59	277	±8,32	276	±9,76	268	±59,44	100.4
1.14.1	0	31460	81	1628.4	3.57	0.3078	2.76	0.0431	1.67	0.6	0.0517	2.20	272	±4,45	272	±6,63	275	±50,46	99.9
1.16.1	0	36636	93	5.5	1.2	0.3093	2.71	0.0434	1.65	0.61	0.0516	2.15	274	±4,45	273	±6,54	269	±49,32	100.2
1.21.1	0.1512	83794	224	4.4	2.84	0.2946	2.53	0.0415	1.79	0.71	0.0515	1.79	262	±4,61	262	±5,87	262	±41,08	100.0
BIR 5																			
5.1.1	0.1198	301125	464	65.6	1.23	0.3221	2.1	0.0450	1.7	0.82	0.0519	1.17	284	±4.68	284	±5.09	280	±26.87	100.1
5.2.1	0	258843	399	149.2	0.65	0.3215	2.0	0.0450	1.7	0.82	0.0519	1.14	283	±4.57	283	±4.95	280	±26.04	100.1
5.3.2	0.3204	213005	263	17.7	1.33	0.4129	2.6	0.0561	2.0	0.77	0.0533	1.66	352	±6.95	351	±7.80	344	±37.53	100.3
5.5.1	0	104989	160	5435.3	0.84	0.3245	2.2	0.0455	1.7	0.76	0.0518	1.45	287	±4.69	285	±5.51	275	±33.19	100.4
5.6.1	0	212799	326	24.7	1.66	0.3244	2.0	0.0452	1.6	0.80	0.0520	1.21	285	±4.44	285	±4.98	286	±27.69	99.9
5.6.2	0.5068	233171	362	23.1	1.20	0.3206	3.7	0.0447	2.8	0.75	0.0520	2.45	282	±7.68	282	±9.17	287	±55.90	99.7
5.7.1	1	224920	346	279.2	1.47	0.3241	6.2	0.0451	4.7	0.76	0.0521	4.02	284	±13.13	285	±15.50	291	±91.74	99.7
5.8.1	0.0827	296845	459	110.0	1.35	0.3234	2.0	0.0449	1.7	0.82	0.0523	1.14	283	±4.56	285	±4.97	297	±25.92	99.4
5.9.1	0.07	266131	415	60.5	0.76	0.3411	1.9	0.04439	1.6	0.83	0.0557	1.10	280	±4.53	298	±5.15	441	±24.62	93.9
5.9.2	0	285384	443	15005.5	1.39	0.3240	2.1	0.0447	1.7	0.81	0.0526	1.22	282	±4.57	285	±5.12	311	±27.71	98.9
5.10.1	0	327999	510	17269.1	1.02	0.3236	2.1	0.0446	1.7	0.83	0.0527	1.14	281	±4.69	285	±5.10	314	±25.93	98.7
5.11.1	0	130952	206	6785.9	1.15	0.3157	2.0	0.0442	1.6	0.81	0.0518	1.20	279	±4.45	279	±4.94	277	±27.40	100.0
5.12.1	0	278617	436	14429.6	1.30	0.3162	2.0	0.0443	1.7	0.83	0.0518	1.12	279	±4.57	279	±4.92	276	±25.65	100.1
5.13.1	0	206799	325	59.9	1.57	0.3156	2.0	0.0441	1.7	0.82	0.0519	1.16	278	±4.57	279	±4.97	280	±26.47	99.9
5.14.1	0	392023	615	20346.0	0.72	0.3164	1.9	0.0442	1.6	0.84	0.0519	1.06	279	±4.45	279	±4.75	281	±24.25	99.9
5.15.1	1	114661	185	42.6	2.07	0.3237	6.3	0.0430	4.9	0.78	0.0546	3.94	271	±13.11	285	±15.78	397	±88.25	95.2
BIR 9																			
9.1.1	1.0000	435483	629	458.3	0.88	0.6015	4.8	0.0768	3.0	0.63	0.0568	3.72	477	13.85	478	18.44	485	82.18	99.7
9.2.1	0	242999	615	12650.5	1.84	0.3146	2.0	0.0438	1.5	0.77	0.0521	1.29	277	4.20	278	4.91	288	29.41	99.6
9.4.1	0.8732	122109	298	8.3	4.56	0.3412	5.4	0.0455	4.1	0.77	0.0544	3.45	287	11.61	298	14.00	387	77.37	96.2
9.5.1	0	322837	807	24.9	1.18	0.3156	3.1	0.0444	2.4	0.77	0.0516	1.96	280	6.48	279	7.51	267	44.99	100.5
9.7.1	1	533797	1335	120.6	0.59	0.3175	6.2	0.0443	4.7	0.76	0.0519	4.03	280	13.01	280	15.37	283	92.21	99.9
9.8.1	0.0000	407786	923	34.0	0.95	0.3702	2.0	0.0490	1.6	0.81	0.0548	1.17	308	4.79	320	5.43	404	26.16	96.5
9.9.1	0	140586	231	7767.4	5.77	0.5147	2.1	0.0676	1.6	0.76	0.0553	1.38	421	6.52	422	7.30	422	30.70	100.0
9.13.1	0.1736	342835	8	29.2	1.42	0.3261	2.2	0.0455	1.7	0.78	0.0520	1.38	287	4.82	287	5.53	287	31.60	100.0

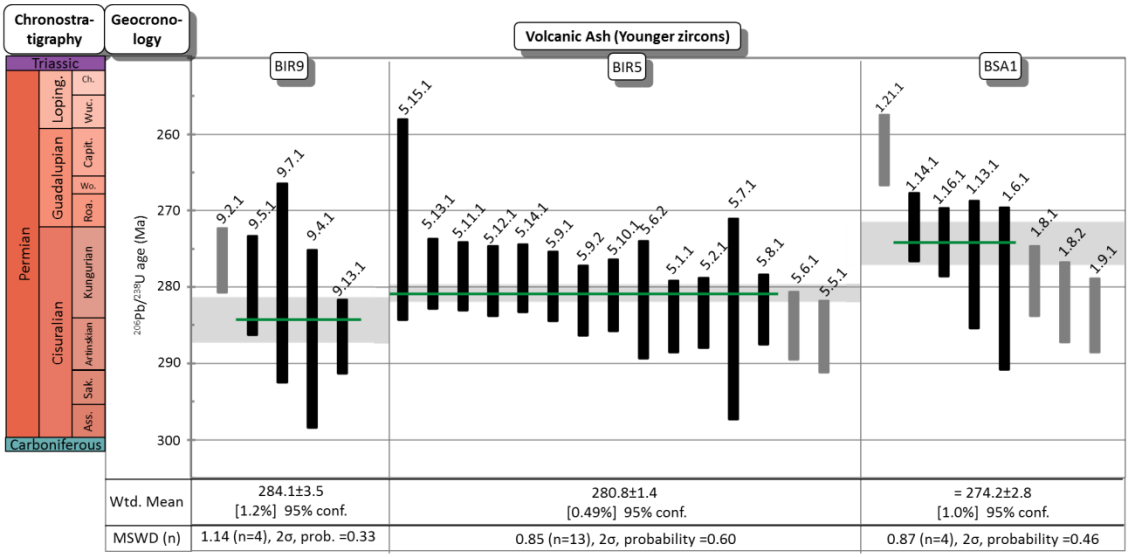

Figure 5 – Zircon U-Pb average weighted mean plot diagram for samples BIR9, BIR5 end BSA1. Each vertical bar represents an analyzed spot, being the ones in black chosen for numerical age calculation. The horizontal green line is plotted at the weighted mean age of the considered analysis, and the shaded grey region corresponds to ±2σ (95%) confidence interval of each sample. The weighted mean, uncertainty, confidence level, MSWD (mean square weighted deviation), and amount of spots used (n) are all reported together with the data.

Among the twenty-two spots in PFD BIR5, sixteen presented satisfactory results (Table 1) and six exhibited low concordance in the data. For 206Pb/238U weighted mean age calculation one spot (5.3.2) was rejected and two spots were disregarded to obtain MSWD values ≈1. Thirteen analytically concordant spots were chosen for dating (Figure 5), with twelve degrees of freedom, resulting in a 206Pb/238U weighted mean age of 280.8±1.4 Ma, with 95% reliability and MSWD = 0.85 (probability of 0.60) (Reiners et al., 2018). This age corresponds to Kungurian Stage.

In the twenty-seven spots analyzed from PFD BSA1, eight presented satisfactory results (Table 1), thirteen showed concordance error in the dataset, and six exhibited higher ages. To calculate the 206Pb/238U weighted mean age, four spots were rejected, one due to younger date and three due to older dates. Four analytically concordant spots were considered (Figure 5), with three degrees of freedom (Reiners et al., 2018), obtaining $^{206}Pb/^{238}U$ weighted mean age of 274.2±2.8 Ma, with 95% reliability and MSWD = 0.87 (probability = 0.46) (Reiners et al., 2018). This age corresponds to Kungurian Stage.

The determination of the numerical ages of PFDs identified in the HV-44-RS (Herval) survey is of great importance for the stratigraphic knowledge of the southern sector of the Paraná Basin, as it enables PFDs to be considered as guide layers, allowing their classification to be as formal lithostratigraphic units, hence being able to

be addressed proper names. According to the North American Stratigraphic Code (Articles 24 and 30, NACSN, 2005), the name is formed using the genetic term of the lithology (in this case is bentonite) together with the name of the formation (in this case is Irati and Serra Alta) to create the acronym that corresponds to Bentonite Irati (BIR), level nine and five (units BIR9 and BIR5), and to create the acronym that corresponds to Bentonite Serra Alta (BSA) level one (unit BSA1). The establishment of these three guide layers allowed the adjustment of HV-44-RS section on the chronostratigraphic chart, hence allowing the correlation of isochronous events and the interpretation of the deposition dynamics during the Permian.

5. DISCUSSION

5.1. PFDs (bentonites) provenance and zircon properties

The indicators of contemporary volcanogenic provenance in relation to deposition of the PFDs BIR5, BIR9 and BSA1 are defined by their faciological, mineralogical, geochronological and tephrochronological characteristics. The faciology of the studied levels present contrasting characteristics along the profile, such as tabular and thin layers (varying from 2 to 12 cm), abrupt discordant contact, absence of sedimentary structures (texturally homogeneous), consisting on claystones of shades varying from grey, green, brown and/or yellow (Figure 2). These characteristics are indicative of the faciological signature of lithified PFDs as established by Bohor and Triplehorn (1993), Ddani et al. (2005) Huff (2016). At the three levels, XRD analysis reveal mineralogical composition that consists predominantly of dioctahedral montmorillonite, as identified in other locations and units of the Paraná Basin's Supersequence Gondwana I (Maynard et al., 1996; Calarge et al., 2003; Silva et al., 2017), and are compatible with deposition and transformation of the volcanic glass of the PFDs (Fisher and Schmincke, 1984; Bohor and Triplehorn 1993; Meunier, 2005; Potter et al., 2005; Spears, 2012) in marine environment. Due to the chemical instability of volcanic glass, its transformation into smectites occurs by post-depositional processes similar to that established by Velde

(1992), McKinley et al. (2003), Meunier (2005), Ddani et al. (2005) and Potter et al. (2005). The assemblies of resistant crystals dispersed in the matrix confirm magmatic origin, with particle size below very fine sand (30 to 100 microns), without signs of alteration or having been submitted to sedimentary transport and reworking processes, similar to that observed in other locations (Pupin, 1980; Fisher and Schmincke, 1984; Bohor and Triplehorn, 1993; Spears, 2012). These characteristics classify the PFDs in this study as bentonite, derived from the chemical transformation of distal volcanic ashes.

The zircons present in PFDs BIR5, BIR9 and BSA1 (Figure 3) are idiomorphic and have no evidence of reworking due to sedimentary or metamorphic related processes (Figure 4). The morphology of the crystals suggests assimilation processes in the early to intermediate stages of crystallization in the magmatic chamber, lasting for sufficient period to enable new growths (e.g. Corfu et al., 2003). From the core to the edge, the parallel oscillatory banding of the zircons is characteristic of an igneous genesis by growth zoning (Vavra, 1990; Vavra, 1993; Corfu et al., 2003), which in CL can be seen as alternate bands with low luminescence (higher concentration U) and high luminescence (lower U concentration). The zircon's zoning is not perfectly concentric, therefore domains in which its growth was interrupted or melted could be registered, as well as subsequent overgrowth (e.g. 8.8.1., 5.10.1, 9.7.1 in Figure 4). These are features linked to magmatic events, caused by relative sub-saturation variations of Zr and Si in the magma (Hanchar and Hoskin, 2003; Hoskin and Schaltegger 2003; Reiners et al. 2018). Similarly, these characteristics are observed in the zircons of the PetroSix Mine (Santos et al., 2006; Rocha-Campos et al. 2019), in which along with convergent data such as age and genesis of volcanic ashes, allows to suggest a common source and establish tephrochronological correlations between the studied PFDs and the PatroSix Mine PFDs.

The geochemical data of the ablated spots in zircons such as U content (ppm), $f206_c$, Th/U ratio and concordance (Table 1) reinforce its magmatic origin (Belousova et al., 2002; Hanchar and Hoskin, 2003; Hoskin and Schaltegger 2003). In spot 9.7.1 it is noticeable the U content of 1335 ppm, hence the presence of metamictization would be expected. However, based on the data concordance value of 99.9% and the zoning characteristics under CL analysis it is observed that this process did not occur. Most of the spots presented dates with tendency to be concordant. To obtain and group the

$^{206}Pb/^{238}U$ weighted average age, spots with high content of common Pb, inherited grains and results with $^{206}Pb/^{238}U$ discordant dates were not considered. The use of such methodology in this work enabled the first age determination of PFDs of the Irati Formation which are 284.1 ± 3.5 (2σ; MSWD = 1.14, n = 4) and 280.8 ± 1.4 Ma (2σ; MSWD = 0.85, n = 13), and of the PFDs of the Serra Alta Formation which is 274.2 ± 2.8 (2σ; MSWD = 0.87, n = 4). These results are considered the best geochronological estimates for those units in the southern portion of the Paraná Basin. The three numerical ages (Figure 4) were placed along the section of the core HV-44-RS (Figure 2) and are representative of the contemporaneity between volcanic activity and in situ sedimentation of PFDs (Rossignol et al. 2019), also setting them as stratigraphic units that were deposited during the Cisuralian.

There are several differences between the zircons of PFDs BIR9 and BSA1 in relation to PFD BIR5, such as crystal size, tonality, presence of solid inclusions, germinations, textures and isotopic composition (Figure 6). The zircons of BIR9 and BSA1 are euhedral, present short prismatic shapes, lengths between 100-200 μm, and ratios l/w from 2:1 to 4:1. They are colourless hyaline, without solid inclusions or germinations (e.g. BSA1 - figures 3 and 5) and in CL analysis they tend to display U-enriched core when compared to its edges. The low numerical concordance between the ages determined in the PFDs BIR9 and BSA1 provided greater data uncertainty, hence creating a wider dating variability and result on a few ages that are concordant with the relatively high MSWD (Figure 5), thus indicating greater heterogeneity in zircons (Keller et al., 2018). Miller et al. (2007) characterize this heterogeneity in ages as caused by antecrysts, which are crystals from the same magmatic setting, but were previously crystallized and recycled during successive magmatic injections. These can be mistaken as xenocrysts or inherited crystals, but their genesis is different (Miller et al., 2007). On PFD BIR9 inherited zircons aged around 470 Ma (Figure 4 and Table 1) were identified, similar to that observed by Rocha-Campos et al. (2019) on the PetroSix profile.

In PFD BIR5 the zircon grains are euhedral, present long prismatic shape, with lengths between 140-400 μm and l/w ratios from 4:1 to 14:1 (with an average of 5:1). They are hyaline, colourless to orange, commonly with solid inclusions, twinning, fractures and/or dissolution cavities of other minerals (e.g. BIR5 - figures 3 and 5). In CL

analysis, most grains present zoned bands that tend to be wider and edges more enriched in U than its core. The determined age concordance provided a relatively small dispersion over the mean, with PFD BIR5 showing homogeneous zircon population (MSWD=0.85).

PFDs BIR9 and BSA1 present thickness of 2 and 5 cm respectively, and have an assembly of resistant minerals of volcanic origin composed by Zr, Ap, Bt, Ilm and Mag. PFD BIR5 is 12 cm thick (Figure 2) and present diversified mineralogy composed by Zr, Ap, Bt, Ilm, Mag, Kf, β-Qz and Msc (Figure 3). According to the mineralogy, it is possible to infer that PFDs BIR9 and BSA1 present compatible provenance from volcanisms with tendency for intermediate composition, while BIR5 presents a tendency for acid composition (e.g. Corfu et al., 2003; Hoskin and Schaltegger, 2003). Zirconium is an incompatible element and enriches towards the final magmatic liquid (e.g. Hoskin and Schaltegger, 2003; Reiners et al., 2018), being that the magmatic source of PFD BIR5 is more enriched in zirconium, hence favoring the rapid crystallization of zircon with growth figures as thick bands. The higher concentration of zirconium and uranium suggests that the magma was enriched in volatile phases (e.g. H_2O, CO_2 and SO_2), being more explosive and capable of producing a greater amount of ashes during the eruption, which may have influenced the larger thickness of PFD BIR5 (12cm) (Figure 2). Another evidence is the existence of β-Qz on PFD BIR5, a quartz polymorph that is formed at high temperature and low pressure. According to Miller et al. (2007), the relatively low number of concordant age clusters for the obtention of MSWD ≈1 (Figure 5), which is associated with textural evidence, may indicate that the magma's permanence in the magmatic chamber was faster when compared to the magma that generated BIR9 and BSA1.

The most accepted origin theory for the PFDs of the Supersequence Gondwana I of the Paraná Basin are that the volcanic ashes were produced at the Choiyoi Magmatic Province (e.g. López-Gamundí, 2006; Rocha-Campos et al., 2011; 2019; Limarino et al., 2013; Sato et al., 2015; Nelson and Cottle, 2019; Bastías-Mercado et al., 2020). These PFDs represent the NCE_{cV3} type in the Zuffa (1980; 1985; 1987) genetic provenance classification, being considered as episodic deposits of sin-eruptive periods (Miller et al., 2007) of the volcanic province located outside the tectonic context of the basin (e.g. Zuffa, 1987; Orton, 1996, De Rosa et al., 1986; Critelli and Ingersoll, 1995). The deposits were preserved due to the existence of a favorable depositional environment

during this period in the Southern Gondwana (López-Gamundí, 2006; Rocha-Campos et al., 2011; 2019; Limarino et al., 2013; Sato et al., 2015; Nelson and Cottle, 2019; Bastías-Mercado et al., 2020). The differences observed between PFDs and their relation with volcanic pulses of intermediate to acidic composition in the volcanic province Choiyoi reinforce the existence of compositional variation on magmatism over time.

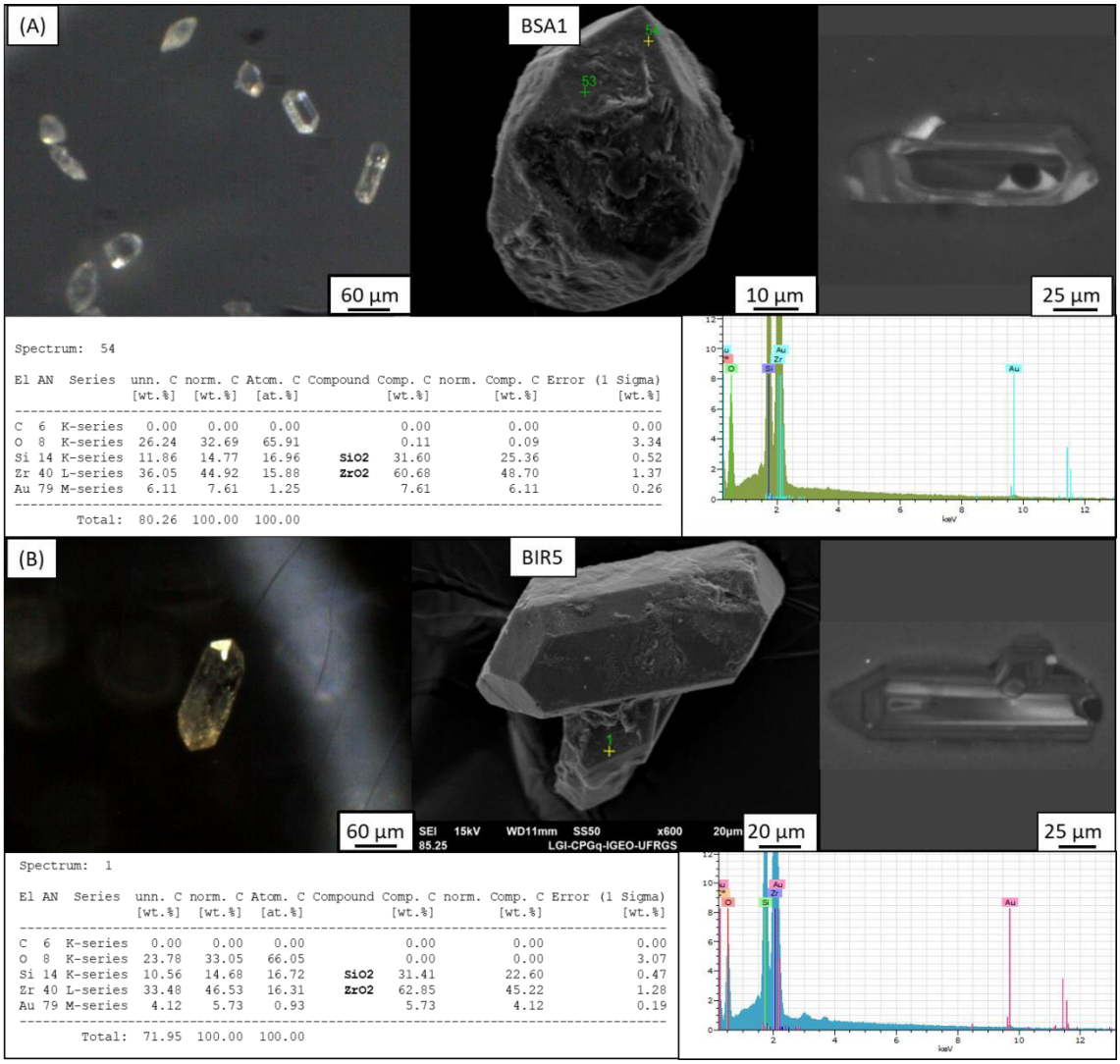

Figure 6 – Characteristics of volcanogenic zircons, highlighting the crystals' morphology under binocular stereomicroscope and SEM (secondary electron image). EDS analysis table of chemical composition and CL image of the analyzed grain. (A) Zircon of PFD BSA1 level. (B) Zircon of PFD BIR5 level.

5.2. Chronostratigraphy of Irati Formation

By associating the ages obtained for the three PDFs with the observed features in the description of the drill core HV-44-RS (Araújo, 2001; Xavier et al., 2018), it is possible to evaluate the behavior of the sedimentation rate of the sequence that composes the Irati Formation (Figure 7A) (e.g. Boggs, 2014). Through the chronological adjustment based on the PFDs dating, the chronostratigraphy methodology allows the determination of ages of the events identified along the stratigraphic section using chronostratigraphy (Figure 7B) and tephrostratigraphy of other PFDs (Figure 7C) identified in the basin.

The curve (Figure 7A) represents the behavior of the sedimentation rate, considering that the changes on its slope are related to modifications in the sedimentation rates, associated or not with eustatic changes, therefore characterized by the sequence limits of the S1, S2 and S3 system tracts by Xavier et al. (2018). Considering the package of bituminous shales, the correlation curve tends to be horizontal and therefore with a wider time range. Two anoxic events were identified in the Irati Formation with an approximate duration of 1.2 Myr and 6 Myr respectively, whilst there is decrease in the sedimentation rate and installation of the stage of starved basin. For the periods that show lowstand systems tracts (LST) in the HV-44-RS core, the relative numerical ages were ~ 284.5 Ma and ~ 281.2 Ma, considering that the entire period of sedimentation of the Irati System lasted for approximately 12 Myr (Figure 7B). Another remarkable event identified was the level with concentration of mesosaurid bonebeds, formed by disarticulated and dispersed skeletons (Lavina, 1991; Araújo, 2001; Ronh, 2007; Xavier et al., 2018), as product of transport by distal tempestites, that was estimated to have a relative numerical age of 280.6 Ma.

It is consensus that the records of PFDs identified in the studied range are related to the San Rafaelic Orogenic Phase (SROP) and represent episodic deposits of sin-eruptive periods of the Lower Choiyoi Igneous Province (Rocha-Campos et al., 2011; 2019; Sato et al., 2015). The frequency of PFDs identified in the stratigraphic profile establishes the period as an interval of intense volcanic activity (Figure 7C) in the extrabacinal magmatic belts (e.g. Orton, 1996; Rossignol et al. 2019). The prevailing conditions in the Paraná Basin such as low energy underwater environment and

restricted income of terrigenous sediments of the Assistência Member were fundamental for the preservation of the PFDs throughout the section. Without these specific conditions, PFDs would have been remobilized and their contents dispersed in the siliciclastic sedimentary package (e.g., Zuffa, 1980), which was possibly what took place during the sedimentation period of the Taquaral Member (e.g., Canile et al., 2016).

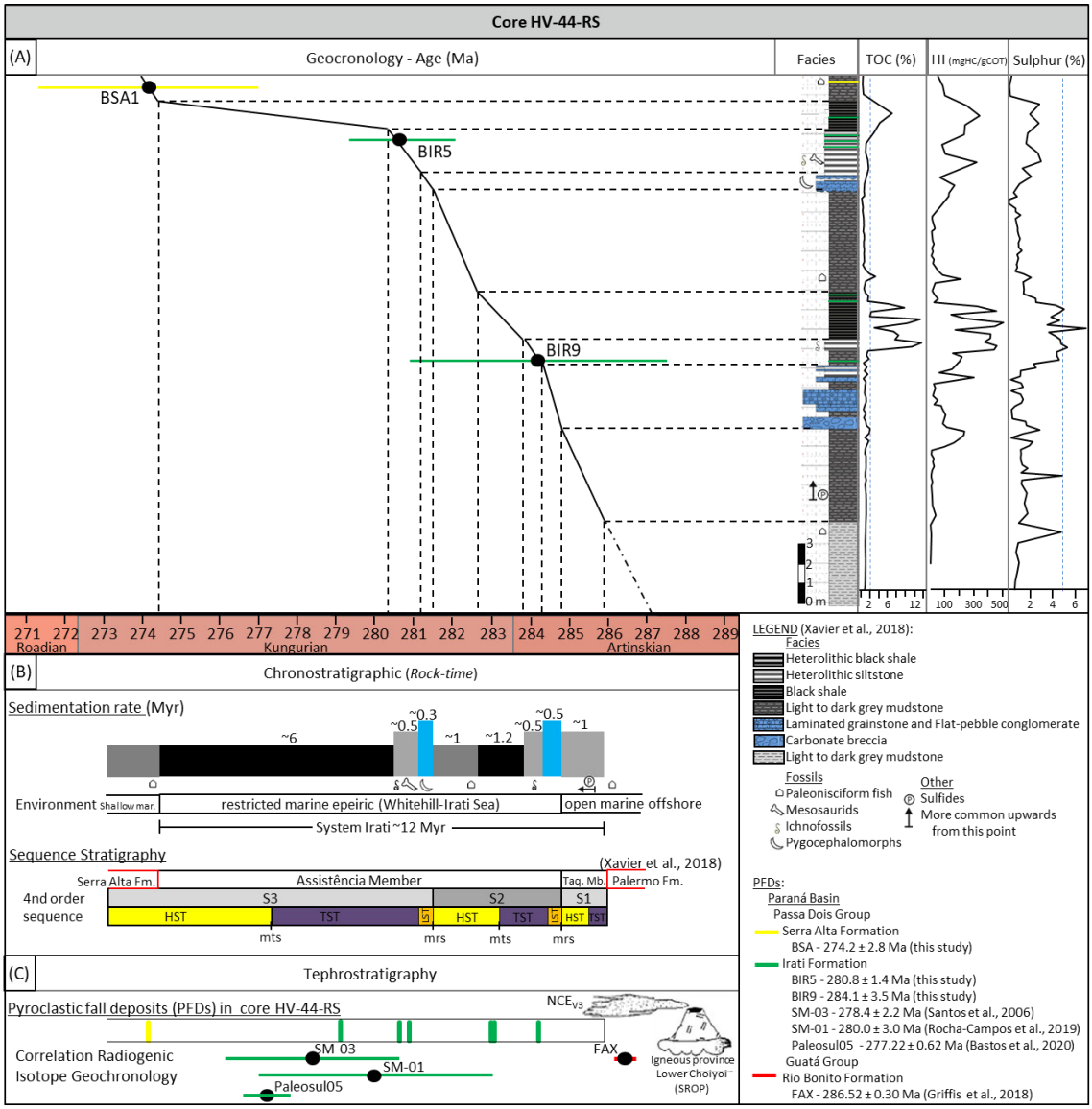

Figure 7 - Graph of the HV-44-RS core deposition rate based on the three levels of PFDs and chronostratigraphic correlations. (A) The inclination of the correlation curve is based on numerical ages placed in the geochronological column and on the changes on the system tract interpreted by Araújo (2001) and Xavier et al. (2018). The profile and biostratigraphy of HV-44-RS core were obtained from Xavier et al. (2018). Chemostratigraphic data for total organic carbon (TOC), hydrogen index (HI) and Sulfur (S) were obtained from Araújo (2001). (B) Distribution of sedimentary packages on the HV-44-RS core in terms of chronostratigraphic time, sedimentation rate of the sedimentary packages and distribution of sequence stratigraphy in Chronostratigraphy. (C) Chronostratigraphic distribution of the PFDs identified in the HV-44-RS core and tephrochronological correlation with the PFDs: SM-03 Santos et al. (2006); SM-01 by Rocha-Campos et al. (2019); and FAX by Griffis et al. (2018). Illustrated representation of the PFDs provenance, being of the NCE_{cV3} type in the classification of Zuffa (1980) and inherited from the Lower Choiyoi.

The numerical ages of PFDs BIR5 and BIR9 obtained in this work allowed tephrochronological correlations with PFDs SM-03 (278.4 ± 2.2 Ma, Santos et al., 2006) and SM-01 (280, 0 ± 3.0 Ma, Rocha-Campos et al., 2019) described in the Assistência Member of PetroSix Mine , 757 km from the HV-44-RS survey site (Figure 1; Figure 7C). Therefore, this result highlights the wide lateral extension of the Irati Formation and places it as a reference unit throughout the Paraná Basin. Recently, Bastos et al. (2021) obtained new ages by CA-TIMS of the PFD Paleosul05 core from Petrosix (277.22 ± 0.57 Ma). However, brief characterization of this PFD was presented (e.g. Boehnke and Harrison, 2014), making its interpretation challenging. Not all zircons analyzed were euhedral, and several geochronological results presented a numerical age based on only one grain (n = 1), thus obtaining MSWD close to 0 (MSWD = 0.057). Its representativity should be reassessed since the interpretation is inconsistent with geochronometric techniques recommended for numerical age determination (NACSN, 2005; Reiners et al., 2018). Due to the method used (Hanchar and Hoskin, 2003; Mattinson, 2005), two genetic conditions are possible (Belousova et al., 2002; Corfu et al., 2003): I) most zircons have inherited cores, similar to the zircons of PFDs BIR9 and BSA1, or II) occurrence stratigraphic level must correspond to a detrital deposit, with zircons from Cambrian terrains (Bastos et al., 2021) and coexisting epiclastic volcanic ashes (e.g. Zuffa, 1980). Regardless the situation, in Figure 7C it is possible to observe that the age of the zircon grain used in CA-TIMS for geochronological analysis is from a sedimentary deposit, and may represent the younger age of deposition of the layer (e.g. Boggs, 2014).

The ages determined also allowed the evaluation of relations in regards to the PFD FAX of the Rio Bonito Formation (286.5 ± 0.3 Ma, Griffis et al., 2018). As for the Rio Bonito Formation PFD dating of by 281.4 ± 3.4 Ma Mori et al. (2012), there is no conflict with this work because the age was determined based on the $^{206}Pb/^{204}Pb$ ratios, differently from what is recommended for Phanerozoic materials dating, which are based on in the $^{206}Pb/^{238}U$ ratio (Jaffey et al., 1971; Mattinson, 2000; Boggs, 2014; Reiners et al., 2018). It should be noted that this same PFD was later dated by Griffis et al. (2018), using the U-Pb methodology by CA-TIMS (Mattinson, 2005; Schaltegger et al., 2015), of an age of 297.77 ± 0.35 Ma (HNC01), which is compatible with the expected age for the Rio Bonito Formation.

6. CONCLUSIONS

The study of the Irati Formation in the southern portion of the Paraná Basin along with the new ages obtained on zircons from PFDs levels, limits the Irati System's duration in southern Brazil between 286 Ma to 274.5 Ma, hence being placed chronostratigraphically in the Cisuralian Epoch. The results are important for improving paleogeographic knowledge and global chronostratigraphy (e.g. Qie et al., 2019). The study established the following conclusions:

1. The verification of three PFDs in the Irati formation in drill core HV-44-RS, the southern domain of the Passa Dois Group in the Paraná Basin, was based on: I) faciology, constituting a homogeneous layer of claystone, abrupt contact and grey, green, brown and/or yellow emplacement; II) mineralogy, dominant composed of dioctahedral montmorillonite and the presence of magmatic minerals; III) U/Pb concordant ages by LA-ICPMS in volcanogenic zircons, numerical ages of MSWD≈1; and IV) tefrochronological and geochronological-stratigraphic correlations (decrease in age according to deposition).
2. The PFDs presented three new geochronological ages: BIR9 (284,1 ± 3,5 Ma; 2σ ; MSWD = 1,14, n = 4), BIR5 (280,8 ± 1,4 Ma; 2σ; MSWD = 0,85, n = 13) and BSA1 (274,2 ± 2,8 Ma; 2σ; MSWD = 0,87, n = 4).
3. The levels of PFDs in HV-44-RS core were stratigraphically placed, therefore enabling the integration of the geochronological results of this work with lithostratigraphy, biostratigraphy, sequence stratigraphy, chemostratigraphy and regional tephrochronological correlations. The analysis enable the establishment of new contributions to the global chronostratigraphy of the Cisuralian (early Permian), such as the deposition rate of the sedimentary packages of the Irati Formation recorded in drill core HV-44-RS. The results establish lasting of the Irati System for approximately 12 Myr (between 286 to 274 Ma) with two periods of anoxia with very different duration intervals of 1.2 Myr and 6 Myr respectively. It was also possible to estimate the relative numerical age of 284.5 Ma and 281.2 Ma to establish LST in the Paraná Basin, and of approximately 280.6 Ma for the vertebrate mortality event.
4. The tephrochronological correlation with PFDs studied in the northern sector of the basin (PetroSix Mine), 757 km distant, highlights that the Irati Formation is a broad stratigraphic marker with wide coverage throughout the Paraná Basin.
5. The ages determined contribute to the chronostratigraphic adjustment of the Supersequence Gondwana I and to the understanding of events observed throughout the studied stratigraphic section. The new isotopic geochronological dating (Figures 5 and 7A) allowed proposing updated models of regional depositional and reconstruction of the Paraná Basin. Together with interpretations of the stratigraphy of the HV-44-RS core (Figure 7B) and the regional geochronological correlation (Figure 7C), it was possible to extend the interpretations of the factors that led to the creation of the Irati-Whitehill Sea System in the Cisuralian Epoch.

6. The studies of these PFDs reinforce the hypothesis of provenance linked to the Choiyoi Magmatic Province, since the volcanic ashes of the PFDs represented compositional variations in magma from acidic and intermediate character.

ACKNOWLEDGMENTS

The authors thank the Conselho Nacional de Desenvolvimento Científico e Tecnológico (CNPq) for financial support (process 140596/2016-0), and the Geological Survey of Brazil (CPRM), for the allowing access to the drill core HV-44-RS as well as retrieving samples for the study. We also thank the technicians from UFRGS laboratories.

REFERENCES

Aborrage, A.M. and Lopes, R.C., 1986. Projeto A Borda Leste da Bacia do Paraná: Integração Geológica e Avaliação Econômica. CPRM/DNPM, São Paulo, Porto Alegre. 374p.

Alan, P.D., 2018. Radiogenic Isotope Geology, 3 ed. United Kingdom: Cambridge University Press, p.99-133. DOI: 10.1017/9781316163009

Araújo, L.M., 2001. Análise da expressão estratigráfica dos parâmetros de geoquímica orgânica e inorgânica nas sequências deposicionais Irati. PhD Thesis, Instituto de Geociências, Universidade Federal do Rio Grande do Sul, 2 v., 307 pp.

Araújo, L.M., Rodrigues, R., Scherer, C.M.S., 2004. Interrelação entre a fábrica sedimentar, o conteúdo orgânico e o potencial redox do ambiente deposicional, deduzida das litofácies de rampa distal das sequências deposicionais da Formação Irati, Permiano da Bacia do Paraná. B. Geoci. Petrobras, Rio de Janeiro, 12(2), p.429-434.

Bastías-Mercado, F., González, J., Oliveros, V., 2020. Volumetric and compositional estimation of the Choiyoi Magmatic Province and its comparison with other Silicic Large Igneous Provinces. Journal of South American Earth Sciences, 103, 102749. doi:10.1016/j.jsames.2020.102749

Bastos, L.P.H., Rodrigues, R., Pereira, E., Bergamaschi, S., Alferes, C.L.F., Augland, L.E., Domeier, M., Planke, S., Svensen, H.H., 2021. The birth and demise of the vast epicontinental Permian Irati-Whitehill sea: Evidence from organic geochemistry, geochronology, and paleogeography. Palaeogeography, Palaeoclimatology, Palaeoecology 562, p.13, 110103. https://doi.org/10.1016/j.palaeo.2020.110103.

Belousova, E.A., Griffin, W.L., O'reilly, S.Y., Fisher, N.I., 2002. Igneous zircon: trace element composition as an indicator of source rock type. Contributions to Mineralogy and Petrology. 143, p.602–622.

Boggs, S.Jr., 2014. Principles of Sedimentology and Stratigraphy. British Library Cataloguing-in-Publication Data. 5th Ed.,p. 434-474.

Bohor, B,F. and Triplehorn, D.M., 1993. Tonsteins: altered volcanic-ash layers in coal-bearing sequences. Geological Society of America Special Paper. v. 285, p. 1-44.

Cagliari, J., Philipp, R.P., Buso, V.V., Netto, R.G., Hillebrand, P.K., da Cunha Lopes, R., Basei, M.A.S., Faccini, U.F., 2016. Age constraints of the glaciation in the Paraná Basin: Evidence from new U-Pb dates. Journal of the Geological Society, 173(6), 871–875.

Canile, M.C., Babinski, M., Rocha-Campos A.C., 2016. Evolution of the Carboniferous-Early Cretaceous units of Paraná Basin from provenance studies based on U-Pb, Hf and O isotopes from detrital zircons. Gondwana Research, 40, p.142–169. http://dx.doi.org/10.1016/j.gr.2016.08.008

Césari, S.N., Limarino, C.O., Gulbransen, E.L., 2011. An Upper Paleozoic biochronostratigraphic scheme for the western margin of Gondwana. Earth-Science Reviews, 106, p.149–160.

Cisneros, J.C., Marsicano, C., Angielczyk, K.D., Smith, R.M.H., Richter, M., Fröbisch, J., Kammerer, C.F., Sadleir, R.W., 2015. New Permian fauna from tropical Gondwana. Nature Communications, 6(1), 1-8. Doi: 10.1038/ncomms9676.

Condon, D. J., Schoene, B., McLean, N.M., Bowring, S.A., Parrish, R., 2015. Metrology and traceability of U–Pb isotope dilution geochronology (EARTHTIME Tracer Calibration Part I). Geochimica et Cosmochimica Acta, 164(1), p.464–480.

Corfu, F., Hanchar, J.M., Hoskin, P.W.O., Kinny, P., 2003. Atlas of zircon textures, in: Hanchar, J.M. and Hoskin, P.W.O., (Eds.), Zircon, Reviews in Mineralogy and Geochemistry, 53. Mineralogical Society of America, Washington, DC, USA, p.468– 500.

Costa, L.S., 2016. A proveniência dos sedimentos e cinzas vulcânicas dos sedimentos Permianos da Bacia do Paraná: implicações para a história geológica do sul-sudoeste de Gondwana. Tese (Doutorado). Brasília: Universidade de Brasília – UnB.

Critelli, S. and Ingersoll R.V., 1995. Interpretation of neovolcanic versus paleovolcanic sand grains: an example from Miocene deep-marine sandstone of the Topanga Group (Southern California), Sedimentology, 42, p.783-804.

Ddani, M., Meunier, A., Zahraoui, M., Beaufort, D., EL Wartiti, M., Fontaine, C., Boukili, B., EL Mahi, B., 2005. Clay mineralogy and chemical composition of bentonites from the Gourougou volcanic massif (northeast Morocco). clays and clay minerals, v. 53, p. 250-267.

De Rosa, R., Zuffa, G.G., Taira, A., Leggett, J.K., 1986. Petrography of trench sands from the Nankai Trough, southwest Japan: implications for long distance transportation. Geological Magazine, v. 123, p. 477-486.

Einsele, G. and Seilacher, A. (Ed.), 1982. Cyclic and Event Stratification. Springer-Verlag, Berlin, 536 pp.

Einsele, G., Chough, S.K., Shiki, T., 1996. Depositional events and their records-an introduction. Sedimentary Geology. 104, p.1-9.

Fisher, R.V. and Schmincke, H.U., 1984. Pyroclastic Rocks. Springer–Verlag, Berlin. 472 pp.

Gerdes, A. and Zeh A., 2006. Combined U–Pb and Hf isotope LA-(MC-)ICP-MS analyses of detrital zircons: Comparison with SHRIMP and new constraints for the provenance and age of an Armorican metasediment in Central Germany. Earth and Planetary Science Letters, 249, 47–61. https://doi.org/10.1016/j.epsl.2006.06.039.

Gradstein, F.M., Ogg, J.G., Schmitz, M.D., Ogg, G.M., 2012. The Geologic Time Scale 2012. Amsterdam: Elsevier, 1176 pp.

Griffis, N.P., Montañez, I.P., Mundil, R., Richey, J., Isbell, J., Fedorchuk, N., Linol, B., Iannuzzi, R., Vesely, F., Mottin, T., da Rosa, E., Keller, B., Yin, Q.Z., 2019. Coupled stratigraphic and U-Pb zircon age constraints on the late Paleozoic icehouse-to-greenhouse turnover in south-central Gondwana. Geology, v. 47(12), p.1146–1150, https://doi.org/10.1130/G46740.1.

Griffis, N.P., Mundil, R., Montañez, I.P., Isbell, J., Fedorchuk, N., Vesely, F.F., Iannuzzi, R., Yin, Q.Z., 2018. A new stratigraphic framework built on U-Pb single-zircon TIMS ages and implications for the timing of the penultimate icehouse (Paraná Basin, Brazil). Geological Society of America Bulletin 130, p.848–858.

Hanchar, J.M. and Hoskin, W.O., 2003. Zircon. Mineralogical Society of America Reviews in Mineralogy and Geochemistry 53, p.500.

Hiess, J., Condon D J., McLean, N., Noble S.R., 2012. 238U/235U systematics in terrestrial U-bearing minerals. Science 335(6076), p.1610–1614.

Holz, M., França, A.B., Souza, P.A., Iannuzzi, R., Rohn, R., 2010. A stratigraphic chart of the Late Carboníferous/Permian succession of the eastern border of the Paraná Basin, Brazil, South America. J. South Am. Earth Sci. 29, 381–399. https://doi.org/10.

Hoskin, P.W.O. and Schaltegger, U., 2003. The composition of zircon and igneous and metamorphic petrogenesis. In: Hanchar, J.M., Hoskin, P.W.O. (Eds.), Zircon. Mineralogical Society of America. Reviews in Mineralogy and Geochemistry, 53, p.27-62.

Huff, W.D., 2016. K-bentonites: A review. American Mineralogist, 101, 43–70.

Iannuzzi, R., 2013. The Carboniferous-Permian floral transition in the Paraná Basin. Lucas, S.G., et al. (Eds.), The Carboniferous-Permian Transition. New Mexico Museum of Natural History and Science, Bulletin 60.

Iannuzzi, R., Souza, P.A., Holz, M., 2010, Stratigraphic and paleofloristic record of the Lower Permian postglacial succession in the southern Brazilian Paraná Basin. In: López-Gamundí, O.R., and Buatois, L.A. (Eds.), Late Paleozoic Glacial Events and Postglacial Transgressions in Gondwana: Geological Society of America Special Paper 468, p. 113–132, doi: 10.1130/2010.2468(05).

Jackson, S.E., Pearson, N.J., Griffin, W.L., Belousova, E.A., 2004. The application of laser ablation-inductively coupled plasma-mass spectrometry to in situ U/Pb zircon geochronology. Chemical Geology. 211, 47-69. https://doi.org/10.1016/j.chemgeo.2004.06.017.

Jaffey, A.H., Flynn, K.F., Glendenin, L.E., Bentley, W.C., Essling, A.M., 1971. Precision Measurement of Half-Lives and Specific Activities of 235U and 238U. Phys Rev. C.,4, 1889-1906. https://doi.org/10.1103/PhysRevC.4.1889.

Jerram, D. and Petford, N., 2014. Descrição de rochas ígneas: Guia geológico de campo. 2. ed. Trad.: Ana Maria Pimentel Mizusaki and Rualdo Menegat. Porto Alegre: Bookman, 280 p.

Keller, C.B., Schoene, B., Samperton, K.M., 2018. A stochastic sampling approach to zircon eruption age. Interpretation. Geochemical Perspectives Letters, 8, p.31-35. doi:10.7185/geochemlet.1826

Lajoie, J. and Stix, J., 1992. Volcaniclastic Rocks. In: Facies Models: Response to Sea-level Change (Ed. by Walker R.G. and James N.P.), Geological Association of Canada., Waterloo, Ontario. pp. 101-118.

Lana, C., Farina, F., Gerdes, A., Alkmim, A., Gonçalves, G., Jardim, A. C., 2017. Characterization of zircon reference materials via high precision U–Pb LA-MC-ICP-MS. Journal of Analytical Atomic Spectrometry, 32(10), p.2011–2023. doi:10.1039/c7ja00167c.

Lavina, E., 1991. Geologia sedimentar e paleogeografia do Neopermiano e Eotriássico (intervalo Kazaniano-Scythiano) da Bacia do Paraná. Doctorate Thesis. Universidade Federal do Rio Grande do Sul (UFRGS), Porto Alegre 457p.

Limarino, C.O., Césari, S.N., Spalletti, L.A., Taboada, A.C., Isbell, J.L., Geuna, S., Gulbranson, E.L., 2013. A paleoclimatic review of southern South America during the late Paleozoic: a record from icehouse to extreme greenhouse conditions. Gondwana Research, 25 (4), p.1396–1421.

Llambías, E.J., Kleiman, L.E., Salvarredy, J., 1993. El magmatismo Gondwanico. In: Ramos, V.A. (Ed.), Geología y Recursos Naturales de Mendoza, Relatorio 12 Congreso Geológico Argentino y 2 Congreso de Exploración de Hidrocarburos, Mendoza, p.53-64.

López-Gamundi, O.R., 2006. Permian plate margin volcanism and tuffs in adjacent basins of west Gondwana: age constrains and common characteristics. Journal of South American Earth Sciences 22, p.227–238.

Ludwig, K.R., 2012. User's manual for Isoplot 3.75. A geochronological toolkit for Microsoft excel. Berkeley Geochronological Center, Special Publication, 5, p.75.

Lyons, P.C., Spears, D.A., Outerbridge, W.F., Congdon, R.D., Evans, H.T., 1994. Euramerican tonsteins: overview, magmatic origin, and depositional-tectonic implications. Palaeogeography, Palaeoclimatology, Palaeoecology, 106(1-4), p.113–134. doi:10.1016/0031-0182(94)90006-x

Matos, S.A., Warren, L.V., Varejao, F.G., Assine, M.L., Simões, M.G., 2017. Permian endemic bivalves of the ‘‘Irati anoxic event”, Paraná Basin, Brazil: Taphonomical, paleogeographical and evolutionary implications. Palaeogeography, Palaeoclimatology, Palaeoecology 469, p.18–33.

Mattinson, J.M., 2000. Analysis of the relative decay constants of 235U and 238U by multi-step CA-TIMS measurements of closed-system natural zircon samples. Chemical Geology, 275 (3–4), p.186-198.

Mattinson, J.M., 2005. Zircon U-Pb chemical abrasion (“CA-TIMS”) method: Combined annealing and multistep partial dissolution analysis for improved precision and accuracy of zircon ages: Chemical Geology, 220, p.47–66. doi:10.1016/j.chemgeo.2005.03.011.

Maynard, J.B., Chocyk-Jaminski, M., Gaines, R.R., Huff, W.D., Krekeler, M.P., Prokopenko, M., Summers, A.M., 1996. Bentonites in the Late Permian (Tatarian) Irati Formation of Brazil; geochemistry and potential for stratigraphic correlation. Abstr. Programs - Geol. Soc. Am. 28, 280.

McKinley, J.M., Worden, R.H., Ruffell, A.H., 2003. Smectite in sandstones: a review of the controls on occurrence and behaviour during diagenesis. In: Worden, R.H. and Morad S. (Eds.), Clay Mineral Cements in Sandstones, International Association of Sedimentologists Special Publication 34, Blackwell Publishing, Oxford, p.109–128.

McLean, N.M., Condon, D.J., Schoene, B., Bowring, S.A. 2015. Evaluating uncertainties in the calibration of isotopic reference materials and multi-element isotopic tracers (EARTHTIME Tracer Calibration Part II). Geochimica et Cosmochimica Acta, 164, p.481–501.

Meunier, A., 2005. Clays. Berlin: Springer-verlag, 472p.

Miall, A.D., 2016. Stratigraphy: A Modern Synthesis. University of Toronto, Springer. P.311-370. Doi:10.1007/978-3-319-24304-7.

Milani, E.J., França, A.B., Schneider, R.L., 1994. Bacia do Paraná. Boletim Geociências da Petrobrás 8 (2), 69–82.

Milani, E.J., 1997. Evolução tectono-estratigráfica da Bacia do Paraná e seu relacionamento com a geodinâmica fanerozóica do Gondwana sul-ocidental. Tese de doutorado, 2v. Universidade Federal do Rio Grande do Sul (UFRGS), Porto Alegre. 255p.

Milani, E.J. and Ramos, V.A., 1998. Orogenias paleozóicas no domínio sul-ocidental do Gondwana e os ciclos de subsidência da Bacia do Paraná. Rev. Bras. Geocências 28, 473–484. https://doi.org/10.5327/rbg.v28i4.651.

Milani, E.J. and Zalán, P.V., 1999. An outline of the geology and petroleum systems of the Paleozoic interior basins of South America: Episodes, 22, 199-205.

Milani, E.J., Melo, J.H.G., Souza, P.A., Fernandes, L.A., França, A.B., 2007. Bacia do Paraná. Boletim de Geociências Petrobras 15, 265–287.

Milani, E.J. and De Wit, M.J., 2008. Correlations between the classic Paraná and Cape-Karoo sequences of South America and southern Africa and their basin infills flanking the Gondwanides: du Toit revisited. Geological Society, London, Special Publications, 294, 319-342. doi:10.1144/SP294.17.

Miller, J., Matzel, J., Miller, C., Burgess, S., Miller, R., 2007. Zircon growth and recycling during the assembly of large, composite arc plutons. Journal of Volcanology and Geothermal Research. 167, p.282–299.

Mori, A.L.O., Souza, P.A., Marques, J.C., Lopes, R.C., 2012. A new U-Pb zircon age dating and palynological data from a Lower Permian section of the southernmost Parana Basin, Brazil: Biochronostratigraphical and geochronological implications for Gondwanan correlations. Gondwana Research, 21(2-3), p.654–669. https://doi.org/10.1016/j.gr.2011.05.019.

NACSN (North American Stratigraphic Code), 2005. North American stratigraphic code. American Association of Petroleum Geologists Bulletin, 89, p.1547-1591.

Nelson, D.A. and Cottle, J.M., 2019. Tracking voluminous Permian volcanism of the Choiyoi Province into central Antarctica. The Geological Society of America, 11(3), p.386–398. doi:10.1130/l1015.1.

Ogg, J.G., Ogg, G., Gradstein, F.M., 2016. A Concise Geologic Time Scale: 2016. Elsevier, Amsterdam 240 pp.

Orton, G.J., 1996. Volcanic environments. In: Reading H.G. (Ed.), Sedimentary Environments: Processes, Facies and Stratigraphy, 3rd ed, Blackwell Publishing, p.485-567 pp.688.

Potter, P.E., Maynard, J.B., Depetris, P.J., 2005. Mud and Mudstone: Introduction and Overview. Berlin: Springer

Pupin, J.P., 1980. Zircon and granite petrology. Contributions to Mineralogy and Petrology, 73, p.207-220.

Qie, W., Algeo, T.J., Luo, G., Herrmann, A., 2019. Global events of the Late Paleozoic (Early Devonian to Middle Permian): A review. Palaeogeography, Palaeoclimatology, Palaeoecology, 531. https://doi.org/10.1016/j.palaeo.2019.109259

Reading, H.G., 1996. Sedimentary Environments: Processes, Facies and Stratigraphy. 3rd Edition, Blackwell, Oxford, p.689.

Reiners, P.W., Carlson, R.W., Renne, P.R., Cooper, K.M., Granger, D.E., McLean, N.M., Schoene, B., 2018. Geochronology and Thermochronology. John Wiley & Sons. p.39-82. ISBN: 978-1-118-45578-4.

Rocha, H.V., Mendes, M., Pereira, Z., Rodrigues, C., Fernandes, P., Lopes, G., Sant'Anna, L.G., Tassinari, C.C.G., Lemos de Sousa, M.J., 2020. New palynostratigraphic data of the Irati (Assistência Member) and the Corumbataí formations, Paraná Basin, Brazil, and correlation with other south American basins. Journal of South American Earth Sciences 102. https://doi.org/10.1016/j.jsames.2020.102631

Rocha-Campos, A.C., Basei, M.A., Nutman, A.P., Kleiman, L.E., Varela, R., Llambias, E., Canile, F.M., da Rosa, O., de, C.R., 2011. 30 million years of Permian volcanism recorded in the Choiyoi igneous province (W Argentina) and their source for younger ash fall deposits in the Paraná Basin: SHRIMP U-Pb zircon geochronology evidence. Gondwana Research. 19, p.509–523.

Rocha-Campos, A.C., Basei, M.A.S., Nutman, A.P., Santos, P.R., Passarelli, C.R., Canile, F.M., Rosa, O.C.R., Fernandes, M.T., Santa Ana, H., Veroslavsky, G., 2019. U-Pb Zircon Dating of Ash Fall Deposits from the Paleozoic Paraná Basin of Brazil and Uruguay: A Reevaluation of the Stratigraphic Correlations. The Journal of Geology, The University of Chicago. 127, p.167–182.

Rossignol, C., Hallot, E., Bourquin, S., Poujol, M., Jolivet, M., Pellenard, P., Dabard, M.P., 2019. Using volcaniclastic rocks to constrain sedimentation ages: To what extent are volcanism and sedimentation synchronous? Sedimentary Geology, 381, p.46–64. doi:10.1016/j.sedgeo.2018.12.010

Santos, R.V., Souza, P.A., de Alvarenga, C.J.S., Dantas, E.L., Pimentel, M.M., de Oliveira, C.G., de Araújo, L.M., 2006. Shrimp U–Pb zircon dating and palynology of bentonitic layers from the Permian Irati Formation, Paraná Basin, Brazil. Gondwana Research 9(4), p.456-463.

Sato, A.M., Llambías, E.J. Basei, M.A.S., Castro, C.E., 2015. Three stages in the Late Paleozoic to Triassic magmatism of southwestern Gondwana, and the relationships with the volcanogenic events in coeval basins. Journal of South American Earth Sciences 63, p.48-69. http://dx.doi.org/10.1016/j.jsames.2015.07.005

Schaltegger, U., Schmitt, A., and Horstwood, M., 2015, U-Th-Pb zircon geochronology by ID-TIMS, SIMS, and laser ablation ICP-MS: Recipes, interpretations, and opportunities: Chemical Geology, 402, p.89–110. https://doi.org/10.1016/j.chemgeo.2015.02.028.

Schmitz, M.D. and Bowring S.A., 2001. U–Pb zircon and titanite systematics of the Fish Canyon Tuff: an assessment of high precision U–Pb geochronology and its application to young volcanic rocks. Geochimica et Cosmochimica Acta, 65, p.2571–2587.

Schneider, R.L., Mühlmann, H., Tommasi, E., Medeiros, R.A., Daemon, R.F., Nogueira, A.A., 1974. Revisão estratigráfica da Bacia do Paraná. In: Anais do XXVIII Congresso Brasileiro de Geologia, Porto Alegre-RS, v1. Sociedade Brasileira de Geologia, Rio de Janeiro, p. 41–65.

Silva, A. F., Dani, N., Remus, M.V.D., Guerra-Sommer, M., Horn, B.L.D., 2017. Bentonitas da Formação Irati no setor sul da Bacia do Paraná. Geologia USP, Série Científica, v. 17(1), p.75-88.

Spears, D.A., 2012. The origin of tonsteins, an overview, and links with seatearths, fireclays and fragmental clay rocks. International Journal of Coal Geology, 94, p.22–31.

Steiger, R.H. and Jager, E., 1977. Subcommission on Geochronology: Convention on the use of decay constants in geochronology and cosmochronology. Earth and Planetary Science Letters. 36, 359–62.

Stephenson, M.H., 2016. Permian palynostratigraphy: a global overview, in The Permian Timescale, Lucas, S.G., and Shen, S.Z. (eds). The Permian Timescale. Geological Society, London, Special Publications, vol. 450. https://doi.org/10.1144/SP450.2.

Van Achterbergh, E., Ryan, C.G., Jackson, S.E., Griffin, W.L., 2001. Data reduction software for LA-ICP-MS: appendix. In: Sylvester P.J. (Ed.), Laser Ablation-ICPMass Spectrometry in the Earth Sciences: Principles and Applications (vol. 29, 239-243). Ottawa: Mineralog. Assoc. Canada (MAC) Short Course Series.

Vavra, G., 1990. On the kinematics of zircon growth and its petrogenetic significance: a cathodoluminescence study. Contributions to Mineralogy and Petrology, 106, 90-99.

Vavra, G., 1993. A guide to quantitative morphology of accessory zircon. Chemical Geology, 110, 15-28.

Vázquez, M.S. and Césari, S.N., 2017. The Permian palynological Lueckisporites-Weylandites Biozone in the San Rafael Block and its correlation in Western Gondwana. Journal of South American Earth Sciences, 76, p.165-181. http://dx.doi.org/10.1016/j.jsames.2017.02.009.

Velde, B., 1992. Introduction to Clay Minerals: Chemistry, origins, uses and environmental significance. Chapman & Hall, Hong Kong, 198 pp, DOI 10.1007/978-94-011-2368-.

Walker, J.D., Geissman, J.W., Bowring, S.A., Babcock, L.E., 2018. Geologic Time Scale v. 5.0: Geological Society of America, https://doi.org/10.1130/2018.CTS005R3C.

Walker, R.G. and James, N.P., 1992. Facies models: response to sea level change. Geological Association of Canada. Canada. p.101–118.

White, I.C., 1908. Relatório sobre as coal measures e rochas associadas ao sul do Brasil. Rio de Janeiro: Comissão das Minas de Carvão de Pedra do Brasil, 300 p.

Worden, R.H. and Burley, S.D., 2003. Sandstone diagenesis: the evolution of sand to stone. In: Burley, S.D., Worden, R.H. (Eds.), Clastic Diagenesis: Recent and Ancient. International Association of Sedimentologists, vol. 4. Blackwells, Oxford, pp.3–44.

Xavier, P.L.A., Silva, A.F., Soares, M.B., Horn, B.L.D., Schultz, C.L., 2018. Sequence stratigraphy control on fossil occurrence and concentration in the epeiric mixed carbonate-siliciclastic ramp of the Early Permian Irati

Formation of southern Brazil. Journal of South American Earth Sciences, 88,157–178. https://doi.org/10.1016/j.jsames.2018.08.014.

Zalán, P.V., Wolff, S., 1990. The Paraná Basin, Brazil. In: Leighton, M. W., Kolata, D. R., Oltz, D. F., Eidel, J. J. Interior cratonic basins. American Association of Petroleum Geologists, Memoirs, 51, p.681–708.

Zuffa, G.G., 1980. Hybrid arenites: their composition and classification. J. Sediment. Petrol. 50, 21–29. https://doi.org/10.1306/212F7950-2B24-11D7-8648000102C1865D.

Zuffa, G.G., 1985. Optical analyses of arenites: influence of methodology on compositional results. In: Provenance of Arenites. Springer, Dordrecht, p. 165-189.

Zuffa, G.G., 1987. Unravelling Hinterland and Offshore Palaeogeography from Deep-water Arenites. In: Leggett, J. K.; Zuffa, G. G. Marine Clastic Sedimentology: Concepts and Case Studies. Dordrecht: Springer, p. 39-61.

Artigo 2 - Evolution and transformations of Pyroclastic fall deposits (PFDs) of Permian Paraná Basin (Bentonite and tonstein) and tephras from Salta. Contributions to provenance in sedimentary sequences

Acknowledgement of receipt of your submitted article

Sedimentary Geology <em@editorialmanager.com>
Ter, 27/04/2021 17:16

Dear Mr. Silva,

Your submission entitled "Evolution and transformations of Pyroclastic fall deposits (PFDs) of Permian Paraná Basin (Bentonite and tonstein) and tephras from Salta. Contributions to provenance in sedimentary sequences" has been received by Sedimentary Geology.

Your paper will be considered as belonging to the category Research Paper. Please contact us if this is not correct.

Please note that submission of an article is understood to imply that the article is original and is not being considered for publication elsewhere. Submission also implies that all authors have approved the paper for release and are in agreement with its content.

You will be able to check on the progress of your paper by logging on to https://www.editorialmanager.com/sedgeo/ as Author.

Your manuscript will be given a reference number in due course.

Thank you for submitting your work to this journal.

Kind regards,

Editorial Manager
Sedimentary Geology

Evolution and transformations of Pyroclastic fall deposits (PFDs) of Permian Paraná Basin (Bentonite and tonstein) and tephras from Salta. Contributions to provenance in sedimentary sequences.

Aurélio Fagundes Silva[1]*, Norberto Dani[1], Carla Cristine Porcher[1], Marcus Vinicius Dorneles Remus[1], Taís Fontes Pinto[1], Ricardo Maahs[1]

[1]Universidade Federal do Rio Grande do Sul – UFRGS. Instituto de Geociências, Pós-graduação em Geociências, Avenida Bento Gonçalves, 9500, CP 15001, CEP 91501-970, Porto Alegre, RS, Brasil

E-mails: aureliofagundes@hotmail.com, norberto.dani@ufrgs.br, carla.Porcher@ufrgs.br, marcus.remus@ufrgs.br, tais.fontes1@gmail.com, maahs.geologia@gmail.com

*Corresponding author.

Abstract: Facies Models; Tephra; Eodiagenesis; Clay Minerals; Exogenous geochemistry, GSSP

ABSTRACT

Pyroclastic fall deposits (PFDs) are formed in volcanic events, are transported long distances by the atmosphere and deposit a thin layer of tephra on the ground. They are important for establishing geochronological numerical ages in stratigraphic analysis. This paper characterized three PFDs in sedimentary packages, one in situ PFD (tephra) and two tuff PFDs in old deposits (bentonite and tonstein), through six different

analytical methods (facies analysis, descriptive petrography, Scanning Electron Microscopy, Diffraction of X-Ray, infrared and X-Ray Fluorescence). We obtained different mineralogical and chemical compositions, through which we define the crystal-chemical structures of the tephra, smectite and kaolinite, which can serve as guides for characterization work. We also describe some of the main magmatic minerals observable in binocular stereomicroscope and petrography. We used the data obtained to interpret the possible kinetic reactions and thermodynamic equilibrium that occurred under each PFD in the deposited environment. At the end of the discussion, we used the characteristics described about each PFD to explain the obvious physiological characteristics in the field.

1. INTRODUCTION

Sedimentary basins are areas below the base level (average sea level) that are filled with stratified sediments. Their sedimentary packages are thus used, among other uses, to interpret the history of the Earth (Reading, 1996; Miall, 2016). Interspersed with sedimentary packages, volcanic deposits, such as lava flow, pyroclastic flow and pyroclastic fall deposits (Figure 1) (Fisher and Schmincke, 1984; Lajoie and Stix, 1992; Mcphie et al. 1993; Orton, 1996), are used to obtain Geochronological numerical ages (NACSN, 2005; Reiners et al., 2018). Among these volcanic deposits, pyroclastic fall deposits (PFDs) are the most widely used in stratigraphic analyzes (Gradstein et al., 2012; Gradstein et al., 2020).

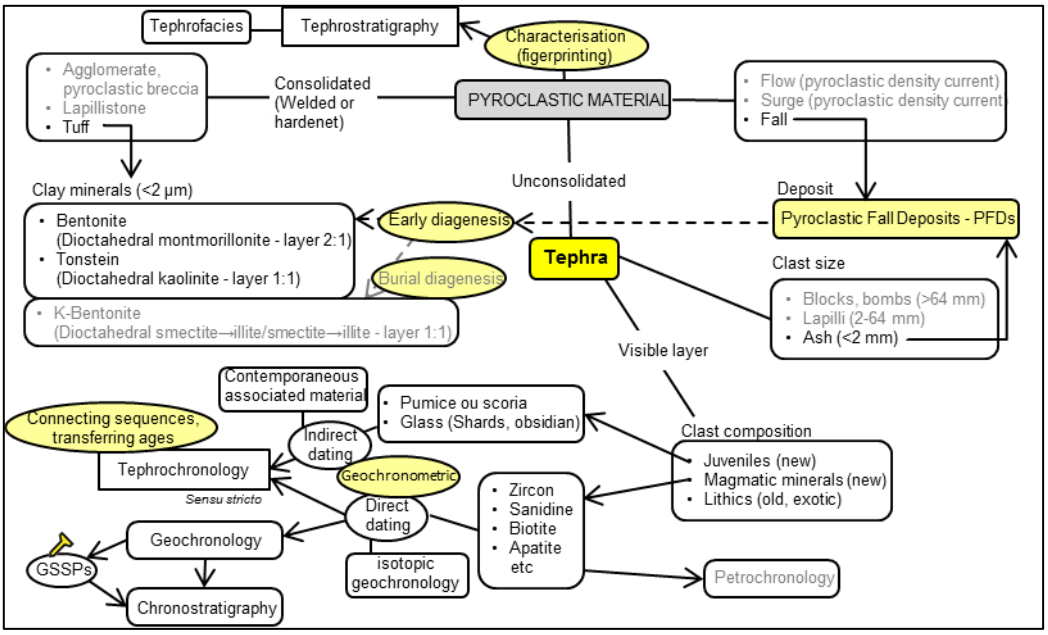

Figure 1 - Nomenclature of tephra and derivative terms and their relationships with one another and with other words, including near-synonym pyroclastic material (Modified from Lowe, 2008). Emphasis was placed on the topics discussed in this article.

PFD formations are related to very energetic eruptions, such as Plinian and Phreatomagmatic eruptions, producing fine juvenile vesiculated pyroclastic fragments (eg shards, pumice, glass) (Figure 1) (e.g. Zuffa, 1980; 1987; Orton, 1996; Hermanns et al. 2000; Hermanns and Schellenberge, 2008). These fine fragments are ejected several

tens of kilometres high and transported by high-speed winds and long distances. The fragments will start to fall when the transport becomes inefficient. The spatial distribution of PFD can cover hundreds to thousands of square kilometres (Zuffa, 1985; 1987), covering areas the size of continents (Suthren, 1985; Lajoie and Stix, 1992; Orton, 1996; Meunier, 2005). If the PFD is preserved, it will form a friable tabular layer of volcanic ash in abrupt contact with the depositional surface (e.g. Fisher and Schmincke, 1984; Lajoie and Stix, 1992; Mcphie et al. 1993; Orton, 1996; Hermanns et al. 2000; Hermanns and Schellenberge, 2008). In this volcanic ash layer, juvenile vesiculated pyroclastic fragments will make up the majority (Figure 1), with a low quantity of lithic fragments of the volcanic cone (e.g. rock fragments) and crystalline magmatic minerals (eg β-quartz, sanidine , biotite, zircon, apatite, olivine, pyroxene) (Fisher and Schmincke, 1984; Bohor and Triplehorn, 1993; Critelli and Ingersoll, 1995; Spears, 2012; Huff, 2016).

The pyroclastic fragments contained in the PFD are metastable and are easily altered by post-depositional processes, changing their textural and mineralogical characteristics. These alterations are conditioned mainly by the type of sedimentary environment and tectonic conditions of the basin, occur with an attempt to achieve geochemical and textural equilibrium with their environment (Curtis, 1977; Chamley, 1989; Velde and Vasseur, 1992; Worden and Morad, 2003; Meunier, 2005), changing mainly to clay minerals or zeolites (eg Fisher and Schmincke, 1984; Lajoie and Stix, 1992; Bohor and Triplehorn, 1993; Mcphie et al. 1993; Critelli and Ingersoll, 1995; Mørk et al., 2001; Zhu et al., 2012; 2016; McKinley et al., 2003; Tucker, 2003; Worden and Morad, 2003; Meunier, 2005; Potter et al., 2005; Spears, 2012; Huff, 2016). Thus, post-depositional alteration, mainly eodiagenesis alteration (or early diagenesis) (Worden and Burley, 2003), and can transform PFD into tuff (Figure 1) (e.g. Ddani et al, 2005; Spears, 2012; Dai et al., 2017; Arzadún et al., 2018; Shen et al., 2021).

If deposited in marine or lake environments, PFDs tend to form tuffs made up of clay minerals of montmorillonite constitution (bentonite) (Figure 1), and if deposited in paludal environments, PFDs tend to form tuffs made up of clay minerals of kaolinite constitution (tonstein) (e.g. Meunier, 2005). When altered to tuff, the constituents of pyroclastic fragments are changed, losing their main distinguishing feature of classification, but their abrupt contact stratification and their magmatic minerals have been preserved (e.g. Bohor and Triplehorn, 1993). Thus, when possible tuffs are

identified in a sedimentary package, x-ray diffractometry (XRD) analysis will identify the types of mineralogical compositions and the types of clay minerals, providing a better characterization of the evidence of PFDs. Similarly, petrographic analysis can be done. Some works that skip the stages of mineralogical characterizations in PFDs, may make mistakes in geochronological characterizations, resulting in dating detrital zircons instead of volcanic zircons.

The occurrence of in situ (tephras) or altered (tuff) PFDs in sedimentary packages is characterized by facies (or tephrofacies - Figure 1). According to James and Dalrymple (2010), a facies is defined by “a body of rock characterized by a particular combination of lithology and physical and biological structures that bestow an aspect ("facies") that is different from the bodies of rock above, below and laterally adjacent. The characteristics used to define facies are generally those that have genetic significance". Thus, in stratigraphic classification the PFDs are considered an informal stratigraphic unit (Murphy and Salvador, 1999; NACSN, 2005), composing a distinct rock body with unique properties and attributes for the systematic organization of stratigraphy (Figure 1). The magmatic minerals of PFDs are widely used in geochronological studies (Alan, 2018; Reiners et al., 2018). Because it represents temporally restricted deposits (deposition in minutes, hours or days) related to episodic events (Einsele and Seilacher 1982, Zuffa, 1987; Einsele et al., 1996; Boggs, 2014), their numerical age establish chronostratigraphic ages for the sedimentary package. PFDs are used mainly in sedimentary units deposited during the Phanerozoic (Jaffey et al., 1971; Mattinson, 2000; NACSN, 2005; Boggs, 2014; Reiners et al., 2018), being the main definition unit of the various Global Boundary Stratotype Sections and Points (GSSPs) (Gradstein et al., 2012; Ogg et al., 2016; Boggs, 2014; Gradstein et al., 2020).

This paper characterizes three PFDs in sedimentary packages, one PFD in situ (tephra) and two PFDs tuffs in old deposits (bentonite and tonstein), through six different analytical methods. In each PFD, we seek to carry out faciological, mineralogical and crystal-chemical studies, describing physical properties evident in facies, petrography and scanning electron microscopy (SEM), and combined these observations with the properties obtained in X-ray diffraction (XRD) analysis.), infrared (IR) and X-ray fluorescence (XRF). We obtained different mineralogical and chemical compositions, through which we define the crystal-chemical structures of tephra, smectite and

kaolinite. We compared the different crystal-chemical structures among them to discuss the possible kinetic reactions that occurred in the environment during the alteration in the open system regime, and their search in finding the thermodynamic equilibrium in the deposited environment. We also describe some of the main magmatic minerals observable in binocular stereomicroscope and petrography. By explaining the how the formation PFDs occurs, this work contributes to guide the faciological identification of both in situ and altered PFDs in the field.

2. MATERIALS AND METHODS

The three samples of PFDs were collected in different stratigraphic sections and geological contexts.

The sample quaternary tephra volcanic ash was collected at a roadcut along Route 68 on Quebrada De Las Conchas (Lat 25°42′S/Long 65°42′W), south of Salta, Argentina. This PFD is related to the Alemanía Ash volcanic event (~ 3.7 ka) that deposited amidst quaternary deposits of the continental domain. It was preserved in sediment interbedded with thaw lake successions formed in an intermontane basin (sample g65 by Hermanns et al., 2000; Hermanns and Schellenberge, 2008).

The sample Permian bentonite tuff was collected from an outcrop in Aceguá (Lat 31°53'602" S/Long 54°00'125" W), Rio Grande do Sul state, Brazil. This PFD represents the Choiyoi volcanic event (275 Ma; Santos et al., 2006). The PFD was preserved in argillaceous sediment interbedded with Permian lacustrine successions of the Irati Formation of the Paraná Basin (Silva et al., 2017).

The sample Permian tonstein tuff was collected at the Faxinal Coalfield, 25 km south of Arroio dos Ratos municipality (Lat 30°15′58.22″S/Long 51°42′13.36"W), Rio Grande do Sul state, Brazil. This PFD represents the Choiyoi volcanic event (286 Ma). The PFD was preserved in argillaceous sediment interbedded with Permian paludal successions of the Rio Bonito Formation of the Paraná Basin (Guerra-Sommer et al., 2008).

The samples were submitted to mineralogical and geochemical analyzes in the laboratories of the Instituto de Geociências of the Universidade Federal do Rio Grande do Sul (UFRGS) - Brazil. The petrographic thin sections, X-ray diffraction (XRD) and X-ray fluorescence (XRF) analyzes were performed in Centro de Estudos em Petrologia e Geoquímica (CPGq). Scanning electron microscopy (SEM) and energy-dispersive X-ray spectroscopy (EDS) analyzes were performed at the Laboratório de Geologia Isotópica (LGI). The separation of resistate minerals was carried out on the Centro de Estudos em Geologia Costeira (CECO). The infrared (IF) analyzes were carried out at the Central Analítica do Instituto de Química (CA-IQ) at UFRGS.

Two petrographic thin sections were made. The tonstein thin section was made using conventional preparation of the petrographic slide. Bentonite consists of expansive clay (smectite) and in contact with water it expands. Thus, the bentonite thin section was made differently, using mineral oil to avoid the use of water . The samples were impregnated with epoxy resin, and all thin sections were ground to a thickness of about 0.03 mm.

To perform SEM analysis the material preparation was to glue small rock fragments into a surface with carbon and SEM-specific double-sided tape . The mounted fragments were then kept on oven at 40º C for 12 h to minimize the amount of water adsorbed. The fragments were carbon- and gold-coated before being analyzed. The SEM used was a JEOL JSM 6060. Coupled to the SEM, we use the X-ray Energy Dispersive Spectrometer (EDS), from Bruker Nano X Flash Detector 5030.

The mineralogical composition determined through XRD (Siemens D 5000 equipment - CuKα, 40 mA and 25 kV) was performed in different techniques to identify two fractions. Whole-rock analysis (WR) were performed using disoriented grains (3 to 28º 2 0.02º/1s) and other tecniques were used to determine minor fractions (3 to 28º 2 0.02º/1s) (e.g. Meunier, 2005). The minor fractions consisted of volcanic ash < 4 μm and bentonite and tonstein < 2 μm. Three analytical techniques were employed to analyze the minor fraction: I) oriented mineralogy after air drying (N); II) saturation with ethylene glycol (EG); and III) calcination at 550º C for 2h (C). Complementary analysis was performed on the bentonite sample, aiming to identify the b-parameter, through XRD in

fraction <2 μm in disoriented mode (61° to 64° 2Θ 0.01°/10s), and to study the interlayer cations in the clay mineral by saturation with interlayer cations.

The cation exchange technique was performed according to Christidis (2007), however with minor changes nos cátions para saturação (Ca2+ and K+). The bentonite sample was ground and dispersed in distilled water using ultrasound, later concentrating the fraction <2 μm by centrifugation. The fraction was saturated by solutions of 1 ml of 1N CaCl2 (2x) and 1 ml of 1N KCl (1x) to sequentially position the Ca2+, K+ and again Ca2+ elements in the interlayer. Each saturation exchange was followed by five washings and centrifugation with deionized water. After the fifth wash, AgNO3 was tested in the wash water to verify the absence of the compound used for saturation. Observing that no white precipitate was formed, the concentrates were analyzed by XRD in N and EG mode (3 to 38° 2 0.02°/1s).

For IR analyses, a tablet was made by mixing 1 mg of sample with 100 mg of KBr, homogenized and pressed. The tablets were heated at 60 °C for 10 hours to minimize the amount of water adsorbed. Data was collected using the IRPrestige-21 spectrometer operating in the mid-infrared region (range 4000 - 400 cm-1 Wavenumbers) in absorbance mode. The results were evaluated in the region of high energy between 4000 to 3000 cm-1, and low energy between 1300 to 400 cm-1 (e.g. Madejová and Kornadel, 2005).

The technique used for whole-rock chemistry in XRF consisted of 10 g of whole-rock grounded in agate grade and sieved through a 200 mesh sieve (smaller than 0.074 mm). Fused samples were prepared to analyze larger-elements (a form of oxides and loss to fire) and pressed for trace element analysis (ABNT, 1985). The determination of chemical concentrations of major and minor elements was made in an XRF Rigaku spectrometer using calibration curves constructed from a set of international rock standards (Govindaraju, 1994).

The separation of resistant minerals followed the methodology of Bohor and Triplehorn (1993) and Reiners et al. (2018), using the wet sieving process (500 Mesh - 0.025 mm) and heavy liquid (bromoform). At the end of the process, heavy and light mineral concentrates were separated for each sample. Each concentrate was analyzed on stereomicroscope to recognizemacroscopic protperties of the minerals (color,

external morphology, degree of transparency, presence of inclusions, fractures and alterations). The aim was to pick magmatic grains on both concentrates, however particular attention was given to the heavy concentrates. The picked grains were taken to SEM for imaging and compositional characterization by EDS (Bruker Nano X Flash Detector 5030).

The calculation of the a structural formula of bentonite satisfied the five prerequisites of Cível and Komadel (1994). Hence, the formula represents probable results of the distribution of central atoms in the structure. The determination of the structural formula was based on chemical analyzes as oxides using XRF, along with the mineralogical data obtained in XRD and IR (e.g. Cível and Komadel, 1994; Madejová and Kornadel, 2005). For the calculation of the molecular mass of the elements, the following atomic mass values were used: Si^{4+} (28.086), Al^{3+} (26.986), Fe^{3+} (55.845), Mg^{2+} (24.305), Ca^{2+} (40.078), K^{+} (39.098), H^{+} (1.0079) and O^{2-} (15.999) (Souza and Railsback, 2012). Formula units $[T_4M_2I_xO_{10}(OH)_2]$ (tetrahedra (T), octahedra (M) and interlayer cations (I)) (e.g. Civil and Komadel, 1994) were used to calculate the structural formula of the of montmorillonite (layer 2:1 di-octahedral), being calculated using the formula $(Si_{4-x}\ Al_x)\ [Al_{2-y}\ (Mg^{2+},\ Fe^{3+})_y]($ Ca^{2+}, Mg^{2+}, $K^{+})O_{10}(OH)_2.H_2O$. Tonstein did not have its structural formula calculated because it showed great heterogeneity in the sample, hence not satisfying one of the assumptions of Cível and Komadel (1994). The tonstein sample showed heterogeneity and not satisfied the five prerequisites of Cível and Komadel (1994). Thus, for study purposes, the chemical formula units [T4M4O10 (OH) 4] of kaolinite (1: 1 di-octahedral layer) was established.

3. RESULTS

The three PFDs studied exhibited similar facies characteristics (Figure 2). All samples showed discrete tabular layered facies, abrupt contact, horizontalized and extended across the entire outcrop section. They were lithologically massive , presented thin thickness (approximately 5 cm). They appeared to be monomineralic appearance,

which was distinguishable from other layers due to their compositional and tonal difference (e.g. Zuffa, 1987; Fisher and Schmincke 1984; Lajoie and Stix, 1992; Orton, 1996; Huff, 2016). Differences between these PFDs were (Figure 2):

- The PFD composed by volcanic ash was solid and friable (not lithified). Its color was white and macroscopically presented monomineralic composition of well-selected fragments of tephras, of silt and clay size (Hermanns et al., 2000; Hermanns and Schellenberge, 2008).
- The bentonite PFD of the Irati Formation was composed by greenish claystone and presented silky texture (Silva et al., 2017).
- The tonstein PFD of the Rio Bonito Formation stands out in the outcrop section in the middle of the coal layer due to its composition of white clay, highlighting a thickness close to 10 cm . The tonstein presents fossils (Simas et al., 2013).

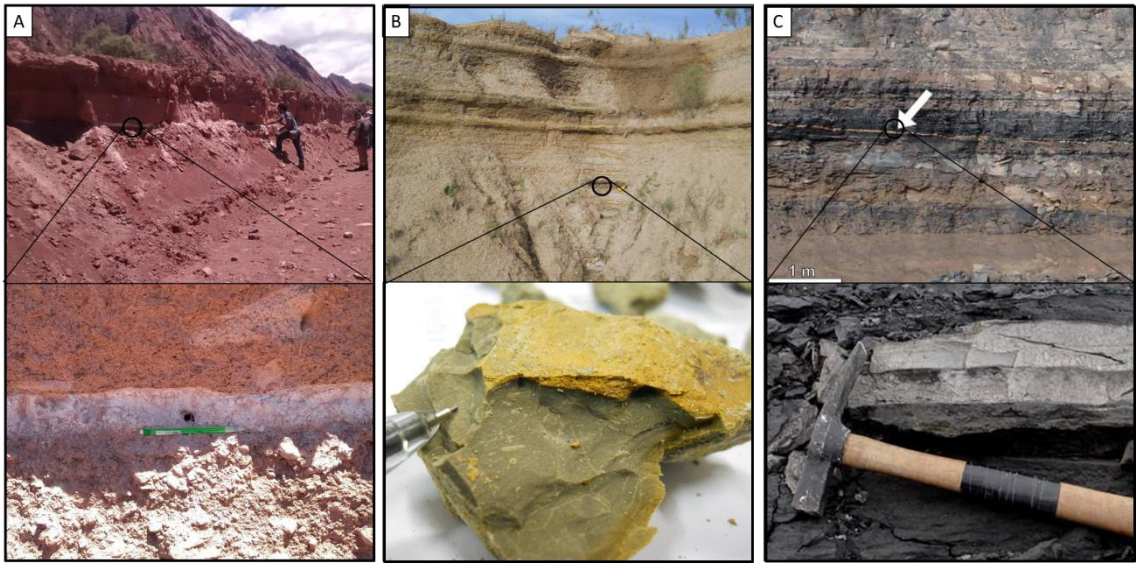

Figure 2 - Outcrops are showing the locations of collected PDF samples used in this work. In (A) presents the stratigraphic profile that the volcanic ash sample was collected. In (B) shows the stratigraphic profile that the bentonite sample was collected (modified from Silva et al., 2017). In (C) presents the stratigraphic profile that the tonstein sample was collected. In face A and C, the PFD layer's continuity can be observed (modified from Simas et al., 2013).

This apparent physiological correspondence encouraged the search to analyze them in other methods and techniques for the purpose of comparison.

In a binocular stereomicroscope, it is observed that the tephras are in the ash fraction (<2mm) (Figure 3), showing fractions of coarse ash (range from 2 mm to 0.062

mm) and fine ash (0.062 mm to aerosols) (e.g. Figure 1) (Fisher, 1961). Its clasts have three main habits (e.g. Jerram and Petford, 2014).

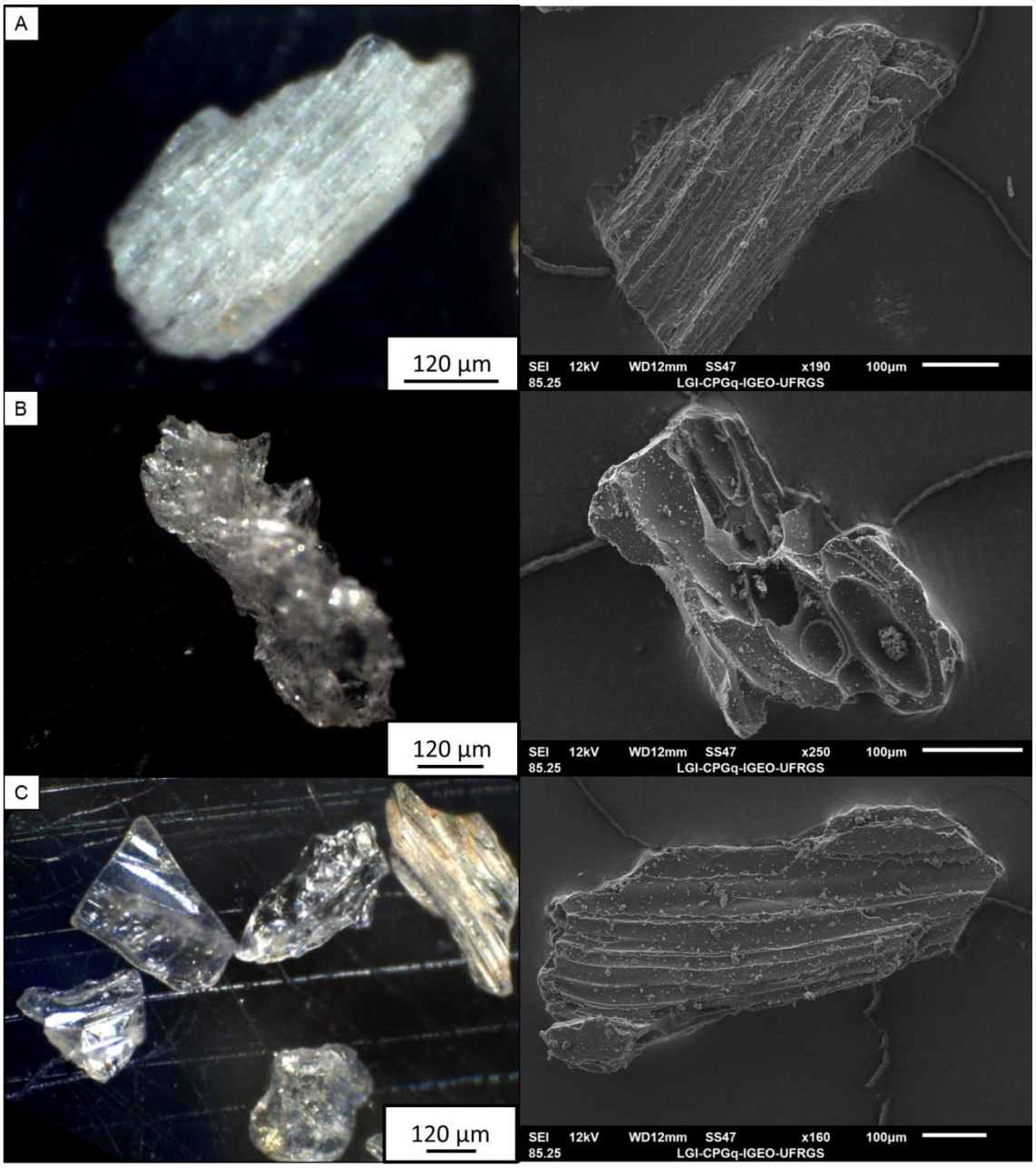

Figure 3 - Photomicrograph of tephra constituent fragments in binocular stereomicroscope at 80-fold magnification (to the left) and and secondary electron images (SEI) in SEM (right). In (A) shows the pictures of the pumices. In (B) and (C) shows images of volcanic glass in two different textures.

The material identified on the ash fraction are composed by by different fragments (Orton, 1996). Fragments of pumices occurred as fibrous material (Figure 3A). They presented translucent white coloration, tubular morphology, many small and elongated tubular vesicles . There were thin walls and sloping glass walls . Volcanic glass (Figure 3B) was translucent and exhibited relatively thick-walls junctions and/or concave fractures that preserved rounded vesicular structures. Three concave Y-shaped plates represent the junction of three bubbles, and two moon-shaped walls represented the junction of two bubbles (named as splinters by Bohor and Triplehorn, 1993). Volcanic glass (Figure 3C) composed of nearly flat plates, translucid and well-developed conchoidal fracture, also called obsidian, formed by the fragmentation of the walls that included large flattened vesicular cavities. The morphology of this fragment is quite variable, ranging from half-moon , spikes , cusps and filaments.

The petrographic analysis of bentonite presented phantoms (glass shards with bubbles) (Figure 4A) that were interpreted as pseudomorphs of old shards (e.g. Bohor and Triplehorn, 1993; Ddani et al., 2005; Meunier, 2005). These phantoms were texturally oriented in two directions (Figure 4B). When observed at higher magnification it was observed that the phantoms resulted of total polygenetic alteromorph of tephras (Figure 4B). They presented a dark brown clay mass film of low birefringence . A mineral surrounds this film with a micaceous habit, perfect basal cleavage and birefringence equal to that of mica. SEM imaging evidenced the crenulate morphology and random factory of the smectite crystals (Figure 4C). The crystals could be observed as small pseudo-hexagonal to hexagonal leaves (size approximately 4 μm) and thickness of a few nanometers (nm).

The petrography of tonsteins evidenced their heterogeneous textural aspect, which was a characteristic also observed in other works (e.g. Fisher and Schmincke, 1984; Bohor and Triplehorn, 1993; Worden and Morad, 2003; Dai et al., 2017; Shen et al., 2021). The heterogeneity was due to the three generations of kaolinite presented on the sample: I) Vermicular kaolinite (Figure 5A), of habit similar to a book or worm. Consisted of elongated and curved stacks of pseudo-hexagonal platelets of up to 5 mm height; II) Pseudomorph kaolinite formed by alteration of silicate minerals (possibly replacement of feldspars and micas), with straight contact (Figure 5B); III) Microcrystalline kaolinite filling voids, replacement result of fine-grained material (Figures 5A and B). It was

possible to observe pseudo-hexagonal kaolinite platelets, well ordered in elongated stacks of about 15µm height (Figure 5C). These were dispersed in a thin clay matrix composed of microcrystalline kaolinite of a few micrometres (µm).

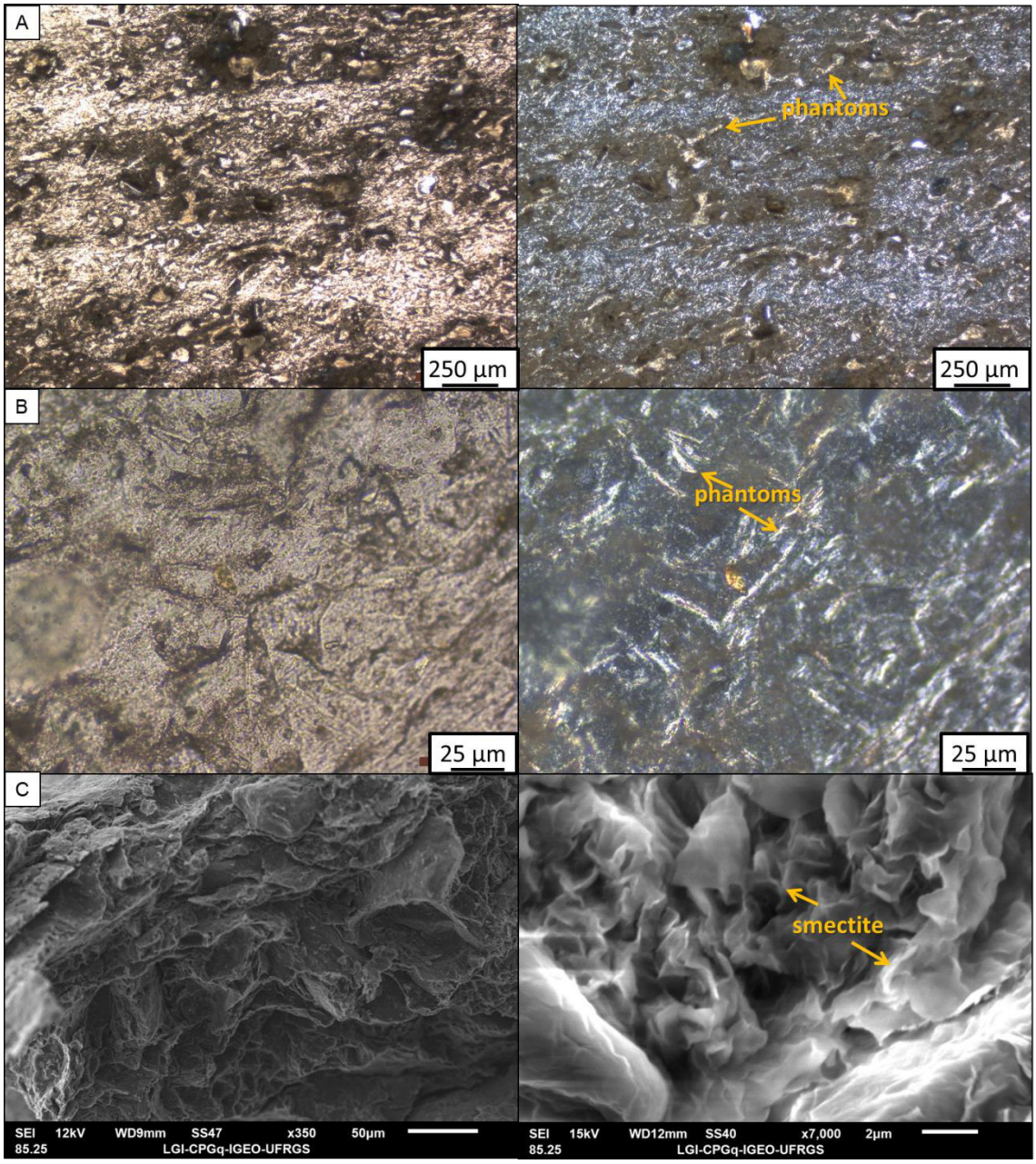

Figure 4 - Smectite in bentonite, altered volcanic ashes. (A) Thin-section optical photomicrographs (parallel and crossed polarizers). (B) Thin-section optical photomicrographs. C) Secondary electron images in SEM (right) of fine smectite crystal with random fabric.

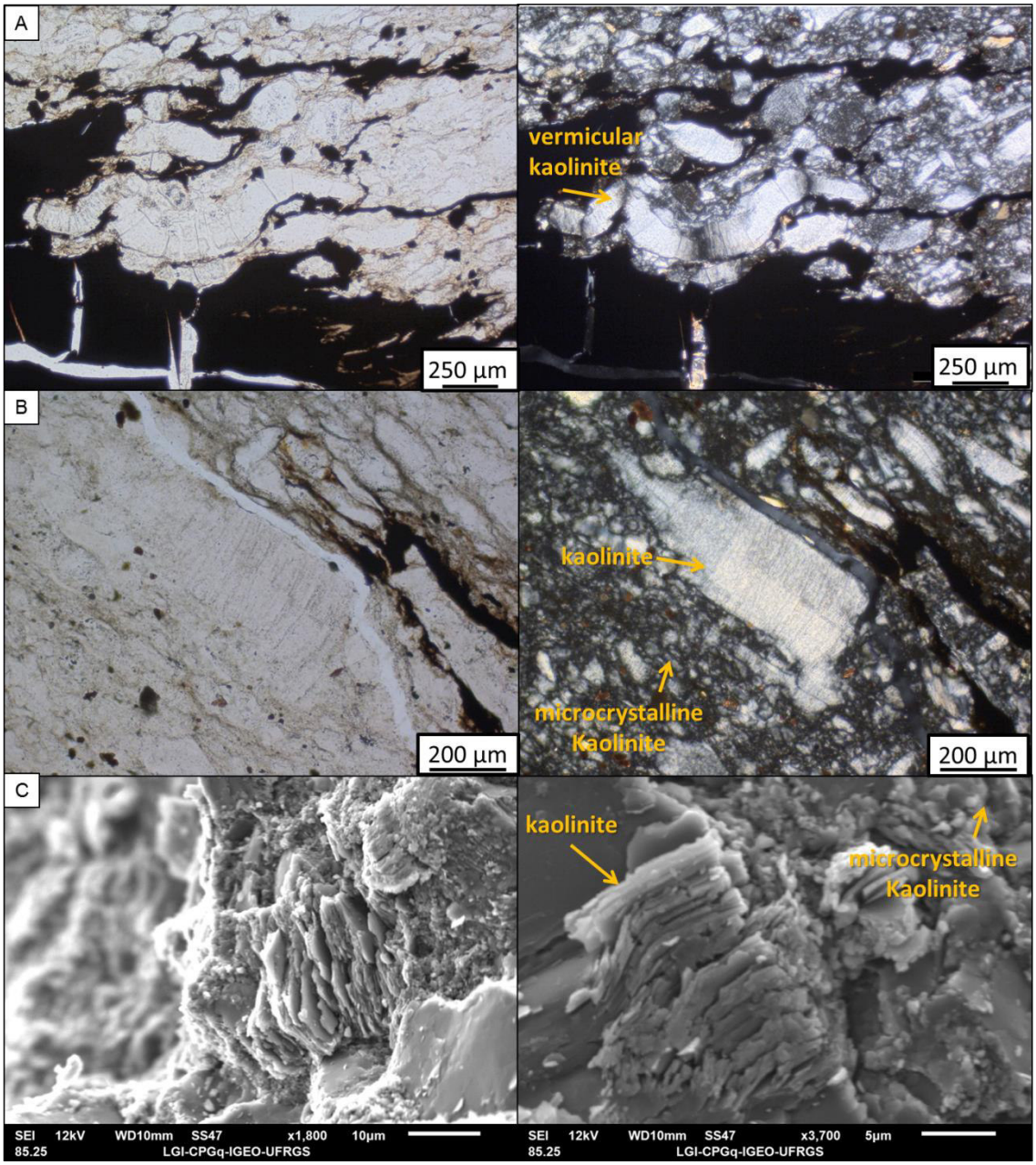

Figure 5 - Kaolinite in tonsteins, altered volcanic ashes. (A) Thin-section optical photomicrographs (parallel and crossed polarazires) vermiform kaolinite plant fragments may also be mixed. (B) optical pseudomorph of plagioclase argillized in Kaolinite. (C) Secondary electron images in SEM (right) of vermicular kaolinite.

The XRD analyzes of the volcanic ashes presented structural disorder, which could be observed by its amorphous condition that forms a diffraction band between 15º to 28º 2θ in the two fractions analyzed (whole-rock and less than 4 µm) (Figure 6 - volcanic ash-XRD). Peaks of crystalline arrangements were identified, such as quartz (Qz) (d: 3.34 Å) and possibly tridymite (Tr) (d: 4.25 Å, 4.05 Å and 3.21 Å). The d: 7.61 Å band of the oriented analyzes of the < 4 µm fraction showed presence of gypsum. It appeared as

low-intensity line in the disoriented whole-rock diffractogram, and the best crystallization line in the diffractograms of the < 4 μm fraction, represented by an intense and narrow baseline. The 10.0 Å peak in both fractions represented the d_{001} peak of micas/illite group minerals (Meunier, 2005). The peak might be the sameas the illite observed in the lithic fragments contained in the PFD. Specific XRD analysis of the lithic fragment (Figure 7) showed diverse mineralogy (smectite, chlorite, mica/illite, Kaolinite, quartz and tridymite), hence possibly being interpreted as fragment of the volcanic cone.

The high energy IR spectrum, which is in the range from 3400 to 3700 cm^{-1}, is the region of the vibrational frequencies of hydroxyl structural groups (OH) in silicates (Cível and Komadel, 1994; Madejová, 2003; Madejová and Kornadel, 2005). The volcanic ashes analysis presented spectrum with poorly defined vibrational frequency. The absorption peak at 3628 cm^{-1} and the basal broadening of the band represented possible tetrahedral bonds under low crystallinity conditions. In regards to the low-energy IR spectra, the absorption bands at 1037 cm^{-1}, 781 cm^{-1} and 460 cm^{-1}, could be assigned to the symmetric Si-O-Si vibration and was consistent with the quartz and amorphous silica mineral (Madejová, 2003, Madejová and Kornadel, 2005). The band at 729 cm^{-1} might be related to aluminium and silicon polymer with greater participation of silica or aluminium in a tetrahedral condition. However, information about this band is very scarce in the literature, hence the correct identification of the band occurs with low certainty. The chemical composition corresponded approximately to the sample g65 by Hermanns et al. (2000) and Hermanns and Schellenberge (2008). It is comprised by SiO_2 levels at 78.3% and total alkali levels ranging from 8.4% to 8.9%. In the case of volcanic ash, it showed SiO2 contents of 72.51% and total alkalis of 9.32%, corresponding to rhyodacite volcanism.

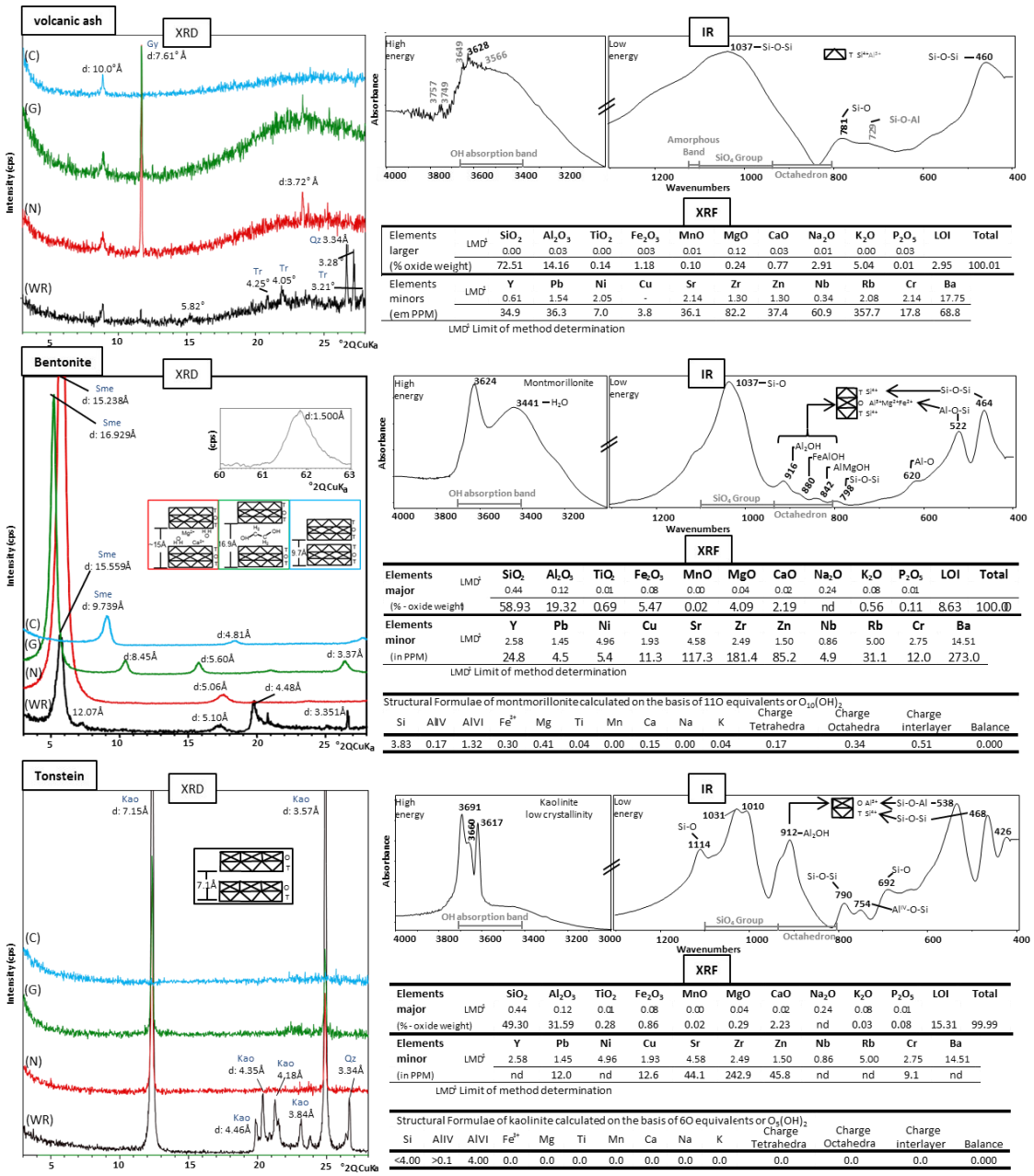

Elements larger (% oxide weight)	LMD*	SiO_2	Al_2O_3	TiO_2	Fe_2O_3	MnO	MgO	CaO	Na_2O	K_2O	P_2O_5	LOI	Total
		0.00	0.03	0.00	0.03	0.01	0.12	0.03	0.01	0.00	0.03		
		72.51	14.16	0.14	1.18	0.10	0.24	0.77	2.91	5.04	0.01	2.95	100.01

Elements minors (em PPM)	LMD*	Y	Pb	Ni	Cu	Sr	Zr	Zn	Nb	Rb	Cr	Ba
		0.61	1.54	2.05	-	2.14	1.30	1.30	0.34	2.08	2.14	17.75
		34.9	36.3	7.0	3.8	36.1	82.2	37.4	60.9	357.7	17.8	68.8

*LMD Limit of method determination

Elements major (% - oxide weight)	LMD*	SiO_2	Al_2O_3	TiO_2	Fe_2O_3	MnO	MgO	CaO	Na_2O	K_2O	P_2O_5	LOI	Total
		0.44	0.12	0.01	0.08	0.00	0.04	0.02	0.24	0.08	0.01		
		58.93	19.32	0.69	5.47	0.02	4.09	2.19	nd	0.56	0.11	8.63	100.00

Elements minor (in PPM)	LMD*	Y	Pb	Ni	Cu	Sr	Zr	Zn	Nb	Rb	Cr	Ba
		2.58	1.45	4.96	1.93	4.58	2.49	1.50	0.86	5.00	2.75	14.51
		24.8	4.5	5.4	11.3	117.3	181.4	85.2	4.9	31.1	12.0	273.0

*LMD Limit of method determination

Structural Formulae of montmorillonite calculated on the basis of 11O equivalents or $O_{10}(OH)_2$

Si	AlIV	AlVI	Fe^{3+}	Mg	Ti	Mn	Ca	Na	K	Charge Tetrahedra	Charge Octahedra	Charge interlayer	Balance
3.83	0.17	1.32	0.30	0.41	0.04	0.00	0.15	0.00	0.04	0.17	0.34	0.51	0.000

Elements major (% - oxide weight)	LMD*	SiO_2	Al_2O_3	TiO_2	Fe_2O_3	MnO	MgO	CaO	Na_2O	K_2O	P_2O_5	LOI	Total
		0.44	0.12	0.01	0.08	0.00	0.04	0.02	0.24	0.08	0.01		
		49.30	31.59	0.28	0.86	0.02	0.29	2.23	nd	0.03	0.08	15.31	99.99

Elements minor (in PPM)	LMD*	Y	Pb	Ni	Cu	Sr	Zr	Zn	Nb	Rb	Cr	Ba
		2.58	1.45	4.96	1.93	4.58	2.49	1.50	0.86	5.00	2.75	14.51
		nd	12.0	nd	12.6	44.1	242.9	45.8	nd	nd	9.1	nd

*LMD Limit of method determination

Structural Formulae of kaolinite calculated on the basis of 6O equivalents or $O_5(OH)_2$

Si	AlIV	AlVI	Fe^{3+}	Mg	Ti	Mn	Ca	Na	K	Charge Tetrahedra	Charge Octahedra	Charge interlayer	Balance
<4.00	>0.1	4.00	0.0	0.0	0.0	0.0	0.0	0.0	0.0	0.0	0.0	0.0	0.000

Figure 6 – Table of the analytical results of XRD, IR and XRF of the three samples analyzed. The diffractogram represents the analyses of whole-rock disoriented (WR), natural (N), glycolate (G) and calcined (C). The bentonite diffractogram also shows the breakdown of parameter B of line d_{060}. The mineralogy found corresponds to tridymite (Tr), gypsum (Gy), quartz (Qz), smectite (Sme), and kaolinite (Kao). The IR graphs are presented in absorbance mode, with the high energy Spectrum from 4000 to 3000 cm^{-1}, and the low energy Spectrum from 1300 to 400 cm^{-1}. The whole-rock XRF presents geochemical data of major and minor elements. The chemical formula calculation is based on 11 oxygen equivalents for montmorillonite, whereas for kaolinite, the hypothetical formula was considered.

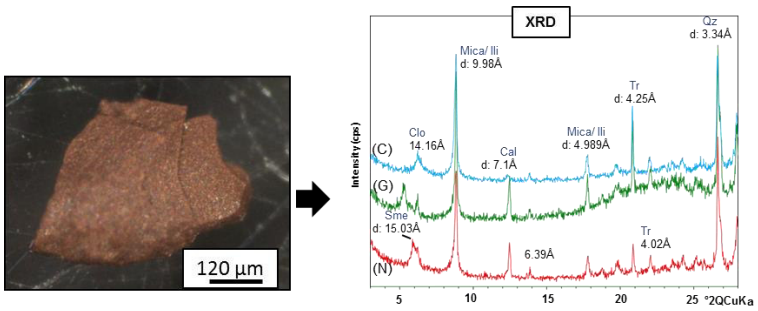

Figure 7 - Diffractogram of 3 at 28º 2θ 0.02º/1s of the whole-rock analyses-oriented natural (N), glycolate (G) and calcined (C) volcanic lithic fragment. The mineralogy found corresponds to smectite (Sme), chlorite (Clo), mica (or illite), tridymite (Tr), and quartz (Qz).

The mineralogical analyses of bentonite show that it consists mainly of montmorillonite (Figure 6 - Bentonite), with a predominance of Al in the octahedral position, with high crystallinity and having Ca^{2+} in the interlayer position (e.g. Ddani et al., 2005; Meunier 2005; Silva et al., 2017). In XRD analyses, the whole-rock diffractogram shows the d: 3.35Å line corresponding to quartz and an intense low-angle diffraction line with spacing around 15.5 Å, consistent with the d_{001} of smectites (Velde and Vasseur, 1992; Meunier, 2005). The presence of expansive clay is evident in the analyzes of the oriented fine fraction (<2µm), in the glycolate mode (EG) with the modification of the basal interlayer spacing to close to 17.0 Å and in the 550°C calcined (C) modes with the collapse to spacings near 9.7 Å. The b-parameter analysis shows the diffraction line of the d_{060} line with a value of 1,500 Å, evidencing that the montmorillonite type is di-octahedral with Al predominance in the octahedral position (Meunier, 2005).

The high-energy IR spectrum confirms the di-octahedral montmorillonite's presence (Madejová, 2003), with the band at 3624 cm^{-1}, along with the bending bands of the octahedral in the hydroxyl structure (930-800 cm^{-1}). In this montimorillonite, the low-energy IR spectrum shows that octahedrons are made up of Al (916 cm^{-1}), Fe (880 cm^{-1}) and Mg (842 cm^{-1}) (Madejová, 2003; Madejová and Kornadel, 2005). In the IR spectrum's high-energy region, the absorbance of the 3441 cm^{-1} band is due to the hydrogen bonds' vibrations (H-O-H) of ordered water molecules. In the low energy region of the spectrum, in addition to information on the composition of the octahedrons, the absorption bands at 1037 cm^{-1}, 798 cm^{-1} and 464 cm^{-1}, are attributed to the

symmetrical vibration of Si-O-Si in the tetrahedrons, and the 620 cm^{-1} and 522 cm^{-1} bands are attributed to the symmetrical vibration of Al-O-Si in the tetrahedron (Madejová, 2003; Madejová and Kornadel, 2005).

The chemical composition of bentonite agrees with other literature's compositions (e.g. Fisher and Schmincke, 1984). The ion exchange results at the smectite's interlayer position by saturation (Figure 8) demonstrate its low charge, revealing that ions can enter and exit easily. This result shows charge values for smectite between -0.3 and -0.6 per unit cell (or half Si_4O_{10} unit formula). By calculating the structural formula between the charges generated at the octahedral and tetrahedral level (Cível and Komadel, 1994), they showed the value of -0.51 for the balancing at the interlayer position, balanced by ions of de Al^{IV}, Ca^{2+}, Mg^{2+} and K^{+}. The absorbance in the 3411 cm^{-1} bands in the high-energy region of the spectrum shows the presence of H_2O, which may indicate that it was also accompanying the ions in the interlayer position.

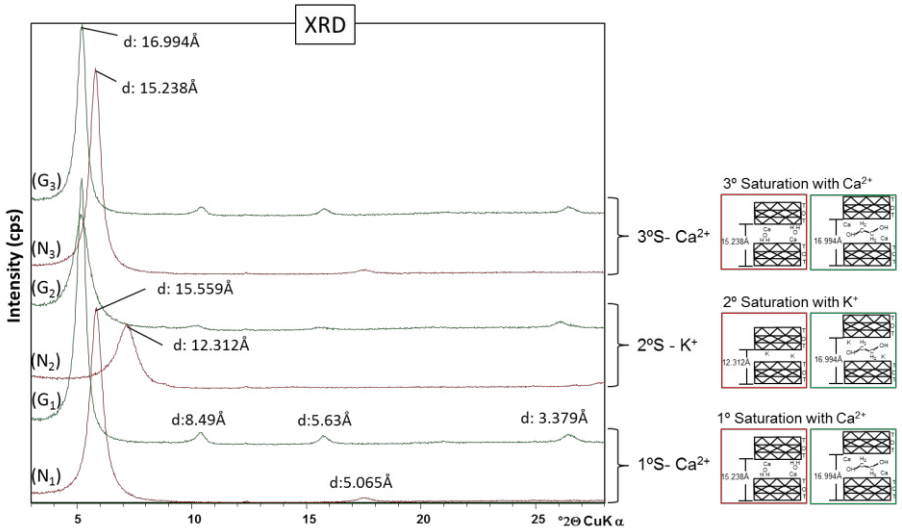

Figure 8 – Diffractograms of the whole-rock disoriented (WR), natural (N) and glycolate (G) samples oriented from the <2 µm fraction with different ions resulting from saturation. The test consisted of sequential saturation of Ca^{2+} Mg^{2+} and K^{+} ions in interlayer position.

The XRD analyses show that tonstein consists mainly of high crystallinity kaolinite (Figure 6 - Tonstein). The diffraction line d001 confirms kaolinite dominance in the rock: 7.15 Å and d_{002}: 3.57 Å in whole-rock (WR). In the analyses of the oriented fine fraction

(<2μm) it is shown that kaolinite is dominant in the clay fraction, and in the calcined (C) mode, it is destroyed.

The high energy region of the IR spectrum with three absorbance peaks at 3691 cm^{-1}, 3660 cm^{-1} and 3817 cm^{-1}, as well as the 1031 cm^{-1} and 1010 cm^{-1} doublet peaks in the low-energy region of the IR spectrum, show the signature of high crystallinity kaolinite (e.g. Madejová et a., 2002; Madejová, 2003). The most intense band at 3691 cm^{-1} represents the symmetric vibration in the stretching phase, the less severe band at 3660 cm^{-1} represents the stretching vibrations outside the plane, indicating a high structural defects kaolinite (e.g. Madejová et a., 2002), and the 3617 cm^{-1} band denotes the hydroxyl group of the tetrahedral and octahedral leaves (Madejová et al., 2002; Madejová, 2003). In the IR spectrum's low-energy region, the bands at 1114 cm^{-1}, 1031 cm^{-1}, 1010 cm^{-1}, 790 cm^{-1}, 692 cm^{-1} and 468 cm^{-1} represent the Si-O-Si vibrations of the tetrahedra. In the octahedron spectrum, it is evidenced by the majority existence of Al (Al2OH in the band 912 cm^{-1}), with the absence of Fe and Mg. The 538 cm^{-1} band represents the absorption of the Si-O-Al (Al octahedron) vibrations in kaolinite, and the 754 cm^{-1} bands are associated with the absorption of O-Si-Al^{IV} (Madejová et a., 2002; Madejová and Kornadel, 2005). The chemical composition of tonstein coincides with other compositions in the literature (e.g. Fisher and Schmincke, 1984; Bohor and Triplehorn, 1993; Spears, 2012).

In the conventional use of sample preparation for dating, the mineral separation methodology using 250 mesh / 200 mesh sieves (Table 1) may fail to retain essential magmatic minerals and obtain proportions of detrital minerals, such as detrital zircons. Hence, it can cause errors, generating a false negative in getting data from the analyzed PFD geochemical analysis. Therefore, during the sample preparation process (e.g. Bohor and Triplehorn, 1993; Reiners et al., 2018), the use of 500 mesh screens is advisable.

Table 1 - Table of ASTM grain size (mesh) and sieve opening (mm) compared to grain-size scale for clastic sediments and size of magmatic minerals.

ASTM	Tyler	Aperture (mm)	Granulometry		Magmatic minerals
70	65 mesh	0,212	Fine sand	Sand / Sandstone	250 µm // 0. 25 mm
80	80 mesh	0,180			
100	100 mesh	0,150			
120	115 mesh	0,125	Very fine sand		
140	150 mesh	0,106			
170	170 mesh	0,090			
200	200 mesh	0,075			
230	250 mesh	0,063			
270	270 mesh	0,053	Coarse Sill	Mud / Mudock	
325	325 mesh	0,045			
400	400 mesh	0,038	Medium Sill		
450	450 mesh	0,032			
500	500 mesh	0,025			30 µm // 0.03 mm

In the conventional use of sample preparation for dating, the mineral separation methodology using 250 mesh / 200 mesh sieves (Table 1) may fail to retain essential magmatic minerals and obtain proportions of detrital minerals, such as detrital zircons. This way, it can cause errors, generating a false negative in getting data from the analyzed PFD geochemical analysis. Therefore, during the sample preparation process (e.g. Bohor and Triplehorn, 1993; Reiners et al., 2018), the use of 500 mesh screens is advisable.

4. DISCUSSION

4.1. VOLCANIC ASH - Alemanía Ash, Argentina

The volcanic ash PFD corresponds to the Alemanía Ash volcanic event, which occurred at approximately 3.7 ka during the Holocene (Figure 9A). Its preservation occurred in a melting lake in an intermontane basin, formed due to a mass gravitational movement that totally obstructed the river that flowed south-north in the De Las Conchas valley (Figure 9B). In the classification by Costa and Schuster (1988), the obstruction caused a type III landslide dam (e.g. Figure 9C), forming a lake that persisted between

approximately 5.6 Ka to 3.7 Ka (Figure 9A). The volcanic ash PFD sample in this work represents the g65 sample by Hermanns et al. (2000) and Hermanns and Schellenberge (2008), deposited at the end of this lake's existence. Their deposition age is calculated by stratigraphic inference of the depositional rate, related to the dating of ^{14}C AMS in levels containing remains shells of *Biomphalaria* (Figure 9A) (Hermanns and Schellenberge, 2008).

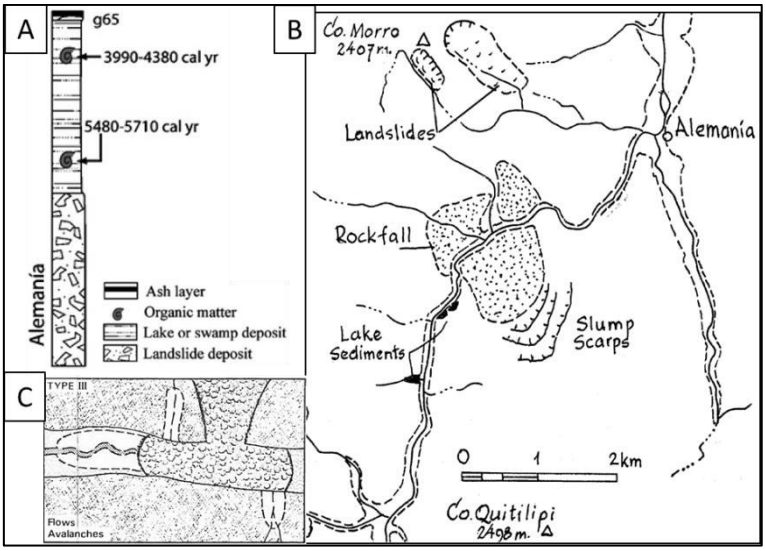

Figure 9 – (A) stratigraphic survey of lake deposits in road cut (modified from Hermanns and Schellenberge, 2008) (B) Thematic map of the Quebrada De Las Conchas mass movement event (modified from Wayne, 1999). (C) Type III classification of a mass movement in the mountains (Costa and Schuster, 1988).

The Alemanía Ash PFD originated from a rhyodacite volcanism located north of Argentina, in the Central Volcanic Zone (CVZ) of the Central Andes (Hermanns et al., 2000; Hermanns and Schellenberge, 2008), presenting the genetic origin of the NCE_{cV2} type (Zuffa, 1980; 1985; 1987). This type of volcanism is formed in magmatic pockets in upper mantle zones and fed by molten silicate fluids from the sialic crust, mantle, or the mixture of both (Orton, 1996; Calas et al., 2006). Magmatism of this type has three main phases that play an important role in the volcanic kinetic process (Figure 10): I) solid phase, containing variable proportions of silicate crystals; II) the fluid phase of melts, of which Si^{4+} and Al^{3} are the most abundant cations and in smaller amounts K^{+}, Na^{+}, Fe^{3+} and Mg^{2+}, among others; III) the phase of volatile elements, of which H_2O, CO_2 and H_2S

are the most abundant gases, and possibly smaller amounts of HCl, CH_4, HF, N_2, SO_2 and O_2 (Orton, 1996; Henderson, 2005; Calas et al., 2006).

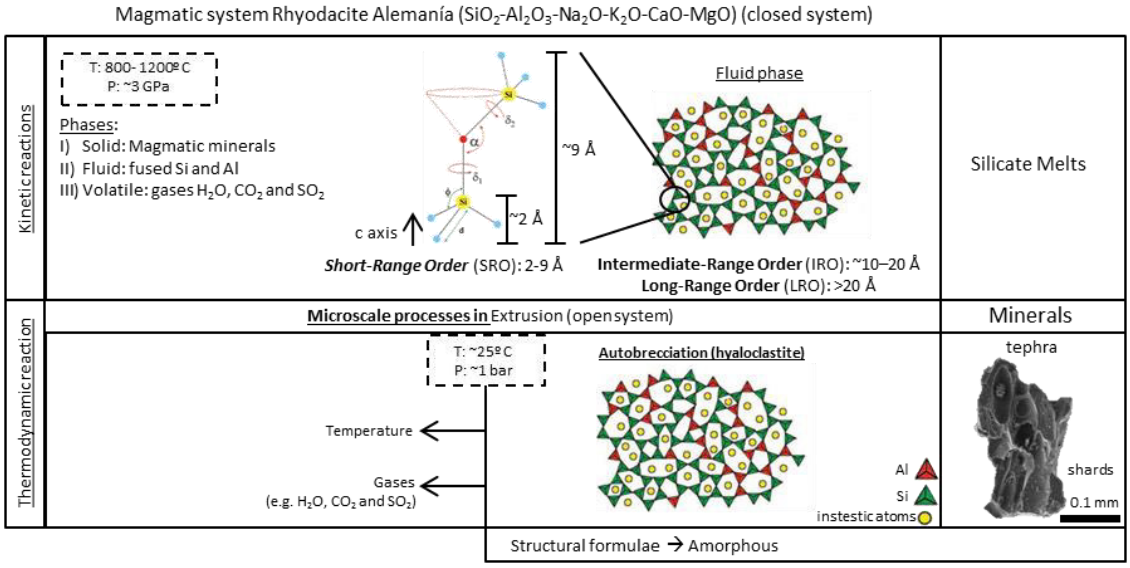

Figure 10 – The synthesis of the general kinetic organization in the magmatic system and the assumption of magmatic cooling for the tephra's solid-state formation at the time of extrusion (modified from Henderson, 2005 and Calas et al., 2006).

The solid phase was formed by elements of the magmatic system consisting of multiple components (e.g. SiO_2-Al_2O_3-Na_2O-K_2O-CaO-MgO magmatic system). These elements were interdependent, combined by chemical affinities (charge and size of cations), concentration, temperature and pressure, developing regular crystalline lattice to form thermodynamically stable minerals at high temperature. Among these minerals, the main ones were probably those of the group of silica, feldspar, olivines, pyroxenes, amphiboles and micas (e.g. Cas and Wright, 1987; Orton, 1996; Gill, 2015), while in the residual liquid, they probably formed accessory minerals, such as zircon, apatite, ilmenite and β-quartz (e.g. Bohor and Triplehorn, 1993).

As the crystallization of magmatic minerals occurred, the composition of the magmatic fluids fractionated, enriching itself in Si^{4+} and Al^{3+}, where they favoured the polymerization and the formation of SiO_4 and AlO_4 tetrahedra linked together through O^{2-} sharing (Figure 10) (e.g. Henderson, 2005).

As is evident from the XRD and IR data (Figure 6 - volcanic ash), the tephras have mostly low crystallinity, composed of disorganized chains of polymerized tetrahedra, filled with the disorder by rapid crystallization. This disorder is demonstrated in the XRD by the band of low-crystallinity phases between 15º to 28º 2θ. At the same time, in the IR, it is represented by the low definition of the band 1037 cm^{-1} and broadening of the vibrational band of the hydroxyl structural groups (~ 3700-3400 cm^{-1}), showing the different angles between the connections of the O-Si-O tetrahedrons (Cível and Komadel, 1994; Madejová, 2003; Madejová and Kornadel, 2005).

The Zachariasen-Warren (Z-W) model (Randall et al. 1930; Zachariasen 1932; Wright, 1990; Henderson, 2005) presents a hypothesis of the crystal-chemical arrangement of the polymerized structures of SiO_4 and AlO_4 tetrahedral bonds in glass, which can be used to understand the fluid phase of the silicate liquid (Figure 10) (Henderson, 2005; Calas et al., 2006; Henderson et al., 2006). The theory divides the crystal-chemical chain into three structural ranges: short-range order (SRO) forming polymers between 2-9 Å; intermediate-range order (IRO), forming polymers ~10-20 Å; and long-range order (LRO), forming polymers above 20 Å (Wright, 1990; Henderson, 2005; Calas et al., 2006).

The formed tetrahedrons consist of short-range order, defined by the bond length (d), tetrahedron angle (Φ) and the coordination number (n), with a radial distance of up to 2 Å. The Si atom is linked to four O atoms making angles (Φ) of approximately 109.5°. This bonding angle is very close to the angle of a perfect tetrahedron (109.47°), whose bonding forces are covalent, thus providing an almost regular crystallinity, similar to that of crystals such as microcrystalline quartz (Wright, 1990; Henderson, 2005). Already in the interconnection of tetrahedrons, the crystalline disturbances begin. In the construction of branched polymers, the interconnection of tetrahedrons occurs through the sharing of oxygen atoms, and it is defined by bond-torsion angles (δ_1, δ_2) and the inter-tetrahedron bond-angle (α). In short-range order, branched polymer chains reach up to a radial distance of up to 9 Å and may exhibit crystallinity, but this is generally where the variation in δ_1 ,δ_2 and α, generates the crystalline disorder (Figure 10).

In branched polymer chains of intermediate-range order (IRO), it extends to a radial distance of ~10–20 Å and is generally disordered, however, it may contain

crystalline order with structural symmetry in the form of SiO_2 polyhedral networks (such as tridymite and cristobalite polymorphs) (Randall et al. 1930; Zachariasen 1932; Calas et al., 2006). The long-range order (LRO) does not exist in the magmatic fluid (e.g., Wright, 1990; Henderson, 2005; Calas et al., 2006; Henderson et al., 2006).

The Zachariasen – Warren (Z–W) model explains that the construction of this chain is guided by the elements existing in the magma, distinguishing between cationic network-forming or deforming elements that use O^{2-} (Ionic radius 1.4 Å) as a sharing (Henderson, 2005; Calas et al., 2006; Ryan, 2019):

- Cationic network-forming elements (coordination number n = 3 or 4), such as Si4 + (Ionic radius 0.26 Å) and Al3 + (Ionic radius 0.39 Å);
- Cationic network-forming or network-deforming elements (coordination number n = 4 or 6), intermediate oxides such as Al3 + (Ionic radius 0.54 Å), Fe2 + (Ionic radius 0.74 Å), Fe3 + (Ionic radius 0.64 Å), Ti (Ionic radius 0.68 Å); and
- Cationic network deforming elements (No. of coordination n = 6 or higher), alkaline elements: Na + (Ionic radius 0.97 Å) and K + (Ionic radius 1.51 Å), and earth alkali: Ca2 + (Ionic radius 0.99 Å), Mg2 + (Ionic radius 0.66 Å).

Chemical analyses of volcanic ash (Figure 6) show that magma moments before extrusion had contents around 72% and Al_2O_3 around 14%, while the levels of total alkalis (MgO, CaO, Na_2O and K_2O) were around 9% (Figure 6).

In the volcanic ash, the Si-O-Si bonds identified in the IR data represent the tetrahedra's crystallinity in the Short-range Order chain (Figure 6) and demonstrate that the volcanic ash does not contain octahedral bonds in its structure. In the XRD data, possibly the Short-range Order chains are responsible for forming the low crystallinity phases band between 15º to 28º 2θ, represented by several angles between the tetrahedral bonds.

These proportions allow us to interpret that the magmatic compositions were concentrated in network-forming elements. The growth of the polymer chain was due to the chemical composition of the fluid phase of melts. Thus, the thermodynamic conditions at high-temperature in the magma developed the tetrahedron that makes up the Short-range Order chains, while the kinetic interactions condition processes of diffusive transport of elements and nucleation between tetrahedrons, producing polymer chains with disordered intermediate regions (Calas et al., 2006; Henderson et al. 2006).

In magma, the cationic element Al^{3+} prefers to form tetrahedrons (Al^{IV}), presenting coordination number 4 and also being a network forming-element (Henderson, 2005), but limiting polymer growth by needing to be compensated by another cation (e.g. -SiO2 -O-Al = O). The 729 cm^{-1} band was not precisely identified in the bibliography. Still, it is probably associated with O-Si-Al^{IV} absorption since the chemical analysis shows the existence of 14% of Al_2O_3 in the composition, and the value is close to the value indicating the absorption of O-Si-Al^{IV} in the tonstein (band 754 cm^{-1}; Figure 6).

Because Si^{4+} is a network forming element, the polymer chains will be more elongated the higher the concentration of Si^{4+} in the magma (e.g. -SiO2-O-SiO2-). Small crystalline peaks in XRD denote that there is some crystallinity in the IRO range. They may represent tridymite ($6SiO_4$) (Figure 6 and Figure 11), which is a high temperature, low pressure, polymorphic quartz mineral common in high temperature acidic effusive magmatic rocks.

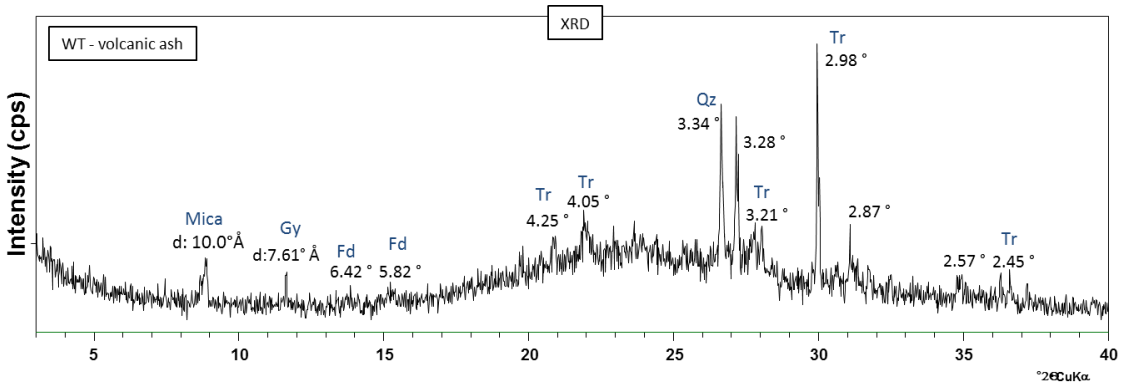

Figure 11 – Diffractogram of the whole-rock disoriented (WR) analysis from 3 to 40º 2□ 0.02º/1s. The mineralogy found corresponds to tridymite (Tr), Gypsum (Gy), quartz (Qz), feldspar (Fd), and mica.

The 9% network-modifying elements, such as ions alkali (e.g. -SiO_2-O-Na) and alkaline-earth (e.g. -SiO_2-O-Mg-OH), limited the growth of polymers in the magma and conditioned changes in the physical properties of the magma by disrupting tetrahedron network connectivity due to charge compensation (Henderson, 2005; Calas et al., 2006; Henderson et al. 2006).

During the extrusive magmatic process of Alemanía Ash, its SiO_2 and Al_2O_3 contents (around 86%), conditioned its high viscosity. The presence of volatiles (e.g. H_2O, CO_2, SO_2 and H_2S) influenced the eruption energy, leading to a Plinian-type eruption. The power of the extrusion imposed stress on the magma and the rapid cooling to the solid-state (non-crystallized), providing the formation of pyroclastic material (Figure 1) through the self-bridging process known as hyaloclastite (Figure 3) (Orton, 1996). These pyroclastics are composed of morphologically immature tephras and have the record of bubbles of expanded volatiles at the time of extrusion, consisting primarily of volcanic glass and pumice (Figure 3) (e.g. Fisher 1961; Orton, 1996; Calas et al., 2006).

The fall of higher density materials led to the concentration of lighter fractions in the eruptive column, constituting a volcanic ash cloud with most pyroclastics smaller than <2mm (Figure 1) (e.g. Jerram and Petford, 2014; Meunier, 2005). Loaded by wind agents (e.g. Fisher and Schmincke, 1984; Lajoie and Stix, 1992; Orton, 1996), it dispersed asymmetrically around the volcanic cone turbulence, and horizontal laminar flow ceased (Hermanns et al., 2000), depositing on the glacial terrain. Portions of the deposits fall on the thaw lake (Figure 9B).

Upon depositing in the aqueous medium, the small size of the amorphous, porous and fractured particles (Figure 3), capable of having an electrical charge, provided a large specific surface for hydration by capillary percolation of the water molecule (Figure 12). The water molecules acted as a dipole, orienting the O^{2-} side in the positive portion of the Si^{4+} and Al^{3+} ions. Thus, the tephra that would contain <1% by weight of water, after hydration, would contain about 6% by weight, forcing it to flocculate. Water molecules could also have leached ions (e.g. Si^{4+}, Al^{3+}, Fe^{2+}, S^{2-}, Na^{2+}, Mg^{2+} and Ca^{2+}) contained in interstitial spaces of the polymer chains of the tephras (Figure 12) (Orton, 1996; Henderson, 2005).

The lake was supplied with fresh water from glaciers, and it presented low salts levels in solution. Thus, the low concentration of ions in the solution conditioned a pH near neutral value (pH≥7) and low chemical potential for kinetic reactions. As the interstitial atoms were leached, salinity increased. Some of the elements could react with OH^- and form compounds of the hydroxyl group (e.g. KOH, NaOH, $Ca(OH)_2$ and

$Mg(OH)_2$), increasing alkalinity (Figure 12) (e.g. Brookins, 1988). Leaching ceased as entropy lowered and reached the stoichiometric equilibrium state of the environment's saturation, stagnating the kinetic reaction and preserving the tephras' dissolution (Grim and Güven, 1978; Meunier, 2005; Meunier et al., 2016). The increase in pH by the compounds of the hydroxyl group was not high enough to start the process of remobilization of Si^{4+} (pH <9) (Brookins, 1988). Moreover, the PFD deposition's permanence in the glacial lake was very rapid. After depositing the PFD, the dam breaks, ending with the lake and dehydrating the tephra layer (Figure 9; figure 10).

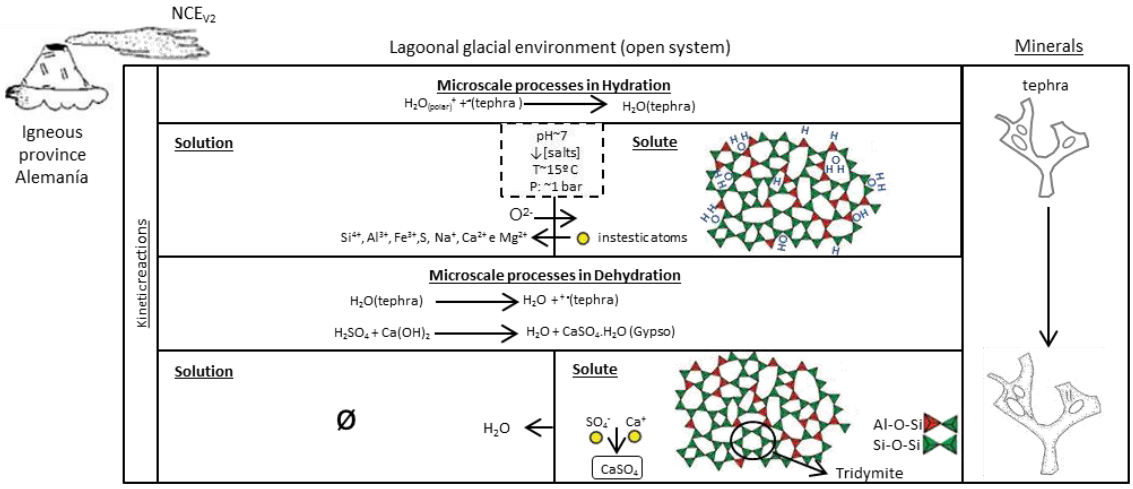

Figure 12 - A synthesis of the general controls on tephra activity in PFDs, as described in this paper. Interpreted diagenetic minerals are based on petrography, SEM, XRD, IR and XRF data, and clay beds.

The presence of gypsum in studied samples detected by the XRD (Figure 6) induces the interpretation that portions of the leached interstitial atoms were sulfur (e.g. SO_2 and H_2S), which would have oxidized and subsequently in the dehydration process reacted with the $Ca(OH)_2$ also present in the lake solution to form this salt (e.g. Mohriak et al., 2008).

$$Ca(OH)_2 + H_2SO_4 \rightarrow CaSO_4 + 2H_2O$$

The white colour of the volcanic ash PFD (Figure 2A) is due to the predominance of tephra fragments as a constituent, mainly pumice fragments (Figure 3).

4.2. BENTONITE IRATI

The volcanic ash that formed the Irati bentonite occurred during the Cisuralian (early Permian), from active volcanism in the Choiyoi volcanic province (Rocha-Campos et al., 2011; Limarino et al., 2013) and that was transported over a considerable distance until its deposition in the Paraná Basin. These ashes deposited in a shallow epicontinental sea that extended over a vast area of Southern Gondwana (Sato et al., 2015), called Mar Irati-Whitehill, with 4 x 10^6 km^2 (four million km^2) (Matos et al. 2017; Bastos et al., 2021), forming a layer of PFD of the NCE_{cV3} type (Zuffa, 1980; 1985; 1987).

Geochronology dating of zircons (Alan, 2018; Reiners et al., 2018) of the PFDs, Santos et al. (2006) obtained for the PFD SM-03 show numerical ^{206}Pb / ^{238}U age of 278.4 ± 2.2 Ma (1σ; MSWD = 1.01, n = 7), and Rocha-Campos et al. (2019) obtained for the PFD SM-01 yield a numerical $^{206}Pb/^{238}U$ age of 280.0 ± 3.0 Ma (1σ; MSWD = 0.9, n = 15), correlating to volcanisms of the andesite / rhyodacite compositions (Silva et al., 2017).

Upon deposition, in addition to the tephras becoming hydrated, the free cations aided in flocculation, binding on the surface and forming colloids of multiple internally charged electrically, sized particles in the range of 10^{3-} to 10^{6-} mm, cancelling the external surface charge and making it sufficient dense to deposit (e.g. Meunier, 2005). The partially restricted environment that persisted in the Irati-Whitehill Sea during the Assistência Member formation (Araújo, 2001; Xavier et al., 2018; Bastos et al., 2021), with low leaching on the marine substrate, enabled the preservation of PFDs. Environmental conditions were of great importance (e.g. Worden and Burley, 2003; Meunier, 2005), where the Irati-Whitehill Sea presented mixed siliciclastic-carbonate-evaporitic environments (Araújo, 2001; Matos et al., 2017; Xavier et al. 2018; Bastos et al., 2021), with salt concentrations close to 35 ‰ (Figure 13) (Araújo et al., 2004), slightly alkaline waters (seawater pH close to 8.3) and several free cations with low ionic potential in aqueous media (e.g. K^+, Na^+, Ca^{2+}, Mg^{2+}, Cl^-, F^-, SO_4^{2-} and HCO^{3-}).

These geochemical conditions provided high entropy between the colloids and the environment, promoting exothermic reactions. The difference in chemical concentration

inside and outside the colloid generated a difference in chemical potential, initiating kinetic exchanges with the aqueous medium in the process of hydrolysis in the context of an open system and a more basic pH. These reactions consisted mainly of the interaction between ionized water molecules (e.g. OH^- and H_3O^+) and the breakdown of the polymers of the metastable tephras contained in the colloids (Figure 13). The polymers were in an ionic solution, and an excess of ions was leached by ionic inter-diffusion into the solution (e.g. Chamley, 1989; Bohor and Triplehorn, 1993; McKinley et al., 2003; Meunier, 2005; Meunier et al., 2016).

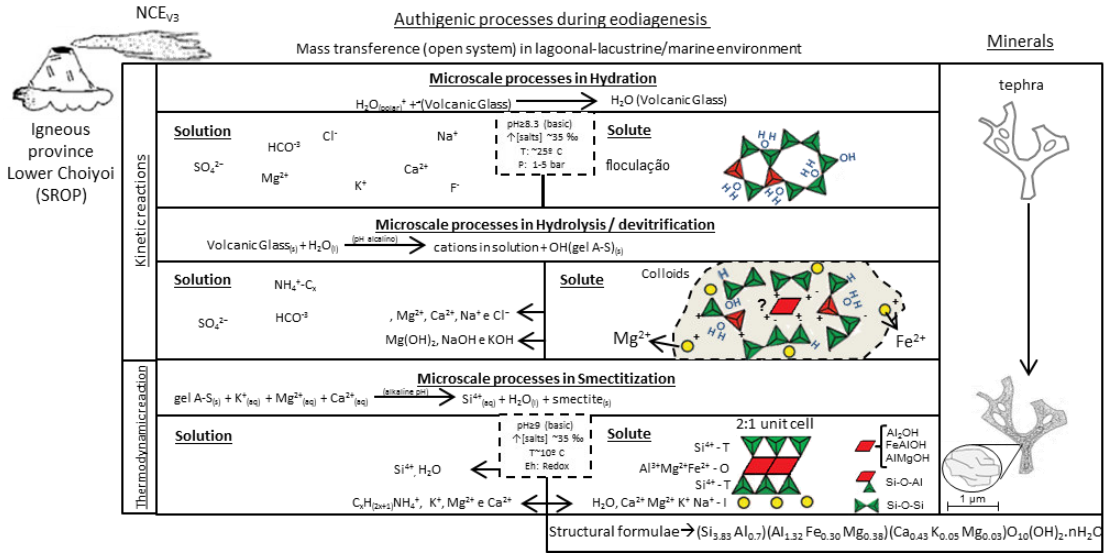

Figure 13 – A synthesis of the general controls on the transformation activity in early diagenesis of tephra to smectite in PFDs, as described in this paper. Interpreted diagenetic minerals are based on petrography, SEM, XRD, IR, XRF, Formula units, and clay beds.

The hydrolysis reactions were complex, with different cations reacting at different rates and at different times. Among the different hydrolysis processes, the main one must have been the ionized water molecules' interaction with the tetrahedral polymers. The hydration energy broke the weak bonds between tetrahedral (such as van der Waal bonds), adding a hydroxyl or replacing the oxygen anions with hydroxyl ions. In the colloids, ionized water molecules' interaction with the tephra's polymerized chains initially caused a partial dissolution process. An example is shown below:

hydrolysis in tetrahedral polymers: $-Si-O-Si-_{(s)} + OH^- + H_3O^+ \rightarrow -Si-OH_{(s)} + HO-Si-_{(s)} + H_2O_{(l)}$

The hydrolysis process may also have released some of the elements that in the new thermodynamic condition have become mobile, such as monovalent alkaline cations (e.g. Na^+, K^+ and Rb^+), bivalent earth alkalines (e.g. Ca^{2+} and Mg^{2+}), halides (e.g. F^-, Cl^-, Br^-, I^-, S^{2-} and IO_3^-), and transition (e.g. Fe^{2+}/Fe^{3+}, Mn^{2+}, Ni^{3+}, Cu^+ and Ti^{4+}) (Brookins, 1988; Chamley, 1989). The cations of alkaline and alkaline earth elements have a high gradient of the ionic potential, diffusing more quickly than other cations and thus exchanged preferentially in this process (Chamley, 1989). The transition elements of intermediate ionic potential tended to be evacuated later. An example is shown below:

hydrolysis and leaching: $-Si-O-Na_{(s)} + OH^- + H_3O^+ \rightarrow -Si-OH_{(s)} + Na^+_{(aq)} + H_2O_{(l)}$

As they were leached, the hydrated ions suffered repulsions from coordinated water molecules, remaining in solution and increasing salinity. Alkaline and alkaline earth elements contained in polymers can also interact with ionized water molecules and form compounds of the hydroxyl groups (e.g. NaOH, KOH, RbOH, $Ca(OH)_2$ and $Mg(OH)_2$), these being strong bases causing alteration in the pH of the solution (Curtis, 1977; Chamley, 1989; Meunier, 2005). An example is shown below:

hydrolysis and leaching: $-Si-O-Na_{(s)} + OH^- + H_3O^+ \rightarrow -Si-OH_{(s)} + NaOH_{(aq)}$ (sodium hydroxide)

All of these processes described previously consist of modification of crystal-chemistry structures, creating an intermediate phase between hydrolysis and devitrification. During this process, hydrated aluminosilicate gel formed in the solute, composed of three phases: I) tephras, II) amorphous aggregates and III) magmatic minerals. Amorphous aggregates are formed by metastable polymer compounds with elements with low ionic potential, containing tetrahedrons of silicon ($-Si_n-OH$) and aluminium ($-Al_n-OH$).

The leaching process by hydrolysis, especially on more mobile alkaline elements, promoted gradually more basic solutions (Curtis, 1977; Chamley, 1989). When reaching pH≥9, the solution destabilized the Si tetrahedra, breaking bonds between tetrahedra and leading to the rapid dissolution of tephra polymers by devitrification (Figure 13) (Brookins, 1988).

The pH level > 9 creates an essential mechanism for the kinetic dissolution of polymers and allows the emergence of neoformations in thermodynamic equilibrium (Fisher and Schmincke, 1984; Gill, 2015). Due to electrostatic forces of attraction between oppositely charged ions contained in the aluminosilicate gel, the tetrahedra (SiO_4^{4-} and $Al_2O_3^{3-}$) undergo a process of recrystallization into more thermodynamically stable crystalline phases (Meunier, 2005). Structural rearrangements occur in the polymers, with the tetrahedra sharing three of the four oxygen atoms to three neighbouring tetrahedra (Figure 13). A lamellar/pseudo-lamellar layer of six hexagonally bonded tetrahedrons forms in a hexagonal symmetry consisting of $6(SiO_3^-)$. In the tetrahedron layer (T), one side is electrically neutral, while the others would be negatively charged due to the apical oxygen (Meunier et al., 2016).

Tetrahedron polymers with covalent bonds were possibly not devitrified, as the bonds would be too strong to break. Comparing the IR data of volcanic ash and bentonite (Figure 6) (3628 cm^{-1}, 1037 cm^{-1}, 781 cm^{-1} and 460 cm^{-1}, Madejová and Kornadel, 2005), the coincidence of the same band in the group of hydroxyl may indicate that the structuring of montmorillonite was inherited from volcanic ash. The bond point would be the tridymite being already organized in a phyllosilicate structure (e.g. Figure 11), formed by hexagonal plane covalent bonds ($6H_2SiO_3$), or similar polymers, which would possibly be the crystalline germination point for other tetrahedrons.

The existence of a negative oxygen charge in the apical vertices of the tetrahedrons allowed tri- and divalent cations, such as Al^{3+} (Ionic radius 0.54 Å), Mg^{2+} (Ionic radius 0.66 Å), Fe^{3+} (Ionic radius 0.64 Å) and Fe^{2+} (Ionic radius 0.74 Å), to be attracted in the quest to annul the negative charges. These elements, as well as possibly also some hydroxyls (e.g. $Al_2(OH)_6$, $Mg_3(OH)_6$, $Fe_3(OH)_6$), underwent isomorphic substitution to form octahedral leaves with a di-octahedral arrangement (two sites occupied in three in the octahedron layer) (Figure 13), in the search for geometric

compatibility with the tetrahedra and taking the energy of the connection to the maximum. Possibly the higher amount of tetrahedra (58.93% SiO_2, Figure 6) compared to the octahedra (19.32% Al_2O_3, 5.47% Fe_2O_3, and 4.09% MgO, Figure 6) would have influenced the fit of the octahedra between two tetrahedral hexagonal leaves, organized in small hexagonal crystalline networks in a unitary block arrangement of type 2:1 tetrahedron-octahedron-tetrahedron (T-O-T). This arrangement formed a sheet similar to a phyllosilicate sheet, however full of defects and intermediate bonds, between ionic and covalent bonds (Figure 13) (McKinley et al., 2003; Worden and Morad, 2003; Meunier, 2005). The water absorbed inside the colloids must have somehow interfered with the ratio of the trivalent and bivalent elements that would constitute the octahedral layer, influencing the entry of bivalent cations. The octahedrons' crystal-chemistry arrangement (monoclinic symmetry) showed parallel cleavage in the basal planes, partially displacing the lower tetrahedron layer about the upper tetrahedron layer (Figure 13).

According to the IR of the Irati bentonite (band 620 cm^{-1} and 522 cm^{-1}; Madejová and Kornadel, 2005) and its structural formula (Figure 6), a small portion of the tetrahedron Al2O33- remained on the tetrahedral leaves (Al^{IV}). However, a large amount became octahedral to compose the octahedral leaves (Figure 6). The IR data (Figure 6) demonstrate that the octahedral sites are occupied mainly by Al2OH oxide (band 916 cm^{-1}), and to a lesser extent, by AlMgOH oxides (band 842 cm^{-1}) and AlFeOH (band 880 cm^{-1}) (e.g. Madejová et al., 2002). The absence of octahedrons in the IR of volcanic ash and the presence in the IR of Bentonite supports this theory of octahedrons' formation.

Connected to the octahedral, the tetrahedral charges were almost completely neutralized. Due to the approximate concentration of 4.25% of Al^{IV} in the tetrahedron (4:0.17, Figure 6), the tetrahedral leaves showed approximately -0.17 per unit cell of load deficiency. On the other hand, the octahedral leaves showed load deficiency due to the isomorphic substitution of different elements that have coordination 6 (e.g. Al^{3+} by Mg^{2+} and/or Fe^{3+} by Fe^{2+}). With Al^{3+} occupying approximately 66% of octahedron sites, Mg^{2+} occupying approximately 20% and Fe^{3+} occupying about 15%. Thus, the octahedral leaves showed approximately -0.34 per unit cell (or half unit formula Si_4O_{10}) of charge deficiency.

The arrangement of the T-O-T phyllosilicate crystals allowed the electric charge unbalance to be transferred to the outer surfaces of the tetrahedra, showing a charge deficiency in the interlayer around -0.51 per unit cell (Figure 6), within the low negative charge characterization of bentonite (-0.3 and -0.6 per unit cell, Figure 8).

Due to high salt concentrations in the environment, cations settled at the T-O-T leaves' interfaces to compensate for the negative charge. Among the possible cations could be monovalent cations (K^+, Na^+ and NH_4^+) and bivalent cations (Ca^{2+} and Mg^{2+}), and adsorbed water (H_3O^+). The monovalent cations would be adsorbed without associated water molecules. However, because the alkaline earth bivalent cations have a high gradient of chemical potential for hydration, they were more proportionally indexed, mainly by Ca^{2+}, which occupied around 86% (Figure 13), carrying water molecules together to the interlayer zone (e.g. Figure 8) (Meunier et al., 2016). There is a possibility that organic molecules may have been installed in the interlayer layer, according to the length of the carbon chain (nc) (e.g. organic molecule $C_xH_{(2x+1)}NH_4^+$; Christidis, 2007).

Bonded by Van der Waals type forces, they formed an interlayer that ensured the T-O-T stability and allowed it to remain thermodynamically stable (Brindley and Brown, 1980; McKinley et al., 2003; Worden and Morad, 2003). This stabilization neutralized the electric charge and allowed the formation of the montmorillonite crystal, the most thermodynamically stable crystalline phases (McKinley et al., 2003; Worden and Morad, 2003; Meunier, 2005).

In the T-O-T layers of montmorillonite, each tetrahedron has a height of around 2.15 Å (Meunier et al., 2016), and each octahedral sheet also has a size of about 2.15 Å. Together, the T-O-T leaves would have around 6.45 Å, and they would be loosely bound to cations in the interlayer that would have the expanding power between 10 Å to 18 Å (Figure 6) (McKinley et al., 2003; Worden and Morad, 2003; Meunier, 2005).

Thus, the crystal-chemistry of montmorillonite would be similar to that of phyllosilicate, however full of defects. The leaves would be able to extend for a few micrometres (Figure 4C), forming hexagonal smectite layers of approximately 4 μm^2. The interlayer's anions also served to aggregate other T-O-T leaves, making it possible for aggregates of T-O-T leaves to form thin flakes of crenulated morphology with the

random habit (Figure 4C). The interlayer storage would never be definitive because the low charge, controlled by Van Der Waals forces, would allow the interlayer cations to be easily exchanged by kinetic exchange reactions with the dissolved cations in the environment in the search for stoichiometric equilibrium when their respective concentrations were higher (e.g. Meunier, 2005; Meunier et al., 2016).

In the process of neomorphism (Worden and Burley, 2003), replacement and recrystallization of the tephra in smectite, a chemical transformation occurred and preserved textural evidence of phantoms from the previous phase consisting of tephra (Figure 4B). One explanation for this process may be that as dissolution reactions followed, permeability and porosity were reduced or eliminated, making fluid percolation difficult. This caused clay "thin-film" rims to be preserved around still unaltered tephras core. The thin film's outer coating acted as a shield, making dissolution extremely slow, in the context of a more closed system, making it possible to form the so-called phantoms textures of a shard (e.g. Suthren, 1985). Observed in the petrographic microscope at a 50 x magnification (Figure 4B), di-octahedral smectite represents the dark-coloured, low-birefringence mass, like films on the phantoms. In contrast, the phantoms show the white colouration of high birefringence micaceous habit and laminar morphologies, platy-like shapes (Mcphie et al. 1993) and sometimes preserves the Y shape of some tephras (e.g. Ross, 1928; Lowe, 2008; Beerbaum, 2018). The phantom fabric's arrangement, texturally oriented in two directions (Figure 4A), indicates that the deposition was possibly disoriented and originally not welded. An apparent orientation of the phantoms may have been induced later through mechanical compaction.

Once the smectite was formed, the low entropy conditioned equilibrium for about 275 Ma, between the PFD and the conditions imposed in the lithosphere by the plate tectonics' changes, demonstrating long-term thermodynamically stable phases in the exogenous environment. Chemically (Figure 6), the bentonite matches literature bentonite (Fisher and Schmincke, 1984), containing between: 55 to 75% SiO_2; 15-25% Al_2O_3; about 5% Fe_2O_3; about 3% MgO; K_2O and Na_2O usually <1%, with $[K_2O]>[Na_2O]$. However, bentonite's chemical values usually show variations due to interlayer elements and the low presence of other minerals, such as authigenic and detritic magmatic. Comparing the geochemical data of volcanic ash and bentonite (Figure 6), there is incorporation Al^{3+} and alkaline earth (e.g. Mg^{2+} and Ca^{2+}), and significant

leaching of other ions, mainly Si^{4+} and alkalis (e.g. Na^{+}, K^{+}). The reason for the gain of Mg (Ionic radius 0.66 Å), and loss of K (Ionic radius 1.51 Å) and Na (Ionic radius 0.97 Å) may be due to radius size. Ions with larger radii tended to stay in solution as more water molecules hydrated them. Grim and Güven (1978) propose that the absorption of Mg^{2+} may have come from solutions or from the tephra itself, in a feedback condition, with the leaching of alkalis and subsequent incorporation, in a search for thermodynamic equilibrium.

The tonality of the facies reflects the chemical and mineralogical composition. Thus the presence of alkaline/alkaline earth elements in the interlayer, mainly by Ca^{2+}, and to a lesser extent K^{+}, Mg^{2+}, conditioned its greenish to yellowish colour (Figure 2B). Changes in these ratios can vary the colours of other PFDs. The presence of alkaline/alkaline earth elements generally forms light colours, such as brown, green, yellow, brown, and pink. In contrast, transition elements, particularly iron and organic matter, can form PFDs of dark to medium brown colouration (Jerram and Petford, 2014).

4.3. TONSTEIN RIO BONITO, south Brazil

The volcanic ash that formed the tonstein occurred during the Cisuralian (early Permian), originating from volcanic events in the Choiyoi volcanic province (Rocha-Campos et al., 2011; Limarino et al., 2013) and ash was transported for several kilometres away. These are deposited on the eastern margin of the Paraná Basin (the Rio Grande do Sul State) in a paludal sub-aerial environment (e.g. Guerra-Sommer et al., 2008; Dai et al., 2020). The oxidizing environment of the Rio Bonito Formation was freshwater, containing low salinity (e.g. Na^{+}), acid-neutral pH (pH $\leqq$ 7), low depositional energy, low detrital input and rapid burial (Guerra-Sommer et al., 2008). The Faxinal PFD (FAX) originated from rhyodacite/dacite to trachyandesite volcanism (Formoso et al. 1997; Alessandretti et al. 2013) and has a numerical age of 286.52 ± 0.30 Ma (MSWD = 1.15) (Griffis et al., 2018), being also an $NCE_{c\ V3}$ type PFD (Zuffa, 1980; 1985;

1987) of provenance from the volcanic events of Choiyoi Province (Rocha-Campos et al., 2011).

The first hydration reactions, hydrolysis and devitrification, occurred similarly to the situation described for volcanic ash and bentonite, converging to an intermediate hydrated aluminosilicate gel (Figure 14) (Eberl and Hower, 1975). The deposition of PFD associated with organic matter, such as plant fragments, showed interactions with moderately acidic fluids, with organic compounds present acting as catalysts (e.g. CO_2) (e.g. Worden and Burley, 2003; Spears, 2012).

As observed in the volcanic ash PFD, there is no presence of octahedrons in the tephras' crystal-chemical arrangement (Figure 6), thus forming during the post-depositional alteration. However, it is not defined at what point in the post-depositional alteration the octahedrons are formed, which may have been developed during the intermediate phase of hydrated aluminosilicate gel or during a possible smectitization phase (Bohor and Triplehorn, 1993; Meunier, 2005).

In a second moment, the kaolinization processes of the PFD occur due to high entropy conditions of the PFD with the environment. These processes possibly occurred contemporaneously with the organic matter's bacterial degradation phase or in a more advanced burial situation where the peat early diagenesis phase begins to be converted into lignite (Figure 14). The bacterial actions of decomposition of organic matter, or its maturation, expelled gases (CO_2, CH_4) and organic acids (fluvic and humic), generating acidic fluids (for pH 5-4.7) that acted as catalysts (e.g. Bohor and Triplehorn, 1993; Spears, 2012; Dai et al., 2017).

In the kaolinization process, the acids acted by chemical diffusion as catalytic organic leaching ligands (e.g. CO_2, H_2S, CH_4, $NaHCO_3$, SO_4^-, and HCO_3^-), causing intense leaching processes of silica, water, and cations (Eberl and Hower, 1975; Bohor and Triplehorn, 1993; Meunier, 2005). In aluminosilicate gel and/or smectite, acids leached all interlayer ion bases (e.g. Mg2+, Ca2+, Na+ and K+) portion of the octahedra constructed by Mg^{2+} and $Fe^{2+/3+}$ and part of the tetrahedron excesses. The carbonic acid (HCO_3^-) may have been one of the main agents that helped in the process since it formed from the reaction of CO2 with water. It has a pH of about 5.7 (Figure 14), making it a strong binding solvent:

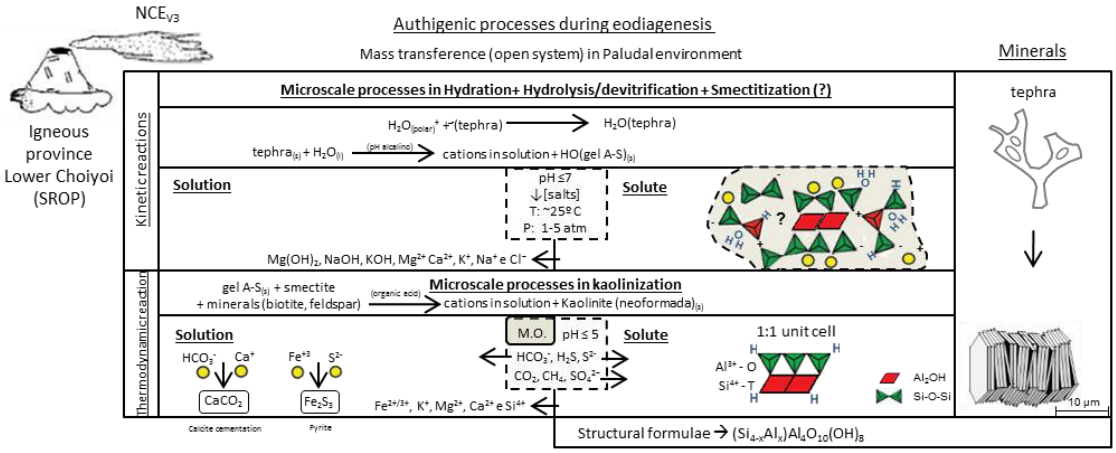

Figure 14 – A synthesis of the general controls on the transformation activity in early diagenesis of tephra to kaolinite in PFDs, as described in this paper. Interpreted diagenetic minerals are based on petrography, SEM, XRD, IR, XRF and Formula units, data and clay beds.

Carbonic acid formation: $CO_2 + 2H_2O \rightarrow HCO_3^- + H_3O^+$

Kaolinization process: $HCO_3^- + H_3O^+$ + -Si-O-Si-O-Al-O-Ca-H -> -Si-O-Si-OH + HO-Al-OH + $CaCO_{2\ (Calcite)}$ + H_2O

Leaching promoted the new formation of the PFD, and the kaolinite crystal (T-O) (Figure 14) ended up being the only inert to chemical attacks, as identified in XRD and IR (Figure 6) (e.g. Eberl and Hower, 1975; Bohor and Triplehorn, 1993; Meunier, 2005). In the Rio Bonito tonstein, the kaolinite formed contains in the tetrahedron a sequence of SiO_2 and a low proportion of Al_2O_3, according to IR data. The octahedron, on the other hand, consists mainly of Al_2O_3 (Figure 6).

Petrography demonstrates the heterogeneity of the tonstein, a characteristic also observed in other works (e.g. Fisher and Schmincke, 1984; Bohor and Triplehorn, 1993; Worden and Morad, 2003; Spears, 2012; Dai et al., 2017; Shen et al., 2021). The recrystallization caused at least three generations of kaolinite:

I. An aggregate of pseudo-hexagonal kaolinite platelets forming elongated stacks with vermicular habit curves called vermicules (or vermiform kaolinite; Figure 14), ranging in diameter from 0.1 µm to 3µm and can grow to a relatively large size (1-3 mm) (Figure 5A).

II. A pseudomorphosis of substituted siliciclastics minerals for kaolinite aggregates, taking advantage of their shapes. Like a feldspar, observable by the "square" shape and straight contact (Figure 5B), or mica, observable by the butterfly-like vermicular texture (Figure 18B).
III. Microcrystalline kaolinite that would have replaced a fine-grained matrix of probable tephras constitution.

The IR data (Figure 6) and its texture in the SEM (Figure 5C), show that kaolinite presents pseudo-hexagonal platelets, not evolving to its polytypes such as dickite, halloysite and/or nacrite (e.g. Madejová, 2003; Worden and Morad, 2003). The purity and high degree of crystallinity of the kaolinite shown in the XRD and IR analyses (Figure 6) show its autochthonous origin (Bohor and Triplehorn, 1993). Also, the presence of fragile vermicular kaolinites demonstrate their authigenic origin and that they were formed in situ by chemical or biochemical processes, the near fragment of phytoclasts that were probably sources of organic acids (Figure 5A) (Bohor and Triplehorn, 1993). The existence of pseudo-hexagonal platelets with a di-octahedral arrangement in both kaolinite and smectite (Meunier, 2005; Meunier et al., 2016), makes it possible to assume that the recrystallizations in kaolinite that formed elongated stacks (vermicules) have smectite as intermediate mineral (e.g. Figure 4C), where the leaching of the pseudo-hexagonal T-O-T leaves by acids has promoted the organization (Figure 5C), as well as recrystallization (neoformation) and growth of the T-O leaves, stacking them through Van Der Waals bonds.

Comparing the geochemical composition of this tonstein with volcanic ash and bentonite (Figure 6), the significant increase in Al_2O_3 is evident, which indicates mass transfer to the environment during the tonstein transformation. Chemically, tonsteins contain approximately: less than 50% SiO_2; 20-40% Al_2O_3; <1% MgO; 0.5-4% Fe_2O_3; <0.5% Na_2O; 0.2-2% K_2O and highly variable amounts of CaO and P_2O_5 (Fisher and Schmincke, 1984). The valence charge of the T-O of kaolinite is zero, and the Al_2O_3:SiO_4 ratio is 1:1, requiring no other charge to balance the structure with the general chemical formula: $Al_4Si_4O_{10}(OH)_8$. Thus, the geochemical data show low values of Na (nd), K (0.03%), Fe (0.86%) and Mg (0.29%) (Figure 6). The Al2O3: SiO4 ratio being around 1: 1.5 (Figure 6), as well as the low amount of other elements (Fe_2O_3, Na_2O, K_2O and MgO), may represent contributions from elements of other minerals that

may occur, such as phosphates, carbonates and organic matter (Figure 15) (e.g. Fisher and Schmincke, 1984). The Ca value of around 2.23% may be due to the presence of authigenic carbonate (Figure 15), just as Fe may represent the ferric iron contained in authigenic pyrites.

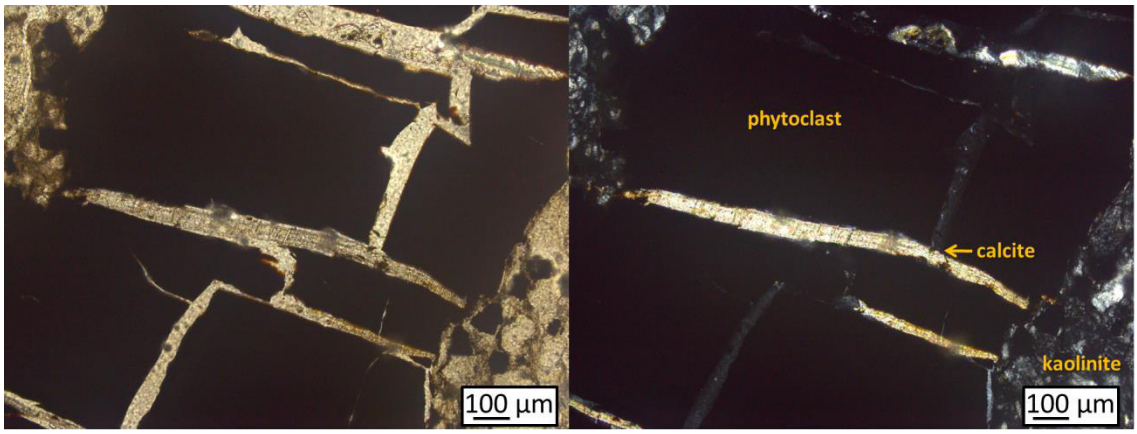

Figure 15 – (A) to (B) 10x magnified photomicrograph showing precipitated authigenic carbonate as cement between phytoclast fragments. Calcite (Cal).

The decomposition of organic matter by activities of sulfate-reducing bacteria mainly released CO_2, but also released powerful sulfur leaching acids (H_2SO_3, H_2SO_4 and SO_4^{2-})). The reducing microenvironment provided by the consumption of O2- by the decomposition of organic matter transformed ferrous iron (Fe^{2+}) accumulated in oxides and ferromagnesian minerals (e.g. biotite, smectites) into ferric iron (Fe^{3+}). Thus ferric iron showed solubility amenable to migration by diffusion to microenvironments to form sulfides, such as Fe^{3+} to form pyrite (FeS_2) (Figure 16) (Curtis, 1977; Fisher and Schmincke, 1984; Bohor and Triplehorn, 1993).

Environmental conditions with low salinity along with the removal of elements from the system (K^+, Na^+, Si^{4+}, Mg^{2+} and Fe^{2+}), were essential factors to keep the medium within the stability field of monomineralic kaolinite (Figure 14), because having ionic concentrations, kaolinite could not be stable (Fisher and Schmincke, 1984; Spears, 2012). The permanence of the Si^{4+} in tetrahedrons and Al^{3+} of the octahedron is exposed to kaolinite natural white hue (Bohor and Triplehorn, 1993) in the PFD

deposited between dark coal layers (Figure 2C). However, PFD deposited amidst this environment can also exhibit brown, grey, or black hues (Bohor and Triplehorn, 1993).

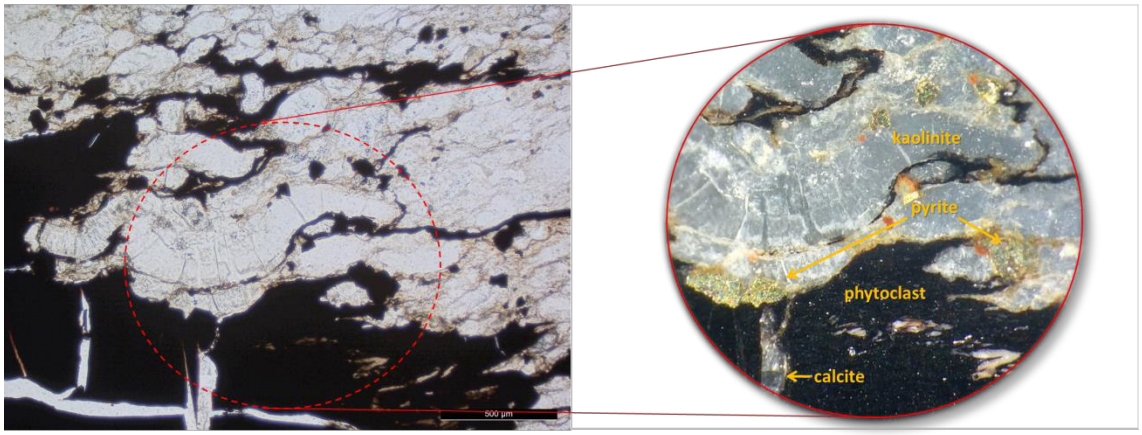

Figure 16 - Thin-section optical photomicrographs (open) (5x magnification) showing euhedral pyrites at the centre. They are recorded in photomicrography in binocular streomicroscope with 80 times magnification.

4.4. MAGMATIC MINERALS

In the Irati bentonite, magmatic minerals that originally formed directly in the magma chamber and resisted the alteration processes were dispersed in the clay matrix (Figure 17). These minerals tend to resist post-depositional alteration for long periods of time because they are crystals (Bohor and Triplehorn, 1993). The characterization of magmatic minerals is described by De Rosa et al. (1986), Bohor and Triplehorn (1993) and Spears (2012). Stand out among these minerals, the zircons (elongated prism with idiomorphic euhedral and bipyramidal features), apatite, biotite, quartz (β-quartz), feldspar (sanidine and plagioclase), ilmenite, magnetite, rutile, sphene (titanite), allanite and/or the amphibole (Fisher and Schmincke, 1984; Bohor and Triplehorn, 1993; Meunier, 2005; Spears, 2012; Huff, 2016; Silva et al., 2017).

Typical physical characteristics that attest to the volcanic origin is the tendency to be well selected, with size typically less than 300 μm (<average sand) (e.g. ash; Figure 1; Table 1), idiomorphic habit (euhedral), without the evidence of alteration or having

undergone transport and sedimentary reworking processes. There may also be fractured and/or broken minerals, called splinters (Jerram and Petford, 2014; Huff, 2016). These characteristics classify these minerals as coming from distal volcanic ash, in agreement with other works and from observations elsewhere (Pupin, 1980; Fisher and Schmincke, 1984; Bohor and Triplehorn, 1993; Spears, 2012).

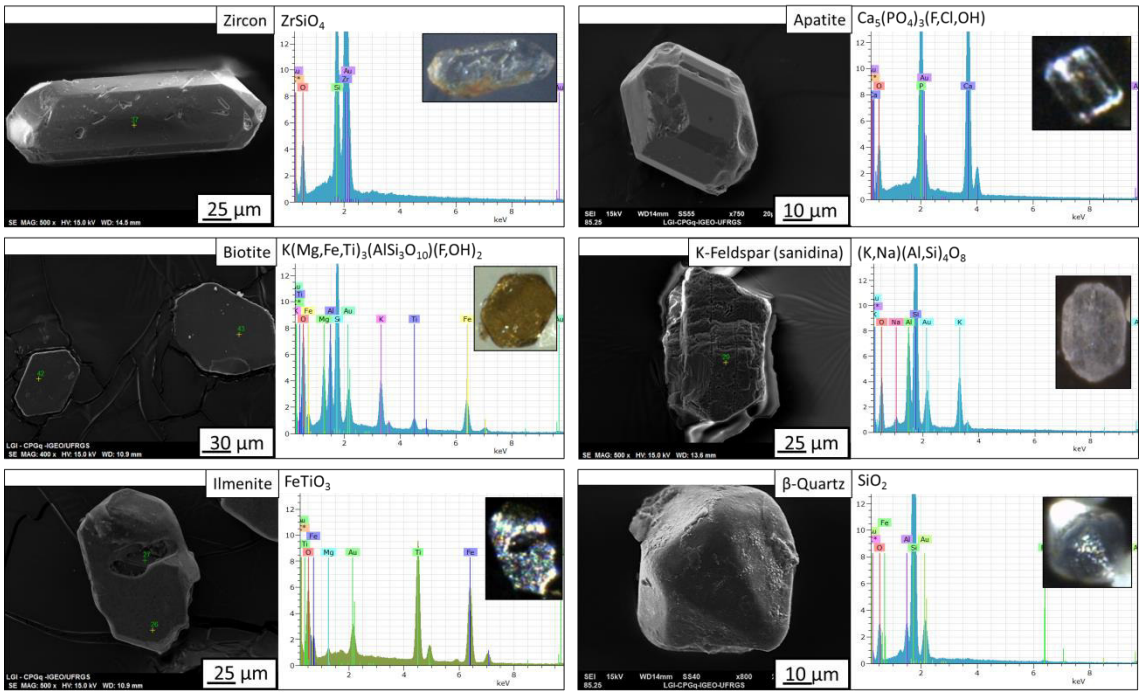

Figure 17 - Different magmatic minerals recognized in the bentonite PFD, recorded in binocular streomicroscope photomicrographs at 80 times magnification, secondary electron images in SEM (right) and chemical composition obtained by EDS. Other PFDs are likely to have the same euhedral mineral characteristics.

Depending on the post-depositional reaction processes, some minerals can be reactive. This is the case for biotite, which is inert during the smectitization process (Figure 18A) and reactive during the kaolinization process (Figure 18B). In the case of the kaolinization process, acid attacks in stabilize anhydrous (e.g. k-feldspar) and hydroxylated (e.g. micas and amphibole) magmatic minerals, mainly ferromagnesian (e.g. biotite), causing pseudomorphic replacement by complete recrystallization into kaolinite (Figure 18B) and leaching of elements (e.g. K^+, Ca^{2+}, Mg^{2+} and $Fe^{2+/3+}$) (Bohor and Triplehorn, 1993; Worden and Burley, 2003; Meunier, 2005; Spears, 2012). Due to

its susceptibility to acid dissolution, other minerals, such as apatite, are usually absent in tonsteins. Other minerals remain insoluble, such as zircon (Figure 18C).

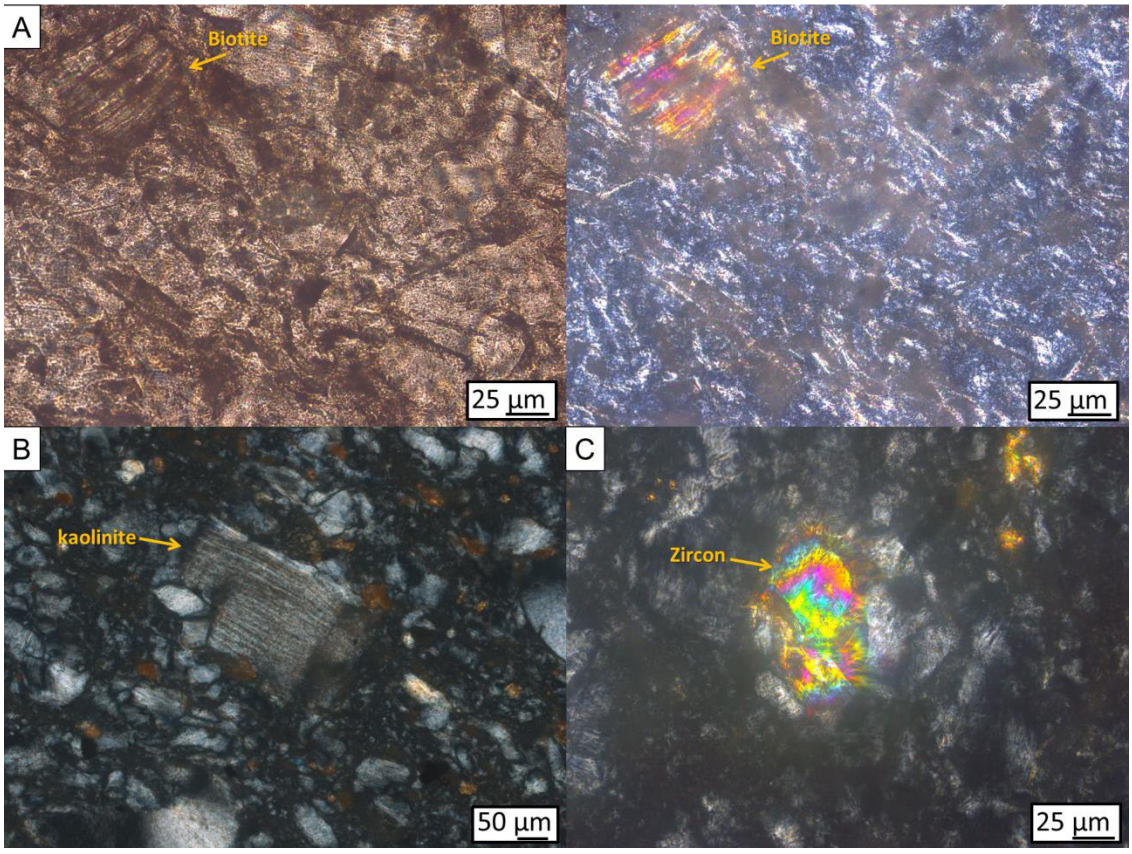

Figure 18 - (B) Photomicrograph 20x magnification showing pseudomorphic replacement of magmatic minerals by kaolinite (e.g. biotite; k-feldspar) (C) Photomicrograph 50x magnification demonstrating the preserved zircon grain.

These minerals are important because, while tephras can be affected by transport, deposition, environmental and post-depositional processes, magmatic minerals are independent of these processes, remaining with their closed crystalline-chemical system (Hanchar and Hoskin, 2003). Thus these minerals can bear direct chemical and isotopic signatures of magmatism. Identification of these signatures can be made through I) assemblages of magmatic minerals, II) mineral chemistry, and III) isotopic analysis of individual magmatic grains (Figure 1) (Potter et al., 2005; Ddani et al., 2005; Huff, 2016).

5. CONCLUSIONS

PFDs undergo complex evolutions involving different processes, such as tectonic (e.g. geotectonic environment and magmatic generation of crustal or mantle melt), volcanic (e.g. magmatic differentiation and type of volcanism event), autoclastic (e.g. mechanical breakdown during magma movement), pyroclastic (e.g. air transport and deposition), environmental (e.g. deposition, preservation, re-deposition and leaching) and post-depositional (e.g. diagenetic alteration and neoformation) (e.g. Fisher and Schmincke, 1984; Lajoie and Stix, 1992; Orton, 1996).

This article characterized and quantified in different methodologies and analytical techniques three PFDs, one in situ tephra (volcanic ash) and two tuffs (bentonite and tonstein). The qualitative petrographic and SEM descriptions were used to identify mineral phases and their relationships, searching for textural and mineralogical identification of the constituents of the PFDs. The joint XRD and IR analyses provided the crystal-chemical characteristics to understand the nucleation and crystallization processes better. The XRF quantitative chemical analysis provided identification of the chemical compositions of major and minor elements, used for the recognition of structural formulas and comparisons between PFDs. The magmatic minerals dispersed in the bentonite PFD clay mass were separated by the method of concentration of resistant minerals, being necessary for establishing the provenance of the PFDs themselves. Thus we got analytical answers necessary for a systematic characterization study at each PFD level (e.g. Zuffa 1987).

The analytical results obtained showed that while the volcanic ash showed an amorphous characteristic, the bentonite showed a dioctahedral montmorillonite composition and the tonstein showed a kaolinite dioctahedral composition.These different mineralogical compositions define their appearance for sedimentary facies. The comparison between them demonstrates that field identification of tuffs can be hindered by post-depositional processes. However, they preserve their layer characteristics with abrupt contact and some of the magmatic minerals.

We present a model of how high-temperature kinetic reactions occur in endogenous volcanic and pyroclastic processes informing the primary constituents of

PFDs (disorder, high entropy). The tephras grains formed to represent the magmatic disorder cooled to the solid-state. Subsequently, we discussed its exogenous weathering processes in the physical-chemical conditions of the environment, entropic exchanges by chemical weathering in an open system condition, migrations between chemical elements at low temperature (disorder, high entropy), up to the thermodynamic equilibrium condition for crystal-chemical recrystallization (order, low entropy) in the post-depositional (early diagenesis) processes of smectitization and kaolinization.

At the end of the discussion on each PFD formation, crystal-chemistry reconstruction was used to characterize the texture and faciologic hue described in the field. Comparison of recent and old PFDs is one of the techniques of facies model constructions (e.g. Walker and James, 1992; James and Dalrymple, 2010; Miall, 2016). Thus, it is hoped that these three described PFDs could serve as an essential model and guide for stratigraphers for in-field faciologic recognition of in situ and altered PFDs. It will lead to new discoveries of PFDs in sedimentary sequences (e.g. Zuffa 1987). Their magmatic minerals, by radioisotope geochronology (or radiometric dating), have the ability to calibrate events in Earth's history for a numerical time and provides a numerical age framework for the geologic time scale, being important for Chronostratigraphy geochronometric (Figure 1). The PFD is integral to the practice of time scale construction. The more PFDs identified, the more they will add geochronological dates to chronostratigraphic interpretations of a sedimentary unit's geological history, a geological period, and a paleogeographic region.

ACKNOWLEDGEMENTS

The authors thank the National Council for Scientific and Technological Development (CNPq) for financial support (process 140596 / 2016-0), and the Programa de Pós-graduação em Geociências at UFRGS (PPGGeo-UFRGS), for the research infrastructure made available to the project and the technicians from UFRGS laboratories.

REFERENCES

Alan, P.D., 2018. Radiogenic Isotope Geology, 3 ed. Cambridge University Press. United Kingdom: p.99-133. Doi: 10.1017/9781316163009.

Alessandretti, L., Philipp, R.P., Chemale, F., Brückmann, M.P., Zvirtes, G., Metté, V., Ramos, V.A., 2013. Provenance, volcanic record, and tectonic setting of the Paleozoic Ventania Fold Belt and the Claromecó Foreland Basin: implications on sedimentation and volcanism along the southwestern Gondwana margin. Journal of South American Earth Sciences. 71 pp.

Araújo, L.M., 2001. Análise da expressão estratigráfica dos parâmetros de geoquímica orgânica e inorgânica nas sequências deposicionais Irati. PhD Thesis, Instituto de Geociências, Universidade Federal do Rio Grande do Sul, 2 v., 307 pp.

Araújo, L.M., Rodrigues, R., Scherer, C.M.S., 2004. Interrelação entre a fábrica sedimentar, o conteúdo orgânico e o potencial redox do ambiente deposicional, deduzida das litofácies de rampa distal das seqüências deposicionais da Formação Irati, Permiano da Bacia do Paraná. Boletim de Geociências da Petrobras, 12(2), 429-434.

Arzadún, G., Tomezzoli, R.N., Trindade, R., Gallo, L.C., Cesaretti, N.N., Calvagno, J.M., 2018. Shrimp zircon geochronology constrains on Permian pyroclastic levels, Claromecó Basin, South West margin of Gondwana, Argentina. Journal of South American Earth Sciences. v.85. p.191–208. https://doi.org/10.1016/j.jsames.2018.05.001.

Bastos, L.P.H., Rodrigues, R., Pereira, E., Bergamaschi, S., Alferes, C.L.F., Augland, LE, Domeier, M., Planke, S., Svensen, H.H., 2021. The birth and demise of the vast epicontinental Permian Irati-Whitehill sea: Evidence from organic geochemistry, geochronology, and paleogeography. Palaeogeography, Palaeoclimatology, Palaeoecology, 562, 1-13 110103. https://doi.org/10.1016/j.palaeo.2020.110103.

Beerbaum, C.T., 2018. Characterization of glasses in volcanic ash soils in El Ángel, Ecuador (Bachelor thesis). University of Cologne, Institute of Geography. p. 65.

Boggs, S.Jr. (Ed.), 2014. Principles of Sedimentology and Stratigraphy. British Library Cataloguing-in-Publication Data. 5th, p. 434-474.

Bohor, B.F. and Triplehorn, D.M., 1993. Tonsteins: altered volcanic-ash layers in coal-bearing sequences. Geological Society of America Special Paper, 285, 1-44.

Brindley, G.W. and Brown, G., 1980. Crystal structures of clay minerals and their X-ray identification. Mineralogical Society Monograph, 5, 495pp.

Brookins, D.G., 1988. Eh-pH diagrams for geochemistry, Springer-Verlag New York, 176pp.

Calas, G., Henderson, G.S., Stebbins, J.F., 2006. Glasses and Melts: Linking Geochemistry and Materials Science. Elements, 2, 265–268.

Cas, R.A.F., Wright, J.V., 1987. Volcanic Successions Modern and Ancient: a geological approach to processes, products and successions. In Volcanic Successions Modern and Ancient: a geological approach to processes, products and successions. Allen & Unwin. 528p.

Chamley, H., 1989. Clay Sedimentology. Springer-Verlag, Berlin. pp. 623.

Christidis, G., 2007. Layer Charge and Charge Distribution of Smectites: a Parameter Which Controls Important Physical Properties of Bentonites. Bulletin of the Geological Society of Greece, 40(2), 690-699. doi:http://dx.doi.org/10.12681/bgsg.16357.

Cível, B., Komadel, P., 1994. Structural formulae of layer silicates, in: Quantitative Methods in Soil Mineralogy. In: J.E. Amonette and L.W. Zelazny (Eds.) Soil Science Society of America Miscellaneous Publication, Madison, WI, Soil Science Society of America, pp. 114-136.

Costa, J.E., Schuster, R.L., 1988. The formation and failure of natural dams. Geological Society of America Bulletin, 100, 1054–1068. Doi: 10.1130/0016-7606(1988)100<1054:tfafon>2.3.co;2

Critelli, S., Ingersoll, R.V., 1995. Interpretation of neovolcanic versus paleovolcanic sand grains: an example from Miocene deep-marine sandstone of the Topanga Group (Southern California), Sedimentology, 42, 783-804.

Curtis, C.D., 1977. Sedimentary geochemistry: environments and processes dominated by involvement of an aqueous phase. Philosophical Transactions of the Royal Society, London, 286, 353–372.

Dai, S.C.R., Ward, I.T., Graham, D., French, J.C., Hower, L., Zhao, X., Wang, X., 2017. Altered volcanic ashes in coal and coal-bearing sequences: a review of their nature and significance. Earth-Science Reviews, 175, 44-74.

Dai, S., Bechtel, A., Eble, C.F., Flores, R.M., French, D., Graham, I.T., Hood, M.M., Hower, J.C., Korasidis, V.A., Moore, T.A., Püttmann, W., Wei, Q., Zhao, L., O'Keefe, J.M.K., 2020. Recognition of peat depositional environments in coal: a review. International Journal of Coal Geology. v.219, p.67. 103383.

Ddani, M., Meunier, A., Zahraoui, M., Beaufort, D., EL Wartiti, M., Fontaine, C., Boukili, B., EL Mahi, B., 2005. Clay mineralogy and chemical composition of bentonites from the Gourougou volcanic massif (northeast Morocco). clays and clay minerals, v. 53, p. 250-267.

De Rosa, R., Zuffa, G.G., Taira, A., Leggett, J.K., 1986. Petrography of trench sands from the Nankai Trough, southwest Japan: implications for longdistance transportation: Geological Magazine. 123, 477-486.

Eberl, D.D., Hower, J., 1975. Kaolinite synthesis: the role of Si/al and (alkali)/(H+) ratio in hydrothermal systems. Clays Clay Miner, 23, 301–309.

Einsele, G., Seilacher, A. (Ed.), 1982. Cyclic and Event Stratification. Springer-Verlag, Berlin, 536 pp.
Einsele, G., Chough, S.K., Shiki, T., 1996. Depositional events and their records-an introduction. Sedimentary Geology, 104, 1-9.
Fisher, R.V., 1961. Proposed classification of volcaniclastic sediments and rocks. Geological Society of America Bulletin, 72(9), 1409-1414.
Fisher, R.V., Schmincke, H.U., 1984. Pyroclastic Rocks. Springer–Verlag, Berlin. 472 pp.
Formoso, M.L.L., Calarge, L.M., Garcia, A.J.V., Alves, D.B., Gomes, M.B., Misusaki, A.M., 1997. Permian tonsteins from the Paraná Basin, Rio Grande do Sul, Brazil. 11th Clay Conference, Otawa: Proceedings, pp. 613–621.
Gill, R., 2015. Chemical Fundamentals of Geology and Environmental Geoscience. Ed.3., Wiley, hichester-UK, p.267.
Govindaraju, K., 1994. Compilation of working values and sample description for 383 geostandards. Geostandards Newsletter, 18, 1-158.
Gradstein, F.M., Ogg, J.G., Schmitz, M.D., Ogg, G.M., (Eds.). 2012. The Geologic Time Scale 2012. Amsterdam: Elsevier, pp.1176.
Gradstein, F.M., Ogg, J.G., Schmitz, M.D., Ogg, G.M., (Eds.). 2020. The Geologic Time Scale 2020. 2v. Boston, Elsevier, pp.1400. DOI:https://doi.org/10.1016/C2020-1-02369-3.
Griffis, N.P., Mundil, R., Montañez, I.P., Isbell, J., Fedorchuk, N., Vesely, F.F., Iannuzzi, R., Yin, Q.Z., 2018. A newstratigraphic framework built on U-Pb single-zircon TIMS ages and implications for the timing of the penultimate icehouse (Paraná Basin, Brazil). Geological Society of America Bulletin, 130, 848–858.
Grim, R.E., Güven, N., 1978. Bentonites - geology, mineralogy, properties, and uses. Developments in Sedimentology, n.24, Earth-Science Reviews. p.256.
Guerra-Sommer, M., Cazzulo-Klepzig, M., Menegat, R., Formoso, M.L.L., Basei, M.A. S., Barboza, E.G., Simas, M.W., 2008. Geochronological data from the Faxinal coal succession, southern Parana Basin, Brazil: A preliminary approach combining radiometric U-Pb dating and palynostratigraphy: Journal of South American Earth Sciences, 25(2), 246-256. Doi:https://doi.org/10.1016/j.jsames.2007.06.007.
Henderson, G.S., 2005. The structure of silicate melts: a glass perspective. Canadian Mineralogist, 43, 1921-1958.
Henderson, G.S., Calas, G., Stebbins, J.F., 2006. The Structure of Silicate Glasses and Melts, Elements, 2, 269–273.
Hermanns, R.L., Schellenberge, A., 2008. Quaternary tephrochronology helps define conditioning factors and triggering mechanisms of rock avalanches in NW Argentina. Quaternary International, 178, 261–275.
Hermanns, R.L., Trauth, M.H., Niedermann, S., McWilliams, M., Strecker, M.R., 2000. Tephrochronologic constraints on temporal distribution of large landslides in northwest Argentina. Journal of Geology, 108, 35–52.
Huff, W.D., 2016. K-bentonites: A review. American Mineralogist, 101, 43–70.
Jaffey, A.H., Flynn, K.F., Glendenin, L.E., Bentley, W.C. Essling, A.M., 1971. Precision measurement of the half-lives and specific activities of U235 and U238. Physical Review, C 4, 1889–1907.
James, N.P., Dalrymple R.W., (Ed.), 2010. Facies Models 4. GEOtext 6. Geological Association of Canada. p.3-18.
Jerram, D., Petford, N., 2014. Descrição de rochas ígneas: Guia geológico de campo. 2ª ed. Trad. Ana Maria Pimentel Mizusaki, Rualdo Menegat. Porto Alegre: Bookman, 280 p. (in Portuguese).
Hanchar, M.J., Hoskin, W.O.P., (Ed.), 2003. Zircon. Reviews in Mineralogy and Geochemistry, 53, 500. doi:https://doi.org/10.2113/0530001a.
Lajoie, J., Stix, J., 1992. Volcaniclastic Rocks. In: Facies Models: Response to Sea-level Change (Ed. by Walker R.G. and James N.P.), Geological Association of Canada., Waterloo, Ontario. pp. 101-118.
Limarino, C.O., Césari, S.N., Spalletti, L.A., Taboada, A.C., Isbell, J.L., Geuna, S., Gulbranson, E.L., 2013. A paleoclimatic review of southern South America during the late Paleozoic: a record from icehouse to extreme greenhouse conditions. Gondwana Research, 25(4), 1396–1421.
Lowe, D.J., 2008. Globalization of tephrochronology: new views from Australasia. Progress in Physical Geography, 32(3), 311–335. Doi: 10.1177/0309133308091949
Madejová, J., Keckes, J., Palkova, H., Komadel, P., 2002. Identification of components in smectite/kaolinite mixtures. Clay Minerals, 37, 377–388. Doi: 10.1180/0009855023720042
Madejová, J., 2003. FTIR techniques in clay mineral studies. Vibrational Spectroscopy, 31, 1–10.
Madejová, J., Komadel, P., 2005. Information available from infrared spectra of the fine fraction of bentonites. In: The Application of Vibrational Spectroscopy to Clay Minerals and Layered Double Hydroxides, CMS Workshop Lectures (Klopproge, J.T., Ed.). The Clay Mineral Society: Aurora, CO, USA, pp.65–98.
Matos, S.A., Warren, L.V., Varejao, F.G., Assine, M.L., Simões, M.G., 2017. Permian endemic bivalves of the ‘‘Irati anoxic event”, Paraná Basin, Brazil: Taphonomical, paleogeographical and evolutionary implications. Palaeogeography, Palaeoclimatology, Palaeoecology, 469, 18–33.
Mattinson, J.M., 2000. Revising the “gold standard”, the uranium decay constants of Jaffey, et al., 1971. EOS (Transactions, American Geophysical Union) 81, S444.
McKinley, J.M., Worden, R.H. Ruffell, A.H., 2003. Smectite in sandstones: a review of the controls on occurrence and behaviour during diagenesis. In: Clay Mineral Cements in Sandstones (Ed. by R.H. Worden and S. Morad). International Association of Sedimentologists Special Publication, Blackwell Publishing, Oxford, 34, 109–128.
McPhie, J., Doyle, M., Allen, R., (Ed.), 1993. Volcanic Textures. A guide to the interpretation of textures in volcanic rocks. Centre for Ore Deposit and Exploration Studies, University of Tasmania, 198 p.
Meunier, A., 2005. Clays. Berlin: Springer-verlag, p.472.
Meunier, A., Mexias, A.S., Bortoluzzi, E.D., 2016. O Mundo das Argilas. Editora da UFRGS, p.256. (book in Portuguese/French).

Miall, A.D., 2016. Stratigraphy: A Modern Synthesis. University of Toronto, Springer. p.311-370. Doi:10.1007/978-3-319-24304-7.

Mohriak, W., Szatmari, P., Anjos, S.M.C., 2008. Sedimentação de evaporitos. In:. Sal. Geologia e Tectônica, (eds: Mohriak W., Szatmari P., Anjos S.M.C.). São Paulo: Beca Edições. p. 65-88. (book in Portuguese)

Mørk, M.B.E., Leith D.A., Fanavoll, S., 2001. Origin of carbonate-cemented beds on the Naglfar Dome, Vøring Basin, Norwegian Sea. Marine and Petroleum Geology, 18, 223-234.

Murphy, M.A. and Salvador M., 1999. International Stratigraphic Guide — An abridged version. Episodes, Vol. 22(4), 255-272.

NACSN (North American Stratigraphic Code), 2005. North American stratigraphic code. American Association of Petroleum Geologists Bulletin, 89, 1547-1591.

Ogg, J.G., Ogg, G., Gradstein, F.M., 2016. A Concise Geologic Time Scale: 2016. Elsevier, Amsterdam 240 pp.

Orton, G.J., 1996. Volcanic environments. In: Sedimentary Environments: Processes, Facies and Stratigraphy, 3rd ed (Ed. by Reading, H.G.), Blackwell Publishing, 485-567.

Potter, P.E., Maynard, J.B., Depetris, P.J., 2005. Mud and Mudstone: Introduction and Overview. Berlin: Springer

Pupin, J.P., 1980. Zircon and granite petrology. Contributions to Mineralogy and Petrology, 73, 207-220.

Randall, J.T., Rooksby, H.P. Cooper, B.S., 1930. X-ray diffraction and the structure of vitreous solids. Z. Kristallogr, 75, 196-214.

Reading, H.G., 1996. Sedimentary Environments: Processes, Facies and Stratigraphy. 3rd Edition, Blackwell, Oxford, 689 p.

Reiners, P.W., Carlson, R.W., Renne, P.R., Cooper, K.M., Granger, D.E., McLean, N.M., Schoene, B., 2018. Geochronology and Thermochronology. John Wiley & Sons. p.39-82. ISBN: 978-1-118-45578-4

Rocha-Campos, A.C., Basei, M.A., Nutman, A.P., Kleiman, L.E., Varela, R., Llambias, E., Canile, F.M., Rosa, O.C.R., 2011. 30 million years of Permian volcanism recorded in the Choiyoi igneous province (W Argentina) and their source for younger ash fall deposits in the Paraná Basin: SHRIMP U-Pb zircon geochronology evidence. Gondwana Research, 19, 509–523.

Rocha-Campos, A.C., Basei, M.A.S., Nutman, A.P., Santos, P.R., Passarelli, C.R., Canile, F.M., Rosa, O.C.R., Fernandes, M.T., Santa Ana, H., Veroslavsky, G. 2019. U-Pb Zircon Dating of Ash Fall Deposits from the Paleozoic Paraná Basin of Brazil and Uruguay: A Reevaluation of the Stratigraphic Correlations. The Journal of Geology. 127, 167–182.

Ross, C.S., 1928. Altered Palaeozoic volcanic materials and their recognition. American Association Petrological Geology Bulletin, 12, 143-164.

Ryan, P., 2019. Environmental and Low-Temperature Geochemistry-Ed2. Wiley-Blackwell Ltd. p.376. ISBN 978-1-119-56861-2

Santos, R.V., Souza, P.A., de Alvarenga, C.J.S., Dantas, E.L., Pimentel, M.M., de Oliveira, C.G., de Araújo, L.M., 2006. Shrimp U–Pb zircon dating and palynology of bentonitic layers from the Permian Irati Formation, Paraná Basin, Brazil. Gondwana Research. 9(4), 456- 463.

Sato, A.M., Llambías, E.J. Basei, M.A.S., Castro, C.E., 2015. Three stages in the Late Paleozoic to Triassic magmatism of southwestern Gondwana, and the relationships with the volcanogenic events in coeval basins. Journal of South American Earth Sciences. 63, 48-69. http://dx.doi.org/10.1016/j.jsames.2015.07.005

Shen, M., Dai, S., Graham, I.T., Nechaev, V.P., French, D., Zhao, F., Shao, L., Liu, S., Zuo, J., Zhao, J., Chen, K., Xie, X., 2021. Mineralogical and geochemical characteristics of altered volcanic ashes (tonsteins and K-bentonites) from the latest Permian coal-bearing strata of western Guizhou Province, southwestern China. International Journal of Coal Geology, 237, 1-17. Doi:https://doi.org/10.1016/j.coal.2021.103707.

Silva, A. F., Dani, N., Remus, M.V.D., Guerra-Sommer M., Horn, B.L.D., 2017. Bentonitas da Formação Irati no setor sul da Bacia do Paraná. Revista do Instituto de Geociências – USP. Geol. USP, Série cientifica. 17(1), 75-88. (Text in Portuguese).

Simas, M.W., Guerra-Sommer, M., Mendonça Filho, J.G., Cazzulo-Klepzig, M., Formoso, M.L.L., Degani-Schmidt, I., 2013. An accurate record of volcanic ash fall deposition as, characterized by dispersed organic matter in a lower Permian tonstein layer (Faxinal Coalfield, Paraná Basin, Brazil). Geologica Acta , 11(1), 45–57.

Spears, D.A., 2012. The origin of tonsteins, an overview, and links with seatearths, fireclays and fragmental clay rocks. International Journal of Coal Geology, 94, 22–31.

Suthren, R.J., 1985. Facies analysis of volcaniclastic sediments: A review. In: Sedimentology: Recent Developments and Applied Aspects. (Eds: Brenchley P.J., Williams B.P.J.), Blackwell, oxford. pp.123-146.

Tucker, M.E., 2003. Sedimentary Rocks in the Field, 3ed. Geological Magazine, Chichester: Wiley, 142(2), pp.226. Doi: https://doi.org/10.1017/S001675680536078X.

Velde, B., Vasseur, G., 1992. Estimation of the diagenetic smectite to illite transformation in time-temperature space. American Mineralogist. 77(9-10), pp.697–709.

Walker, R.G., James, N.P. 1992. Facies models: response to sea level change. Geological Association of Canada. Canada. p.101–118.

Worden, R.H., Morad, S., 2003. Clay minerals in sandstones: controls on formation, distribution and evolution. In: Richard H. Worden R.H., Morad S. (Eds.), Clay Mineral Cements in Sandstones. International Association of Sedimentologists (IAS). 34, 3–41.

Worden, R.H., Burley, S.D., 2003. Sandstone diagenesis: the evolution of sand to stone. In: Clastic Diagenesis: Recent and Ancient. (Eds: Burley, S.D., Worden, R.H.). International Association of Sedimentologists (IAS), Blackwells, Oxford. 4. 3–44.

Wright, A.C., 1990. Diffraction studies of glass structure. Journal of Non-Crystalline Solids, 123(1-3), 129–148. doi:10.1016/0022-3093(90)90779-l.

Xavier, P.L.A., Silva, A.F., Soares, M.B., Horn, B.L.D., Schultz, C.L., 2018. Sequence stratigraphy control on fossil occurrence and concentration in the epeiric mixed carbonate-siliciclastic ramp of the Early Permian Irati Formation of southern Brazil. Journal of South American Earth Sciences. 88, 157–178. Doi:https://doi.org/10.1016/j.jsames.2018.08.014

Zachariasen, W.H., 1932. The atomic arrangement in glass. Journal of the American Chemical Society. 54, 3841-3850.

Zhu, S.F., Zhu, X.M., Wang, X.L., Liu, Z.Y., 2012. Zeolite diagenesis and its control on petroleum reservoir quality of Permian in northwestern margin of Junggar Basin. China: Science China Earth Sciences, 55, 386–396.

Zhu, S.F., Zhu, X., Liu, X., Wu, D., Zhao, D., 2016. Authigenic minerals and diagenetic evolution in altered volcanic materials and their impacts on hydrocarbon reservoirs: evidence from the lower Permian in the northwestern margin of Junggar Basin, China. Arabian Journal of Geosciences. 9(2), 1-19. Doi:10.1007/s12517-015-2201-0.

Zuffa, G.G., 1980. Hybrid arenites: their composition and classification. Journal of Sedimentary Petrology, 50, 21-29. https://doi.org/10.1306/212F7950-2B24-11D7-8648000102C1865D.

Zuffa, G.G., 1985. Optical analyses of arenites: influence of methodology on compositional results. In: Provenance of Arenites. Springer, Dordrecht, p. 165-189.

Zuffa, G.G., 1987. Unravelling Hinterland and Offshore Palaeogeography from Deep-water Arenites. In: Marine Clastic Sedimentology: Concepts and case Studies. (Eds: Leggett, J. K.; Zuffa, G. G.). Dordrecht: Springer, p. 39-61.

Artigo 3 - Chronostratigraphy of Cisuralian (early Permian) Irati Formation. Depositional sequence, paleogeographic and paleoenvironmental reconstruction of Western Gondwana

Article Type:Research Paper

Dear Mr. Aurélio Fagundes Silva,

Your submission entitled "Chronostratigraphy of Cisuralian (early Permian) Irati Formation. Depositional sequence, paleogeographic and paleoenvironmental reconstruction of Western Gondwana." has been received by Gondwana Research

You may check on the progress of your paper by logging on to the Editorial Manager as an author. The URL is https://www.editorialmanager.com/gwr/.

Your username is: Aurélio

If you need to retrieve password details, please go to:
https://www.editorialmanager.com/gwr/l.asp?i=163470&l=L4UYJK7N

Your manuscript will be given a reference number once an Editor has been assigned.

Thank you for submitting your work to this journal.

Kind regards,

Editorial Manager
Gondwana Research

For further assistance, please visit our customer support site at http://help.elsevier.com/app/answers/list/p/7923. Here you can search for solutions on a range of topics, find answers to frequently asked questions and learn more about EM via interactive tutorials. You will also find our 24/7 support contact details should you need any further assistance from one of our customer support representatives.

Chronostratigraphy of Cisuralian (early Permian) Irati Formation. Depositional sequence, paleogeographic and paleoenvironmental reconstruction of Western Gondwana.

Aurélio Fagundes Silva[1]*, Norberto Dani[1], Pedro Luis Ammon Xavier[1], Marcus Vinicius Dorneles Remus[1], Cesar Leandro Schultz[1] , Marco Antônio Leandro da Silva[2]

[1]Universidade Federal do Rio Grande do Sul – UFRGS. Instituto de Geociências, Pós-graduação em Geociências, Avenida Bento Gonçalves, 9500, CP 15001, CEP 91501-970, Porto Alegre, RS, Brasil

[2]Universidade Federal Ouro Preto - UFOP. Departamento de Geologia, Escola de Minas, 35400-000 - Ouro Preto, MG, Brasil

E-mails: aureliofagundes@hotmail.com, norberto.dani@ufrgs.br , xavier.pedroluis@gmail.com, marcus.remus@ufrgs.br, cesar.schultz@ufrgs.br, marcomineral@gmail.com

*Corresponding author.

Abstract

During the Cisuralian (early Permian) epoch the Western Gondwana underwent through changes on its physiography and depositional systems. The combination of tectonic factors linked to the Gondwanide Orogeny during the San Rafaelic Orogenic Phase (SROP) and glacio-eustatic aspects of the Late Paleozoic Ice Age (LPIA) allowed the development of the Irati-Whitehill Sea System in the continental interior of

Gondwana. In this paper we analyzed the sedimentary record of the Irati Formation, acquired from a drill core located in southern portion of the Paraná Basin. The improvement of the chronostratigraphy of the whole sequence was enabled through the identification of Pyroclastic Fall Deposits (PFDs) throughout the sedimentary package and determination of their zircon LA-ICP-MS U/Pb numerical ages. For that purpose, the results were integrated with previous studies regarding detailed stratigraphy, sedimentary features (e.g. bonebeds, lithological changes), sequence stratigraphy, deposition rate and tephrochronology. Along with Cisuralian multi-proxies, the correlations between those parameters allowed to better detail the reconstructions of paleogeographic and paleoenvironmental changes during the Cisuralian in Western Gondwana.

Keywords: Stratigraphic Methods; LA-ICP-MS U-Pb dating; Tephrochronology; Sequence Stratigraphy

1. INTRODUCTION

The Permo-Carboniferous basins of Gondwana form positioned at high latitudes, having their own paleobiogeographical and paleoecological elements (Mori et al., 2012; Limarino et al., 2013; Qie et al., 2019), unlike the equatorial zones that have the Benthic Marine Faunas of the Paleo-Tethys Ocean, which are fossil guides commonly used in chronostratigraphic marking of the Permo-Carboniferous period (Gradstein et al., 2012; Ogg et al., 2016; Torsvik and Cocks, 2017). Due to the use of only palynological biochronology (especially spores and pollen) (Vázquez and Césari, 2017; Rocha et al., 2020) and endemic plants (Iannuzzi, 2013), the Gondwana basins have low chronostratigraphic resolution for determining geochronological correlations between units of the Gondwana basins. In addition, evolutionary palynological changes are likely to be influenced by regional climate changes (Azcuy et al., 2007; Stephenson, 2008; Iannuzzi, 2013), and therefore these changes may not necessarily be related to variations in environmental conditions of the basins. Another limiting factor is that the Permian GSSPs (Boundary Stratotype Section and Points) don't have a palynological basis, having any biochronological reference and causing difficulties for global chronostratigraphic correlations (e.g. Césari, et al., 2011; Stephenson, 2016).

However, the Gondwana basins are characterized by the frequent presence of volcano-sedimentary material deposited in arc-related, retro-arc foreland and intracratonic basin settings. Provenance studies on the Gondwana basins correlate pyroclastic fall deposits (PFDs) to extrusive volcanic events related to the Choiyoi Volcanic Province (Milani and De Wit, 2008; Rocha-Campos et al., 2011; Bastías-Mercado et al., 2020). These events scattered volcanic ash carried by atmosphere over wide areas of southwestern Gondwana, depositing small tabular layers and being preserved in low-energy environments (Llambías et al., 1993; López-Gamundí, 2006; Rocha-Campos et al., 2011; 2019; Sato et al., 2015; Griffis et al. 2018; 2019; Nelson and Cottle, 2019). These deposits, when preserved in different parts of the basin and in different basins, may have the potential for correlation studies and acting as regional landmarks (for example, Zuffa, 1987; Orton, 1996; Huff, 2016).

PFDs are considered as geochronological stratigraphic units when identified in sedimentary sequences. This application is due to the fact that they not only represent deposits related to episodes of volcanism events (Einsele and Seilacher 1982, Einsele et al., 1996; Boggs, 2014; Miall, 2016), but also contain minerals suitable for isotopic dating (Alan, 2018; Reiners et al., 2018). Applying isotopic geochronology as a secondary proxy in deposits of volcanic material, such as drop pyroclastic deposits (PFDs), allows the precision of chronostratigraphic correlations between its sedimentary packages (e.g. Rocha-Campos et al., 2011; Sato et al., 2015). Correlating with other methods, such as tectonics, paleogeographic reconstructions, paleoenvironmental reconstructions, chemostratigraphy, palinoestratigraphy and bioestratigraphy of the Gondwana basins, allows for improvements in the chronostratigraphic definitions of the Permo-Carboniferous period (for example, Qie et al., 2019).

Several levels of PFDs can be found in the Paraná Basin, occurring as lithotypes such as tonsteins and bentonite (Huff, 2016; Silva et al., 2017). The PFDs represent geochronological units in the Itararé (Cagliari et al., 2016), Guatá (Rio Bonito Formation) (Griffis et al., 2018) and Passa Dois Groups (Irati and Rio do Rastro Formations) (Santos et al., 2006; Rocha-Campos et al. 2019).

In this work, a drill core from the region of Herval, RS, drilled by (Companhia de Pesquisa de Recursos Minerais - CPRM) (Aborrage and Lopes, 1986), was studied. This drill core contains the complete sequence of the Irati Formation in the Paraná Basin. The objective was to identify PFDs in the Irati Formation and to use a geochronological approach to correlate this new study with PFDs from a site different from previous studies at the PetroSix mine (São Mateus do Sul-PR; Figure 1) (Santos et al., 2006; Rocha-Campos et al., 2019; Bastos et al., 2021). The PFDs identified on the drill core were placed in a high-resolution stratigraphic section from the Irati Formation (Xavier et al., 2018). The numerical ages were inserted in the International Stratigraphic Column (Walker et al., 2018), from which sedimentological parameters were evaluated. Based on that it was possible to estimate rate of deposition, probable age of the episodic events that took place during the Passa Dois Group sedimentation.New chronostratigraphic and tefrochronological correlations were made, together with Paleogeographic and paleoclimatic reconstructions. The results allowed us to estimate

the time of deposition of the Irati Formation and to establish a new Paleoenvironmental Reconstruction of Western Gondwana during the Cisuralian.

2. GEOLOGICAL SETTING

The intracratonic Paraná Basin is one of the most important geological compartments of the South American continent (Figure 1A). It occupies an area of 1.7 $x10^6$ km^2, being a large portion (1.1 $x10^6$ km^2) located in the central-south portion of Brazil (Milani et al., 2007). It is subdivided into six tectonostratigraphic megasequences (Milani, 1997), being the Gondwana I Supersequence (Carboniferous - Lower-Triassic, ~310-245 Ma) of interest of this study (Figure 1B). In this time interval it is registered the last great transgressive-regressive second-order marine cycle of the Paleozoic on the basin. This cycle resulted from regional sea-level oscillations on Gondwana (e.g. Bastos et al., 2021). The oscillations were driven mainly by deglaciation (Late Paleozoic Ice Age - LPIA; Isbell et al., 2003; 2012; Cagliari et al., 2016) and tectonic pulses linked to collisional orogenies of the Gondwanides cycles. The SROP was the cycle that mostly influenced the regional base level changes (Milani and Ramos, 1998; Milani and De Wit, 2008; Rocha-Campos et al., 2011; Sato et al., 2015). Studies on the lithostratigraphic subdivision of the Paraná Basin and its geological significance are presented by Milani (1997), Milani and Ramos (1998), Milani and Zalán (1999), Milani et al. (2007), Milani and De Wit (2008), Holz et al. (2010), Iannuzzi et al. (2010), Iannuzzi (2013) and Rocha-Campos et al. (2019). The Gondwana I Supersenquence is presented in the following lithostratigraphic units: Itararé Group (Lagoa Azul, Campo Mourão and Taciba Formations), Guatá Group (Rio Bonito and Palermo Formations) and Passa Dois Group (Irati, Serra Alta, Teresina and Rio do Rastro Formations) (Figure 1C). The sequence is followed by the Triassic Sanga do Cabral and Piramboia Formations (Milani et al., 2007). In some of these units, there are PFD tuffs that constitute lithotypes of tonsteins and bentonites. They represent geochronological units on the Itararé (Cagliari et al., 2016), Guatá (Rio Bonito Formation) (Griffis et al., 2018) and Passa Dois Groups (Irati and Rio do Rastro Formation) (Santos et al., 2006; Rocha-Campos et al., 2019).

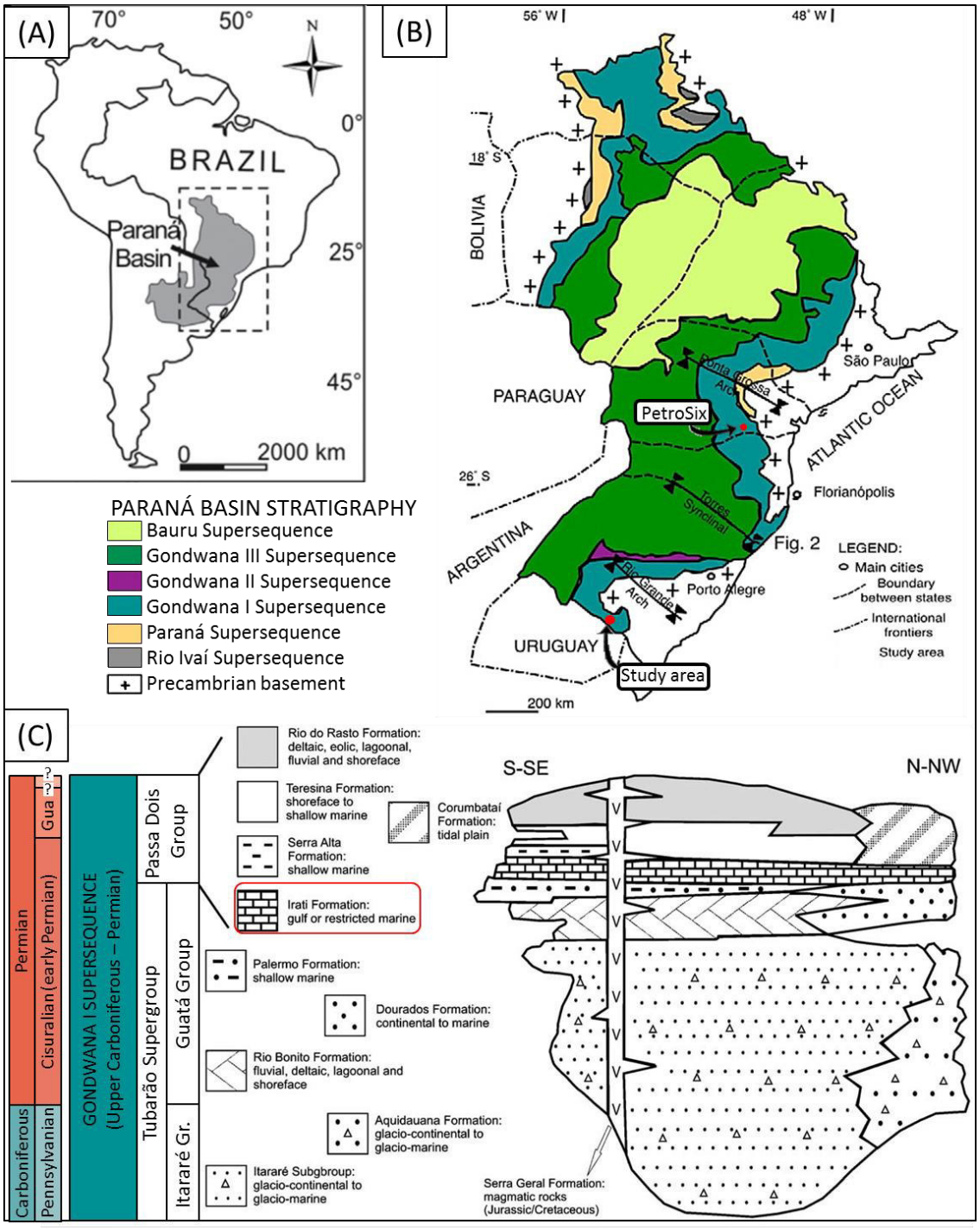

Figure 1 - (A) Extension of the Paraná and the Chaco Paraná Basins in South America. (B) Main features and allostratigraphic units of the Paraná Basin in Brazil (modified from Milani et al., 2007) with the location of the study area (core HV-44 -RS in Herval municipality) and the correlation profile (PetroSix in São Mateus) marked (red dots). (C) Stratigraphic chart of the Gondwana I Supersequence (Carboniferous- Lower-Triassic) with the units of the Paraná Basin, evidencing the Irati Formation (modified from Iannuzzi, 2013).

The Guatá Group and the Irati and Serra Alta Formations represent the maximum extent of marine floodings that occurred in the Paraná Basin during the deposition of Gondwana I Supersequence. The floodings occurred in the context of a second-order highstand systems tracts (HST), being the last transgressive maximum occurring in the Serra Alta Formation (Milani et al., 2007). Holz et al. (2010) proposed three third-order transgressive/regressive cycles in this interval, considering the deposition of the Irati Formation as a single third-order cycle. Applying the concepts of high-resolution stratigraphy in the description of the Irati Formation, three fourth-order sequences were recognized, however with different limits and amplitudes (Hachiro, 1996; Araújo, 2001; Araújo et al., 2004; Reis et al., 2018; Xavier et al., 2018; Holanda et al., 2019). Xavier et al. (2018) identified four stratigraphic surfaces and distinguished three fourth-order cycles: S1, S2 and S3 (the first corresponding to the Taquaral Member and the last two corresponding to the Assistência Member). The paleogeographic and depositional conditions of the Irati Formation were investigated by Araújo (2001), Araújo et al. (2004), Xavier et al. (2018) and Bastos et al. (2021). Araújo (2001) reconstructed the environmental setting based on core analysis throughout the basin and interpreted its depositional environment as a homoclinal ramp, with gentle slope to southwest. Regional associated lithofacies were identified in three distinct depositional systems: carbonatic inner-ramp, mixed siliciclastic-carbonatic mid-ramp and siliciclastic outer-ramp.

The deposition of the Irati Formation is linked to a marine transgression that enabled the formation of an epicontinental sea called the Irati-Whitehill Sea (Lavina, 1991). It was extended over a vast area in southern Gondwana (4 $x10^6$ km^2), occupying the central-south portion of Brazil, and Paraguay, Argentina, Uruguay and South Africa (Matos et al., 2017; Bastos et al., 2021). The sedimentary deposits formed on the Whitehill-Irati Sea had great spatial extension, as well as lithological similarity and fossiliferous identity (e.g. mesosaurids). Thus, the Irati Formation is correlated to several other units such as the Mangrullo (Uruguay), Tacuary (Paraguay), Chacabuco (Argentina), Huab (Huab Basin), and Whitehill (Aranos, Kalahari and Karoo Basins) Formations, and the Black Rock Member (Falkland Island) (Milani and Zalán, 1999; Araújo, 2001; Matos et al., 2017; Bastos et al., 2021).

Deposition in the Irati-Whitehill Sea is characterized by stratified water column, generating anoxic conditions in the distal ramp (Araújo, 2001; Lavina, 1991; Xavier et al., 2018). Progressive marine regression resulted in enhanced water circulation, reducing stratification and generating more oxic background conditions. In this new environment the Serra Alta and Teresina Formations were deposited, corresponding to a marine environment with sedimentation below storm wave base. Subsequently, sedimentation in the basin evolved to a progressive continentalization depositing the Rio do Rastro Formation, which consists of a low-energy fluvial-deltaic-lacustrine and/or fluvial environment, that marks the end of the Passa Dois Group deposition (Schneider et al., 1974; Araújo, 2001; Holz et al., 2010).

3. MATERIALS AND METHODS

The study is based on three bentonite samples (Silva et al., In press) collected on drill core HV-44-RS (coordinates Lat 31 ° 56'42.90 "S / Long 53 ° 53'18.85” W), in the Herval municipality (RS). The survey was carried out by the Geological Survey of Brazil (CPRM) at the end of 1982 (Figure 1; Aborrage and Lopes, 1986). The sampling of the drill core was limited to small quantities per level (17 - 28g). The samples were submitted to mineralogical analysis in the laboratories of the Institute of Geosciences of the Universidade Federal do Rio Grande do Sul (UFRGS), specifically at the Centro de Estudos em Petrologia e Geoquímica (CPGq) and at Centro de Estudos em Geologia Costeira (CECO).

The mineralogical separation of the resistant minerals followed the methodology of Bohor and Triplehorn (1993) and Reiners et al. (2018). The samples were sieved in a 500 mesh sieve using water, hence retaining the fraction above 0.025 mm. It was followed by heavy liquid mineral separation using bromoform. As result, mineral separates of light and heavy minerals were achieved. The zircons were found in the heavy fraction. The identification of the zircon grains was initially performed using a binocular stereomicroscope. We sought to find euhedral grains. The observed

characteristics were morphology, color, degree of transparency, presence of inclusions and dimensions in the range of fine sand and silt (30 to 250 μm or 0.030-0.250 mm). To confirm that the picked grains were zircons, some of them were subjected to scanning electron microscope analysis (SEM) (JEOL JSM 6060) equipped with an energy-dispersive X-ray spectrometer (EDS) (Bruker Nano X Flash Detector 5030). Three levels of PFDs were sampled and named BIR9, BIR5 and BSA1. For each one 50 zircon grains were picked for geochronology dating. The grains were selected and mounted on a double-side sticky tape, subsequently positioned on a form and filled with epoxy resin. Once completely dry, the mount was polished with diamond paste until the best exposure of the zircons was achieved.

The polished sections were analyzed at the Isotopic Geochemistry Laboratory (IGL) of the Geosciences Institute of the Universidade Federal de Ouro Preto (UFOP). Each mount was gold- and carbon-coated and subjected to cathodoluminescence analysis (CL) (JEOL 6510 SEM). CL images were obtained to assess the integrity and internal textures (e.g. zonation) of the mounted grains. The correct assessment of internal structures is necessary to correctly chose the laser ablation spots for dating. The Laser Ablation-Inductively Coupled Plasma-Mass Spectrometry (LA-ICP-MS) U-Pb dating of the volcanogenic zircons was performed on all samples (n = 131, 64 analyses). Sample BIR9 (n = 50, 15 analyses), BIR5 (n = 56, 22 analyses) and BSA1 (n = 25 crystals, 27 analyses). A ThermoScientific Element 2 sector field (SF) ICP-MS coupled to a CETAC LSX-213 G2 laser system was used for U-Pb isotope analyzes of zircons. The equipment ran in standard high-sensitivity mode (STDS), using spot diameter size of 30 μm, laser energy of 15%, laser shot frequency of 10 Hz and shutter delay of 15 s. Detailed description of the method can be found in Gerdes and Zeh (2006) and Lana et al. (2017). The zircon standards used for calibration included GJ-1 and additional BB and Plešovice (Jackson et al., 2004). Glitter Data Reduction Software for laser ablation microprobe was used for data reduction (Van Achterbergh et al., 2001).

Analytical ages were calculated using the radioisotopic decay constant of 137.88, established through the $^{238}U/^{235}U_{zircon}$ zircon ratio by Jaffey et al. (1971) and Steiger and Jager (1977). Considering the ages obtained, those with concordance errors greater than 5% were not considered. The ages were calculated in terms of millions of years before present (Ma) or numerical ages (NACSN, 2005; Reiners et al., 2018). Their

determination were done by plotting on univariate normal distribution diagrams of the $^{206}Pb/^{238}U$ ratio, using IsoplotEx 4.15 software (Ludwig, 2012). The random gaussian variable chosen to represent the analytical uncertainty in plotting was ± 2σ (2 standard deviations from the mean), hence establishing a confidence interval of 95.4%. To represent a good numerical age calibration, it was aimed to group the ages of the $^{206}Pb/^{238}U$ rate that were concordant, and to obtain values of Mean Square Weighted Deviation (MSWD) near 1 (NACSN, 2005; Reiners et al., 2018).

The numerical ages and the stratigraphic records were linked to the chronostratigraphic chart version 5.0 of the Geologic Time Scale (GTS2018) by Walker et al. (2018) for data calibration, as indicated by interregional stratigraphic correlations generated using TimeScale Creator (TS-Creator 7.4) (https://www.timescalecreator.org/index/index.php). To perform the tephrochronological correlation the following levels of PFDs of the PetroSix Mine were used: SM-03 (Santos et al., 2006), SM-01 (Rocha-Campos et al., 2019), and Paleosul05 (Bastos et al., 2021). For regional tephrochronological correlation, PFDs KHA-1a (Werner, 2006), Tunas II PP (López-Gamundi et al., 2013), FAX (Griffis et al., 2018), DPAL2 (Griffis et al., 2019) and EB-1 (Rocha-Campos et al., 2019) were used. The data from Biotic Crises by Iannuzzi (2013) and Lucas (2017a; 2017b) were also used. The Scotese (2014) map was used for paleogeographic reconstruction and the Boucot et al. (2013) map for paleoclimatic reconstruction. The palaeoclimatic data was obtained from Montañez and Poulsen (2013) and Qie et al. (2019). The paleoenvironmental reconstruction was based on paleoenvironmental maps of Araújo (2001), chronostratigraphic correlations, bibliographic reference and tephrochronology of Western Gondwana basins. The bibliographic reference included studies on organic geochemical biomarkers, sedimentary microfacies, sedimentary provenance and isotopic chemostratigraphy of stable elements (Faure and Cole, 1999; Araújo, 2001; Matos et al., 2017; Xavier et al., 2018; Reis et al., 2018; Holanda et al., 2019; Ng et al., 2019; Qie et al., 2019; Martins et al., 2020a; Rocha et al., 2020; Bastos et al., 2021).

4. RESULTS

The facies of the sampled levels from the HV-44-RS drill core present contrasting characteristics along the profile. The levels occured as tabular and thin layers (varying from 2 to 12 cm), with abrupt discordant contact and absence of sedimentary structures (texturally homogeneous). The lithologies consisted of claystone of shades varying from grey, green, brown and/or yellow. At these levels trace minerals occurred dispersed in the clay matrix forming an assembly of crystals of magmatic origin. This occurrence is one of the characteristics that classify the levels as PFDs (Silva et al., 2017; in press). The zircon crystals studied in this work presented euhedral morphology, with bipyramidal prismatic habit and elongated in the direction of the C-axis. These characteristics were in agreement to what is typically observed in crystals of volcanic origin (e.g. Santos et al., 2006; Silva et al., 2017; Rocha-Campos et al., 2019). The grain size was below very fine sand (30 to 250 μm). The zircons of PFDs BIR9 and BSA1 presented length/width (l/w) ratios ranging from 2:1 to 4:1 and lengths from 100-200 μm. The PFD BIR5 presented l/w ratios varying from 4:1 to 14:1 (with an average of 5:1) and lengths between 140-400 μm. There were no evidence that the grains went through alteration, sediment transport or reworking processes, as observed in other works (Pupin, 1980; Fisher and Schmincke, 1984; Bohor and Triplehorn, 1993; Spears, 2012). In cathodoluminescence (CL) the zircons presented parallel oscillatory zoning from the core to the edges. Overgrowths occasionally occurred, which are characteristic of growth zoning during igneous genesis (Vavra, 1990; 1993; Corfu et al., 2003).

The numerical age of PFD BIR9 was based on four analytically concordant spots (n=4), of weighted mean age of $^{206}Pb/^{238}U$ of 284.1 ± 3.5 Ma, with 95% reliability and MSWD = 1.14 (probability = 0.33) (Silva et al., in press) (Figure 2). This age corresponded to the Artinskian period, according to GTS2018 by Walker et al. (2018). The numerical age of PFD BIR5 was based on thirteen analytically concordant spots (n=13), of weighted mean age of $^{206}Pb/^{238}U$ of 274.2 ± 2.8 Ma, with 95% reliability and MSWD=0.87 (probability=0.46), corresponding to the Kungurian period. The numerical age of PFD BSA1 was based on four analytically concordant spots (n=4), of weighted

mean age of $^{206}Pb/^{238}U$ of 274.2 ± 2.8 Ma, with 95% reliability and MSWD=0.87 (probability=0.46), also corresponding to the Kungurian period.

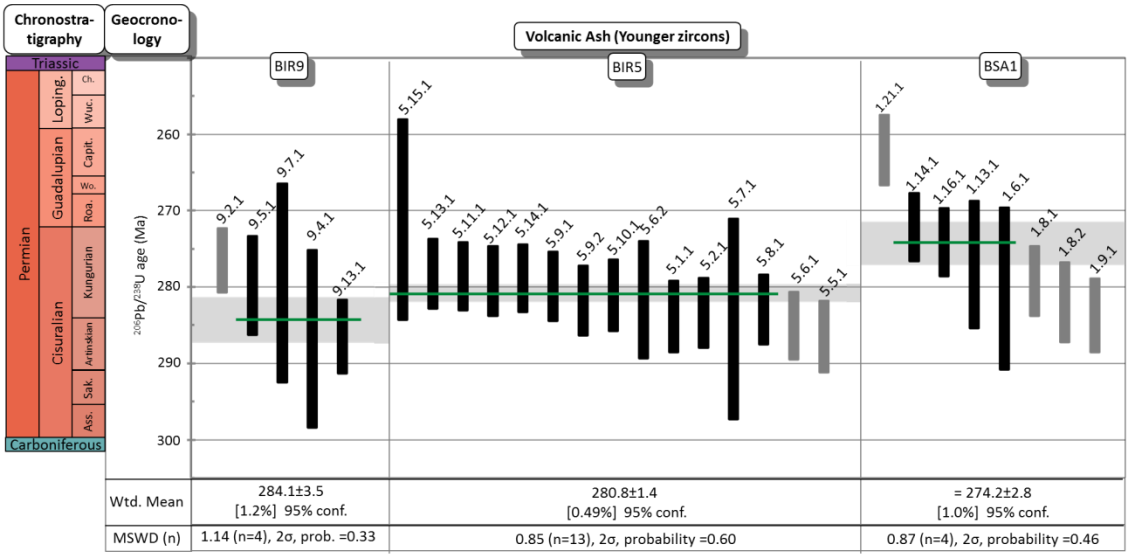

Figure 2 - Zircon U-Pb weighted mean age plot of samples BIR9, BIR5 and BSA1. Each vertical rectangle represents an analysis, being the black ones chosen to calculate the numerical age. The horizontal green line is plotted at the weighted mean age of the analysis, and its ± 2σ (95%) confidence interval is shown as shaded grey region. The weighted mean age, uncertainty, confidence level, the MSWD (mean square weighted deviation), and n are all reported together with the data (Silva et al., in press).

The ages obtained for the three PFDs were associated with the interpretation of the genesis of the deposition of core HV-44-RS (Figure 3A), based on sequence stratigraphy (Araújo, 2001; Xavier et al., 2018). It was possible to evaluate the behavior of the sedimentation rate of the sequence that corresponds to the Irati Formation (Figure 3B) (e.g. Boggs, 2014). Thus, possible to obtain the chronostratigraphic ages of the events identified throughout the stratigraphic section. These events were correlated to the Phanerozoic Global Sequence Synthesis T-R Cycles (2nd order) (TS-Creator 7.4). Using tephrostratigraphy the events were correlated with other PFDs (Figure 3C) identified in coeval basins.

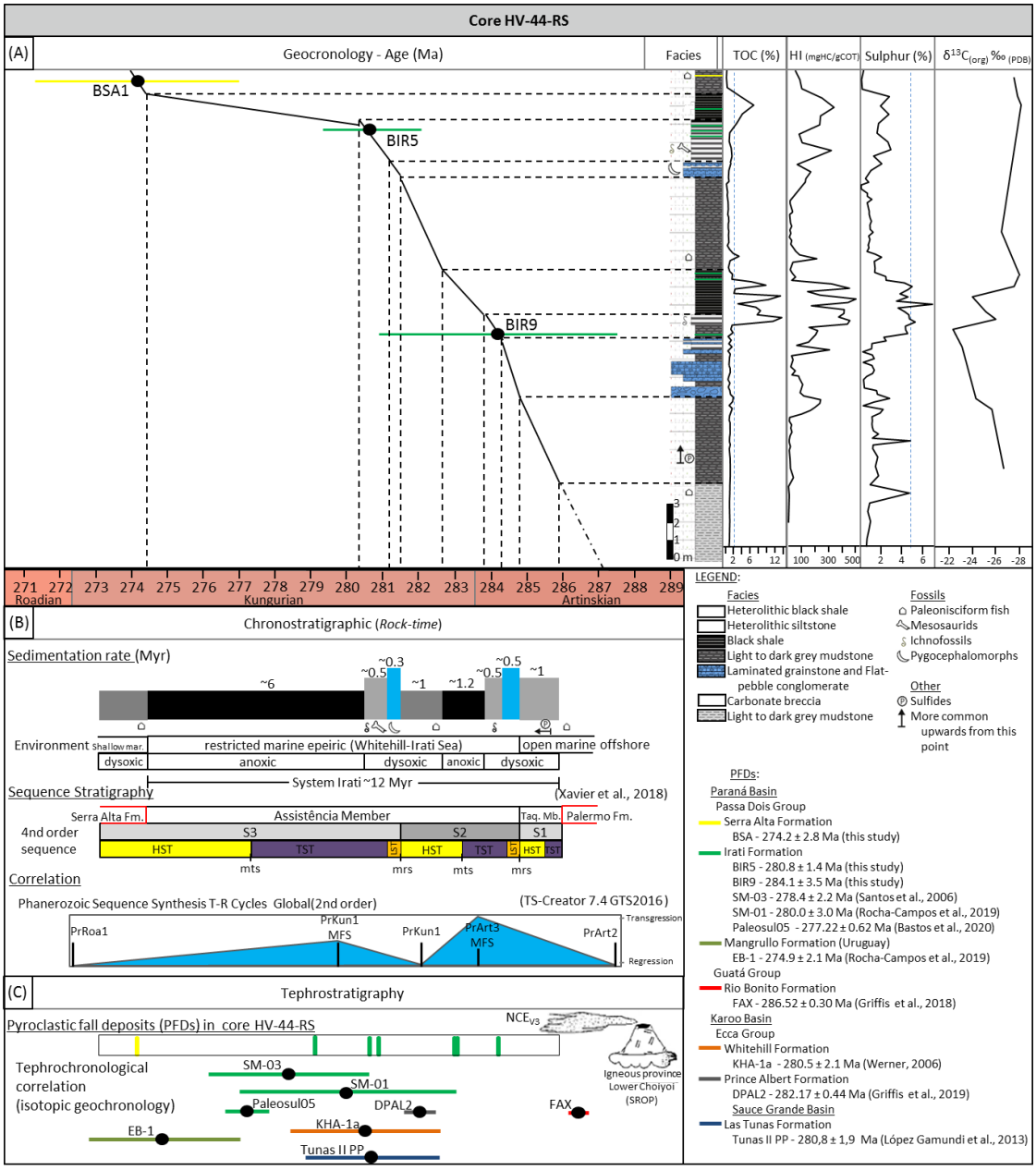

Figure 3 - Deposition rate diagram of drill core HV-44-RS based on three levels of PFDs and chronostratigraphic correlations. (A) Inclination of the correlation curve based on the numerical ages positioned in the geochronological column and changing system tract interpreted by Araújo (2001) and Xavier et al. (2018). The columnar profile and biostratigraphy of drill core HV-44-RS from Xavier et al. (2018). Chemostratigraphic data for total organic carbon (TOC), hydrogen index (HI), sulfur (S) and $\delta^{13}C_{(org)}$ ‰ from Araújo (2001). (B) Distribution of sediment packages of core HV-44-RS along the chronostratigraphic time, sedimentation rate of sedimentary packages, distribution of sequence stratigraphy in time and correlation with Phanerozoic Global Sequence Synthesis T-R Cycles (2nd order) (TS-Creator 7.4). (C) Placement of the chronostratigraphic distribution of the PFDs identified in core HV-44-RS and tephrochronological correlation with PFDs: SM-03 by Santos et al. (2006); SM-01 and EB-1 by Rocha-Campos et al. (2019); Paleosul05 by Bastos et al. (2021); FAX by Griffis et al. (2018); DPAL2 by Griffis et al. (2019); KHA-1a by Werner (2006) and Tunas II PP by López-Gamundi et al. (2013). An illustrative representation of the provenance of the PFDs was made, being of the NCE_{cV3} type in the classification of Zuffa (1980) and provided from the Lower Choiyoi.

The drill core HV-44-RS consisted of grey siltstones, dark to light grey shales, mudstones and claystones. The lower part of the drill core section (Taquaral Member) presented dark grey siltstones and mudstones, without PFDs levels. The upper part (Assistência Member) was composed by a sequence of dark grey shales, bituminous black shales, carbonates, bonebeds and PFDs levels. This allowed the recognition of three depositional sequences in the Irati Formation denominated S1, S2 and S3 (Figure 2A) (Xavier et al., 2018). The faciology and biostratigraphy of the Irati Formation presented on the core were previously described in Xavier et al. (2018). The chemostratigraphy based in total organic carbon (TOC), hydrogen index (HI), Sulfur (S) and $\delta^{13}C_{(org)}$ ‰ are available in Araújo (2001).

The contemporary volcanogenic provenance indicators for the PFDs BIR5, BIR9 and BSA1 were defined by their faciological, mineralogical, geochronological and tephrostratigraphical characteristics (Silva et al., In press). The three numerical ages (Figure 2) determined along the section of the core HV-44-RS (Figure 3) placed the stratigraphic units as being deposited during the Cisuralian. This was representative of the contemporaneity between volcanic activity and sedimentation in-situ of PFDs (Rossignol et al. 2019). The deposition rate, whose curves were related to changes in sedimentation rates, might be associated to eustatic changes characterized by the sequence limits of S1, S2 and S3 systems (Silva et al., In press). Thus, it was interpreted that the sedimentation of the Irati System lasted approximately 12 Myr. There were two anoxic events identified in Irati Formation which lasted about 1.2 Myr and 6 Myr, and two lowstand systems tracts (LST) events in 284.5 Ma and 281.2 Ma approximately. A concentration of mesosaurid bonebeds (Lavina, 1991; Araújo, 2001; Ronh, 2007; Xavier et al., 2018) of relative numerical age of 280.6 Ma was also identified. Thus, it was possible to establish a correlation with the Phanerozoic Global Sequence Synthesis TR Cycles (2nd order) (TS-Creator 7.4). The transgressions PrArt3 and PrKun1 coincided with the anoxic intervals of the Irati Formation.

There is a consensus that the PFDs identified in the studied range relate to the Lower Choiyoi volcanism and were formed during the SROP (Rocha-Campos et al., 2011; 2019; Limarino et al., 2013; Sato et al., 2015). Therefore these PFDs represent

episodic deposits from sin-eruptive periods (Miller et al., 2007) of a volcanic province located outside the tectonic context of the basin (e.g. Zuffa, 1987; Orton, 1996; De Rosa et al., 1986; Critelli and Ingersoll, 1995). The PFDs were classified as NCE_{cV3} according to genetic provenance by Zuffa (1980; 1985; 1987). The numerical ages determined for PFDs BIR5 and BIR9 allowed tephrochronological correlations with the PFDs SM-01 (280.0 ± 3.0 Ma, Rocha-Campos et al., 2019), SM-03 (278.4 ± 2.2 Ma, Santos et al., 2006) and Paleosul05 (277.22 ± 0.57 Ma, Bastos et al., 2021). Those PFDs were described in Petrosix Mine (Assistência Member), which is located 757 km away from the drill core HV-44-RS (Figure 1; Figure 3C). The tephrostratigraphic correlation evidences the lateral extension of the Irati Formation in the Paraná Basin and the correlation with PFDs from other formations evidences the lateral extension of the Irati Formation to other basins. The correlated PFDs were the FAX of the Rio Bonito Formation (286.5 ± 0.3 Ma, Griffis et al., 2018), EB-1 from the Mangrullo Formation (274.9 ± 2.1 Ma, Rocha-Campos et al. 2019), DPAL2 of the Prince Albert Formation (282.17 Ma ± 0.44 Ma, Griffis et al., 2019), KHA-1a of the Whitehill Formation of Karoo Basin (280.5 ± 2.1 Ma, Werner, 2006), and Tunas II PP from Tunas Formation (280.8 ± 1.9 Ma, López-Gamundi et al., 2013)., evidences the lateral extension of the Irati Formation to other basins. The level of mesosaurid bonebeds was interpreted as due to transport by distal tempestites (Lavina, 1991; Araújo, 2001; Ronh, 2007; Xavier et al., 2018). It was possible to correlate this occurrence with the Redtankian extinction event described by Lucas (2006; 2017a; 2017b).

5. DISCUSSION

5.1. Paleogeographic reconstruction of Western Gondwana (Cisuralian)

The numerical ages determined (Figure 2) reinforced that sedimentation of the Irati Formation occurred during the Cisuralian (Figure 3 and Figure 4A), hence enabling chronostratigraphic correlations with tectonic and environmental events (Figure 4).

During the Cisuralian, the Pangean assembly (Hercynian, Variscan, Alleghanian and ancestral Rocky Mountain Orogenies) (Figure 4A) would have submitted to increased compressive tectonics to Western Gondwana (Li and Powell, 2001). This compressive tectonic change would have inhibited the supercontinent migration and reduced it to the Panthalassa paleo-ocean subduction speed. As result, intensification of tectonism would be triggered in the southern margin of Gondwana (Figure 5A) and more significantly inland deformation of the continent. This marks the transition from the Chanic Orogenic Phase to the SROP (Figure 4B and Figure 5B) (ca. 284 to 276Ma) (Kay et al., 1989; del Rey et al., 2019), and the changes in tectonic-sedimentary dynamics in Gondwana basins (Limarino et al., 2013; Sato et al., 2015).

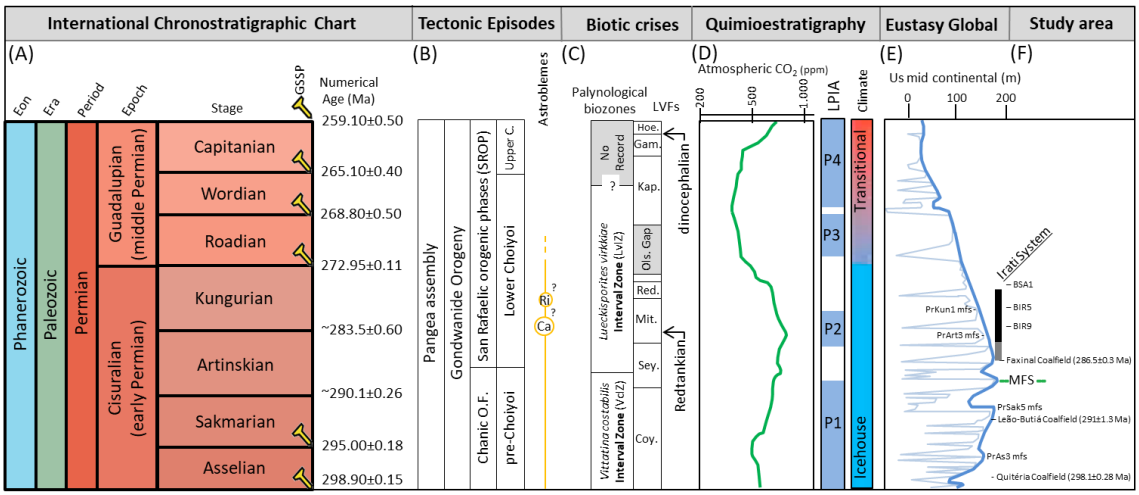

Figure 4 - (A) Geologic Time Scale version 5.0 (GTS2018) used for data calibration (Walker et al. 2018); (B – Tectonic episodes) Global tectonic and Gondwanides Orogeny phases (Modified by Rocha-Campos et al., 2011; Limarino et al., 2013; Sato et al., 2015) and astroblemes Serra da Cangalha (Ca) (diameter 13 km) and Riachão Ring (Ri) (diameter 4.5 km) in Parnaíba Basin (Kenkmann, et al., 2011; Maziviero et al., 2013; Vasconcelos et al., 2013; Crósta et al., 2019); (C – Biotic crises) Palinostratigraphy of the Paraná Basin for the Permian interval showing palynozones (Modified from Iannuzzi, 2013) and Permian timescale based on tetrapod evolution leading the land vertebrate faunachrons (LVFs) (Modified from Lucas, 2017a; 2017b); (D - Quimioestratigraphy) Atmospheric CO_2 levels during the Permian (Modified from Qie, et al., 2019); (E – Eustasy global) Interregional stratigraphic correlations generated using Phanerozoic Global Sequence Synthesis T-R Cycles (2nd order) (Modified from Montañez e Poulsen, 2013 and TS-Creator 7.4); (F - tephrochronological correlation with the study area) Chronological placement of dated samples in the Irati System, Quitéria Coalfield (298.1±0.28 Ma, Griffis et al., 2018) – Leão-Butiá Coalfield (291±1.3 Ma, Simas et al., 2012) and Faxinal Coalfield (286.5±0.3 Ma, Griffis et al., 2018).

The deformation bands formed the proto-cordillera San Rafael by incipient uplift of the magmatic arc related to the subduction (Figure 5B). In the Gondwana basins the tectonism deformed and uplifted the arc-related basins (Madre de Dios, Navidad-Arizaro, Río Blanco, Calingasta - Uspallata and western San Rafael). Due to that, the retro-arc foreland basins went through accelerated subsidence and sin-depositional deformation (Tarija, Paganzo, eastern San Rafael and Sauce Grande - Colorado, Karoo). Whilst the intracratonic basins went through flexural subsidence (Chaco-Paraná, Paraná, Kalahari, Huab, and their extension in the Falkland Islands) (Figure 5B) (Kay et al., 1989; López-Gamundí, 2006; Milani and De Wit, 2008; Limarino et al., 2013; Sato et al., 2015).

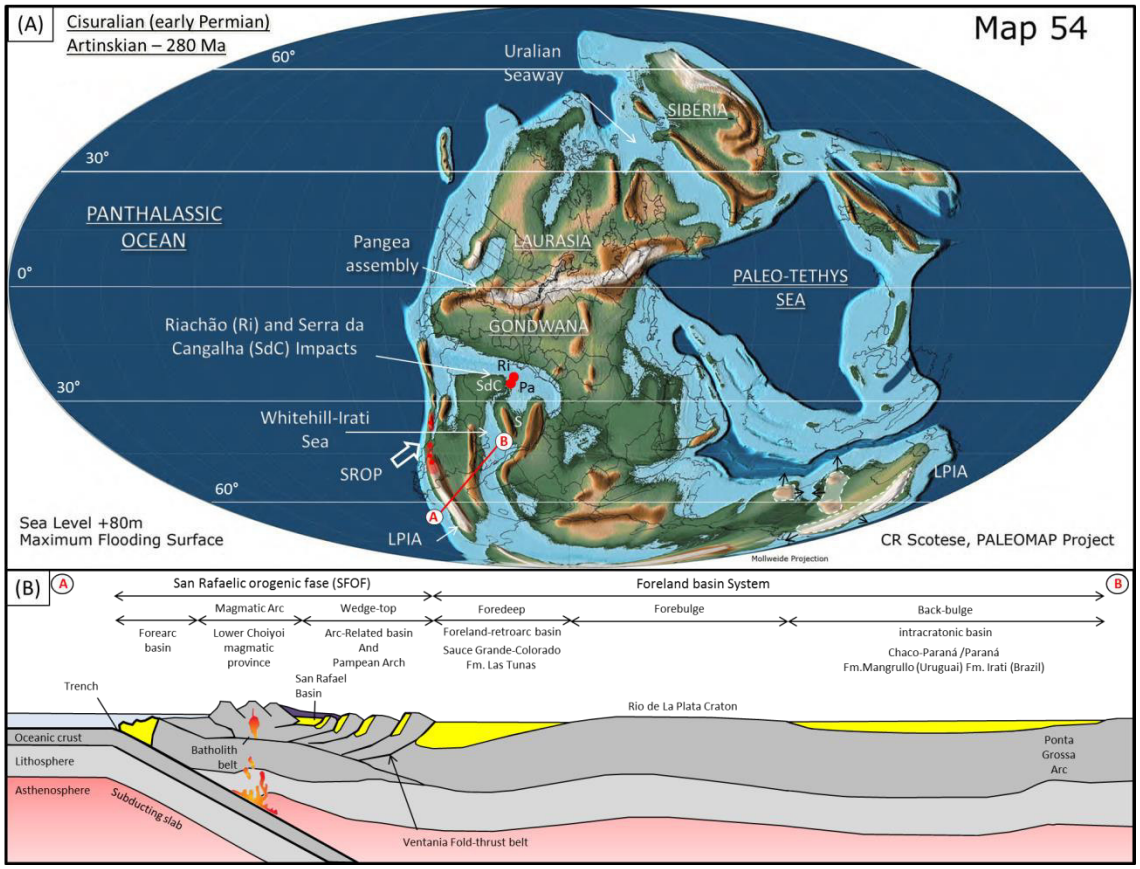

Figure 5 – (A) Paleogeographic map of the Artinskian from Scotese (2014) (54 map). Location of the astroblemes of Riachão (Ri) and Serra da Cangalha (SdC) (Crósta et al., 2019). Parnaíba (Pa) and Sanfranciscana (S) basins. Line A-B represents the geological profile of part B. (B) Tectonic reconstitution of Western Gondwana margins during the Cisuralian. Period of ongoing subduction of the Panthalassa paleo-ocean and inland deformation during the San Rafaelic orogenic Phase (SROP). This deformation would have influenced the Gondwana basins in a foreland basin system context.

The arc-related basins had their connection with the Panthalassa paleo-ocean interrupted and later became extinct. The interruption resulted in an unconformity over Carboniferous-Cisuralian shallow marine clastic deposits (Limarino et al., 2013). Above the unconformity volcanoclastic rocks of dacite-rhyolite composition of the Lower Choiyoi volcanism deposited (Figure 4B) (Kay et al., 1989; Sato et al., 2015). During syn-eruptive periods extrusive magmatic rocks (e.g. lava flows, volcanic breccia, ignimbrites and tuffs) were also deposited. For instance, the CH-1 ignimbrites of the Yacimiento Los Reyunos Formation, San Rafael Basin, of 281.4 ± 2.5 Ma (Rocha-Campos et al., 2011). During inter-eruptive periods, epiclastic deposits (conglomerates and sandstones) were deposited (Rocha-Campos et al., 2011; Kimbrough et al., 2016; Spalletti and Limarino, 2017) and several plutonic rocks were formed, such as Las Piedritas Granodiorite LS 4 of age 278.8+- 3.9 Ma (Los Leones Tonalite to granodiorite Pluton) (Sato et al., 2015).

Due to the compressional regime, the retroarc foreland basins evolved and developed thrusts-belts, known as the Ventania Thrusts-belts System (Figure 5B) (Tomezzoli and Cristallini, 1998). The accelerated subsidence caused the retroarc foreland basins to connect (oriental San Rafael, Sauce Grande–Colorado and Karoo basins), forming a restricted shallow sea that was accompanied by sin-depositional deformation (Figure 5A) (López-Gamundí, 2006; Milani and De Wit, 2008). The Las Tunas Formation in Sauce Grande – Colorado Basin registered sin-depositional deformation that was evidenced by the presence of growth folds on its sedimentary sections. The migration of the depocenter also occurred, driven by the flexural subsidence and by load of sediments from the foreland region (Figure 5A) (López-Gamundí, 2006; Arzadún et al., 2018). Similarly, the retro-arc foreland basin Karoo Basin is associated with the development of the Cape Fold Mountains (Catuneanu et al., 1998). The eastern part of the Sauce Grande Basin and the Karoo Basin evolved from extensional to transtensional regime (Catuneanu et al., 2005; López-Gamundí, 2006; Nelson and Cottle, 2019).

SROP compressive field caused the Western Gondwana craton to go through flexural subsidence (Milani, 1997), hence forming a sag-type intracratonic depression (Milani and Ramos, 1998; Milani and De Wit, 2008). In the Paraná Basin, flexural subsidence caused the regional depositional ramp to had a dip direction to southwest. The ramp geometry of the Irati System was assessed by Araújo (2001), through a

paleogeographic sketch based on the geometric configuration of the isopachs of the fourth-order sequences contained in the Irati Formation. There it was considered that the Irati system consisted of a paleophysiography with an homoclinal ramp geometry with NE-SW dip direction, with smooth regional inclination, between 0.0009° and 0.0015°.

The progressive development of the magmatic arc by the SROP extended over a wide area (Figure 5A). The extension was long enough to allow the progressive closure of the retro-arc foreland and intracratonic basins around the Panthalassa paleo-ocean (Kay et al., 1989; Milani, 1997; Milani and De Wit, 2008; Sato et al., 2015). The Choiyoi volcanic province extended over an area of ~ 1.7 km^2 (Chile and Argentina), presenting rocks of intermediate compositions (andesites to dacites) (Kay et al., 1989; Sato et al., 2015). During the transition to intracratonic basin the subsidence and magmatic arc formation caused a set of back-bulge basins to form (Milani et al., 2007). The formation and connection between basins leaded to extensive continentalization of the vast shallow sea restricted to internal communication between basins (Bastos et al., 2021). This sea, called the Irati-Whitehill Sea, extended through the Western Gondwana region, between the 30° S and 65° S parallels (Figure 5A). It encompassed the basins of southwestern Gondwana (Paraná, Chaco-Paraná, Huab, Kalahari, Karoo and Falkland Islands Basins). The basins have become the largest internal reservoir and depositional center in Western Gondwana, covering an extensive area ($4x10^6$ km^2) (Faure and Cole, 1999; Matos et al., 2017). It is interpreted that the last communication between the basins and the Panthalassa paleo-ocean was at south of the Sierra de La Ventana (Figure 5A) (Araújo, 2001).

Rocha-Campos et al. (2011) concluded that some of the explosive volcanic events in the Choiyoi volcanic province could be of the Plinian to Ultraplinian type. On that case the volcanic ashes would have been transported over long distances, hence being deposited over the southern region of Gondwana (Kay et al., 1989; Rocha-Campos et al., 2011; Sato et al., 2015). PFDs dated in the Las Tunas Formation register the transition between last part of pre- and beginning of Choiyoi magmatism. The pre-Choiyoi (Figure 4B) (Sato et al., 2015) was marked by the PFD Tunas I-PP (lower) of 291.7 ± 2.9 Ma (Arzadún et al., 2018). The beginning of Choiyoi was marked by the PFD Tunas II-PP (upper) of 280.8 ± 1.9 Ma (López-Gamundi et al., 2013; Alessandretti et al.,

2013). Similarly, the Paraná basin registered the transition between the last part of pre-Choiyoi magmatism in the PFDs of the Rio Bonito Formation, that yield ages of 298.23 ± 0.31 Ma (Griffis et al., 2018) to 291 ± 1.3 Ma (Simas et al., 2012). The beginning of the Choiyoi magmatism was also recorded in PFDs of the final stages of the Rio Bonito Formation. The PFD FAX of 286.52 ± 0.30 Ma (Griffis et al., 2018) and the PFDs of the Irati Formation dated in this work of 284.1 ± 3.5 Ma to 280.8 ± 1.4 Ma (Figure 2 and Figure 4F).

The mountain belts formed by the orogeny were high enough to trigger part of the Late Paleozoic Ice Age (LPIA) and create climatic barriers (Figure 5A) (Isbell et al. 2012; Montañez and Poulsen, 2013). The barriers may have induced paleoclimatic changes in Western Gondwana (Figure 4D), establishing drier conditions and favoring the adaptation of forests of gymnosperms of the *Glossopteris flora* (DiMichele et al., 2001; Montañez et al., 2007), and pteridophytes and ferns (Martins et al., 2020b). The climate was gradually warming (Figure 4D) during the Post-glacial stage (Limarino et al., 2013; Qie et al., 2019), hence allowing regions of high latitudes of Gondwana to be dominated by forests of gymnosperms of the Glossopteris flora (DiMichele et al., 2001; Montañez et al., 2007). These adaptations probably lead to morphological changes in the pollen grains of taeniate bisaccate (e.g. Stephenson, 2016), enabling the new Palinozona Lueckisporites virkkiae (Figure 4C) (Stephenson, 2008; Iannuzzi, 2013; Vázquez and César, 2017; Rocha et al., 2020). Simultaneous adaptive changes occurred between terrestrial vertebrates (Ahlberg and Milner, 1994; Sahney et al., 2010) and insect faunas (Harrison et al., 2010).

5.2. Paleoenvironmental Reconstruction during the Cisuralian

The paleoenvironmental reconstruction present in this paper was based on the chronostratigraphic and tephrochronological correlations of the Irati Formation (Figure 3). It was integrated with the stratigraphic sequence interpretation proposed by Xavier et al. (2018), global multi-proxy chronostratigraphic reconstructions (Figure 4) (Montañez

and Poulsen, 2013; Qie et al., 2019), Western Gondwana palaeogeographic reconstruction of Cisuralian (Figure 5) (Scotese, 2014), paleoenvironmental reconstructions of depositional domains (Araújo, 2001), and references of paleoclimatic/paleoenvironmental conditions of the Paraná Basin during the Cisuralian epoch.

During the Asselian and Sakmarian stages the LPIA caused frequent glacio-eustatic oscillations in the level of Panthalassa paleo-ocean during its post-glacial (Limarino et al., 2013; Qie et al., 2019) or P1 stages (Figure 4D) (Qie et al., 2019). It is interpreted that this oscillations was influenced in part by the prolonged $CO_{2\ atm}$ increase (Figure 4D) and in part by Milankovitch orbital-climate controls (Montañez and Poulsen, 2013; Ogg et al., 2016; Griffis et al., 2019). The Gondwanides Orogeny might have influenced on the increase in $CO_{2\ atm}$ due to release of large volumes of greenhouse gases, such as CO_2 and SO_2 (Sato et al., 2015) during the Chanic Orogenic Phase and its pre-Choiyoi orogenic magmatism (Figure 4B). During the Artinskian, the LPIA oscillations decreased (Figure 4D) (Montañez and Poulsen, 2013).

5.2.1. Sequence 1 (S1)

The northern domain of the Paraná Basin covers São Paulo state. There the beginning of the Taquaral Member deposition occurred above an erosional discordance over the Tatuí Formation (Guatá Group) (Chahud, 2020), in shallow platform physiography (Hachiro, 1996; Chahud and Petri, 2010; 2013a; 2013b). The basal portion of the sedimentary package presented faciology typical of high-energy episodic events. It comprised conglomeratic sandstone levels of average thickness between 9.5 and 15 cm, of lenticular bedding with asymmetric cross stratifications and allochthonous fossil fragments. The conglomerates contain grains in granule to pebble size were composed of angular to rounded silexite. They occurred with contact with each other sporadically and dispersed in a medium- to fine-grained sandstone matrix. The fossils were of disarticulated vertebrates such as fish remains (scales, teeth and bone

fragments), acritarchs, crustaceans and algae (Chahud and Petri, 2013a; 2016; Chahud, 2020), all of different sizes. Algae components present red and green color, possibly of *Botryococcus* due to its tolerance to fresh and brackish water (Reis et al., 2018; Martins et al., 2020a). The upper part of the sedimentary package on the other hand consists of typical faciology similar to those observed in the

TOC and HI values (Figure 3A). The biomarkers of the Taquaral Member indicated marine environment with medium salinity, with more significant influence of preserved plants. It also suggested lower relative proportion of preserved amorphous organic matter, which is characterized by the predominance of type III terrestrial organic matter (Reis et al., 2018) with values of $\delta^{13}C_{(org)}$ ranging from -28.9 ‰ to -25.1 ‰ (Bastos et al., 2021). As in other places of the basin (Ng et al., 2019), the HV-44-RS drill core (Figure 3A) presented unoxidized amorphous organic matter and pyrite nodules (Xavier et al., 2018).

On the present study it is assumed that in the southern domain the Taquaral Member of the Irati Formation (open marine offshore environment) constituted a marine environment. It coexisted laterally with the Palermo Formation (shoreface and marine embayments) and Rio Bonito Formation (lacustrine/estuarine and fluvial environments) during the marine transgression during the Cisuralian period (Figure 4). These units were related to the same geotectonic setting (depositional ramp with regional southwestward dip), same paleoenvironment (siliciclastic, high redox potential, intracratonic with free marine circulation and normal salinity) (Araújo et al. 2004; Xavier et al., 2018) and same palynological zone (Rocha et al., 2020). In the paleogeographic reconstruction, the Taquaral Member represented the deepest region of the basin (Figure 6A) and corresponded to Stage I of Bastos et al. (2021). The transition between the Palermo Formation and the Taquaral Member was gradual in portions of the basin (Xavier et al., 2018; Reis et al., 2018). The transition was identified based on decreasing bioturbation records, increasing dark tonality of the shales, changing resistivity and/or increasing TOC values (e.g. Figure 3A).

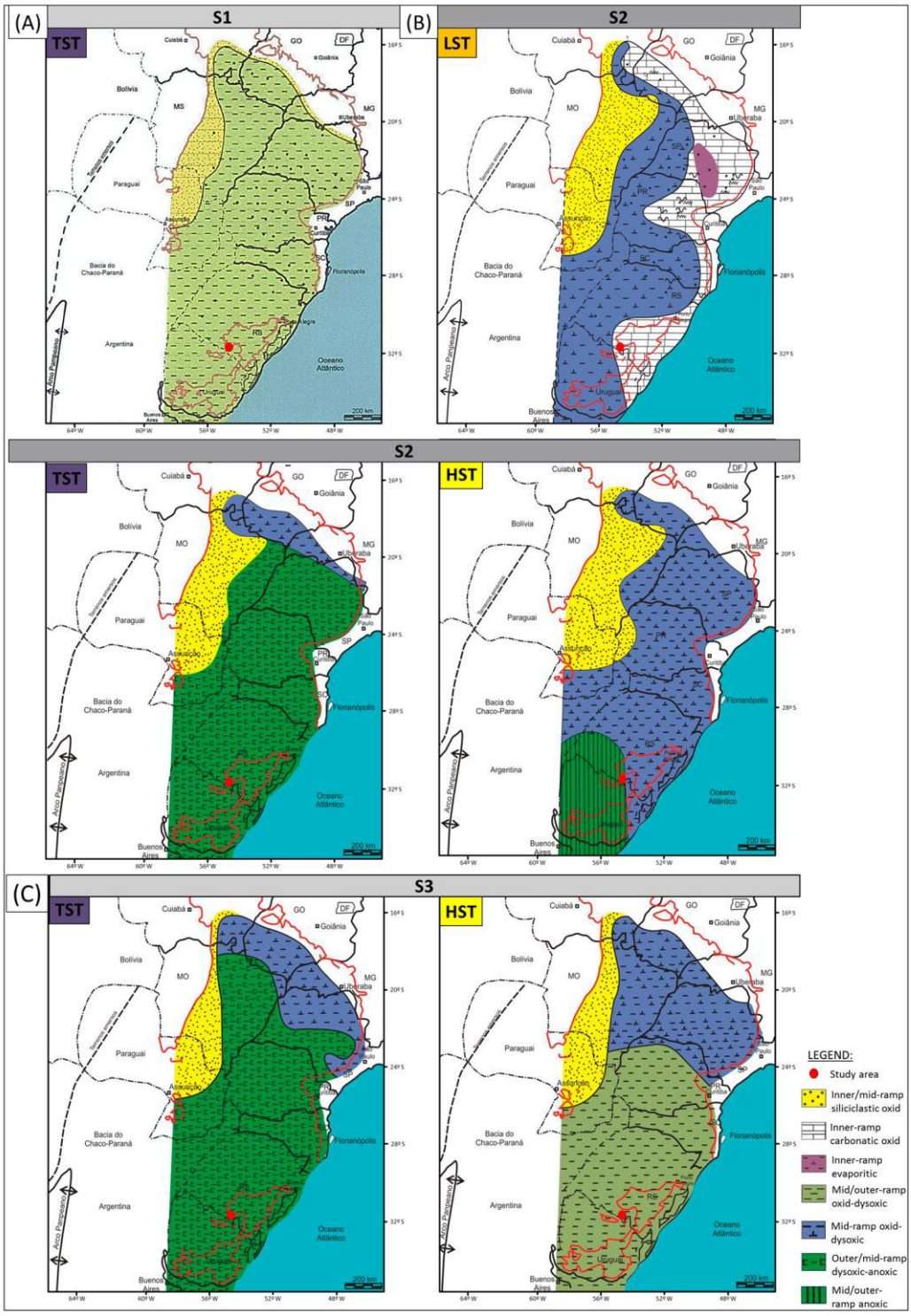

Figure 6 – Depositional sequence of the Irati Formation and paleoenvironmental reconstructions of the depositional domains (modified from Araújo, 2001). (A) Transgressive systems tract (TST) of the S1 sequence by Xavier et al. (2018). (B) Lowstand systems tract (LST), TST and highstand systems tract (HST) of the S2 sequence of Xavier et al. (2018). (C) TST and HST of the S3 sequence by Xavier et al. (2018).

In the southern portion of the Paraná Basin (Rio Grande do Sul state) the paleo-valleys eroded during the post-glacial Pennsylvanian stage (Fedorchuk et al., 2019) and coastal regions (Maahs et al., 2019) were filled by the Rio Bonito and the Palermo Formations. These formations were deposited under a mild to cold seasonal climate (Figure 4D) characterized by dry summers and rainy winters (Holz et al., 2010). They formed carbonaceous deposits in paludal environments of significant heterogeneity, embedded in paleo-valleys (Fedorchuk et al., 2019; Fritzen et al., 2019). *Glossopteris* flora were also associated to this environment (Montañez et al., 2007; Limarino et al., 2013; Mendonça-Filho et al., 2013; Griffis et al., 2019).

The different numerical ages of PFDs (tonsteins) of the Rio Bonito Formation evidenced different deposition intervals in the southern domain of the Paraná Basin. The PFDs located outside the Mariana Pimentel and Leão paleo-valleys (Fedorchuk et al., 2019) are older, and date 298.1 ± 0.28 Ma on the Quitéria Coalfield (Cagliari et al., 2016; Griffis et al., 2018) and 291 ± 1.3 Ma in the Leão-Butiá Coalfield (Simas et al., 2012). Conversely the PFD within the Mariana Pimentel paleo-valley presented Artiskian age of 286.5 ± 0.3 Ma (Faxinal Coalfield - Griffis et al., 2018), which is 12 Myr and 8 Myr younger than the other tonsteins of Rio Bonito Formation. The relationship between the age of PFDs and a global eustasy variation (figure 4), occurs that the Rio Bonito Formation deposited in transgression events. The PrAs3-MFS transgression (TS-Creator 7.4) coincided with the Quitéria Coalfield age around 298 Ma (Figure 4E), the PrSak5-MFS transgression coincided with the Leão-Butiá Coalfield age of 291 Ma, and the PrArt3-MFS transgression coincided with the Faxinal Coalfield age of 286 Ma. The second order maximum flooding surface (MFS) of the Gondwana I Supersenquence can be observed in the upper portion of the Palermo Formation (Milani, 1997; Holz et al., 2010) and was developed around 288 Ma (Figure 4E) (Montañez and Poulsen, 2013).

The age of 286.5 ± 0.3 Ma of PFD FAX (Griffis et al., 2018) was similar to the age of 284.1 ± 3.5 Ma of PFD BIR9 that was determined in this work (Figure 3C). This correlation when associated with the global eustatic information (Figure 4E) enabled interpreting that the Taquaral Member was laterally coeval with the upper part of the Guatá Group (Rio Bonito and Palermo Formations). This close relation possibly occurred after MFS at 288 Ma during the Artinskian stage (Figure 4E) (e.g. Milani et al., 2007).

Furthermore, the global marine transgression that occurred during the Artinskian (~288 Ma) (Figure 4E) might have enabled the connection between the Paraná Basin and the Parnaíba Basin, as suggested by Zalán and Romeiro-Silva (2007). It is interpreted that this connection would have occurred across the Sanfranciscana Basin (Figure 5B), based on the faciological records of the Taquaral Member in the northern domain (Hachiro, 1996; Chahud and Petri, 2010; 2013a; 2013b; 2015; 2019; Chahud, 2020) and the Tabuleiro Member in the Sanfranciscan Basin (Campos and Dardenne, 1997a; Campos and Dardenne, 1997b; Sgarbi et al., 2001). The Taquaral Member in the northern domain presented episodic high energy basal deposits. The Tabuleiro Member had textural maturity, consisting of medium sandstones with planar-parallel bedding. Its mineralogy showed sub-rounded to rounded quartz grains, with high primary porosity (up to 16%) (Campos and Dardenne, 1997a; Campos and Dardenne, 1997b; Sgarbi et al., 2001; Zalán and Romeiro-Silva, 2007).

The paleocurrent of the Tabuleiro Member was from northeast to southwest (S20W) in a north-south axis (Campos and Dardenne, 1997b), hence indicating water circulation from the Parnaíba Basin to the Paraná Basin (e.g. Figure 5B). This allowed us to interpret that the marine transgression of the Parnaíba and Sanfranciscana Basins successfully transposed the São Francisco Arch. Therefore, forming a broad shallow channel over depressions of glacial paleo-valleys of the São Francisco Craton. It is likely that during the transposition of the arch unconsolidated sediments were remobilized and initiated the Taquaral Member deposition. These sediments were formed under warm temperate to arid conditions, likely of silica gossan that then constituted the angular to rounded silexite (Chahud and Petri, 2013a; 2016; Chahud, 2020). Thus, the basal deposits of the Taquaral Member were more likely to be generated by a deltaic system close to the coast and further reworked by waves (e.g. Miall, 2016). Also probably related to an influx of fresh water and presence of considerable continental material (Rocha et al., 2020), rather than an episodic tempestite event (Chahud and Petri, 2013a; 2015; 2016; Chahud, 2020).

Thus, the Taquaral Member deposition in the northern domain of the Paraná Basin indicates deposition in shallow marine environment close to the coast. Whilst the deposition in the southern region of the basin would have remained subaqueous, with increasing energy and dysoxic conditions on the substrate (Reis et al., 2018). Due to

transgression the deposits of the northern domain evolved to thinner marine deposits, similar to those of the southern domain of the basin. Contemporaneously the Tabuleiro Member was deposited on a higher energy environment in the São Francisco Craton. The pelagic/hemipelagic facies of the Taquaral Member are composed mainly of illite, chlorite, and kaolinite (Holanda et al., 2019). Kaolinite formation could be related to chemical weathering of continental materials, including granitic and metamorphic rocks rich in feldspars. The illite and chlorite could be related to physical weathering of basement rocks (e.g. Chamley, 1989; Velde, 1992; Meunier, 2005; Gislason and Oelkers, 2011).

The end of the connection between the basins could be associated with marine regression (Figure 4E), coinciding with the emergence of the Assistência Member and Ecca Group. To reinforce this hypothesis it should be accounted the paleontological chrono-correlation between the species *Petalodontiformes Itapyrodus punctatus* and *XenacanthiformesTaquaralodus albuquerquei*, present in the Taquaral Member and the Pedra do Fogo Formation of the Parnaíba Basin (Chahud and Petri, 2013b; 2014; 2015; 2016; Cisneros et al., 2015; Chahud, 2020). The paleogeographic reconstruction of Scotese (2014) (Figure 5A) differs from the present interpretation.

5.2.2. Sequence 2 (S2)

The environmental transition from the Taquaral Member to the Assistência Member represents a critical moment in Western Gondwana. In the Paraná Basin, there was a complete shift in the depositional system and the paleoenvironment between the Taquaral and the Assistência Members, even though they occurred in the same geotectonic setting. It is presently considered that the change in the depositional system of the Irati Formation could be related to the end of the connection between the Paraná Basin and the Parnaíba Basin. This cessation could have caused a decrease in environmental energy conditions, and consequently increase in the bio-productivity rate and reduction of the redox potential (Araújo, 2001; Xavier et al., 2018).

In the Karoo Basin the PFD DPAL2 that occurred in the Prince Albert Formation (Figure 3C), on the basal part of the Ecca Group, presented numerical age of 282.17 Ma ± 0.44 Ma (Griffis et al., 2019). On the same study it was determined an age of 282 Ma for the T-P2 stratigraphic package of the Ecca Group. Griffis et al. (2019) also associated glacial retreat and increased CO_2 as the cause for the change in the depositional system. A genetic correlation of this package with the Assistência Member was considered. The cause of the shift in the depositional system could also be associated with the extinction between the Parnaíba and Paraná Basins.

Based in paleogeographic reconstructions (Figure 6B), the transition from the Taquaral Member to the Assistência Member was interpreted as product of a marine regression. The regression could be caused by a 3rd or 4th order eustatic decline (Figure 3B) (Xavier et al., 2018), in response to PrArt2 (TS-Creator 7.4). This event marked the beginning of the deposition of the S2 sequence, with Lowstand Systems Tract (LST). It lasted around 0.5 Myr (Figure 3), corresponding to depositional stages II and III of Bastos et al. (2021). There was a sudden change in occurrence of siltstones and mudstones (Taquaral Member) to limestones and mudstones rich in organic matter (Assistência Member). It resulted in a mixed depositional system (siliciclastic-carbonatic-evaporitic system) (Araújo, 2001; Xavier et al., 2018; Bastos et al., 2021) categorized as three depositional domains in LST: shallow inner-ramp, mid and outer-ramp. In the HV-44-RS section, the transition from the Taquaral Member to the Assistência Member is characterized by lowered of base level, marked by the SB_2 surface (Xavier et al., 2018).

The carbonatic oxic inner-ramp was related to shallow water with oxide-dioxide conditions in its substrate. It is characterized by partially oxidized amorphous organic matter and opaque phytoclasts, associated with organic matter of type II/III to III (Reis et al., 2018; Nascimento et al., 2021). The arid climate promoted evaporation and establishment of reducing and hypersaline conditions, the latter estimated at 35 ‰ (Araújo et al., 2004). The hypersaline and sulfur-rich paleoenvironment is supported by the low values of pristane/phytane ratios, presence of C32 lanostane and C32-35 benzohopanes (Reis et al., 2018; Nascimento et al., 2021). The development of biogenic processes by photosynthetic organisms was favored on the environment of water saturated in Ca^{2+} and $2HCO_3^-$ (e.g. Schneider et al., 2000). This would promote the deposition of the authigenic carbonate fabric that had characteristics of subaerial

exposure (Xavier et al., 2018; Ng et al., 2019). Associated with carbonate deposits there was deposition of siliciclastic (Araújo, 2001) and opaque phytoclasts (Reis et al., 2018), and allochthonous to parautochthonous bioclasts such as bivalves, ostracods, and spongy spicules (Ng et al., 2019). The inorganic matter, $i C_{27\alpha\alpha\alpha}$ (20R) cholestane/$C_{29\alpha\alpha\alpha R}$ steranes and hopanes/steranes ratios suggested that carbonates were the product of the photosynthetic metabolic process of halophilic microbial mats (Reis et al., 2018), mainly green algae (or cyanobacteria), possibly generating the high $\delta^{15}N$ isotope values (8-12 ‰, Bastos et al., 2021).

Microbialites formed columnar structures of thrombolite type, associated with sponge spicules and authigenic glauconite with a dark green hue (Ng et al., 2019). The formation of authigenic glauconite related to microbial activity required specific physical-chemical conditions (Odin and Matter, 1981; Amorosi, 2012). The presence of glauconite indicated that the platform remained with constant water depth (possibly shallow <50 m) (e.g. Lavina, 1991), low energy and low sediment input for an increased period of time. It also suggested basic pH and reducing conditions, which are characteristic of marine transgression (starved basin) (Ng et al., 2019). This environment would be prone to flocculation of suspended colloidal particles and slow ion exchange by chemical diffusion of aqueous ions (mainly Fe^{3+}/Fe^{2+}, Si^{4+} and K^{+}) with the pelagic-hemipelagic substrate (e.g. Meunier, 2005). On the substrate, particles of biogenic materials (e.g. limestone bioclasts and siliceous spicules) or terrigenous materials (oxides and clay aggregates) would undergo dissolution processes. Hence, promoting replacement and authigenic growth of glauconite species (e.g. Fe-smectite; Fe-Al-smectite; Fe-K-illite) (Odin and Matter, 1981; Chamley, 1989; Velde, 1992; Meunier, 2005).

The carbonates associated with sapropelic environments conditioned the deposition of a pelagic-hemipelagic fabric in low energy conditions. Episodic high energy events (storms, forming tempestites) disturbed the substrate, hence mobilizing bivalve shells from their original location and forming levels of allochthonous disarticulated carapaces (Araújo, 2001; Matos et al., 2017; Xavier et al., 2018). The mid- and outer-ramp had shallow water and oxide-dioxide conditions on their substrate. The same pelagic-hemipelagic sediments (Araújo, 2001; Xavier et al., 2018) were deposited as relatively thin package (Figure 3A and Figure 6B). The environment presented more

restricted conditions than the Taquaral Member, containing authigenic minerals such as sulphides and sulphates.

Based on paleogeographic and paleoenvironmental reconstructions of S2 it was possible to evaluate how the Irati-Whitehill Sea was formed. The restricted epicontinental type was formed over the continental region of Western Gondwana due to marine regression associated with the connection with the Panthalassa paleo-ocean (Figure 6B) (Araújo, 2001; Xavier et al., 2018; Bastos et al., 2021). The continental area that consisted of razed Precambrian terrains (Figure 1B) contributed to low sedimentary input rate, with predominant pelagic–hemipelagic sediments (Araújo, 2001; Xavier et al., 2018). Synchronously, the terrigenous and water inputs linked to the forming magmatic arc were barred by the foreland basins, bounded by Puna and Pampean Archs (Figure 5) (Limarino et al., 2013).

This condition enabled the basin to form with a negative water balance, hence causing its compartmentalization in sub-basins. For Araújo (2001) and Rohn (2007), the Ponta Grossa Arch presented movement from isostasy during the deposition of the Assistência Member. This triggered the internal compartmentalization of the basin and formation of distinct deposits, into shallower to the north and deeper in the southern domain. In the southern region, eustatic decline associated with regional warming and drier climate developed a rhythmic alternation of dolomitic limestones and shales (Hachiro, 1996; Schneider et al., 2000; Ng et al., 2019). The process was conditioned by variations of Milankovitch orbitals (e.g. Franco et al., 2012). Strictly in the northeastern sector one sub-basin showed negative water recharge, hence developing underwater evaporitic conditions. Evaporation promoted the formation of sulfate-rich brines with salt contents higher than 1g/L (Mohriak et al., 2008). The deposits were composed of up to two meters of evaporitic rocks consisting of dark-colored gypsum ($CaSO_4.H_2O$) and brecciated anhydrite ($CaSO_4$) (Hachiro, 1996; Araújo, 2001; Milani et al., 2007; Chahud and Petri, 2019; Nascimento et al., 2021).

In this same period the closure of the Uralian Seaway and the northeastern margin of the Paleo-Tethys Ocean took place in northern Pangea (Figure 5A and Figure 7A). This would later lead to the collision of Siberia and Laurasia continents, forming the Pangea Supercontinent (Torsvik and Cocks, 2017). The continuous closure of the

seaways restricted circulation between the warm equatorial and north polar water currents, leading to changes in global oceanic and atmospheric circulations (Torsvik and Cocks, 2017). In this condition, arid and semi-arid conditions were installed in a vast equatorial continental region of Pangea. This favored the installation of a globally unique climate system, uniting two arid belts of the equatorial region associated with the Hadley Cell (Figure 7B) (Qie et al., 2019; Jones et al., 2021). The evaporite deposits of the Assitência Member (Figure 7A) were paleoclimatic indicators sensitive to aridification conditions caused by the expansion of Hadley Cells in the equatorial regions during the Cisuralian (Figure 7A) (Martin, 2016; Qie et al., 2019), similarly to the aeolian deposits at Aracaré Formation, Sergipe-Alagoas Basin (Jones et al., 2021). Under this condition Hadley Cells (Figure 7B) would be permanently installed, hence leaving the LPIA restricted to Eastern Australian glaciation P2, Antarctica and high alpines, from the end of Cisuralian up to the Guadalupian stage (Figure 4D) (Isbell et al., 2003; 2012; Montañez and Poulsen, 2013).

The basin likely recharged from continental waters and melting waters from LPIA (Figure 5A) (Isbell et al. 2012; Montañez and Poulsen, 2013; Qie et al., 2019), as initially proposed by White (1908). Meltwater travelled long distances in complex glacial-fluvial and fluvial drainage systems, crossing the paleo-valleys (e.g. Martins et al., 2020a) to the Irati-Whitehill Sea. Above the carbonaceous deposits of the Mariana Pimentel Paleo-valley (~285Ma, Griffis et al., 2018), there were fluvial deposits (Siderópolis Member) (Fedorchuk et al., 2019). These fluvial deposits are likely to record the passage of glacier waters from western Namibia and likely occurred coevally to the Irati Formation (e.g. Tedesco et al., 2016; Fallgatter and Paim, 2019). The $\delta^{13}C$ values of the HV-44-RS drill core ranged from -22 to -28 ‰, suggesting an increase in terrestrial input (Figure 3A). This hypothesis is corroborated by the high isotope ratio of light $\delta^{18}O$ (22 and 28 ‰) (Faure and Cole, 1999), which is above global values for that time (21 to 22 ‰, Qie, et al., 2019). It also suggested that illite possibly formed through physical weathering triggered by glaciers and deposited in the pelagic-hemipelagic sediments of the southern domain of the basin (Holanda et al., 2019).

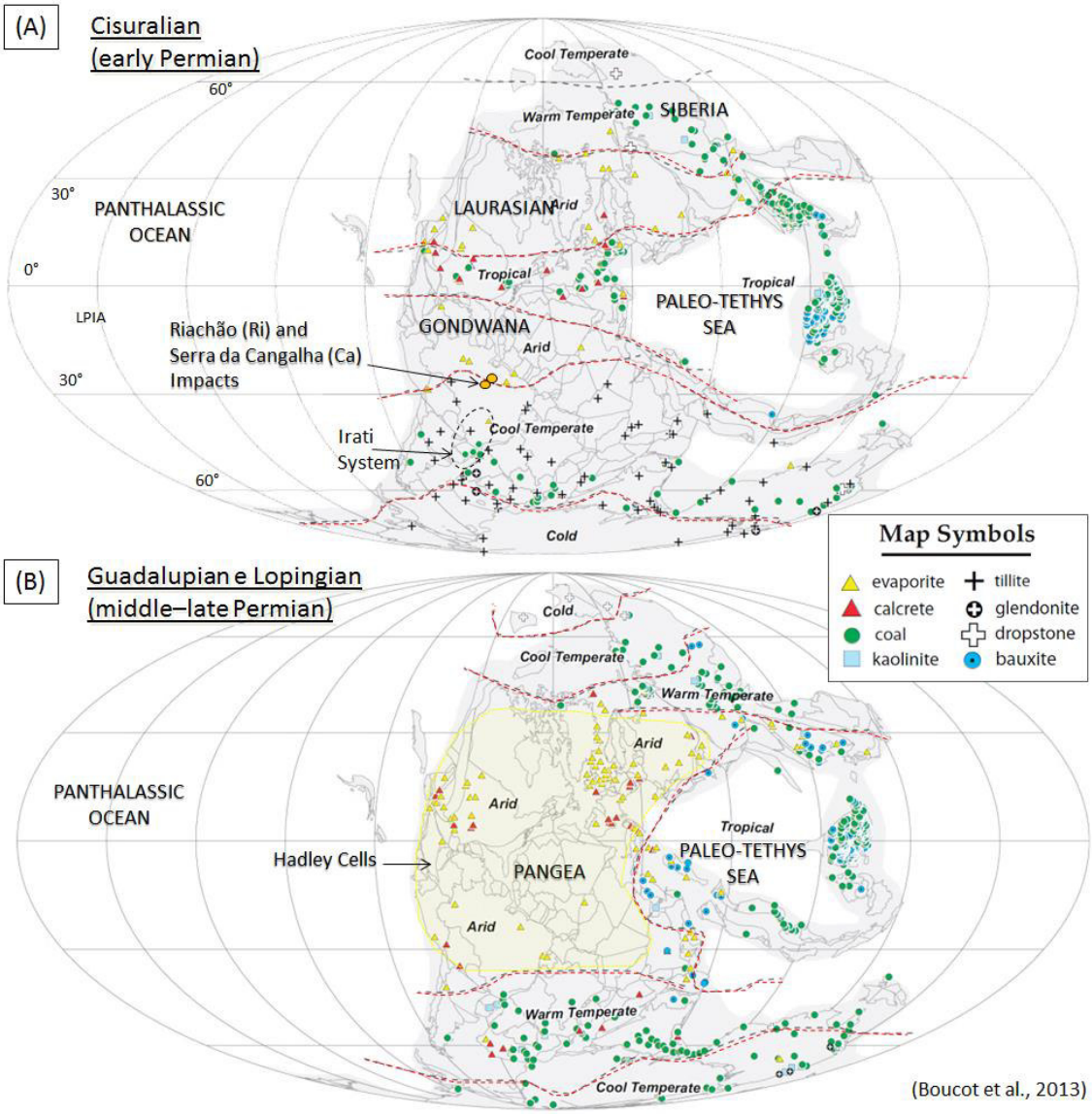

Figure 7 - Phanerozoic paleoclimatic reconstruction of the Permian. (A) Paleoclimatic map of Cisuralian epoch (Modified from Boucot et al., 2013) and location of the Impact cratering in the Parnaíba Basin (Crósta et al., 2019). (B) Paleoclimatic map of the Guadalupian and Lopingian epochs (Modified from Boucot et al., 2013) with respective Hadley Cells (yellow polygon).

Sequence 2 (S2) - TST

During the PrArt3 transgression (Figure 3B) environmental changes occurred. The base level was raised (Figure 6B), as well as the increase of water input from the Panthalassa Ocean (Beurlen, 1957; Lavina, 1991; Araújo, 2001). The increased base level generated accommodation space in the outer-ramp, hence retracting the carbonate

fabric and predominating the pelagic-hemipelagic sediments. North of the Ponta Grossa Arch, the inner-ramp was subjected to aggradation of carbonate with intercalations of pelagic-hemipelagic sediments under slow relative rise in sea level (Araújo, 2001).

In the southern domain the environment of the substrate remained aerobic for approximately 0.5 Myr (Figure 3A). It was marked by sedimentation of pelagic-hemipelagic facies with plane-parallel laminations and bioturbation containing organic matter predominantly composed of type III opaque phytoclasts (Reis et al., 2018).

Subsequently the substrate evolved to dysaerobic to reducing anoxic, with laminated and often bituminous shales with little to no indication of bioturbation (Figure 3A). The shales presented moderate to high TOC values (1% - 12%, up to 26%), S (2% - 6%), HI (200 - 500 mgHC /gTOC) (Faure and Cole, 1999; Araújo, 2001; Milani et al., 2007; Martins et al., 2020a; Nascimento et al., 2021) and high values of U and Mo (Goldberg and Humayun, 2016). The organic matter was heterogeneous, composed of mixture of liptinitic and amorphous kerogen type I/II, II to II/III, originated mainly from phytoplankton (green and red algae), zooplankton and opaque phytoclasts from higher plants (Reis et al., 2018; Martins et al., 2020a; Bastos et al., 2021). This mixture represented a blend of autochthonous organic matter and allochthonous terrigenous organic matter. Evidences showed that this anoxic event was shorter and more intense in relation to the second event (Xavier et al., 2018), lasting around 1.2 Myr (Figure 3B). The chrono-correlation with Prince Albert Formation of Karoo Basin using the PFD-DPAL2 with a numerical age of 282.17 Ma ± 0.44 Ma (Griffis et al., 2019) evidenced that the anoxic event was restricted to the Paraná Basin.

The paralytic conditions and the compositional variation of water input of continental (less dense and warmer) and marine settings (denser and colder) of the Panthalassa paleo-ocean promoted changes on the sedimentation environment. It conditioned asapropelic environment (approximately ≤30 ppm of dissolved salts) and promoted stratification due to thermocline surfaces in the water column. The reduced salinity can be confirmed by biomarkers (lower gammacerane/C_{30}αβ hopane and $C_{28ααα}$(20R) methylcholestane/$C_{29ααα}$(20R) ethylcholestane ratios) (Reis et al., 2018) and stratification in the water column observed by presence of other biomarkers

(tetrahydrophenanthrene and gammacerane at high concentrations) (Martins et al., 2020a).

On the continent a noticeable spread of terrestrial plants such as *Glossopteris flora*, ferns and other pteridophytes (Martins et al., 2020b) occurred. It likely contributed to increase the intensity of the hydrological cycle due to increased transpiration and surface runoff. Also accentuated the biogenic weathering by the action of roots, promoting the release of ions into the Irati-Whitehill Sea (Martin, 2016). Nutrient supply increased due to input of materials of various origins, such as continental (mainly phosphate- PO_4 and nitrates- NO_3), glacial, volcanic ash and the partial mixture between fresh and saltwater. The nutritious environment favored the modification of the oligotrophic surface condition of the aqueous body to eutrophic and the establishment of a complex depositional paleoenvironment (e.g. Martins et al., 2020a).

During this period, bivalve invertebrate fauna developed in coastal or transitional regions, where shallow and calm waters provided an ideal environment for their development (Matos et al., 2017). The sapropelic environment linked to establishment of the carbonate fabric favored the development of euryhaline organisms that were adapted to lower salinity conditions. Thus, the environment was favorable to phytoplankton (e.g. planktonic algae *Botryococcus)* development in the photic zone (Faure and Cole, 1999; Reis et al., 2018; Martins et al., 2020a). A thermocline surface in the water column made the marine substrate depleted in oxygen, sometimes dioxide (suboxide) but mostly anoxic ($0_2 \cong$ zero).

Under low redox conditions in the marine substrate, bacteria would consume the limited oxygen available, and additionally, the nitrates and sulfates for biochemical degradation. Carbon dioxide (CO_2), nitrogen (N_2) and hydrogen sulphide (H_2S) would be released as result of the oxidation and sulfate-reduction processes of the environment. Thus, the environment became hostile to the aphotic fauna, restricting the permanence of benthic invertebrates in the basin substrate. These characteristics favored the preservation and accumulation of high concentrations of bacteria, phytoplankton, and higher plantsas organic matter in the basin substrate (C_{org}) (Reis et al., 2018; Bastos et al., 2021). The evidence of increased phytoplankton productivity could be observed by the high value of light carbon isotopes (Figure 3A) throughout the Assistência Member

($\delta^{13}C_{(org)}$ between -26 and -22 ‰ $_{PDB}$) and the predominance of isopropenoids among biomarkers (Araújo, 2001; Martins et al., 2020a; Nascimento et al., 2021). In addition to evaporative settings (Bastos et al., 2021), the high values of $\delta^{15}N$ in the carbonates may indicate that the organisms used NO_3 in their metabolic processes of bioproduction. It could also indicate that suboxic conditions consumed the dissolved nitrate in substitution of O_2 in the process of oxidation of organic matter (Bastos et al., 2021).

The absence of chlorite and kaolinite clay minerals on the pelagic-hemipelagic sediments in the anoxic substrate was very noticeable. According to Holanda et al. (2019) the lack of chlorite (especially ferritic chlorite) in this interval could be due to the syndepositional process in a highly reduced environment. That would promote the remobilization of iron, which in solution along with sulfur would form authigenic framboidal pyrite (FeS_2). According to Martins et al. (2020b), clay minerals influenced the distribution of preserved organic matter isomers, favoring authigenic formation of clay minerals of the smectite group. Some of these clay minerals could be saponite (Holanda et al., 2019) or montmorillonite, the latter being a clay mineral in equilibrium with the thermodynamic conditions of the system (e.g. Meunier, 2005), as suggested by Martins et al. (2020b).

5.2.3. Sequence 3 (S3)

The depositional cycle S3 was associated with PaKun1 (TS-Creator 7.4) and resulted from a new marine regression and transgression (Figure 3B and Figure 6C), corresponding to stages IV and V by Bastos et al. (2021). In the HV-44-RS drill core, this transition was marked by sequence boundary SB_3 (Xavier et al., 2018). With small thickness and ample deposition time, the S3 evidenced sedimentary condensation formed during this stage that lasted for about 6 Myr (Figure 3B), with a considerable accumulation of fossils (Xavier et al., 2018; Ng et al., 2019). In the northeastern part of the Paraná Basin, a very typical 1-1.5 m thick fine sandstone with parallel to hummocky cross stratification separates the Irati Formation from the Corumbataí Formation (Rohn, 2007). This sandstone presented some articulated mesosaurid bones and hence

evidenced that mesosaurids dominated the entire sea in S3. The second anoxic event in S3 was developed in a different paleogeographic situation than the first event, occurring in a condition with relatively high accommodation space.

The Mangrullo (274.9 ± 2.1 Ma, Rocha-Campos et al., 2019) and Whitehill Formations (280.5 ± 2.1 Ma, Werner, 2006) are composed by bituminous shale and contain mesosaurids. By geochronological and biostratigraphic correlation, both formations were synchronic and equivalent to the S3 of the Assistência Member of the Irati Formation (Figure 3C). Such a condition could have been caused by regional flexural subsidence, due to an intracontinental syneclisis generated by the SROP at 281 Ma (Milani and De Wit, 2008; Bastos et al., 2021). In this new transgressive event, the water column would again be stratified. Although salinity declined (Gam/C30H and βC/C30H ratios; Nascimento et al., 2021), the redox condition remained stable, hence preserving high contents of organic carbon (TOC ≈ 6%) and sulfur (S: 1–3.5%) in the region of the drill core HV-44-RS (Figure 3A) (Araújo, 2001). Dry climate and aerobic condition during carbonate deposition is suggested by the mixture of opaque phytoclasts and partially oxidized pollen grains along with abundance of *taenate bisaccate* pollen grains. The predominance of type III organic matter suggests a more significant contribution from higher *Glossopteris* flora plants and pteridophytes. There was also the influence of green algae (Reis et al., 2018). Organic matter was predominantly of type II / III, while samples from the poorest abundance in organic matter showed predominance of type III organic matter (Reis et al., 2018). Among the biomarkers, higher proportions of phytane and gammacerane were identified, indicating a higher salinity of the environment (Reis et al., 2018).

The biotic conditions were also different during the S3 sequence (Figure 6C). During this period the environment would host fauna of fish and nektonic reptiles, due to the warm, oxygenated and brackish surficial waters. Among vertebrates, the amniote group *Mesosauridae* (*Progranosauria*) was one of the best-known taxa in this unit, containing *Mesosaurus Brasiliensis*, *Stereosternum Tumidum* and *Brazilosaurus* (Santos et al., 2006; Cisneros et al., 2015; Xavier et al., 2018; Chahud and Petri, 2019). These conditions would also host crustaceans and benthic bivalve in the coastal and transitional environment (Matos et al., 2017). The varying disoxide and anoxic siliciclastic basin substrate would sporadically host benthic fauna (e.g. Figure 3A). The

shallow marine paleoenvironment and dry climate influenced the evolution of the amniotes, both related to reproductive adaptation (laying eggs) and predation (seeking food). The paleoenvironmental setting corresponds to the reconstructions established by Bastos et al. (2021).

The beginning of the TST was marked by a layer of tempestite of about 60 cm thickness (Figure 3A) presenting *mesosaurid bonebed*. This level hosted massive concentration of disarticulated remains of those reptiles, carapaces of piogocephalomorph crustaceans and subordinate paleonisciform fishes (Xavier et al., 2018; Ng et al., 2019). This layer is associated with mass mortality events and is interpreted as distal deposits generated by episodic storm events (Lavina, 1991; Xavier et al., 2018). The tempestite phenomenon would promote the transport of shallow marine sediments to offshore environments through high energy flows. These flows would have the capacity to revolve sediments accumulated in the anoxic substrate bottom and to suspend toxic compounds with sulfur and nitrogen, hence causing mortality among nektonic and planktonic organisms in the most superficial and oxygenated regions of the water column (Lavina, 1991).

Correlations with nonmarine biochronology resulted in relative numerical age of approximately 280.6 Ma for this event that concentrated mesosaurid bonebed (Figure 3B). This age is close to the Redtankian Extinction Event (~ 283 Ma) (Figure 4C) proposed by Lucas (2017a; 2017b). These two events are temporally close to the meteorite impact in the Parnaíba Basin (Figure 4), which originated the Serra da Cangalha Dome (Lat 8°05'S/ Long 46°52'W) in the Tocantins state (Figure 5B). The impact produced a 13.7 km diameter crater in the Parnaíba Basin, causing pressure waves, earthquakes and tsunamis (Kenkmann et al., 2011). Estimates show that the meteorite had approximately 1.4 km in diameter (Vasconcelos et al., 2012) and that it released impact energy of roughly $2{,}74 \times 10^{20}$ J. This energy would have the capacity to produce a regional geological catastrophe but wouldn't be strong enough to promote mass extinction (Crósta et al., 2019).

Based on stratigraphic relationships (Kenkmann et al., 2011; Vasconcelos et al., 2013), it was determined that the impact occurred in the transition from Piauí to Pedra do Fogo Formations. However, no apparent sedimentary record of the fall in the basin

was observed. Vasconcelos et al. (2013) observed the formation of chert layers (cataclased and folded) and silicified sandstone around the Serra da Cangalha Dome, hence associating this occurrence with the impact event. Faria (1979) describes thin basal chert layers in the Pedra de Fogo Formation throughout the entire basin, which consisted of chert (mainly chalcedony and microcrystalline silica) interspersed with siltstones, shales and carbonate rocks. Kenkmann et al. (2011) stated that chert occurrence marks the transition from the Piauí to the Pedra de Fogo Formations. The chert layers around the Serra da Cangalha Dome might be related to chert basal layers in the Pedra de Fogo Formation, hence representing the sedimentary record of the bolide's impact in the Parnaíba Basin. The basal chert layers may thus contain both brecciated blocks originated by the secondary drop of the impact, as well as an unusual sequential episode of syndiagenetic silicification process (Faria, 1979). This syndiagenetic process represent the biogeochemical change that resulted from the impact in a restricted environment with intense evaporation. There the silica contained in sediments would have been solubilized and formed $H_3SiO_4^-$ (e.g. Brookins, 1988) due to the condition of high pH (pH> 9). This subsequently triggered the inorganic precipitation of cherts. While the Redtankian Extinction Event (Figure 4C) and mesosaurid bonebeds could possibly represent the effect of the impact (Figure 5B), the organic matter that was preserved on the cherts could represent the extinction of marine organisms of the Parnaíba Basin.

The transition between the Assistência Member to the Serra Alta Formation was gradational (Araújo, 2001; Holz et al., 2010; Reis et al., 2018; Xavier et al., 2018; Ng et al., 2019) and occurred at 274 Ma (Figure 3A). Xavier et al. (2018) established the transition level from the Assistência Member to the Serra Alta Formation at the end of the occurrence of bituminous shale. In terms of sequence stratigraphy, the top of the S3 (SB_4) would be positioned above the base of the Serra Alta Formation, comprising grey laminated siltstones with increased bioturbation. The shales contained type III organic matter, very low TOC (<0.5%), low values of S_2 (<0.5 mg HC/g rock), and HI (<90 mg HC/g TOC), related to non-bituminous shales (Figure 3A; Nascimento et al., 2021). The cease of the stratification on the water column and the gradual decrease in the substrate's anoxic conditions (Figure 4E) allowed the substrate to return to dysoxide-oxide conditions and enabled the rehabilitation of benthic O^{2-} consuming organisms (e.g.

Neregato, 2005; Martins et al., 2020a). Benthic organisms led TOC to decline (Figure 3A) due to the consumption of native organic matter and progressive decrease in $\delta^{15}N$ values (Bastos et al., 2020). The type III organic matter probably had its formation related to the detritic allochthonous terrigenous organic matter (phytoclasts), presumably linked to a more significant influx of freshwater.

According to Schneider et al. (1974), the Serra Alta Formation environment would reproduce conditions similar to those of the Taquaral Member, that is, deposit in calm waters below wave base in a restricted basin. However, relatively high salinity could be observed, as well as installation of regional aridization conditions in the system (Ng et al., 2019). Those changes lead to color variation in pelites from grey/black to pink/red (Warren et al., 2015). The low values of S (pyrite) and Gam/$C_{30}H$, suggest absence of stratification of the water column and relatively high salinity during deposition (Nascimento et al., 2021). The palaeogeography of the Serra Alta Formation is represented by stage V of Bastos et al. (2020).

In the northern domain of the basin, an erosional unconformity (diastema) occurs in the passage of the Assistência Member into the Serra Alta Formation. This erosion formed residual deposits (lags), presenting fish remains, coprolites and phosphatic nodules. During transgressive systems tract those deposits were subsequently overlapped by deposits of a new marine incursion (Warren et al., 2015). According to Milani et al. (2007), this was the last marine transgression in the Paraná Basin (Milani and De Wit, 2008; Bastos et al., 2020).

6. CONCLUSIONS

The study of the Irati Formation in southern Paraná Basin, along with the novel ages determined in zircons of PFD levels, limits the duration of the Irati System to the period between 286 Ma to 274.5 Ma, positioning the formation chronostratigraphically in the Cisuralian epoch (early Permian). The results are essential for advances in

paleogeography, paleoclimate and paleoenvironment and global chronostratigraphy (e.g. Qie et al., 2019). This study allows to establish the following conclusions:

1. The novel geochronological dating (Figure 2) along with interpretations of the stratigraphy of drill core HV-44-RS (Figure 3) allowed the regional depositional reconstruction of the Paraná Basin during the time of the Irati Formation deposition. This reconstruction was done in association with published paleoclimatic data (organic geochemical biomarkers, sedimentary provenance and stable isotope chemostratigraphy). Combining with regional tephrochronology correlation, it was possible to make more confident paleogeographic reconstructions of the Permian basins of Western Gondwana. Hence, improving the discussion of the factors that led to creating the conditions observed in the Irati-Whitehill Sea System during the Cisuralian epoch (Figures 4, 5 and 6). The results show the Irati System remained for approximately 12 Myr (286 - 274 Ma), including two periods of anoxic events with approximate duration of 1.2 Myr and 6 Myr, with relative numerical age of 84.5 Ma and 281.2 Ma for the establishment of LST in the Paraná Basin, and vertebrate mortality event of around 280.6 Ma.
2. Presently it is more evident that there was a close relationship between the Paraná Basin development in the continental interior and the Gondwanides tectonic regime. The Irati-Whitehill Sea System establishment started around 286 Ma and was due to the confluence of tectonic factors, the SROP and glacio-eustasy from the LPIA. The strata architecture of the formation was controlled by depositional conditions (basin style), global eustatic cycles and climatic variations along time. The Western Gondwana lithosphere may have reacted by flexure under the stress generated along the Gondwanides. Isso forneceu um mecanismo eficaz para criar um ambiente deposicional 'intracratônico' dentro de Gondwana, já que a elevação de suas bordas restringia a circulação entre as águas das bacias e o Panthalassa Paleo-oceânico. Meanwhile, allochtnous sediments were input in the basin due to the eroded Precambrian Gondwana terrain, deglaciation and volcanic ashes. Together, eustatic variations, climatic changes and marine biogeochemistry created conditions for the formation of autochthonous material, such as authigenic clay minerals, carbonates, glauconite, fossils and organic matter.
3. The Paraná Basin was connected to the Parnaíba Basin through the Sanfranciscana Basin likely due to the glacio-eustatic transgression of the early Permian. The cease of the connection possibly favored the emergence of the Irati-Whitehil Sea, coinciding with the emergence of the Assistência Member in Paraná Basin and Ecca Group in Karoo Basin.
4. During the Cisuralian the Western Gondwana was the locus of mesosaurid evolution, which is a species of oviparous aquatic tetrapods. They lived during the Kungurian (281 - 273 Ma) in the extensive epicontinental Irati - Whitehill Sea. In the Paraná Basin, mesosaurids are recorded in the S3 of the Irati Formation, while in Uruguay, they occur in the Mangrullo Formation. In the Karoo Basin the mesosaurids are present in the Whitehill Formation. Initially described by White (1908, p. 180), they were used by Alfred Wegener in 1912/1929 as evidence to corroborate the theory of drift of the continents, only accepted after 50 years of discussions and novel data.

ACKNOWLEDGEMENTS

The authors thank the Conselho Nacional de Desenvolvimento Científico e Tecnológico (CNPq) for financial support (process 140596/2016-0), and the Geological Survey of Brazil (CPRM), for the allowing access to the drill core HV-44-RS as well as retrieving samples for the study. We also thank the technicians from UFRGS laboratories.

REFERENCES

Aborrage, A.M. and Lopes, R.C., 1986. Projeto A Borda Leste da Bacia do Paraná: Integração Geológica e Avaliação Econômica. CPRM/DNPM, São Paulo, Porto Alegre 374p.

Ahlberg, P.E. and Milner, A. R. (1994). The origin and early diversification of tetrapods. Nature, 368(6471), 507–514. doi:10.1038/368507a0;

Alan, P.D., 2018. Radiogenic Isotope Geology, 3 ed. United Kingdom: Cambridge University Press, p.99-133. DOI: 10.1017/9781316163009

Alessandretti, L., Philipp, R.P., Chemale, F., Brückmann, M.P., Zvirtes, G., Metté, V., Ramos, V.A., 2013. Provenance, volcanic record, and tectonic setting of the Paleozoic Ventania Fold Belt and the Claromecó Foreland Basin: implications on sedimentation and volcanism along the southwestern Gondwana margin Journal of South American Earth Sciences. 71 pp.

Amorosi, A., 2012. The occurrence of glaucony in the stratigraphic record: distribution patterns and sequenceestratigraphic significance. International Association of Sedimentologists Special Publications 45, 37e54.

Araújo, L.M., 2001. Análise da expressão estratigráfica dos parâmetros de geoquímica orgânica e inorgânica nas sequências deposicionais Irati. PhD Thesis, Instituto de Geociências, Universidade Federal do Rio Grande do Sul, 2 v., 307 pp.

Araújo, L.M., Rodrigues, R., Scherer, C.M.S., 2004. Interrelação entre a fábrica sedimentar, o conteúdo orgânico e o potencial redox do ambiente deposicional, deduzida das litofácies de rampa distal das seqüências deposicionais da Formação Irati, Permiano da Bacia do Paraná. Boletim de Geociências Petrobras, Rio de Janeiro, v. 12, n. 2, p. 429-434, maio/nov.

Arzadún, G., Tomezzoli, R.N., Trindade, R., Gallo, L.C., Cesaretti, N.N., Calvagno, J.M., 2018. Shrimp zircon geochronology constrains on Permian pyroclastic levels, Claromecó Basin, South West margin of Gondwana, Argentina. Journal of South American Earth Sciences, 85, 191–208. doi:10.1016/j.jsames.2018.05.001

Azcuy, C.L., Beri, A., Bernardes-de-Oliveira, M.E.C., Carrizo, H.A., Di Pasquo, M., Saravia, P. Días, González, C., Iannuzzi, R., Lemos, V.B., Melo, J.H., Pagani, A., Rohn, R., Amenábar, C.R., Sabattini, N., Souza, P.A., Taboada, A., 2007. Bioestratigrafia del Paleozóico Superior de América del Sur: primera etapa de trabalho hacia una nueva propuesta. Revista de la Asociación Geológica Argentina, Publicação Especial 11, 9–65.

Bastías-Mercado, F., González, J., Oliveros, V., 2020.Volumetric and compositional estimation of the Choiyoi Magmatic Province and its comparison with other Silicic Large Igneous Provinces. Journal of South American Earth Sciences, 103, 102749

Bastos, L.P.H., Rodrigues, R., Pereira, E., Bergamaschi, S., Alferes, C.L.F., Augland, L.E., Domeier, M., Planke, S., Svensen, H.H., 2021. The birth and demise of the vast epicontinental Permian Irati-Whitehill sea: Evidence from organic geochemistry, geochronology, and paleogeography. Palaeogeography, Palaeoclimatology, Palaeoecology 562, p.13, 110103. https://doi.org/10.1016/j.palaeo.2020.110103.

Beurlen, K., 1957. Faunas salobras fósseis e o tipo ecológico-paleogeográfico das faunas gondwânicas no Brasil. An. Academia Brasileira de Ciência. 29, 229–241.

Boggs, S.Jr., 2014. Principles of Sedimentology and Stratigraphy. British Library Cataloguing-in-Publication Data. 5th Ed.,p. 434-474.

Bohor, B,F. and Triplehorn, D.M., 1993. Tonsteins: altered volcanic-ash layers in coal-bearing sequences. Geological Society of America Special Paper. v. 285, p. 1-44.

Boucot, A.J., Chen, X., Scotese, C.R., 2013. Phanerozoic Paleoclimate: An Atlas of Lithologic Indicators of Climate. SEPM, Concepts in Sedimentology and Paleontology, 11, 478p.

Brookins, D.G., 1988. Eh-pH diagrams for geochemistry, Springer-Verlag New York, 176p.

Cagliari, J., Philipp, R.P., Buso, V.V., Netto, R.G., Hillebrand, P.K., da Cunha Lopes, R., Basei, M.A.S., Faccini, U.F., 2016. Age constraints of the glaciation in the Paraná Basin: Evidence from new U-Pb dates. Journal of the Geological Society, 173(6), 871–875.

Campos, J.E.G. and Dardenne, M.A., 1997a. Estratigrafia e sedimentação da Bacia Sanfranciscana: uma revisão. Revista Brasileira de Geociências, 27(3), 269-282.

Campos, J.E.G. and Dardenne, M.A., 1997b. Origem e evolução tectônica da Bacia Sanfranciscana. Revista Brasileira de Geociências, 27(3):283-294.

Catuneanu, O., Hancox, P.J., Rubidge, B.S., 1998. Reciprocal flexural behaviour and contrasting stratigraphies: a new basin development model for the Karoo retroarc foreland system, South Africa. Basin Research, 10(4), 417-439. doi:10.1046/j.1365-2117.1998.00078.x.

Catuneanu, O., Wopfner, H., Eriksson, P.G., Caincross, B., Rubidge, B.S., Smith, R.M.H., Hancox, P.J., 2005. The Karoo basins of south-central Africa. Journal of African Earth Sciences. 43, 211-253.

Césari, S.N., Limarino, C.O., Gulbransen, E.L., 2011. An Upper Paleozoic biochronostratigraphic scheme for the western margin of Gondwana. Earth-Science Reviews, 106, 149–160.

Chahud, A. and Petri, S., 2010. Anfíbio e Palaeonisciformes da Porção Basal do Membro Taquaral, Formação Irati (Permiano), Estado de São Paulo, Brasil. Geol. USP, Série Científica, São Paulo, 10(1), 29-37.

Chahud, A. and Petri, S., 2013a. Paleontology of Taquaral Member silty shale in the State of São Paulo. Brazilian Journal of Geology, 43(1), 117-123. DOI: 10.5327/Z2317-48892013000100010.

Chahud, A. and Petri, S., 2013b. The silty shale Taquaral Member of the early Permian Irati Formation (Paraná Basin, Brazil). Paleontology and paleoenvironments. Swiss Journal of Palaeontology, 132(2), 119-128. Doi:10.1007/s13358-013-0055-1.

Chahud, A. and Petri, S., 2014. New chondrichthyans from the Irati Formation (Early Permian, Paraná Basin), Brazil: origin, palaeoenvironmental and palaeogeographical considerations. Proceedings of the Geologists Association, (125), 437-445.

Chahud, A. and Petri, S., 2015. Geology and Taphonomy from the Base of the Taquaral Member, Irati Formation (Permian, Paraná Basin), Brazil. Acta Geologica Polonica. 65(3), 379-387.

Chahud, A. and Petri, S., 2016. Paleontologia da fácies arenosa do Membro Taquaral (Permiano) no Estado de São Paulo: estado da arte e contribuições adicionais. Geologia USP. Série Científica, 16(3), 105-115. DOI: https://doi.org/10.11606/issn.2316-9095.v16i3p105-115.

Chahud, A. and Petri, S., 2019. Camada Laje Azul, Formação Irati (Bacia do Paraná, Permiano): Observações Paleontológicas e Paleoambientais. Anuário do Instituto de Geociências – UFRJ. 42(4), 410-416. ISSN 0101-9759 e-ISSN 1982-3908.

Chahud, A., 2020. Geologia e paleontologia do Membro Taquaral (Eopermiano) no afloramento do rio da Cabeça, estado de São Paulo. Estudos Geológicos, v 30(1), p.19-30. Doi:10.18190/1980-8208/estudosgeologicos.v30n1p19-30.

Chamley, H., 1989. Clay sedimentology. Springer, Berlin Heidelberg New York, 623 p..

Cisneros, J.C., Angielczyk, K., Kammerer, C.F., Smith, R.M.H., Fröbisch, J., Marsicano, C.A., Richter, M., 2020. Captorhinid reptiles from the lower Permian Pedra de Fogo Formation, Piauí, Brazil: the earliest herbivorous tetrapods in Gondwana. PeerJ, 8, 1-21. DOI:10.7717/peerj.8719.

Cisneros, J.C., Marsicano, C., Angielczyk, K.D., Smith, R.M.H., Richter, M., Fröbisch, J., Kammerer, C.F., Sadleir, R.W., 2015. New Permian fauna from tropical Gondwana. Nature Communications, 6(1), 1-8. Doi: 10.1038/ncomms9676.

Corfu, F., Hanchar, J.M., Hoskin, P.W.O., Kinny, P., 2003. Atlas of zircon textures, in: Zircon, Reviews in Mineralogy and Geochemistry, 53. In: Hanchar, J. M. and Hoskin, P. W. O., (Eds.). Mineralogical Society of America, Washington, DC, USA, 468–500,

Critelli, S. and Ingersoll, R.V., 1995. Interpretation of neovolcanic versus paleovolcanic sand grains: an example from Miocene deep-marine sandstone of the Topanga Group (Southern California), Sedimentology, 42, 783-804.

Crósta, A.P., Reimold, W.U., Vasconcelos, M.A.R., Hauser, N., Oliveira, G.J.G., Maziviero, M.V., Góes, A.M., 2019. Impact cratering: The South American record—part 1. Geochemistry 79, 1–61. https://doi.org/10.1016/j.chemer.2018.06.001.

De Rosa, R., Zuffa, G.G., Taira, A., Leggett, J.K., 1986. Petrography of trench sands from the Nankai Trough, southwest Japan: implications for long distance transportation. Geological Magazine, v. 123, p. 477-486.

del Rey, A., Deckart, K., Planavsky, N., Arriagada C., Martínez, F., 2019. Tectonic evolution of the southwestern margin of Pangea and its global implications: Evidence from the mid Permian Triassic magmatism along the Chilean-Argentine border. Gondwana Research, 76, 303-321. https://doi.org/10.1016/j.gr.2019.05.007.

DiMichele, W.A., Stein, W.E., Bateman, R.M., 2001. Ecological sorting during the Paleozoic radiation of vascular plant classes. In: Allmon, W.D. and Bottjer, D.J., (Eds.), Evolutionary Paleoecology: New York, Columbia University Press, p. 285–335.

Einsele, G. and Seilacher, A. (Ed.), 1982. Cyclic and Event Stratification. Springer-Verlag, Berlin, 536 pp.

Einsele, G., Chough, S.K., Shiki, T., 1996. Depositional events and their records-an introduction. Sedimentary Geology. 104, p.1-9.

Fallgatter, C. and Paim, P.S.G., 2019. On the origin of the Itararé Group basal nonconformity and its implications for the late Paleozoic glaciation in the Paraná Basin, Brazil. Palaeogeography, Palaeoclimatology, Palaeoecology, 531. https://doi.org/10.1016/j.palaeo.2017.02.039.

Faria, Jr., L.E.C., 1979. Estudo sedimentológico da Formação Pedra de Fogo – Permiano – Bacia do Maranhão. Dissertação de Mestrado, Núcleo de Ciências Geofísicas e Geológicas, Universidade Federal do Pará, 57 p.

Faure, F. and Cole, D., 1999. Geochemical evidence for lacustrine microbial blooms in the vast Permian Main Karoo, Paraná, Falkland Islands and Huab basins of southwestern Gondwana. Palaeogeography, Palaeoclimatology, Palaeoecology, 152, 189–213.

Fedorchuk, N.D., Isbell, J.L., Griffis, N.P., Montañez, I.P., Vesely, F.F., Iannuzzi, R., Rosa, E.L.M., 2019. Origin of paleovalleys on the Rio Grande do Sul Shield (Brazil): Implications for the extent of late Paleozoic glaciation in west-central Gondwana. Palaeogeography, Palaeoclimatology, Palaeoecology, 531(1). https://doi.org/10.1016/j.palaeo.2018.04.013.

Fisher, R.V. and Schmincke, H.U., 1984. Pyroclastic Rocks. Springer–Verlag, Berlin. 472 pp.

Fritzen, M.R., Cagliari, J., Candido, M., Lavina, E.L.C., 2019. Tidal bar cyclicity record in the lower Permian: The Rio Bonito formation, Paraná basin, southern Brazil. Sedimentary Geology, 381(1), 76-83. https://doi.org/10.1016/j.sedgeo.2018.12.011.

Gerdes, A. and Zeh A., 2006. Combined U–Pb and Hf isotope LA-(MC-)ICP-MS analyses of detrital zircons: Comparison with SHRIMP and new constraints for the provenance and age of an Armorican metasediment in Central Germany. Earth and Planetary Science Letters, 249, 47–61. https://doi.org/10.1016/j.epsl.2006.06.039.

Gislason, S.R. and Oelkers E.H., 2011. Silicate rock weathering and the global carbon cycle. In: Harmon R.S. and Parker A. (Eds.), Frontiers in Geochemistry: Contribution of Geochemistry to the Study of the Earth. West Sussex: Wiley-Blackwell. p.84-103.

Goldberg, K. and Humayun, M., 2016. Geochemical paleoredox indicators in organic-rich shales of the Irati Formation, permian of the Paraná Basin, southern Brazil. Brazilian Journal of Geology. 46, 377–393. https://doi.org/10.1590/2317-4889201620160001.

Gradstein, F.M., Ogg, J.G., Schmitz, M.D., Ogg, G.M., 2012. The Geologic Time Scale 2012. Amsterdam: Elsevier, 1176 pp.

Griffis, N.P., Montañez, I.P., Mundil, R., Richey, J., Isbell, J., Fedorchuk, N., Linol, B., Iannuzzi, R., Vesely, F., Mottin, T., da Rosa, E., Keller, B., Yin, Q.Z., 2019. Coupled stratigraphic and U-Pb zircon age constraints on the late Paleozoic icehouse-to-greenhouse turnover in south-central Gondwana. Geology, v. 47(12), p. 1146–1150, https://doi.org/10.1130/G46740.1.

Griffis, N.P., Mundil, R., Montañez, I.P., Isbell, J., Fedorchuk, N., Vesely, F.F., Iannuzzi, R., Yin, Q.Z., 2018. A newstratigraphic framework built on U-Pb single-zircon TIMS ages and implications for the timing of the penultimate icehouse (Paraná Basin, Brazil). Geological Society of America Bulletin 130, 848–858.

Hachiro, J., 1996. O Subgrupo Irati (Neopermiano) Da Bacia Do Paraná. Doctorate Thesis. Universidade de São Paulo (USP), São Paulo 196p.

Harrison, J.F., Kaiser, A., VandenBrooks, J.M., 2010. Atmospheric oxygen level and the evolution of insect body size. Proceedings of the Royal Society B: Biological Sciences, 277(1690), 1937–1946. doi:10.1098/rspb.2010.0001

Holanda, W., Santos, A.C., Bertolino, L.C., Bergamaschi, S., Rodrigues, R., Costa, D.F., Jones, C.M., 2019. Paleoenvironmental, paleoclimatic and stratigraphic implications of the mineralogical content of the Irati Formation, Paraná Basin, Brazil. Journal of South American Earth Sciences 94. https://orcid.org/0000-0001-5815-0480.

Holz, M., França, A.B., Souza, P.A., Iannuzzi, R., Rohn, R., 2010. A stratigraphic chart of the Late Carboníferous/Permian succession of the eastern border of the Paraná Basin, Brazil, South America. J. South Am. Earth Sci. 29, 381–399. https://doi.org/10.

Huff, W.D., 2016. K-bentonites: A review. American Mineralogist, 101, 43–70.

Iannuzzi, R., 2013. The Carboniferous-Permian floral transition in the Paraná Basin. Lucas, S.G., et al. (Eds.), The Carboniferous-Permian Transition. New Mexico Museum of Natural History and Science, Bulletin 60.

Iannuzzi, R., Souza, P.A., Holz, M., 2010, Stratigraphic and paleofloristic record of the Lower Permian postglacial succession in the southern Brazilian Paraná Basin. In: López-Gamundí, O.R., and Buatois, L.A. (Eds.), Late Paleozoic Glacial Events and Postglacial Transgressions in Gondwana: Geological Society of America Special Paper 468, p. 113–132, doi: 10.1130/2010.2468(05).

Isbell, J.L., Henry, L.C., Gulbranson, E.L., Limarino, C.O., Fraiser, M.L., Koch, Z.J., Ciccioli, P.L., Dineen, A.A., 2012. Glacial paradoxes during the late Paleozoic ice age: Evaluating the equilibrium line altitude as a control on glaciation: Gondwana Research, 22(1), 1–19. https://doi.org/10.1016/j.gr.2011.11.005.

Isbell, J.L., Miller, M.F., Wolfe, K.L., Lenaker, P.A., 2003. Timing of late Paleozoic glaciation in Gondwana: Was glaciation responsible for the development of Northern Hemisphere cyclothems?, in Chan, M.A., and Archer, A.W., (Eds.), Extreme Depositional Environments: Mega End Members in Geologic Time: Geological Society of America, Special Paper 370, p. 5–24.

Jackson, S.E., Pearson, N.J., Griffin, W.L., Belousova, E.A., 2004. The application of laser ablation-inductively coupled plasma-mass spectrometry to in situ U/Pb zircon geochronology. Chemical Geology. 211, 47-69. https://doi.org/10.1016/j.chemgeo.2004.06.017.

Jaffey, A.H., Flynn, K.F., Glendenin, L.E., Bentley, W.C., Essling, A.M., 1971. Precision Measurement of Half-Lives and Specific Activities of 235U and 238U. Phys Rev. C.,4, 1889-1906. https://doi.org/10.1103/PhysRevC.4.1889.

Jones, F.H., Scherer, C.M.S., Kifumbi, C. 2021. Aeolian dunes morphodynamics and wind regime reconstruction in mid-latitudes of the Gondwana during Early Permian, Aracaré Formation, Sergipe-Alagoas Basin, Brazil. Aeolian Research. V.50, 100672. doi.org/10.1016/j.aeolia.2021.100672

Kay, S.M., Ramos, V.A., Mpodozis, C., Sruoga, P., 1989. Late Paleozoic to Jurassic silicic magmatism at the Gondwanaland margin: analogy to the Middle Proterozoic in North America?. Geology, 17, 324-328.

Kenkmann, T., Vasconcelos, M.A.R., Crósta, A.P., Reimold, W.U., 2011. The complex impact structure Serra da Cangalha, Tocantins State, Brazil. Meteoritics and Planetary Science, 46(6), 875-889. http://dx.doi.org/10.1111/j.1945-5100.2011.01199.x.

Kimbrough, D.L., Mahoney, J.B., Mescua, J.F., Giambiagi, L.B., and Grove, M., 2016. The Choiyoi silicic large igneous province of Argentina and Chile and its possible influence on Permian environmental

degradation and mass extinction: Geological Society of America Abstracts with Programs, v. 48. DOI: 10.1130/abs/2017AM-308148.

Lana, C., Farina, F., Gerdes, A., Alkmim, A., Gonçalves, G., Jardim, A. C., 2017. Characterization of zircon reference materials via high precision U–Pb LA-MC-ICP-MS. Journal of Analytical Atomic Spectrometry, 32(10), 2011–2023. doi:10.1039/c7ja00167c.

Lavina, E., 1991. Geologia sedimentar e paleogeografia do Neopermiano e Eotriássico (intervalo Kazaniano-Scythiano) da Bacia do Paraná. Doctorate Thesis. Universidade Federal do Rio Grande do Sul (URGS), Porto Alegre 457p.

Li, Z.X., Powell, C.McA., 2001. An outline of the palaeogeographic evolution of the Australasian region since the beginning of the Neoproterozoic. Earth-Science Reviews, 53(3), 237-277. DOI: 10.1016/S0012-8252(00)00021-0.

Limarino, C.O., César, S.N., Spalletti, L.A., Taboada, A.C., Isbell, J.L., Geuna, S., Gulbranson, E.L., 2013. A paleoclimatic review of southern South America during the late Paleozoic: a record from icehouse to extreme greenhouse conditions. Gondwana Research, 25 (4), 1396–1421.

Llambías, E.J., Kleiman, L.E., Salvarredy, J., 1993. El magmatismo Gondwanico. In: Ramos, V.A. (Ed.), Geología y Recursos Naturales de Mendoza, Relatorio 12 Congreso Geologico Argentino y 2 Congreso de Exploracion de Hidrocarburos, Mendoza, pp. 53-64.

López-Gamundí, O., Fildani, A., Weislogel, A., & Rossello, E., 2013. The age of the Tunas formation in the Sauce Grande basin-Ventana foldbelt (Argentina): Implications for the Permian evolution of the southwestern margin of Gondwana. Journal of South American Earth Sciences, 45, 250–258. doi:10.1016/j.jsames.2013.03.011.

López-Gamundi, O.R., 2006. Permian plate margin volcanism and tuffs in adjacent basins of west Gondwana: age constrains and common characteristics. Journal of South American Earth Sciences 22, 227–238.

Lucas, S.G., 2006. Global Permian tetrapod biostratigraphy and biochronology. Geological Society, London, Special Publications, 265(1), 65–93. doi:10.1144/gsl.sp.2006.265.01.04.

Lucas, S.G., 2017a. Permian tetrapod extinction events. Earth-Science Reviews. 170, 31–60. doi:10.1016/j.earscirev.2017.04.008.

Lucas, S.G., 2017b. Permian tetrapod biochronology, correlation and evolutionary events. In: Lucas, S.G. and Shen, S.Z (Eds.), The Permian Timescale. Special Publications, 450(1), 405–444. doi:10.1144/sp450.12.

Ludwig, K.R., 2012. User's manual for Isoplot 3.75. A geochronological toolkit for Microsoft excel. Berkeley Geochronological Center, Special Publication, 5, pp.75.

Maahs, R., Küchle, J., Scherer, C.M.S., Alvarenga, R.S., 2019. Sequence stratigraphy of fluvial to shallow-marine deposits: The case of the early Permian Rio Bonito Formation, Paraná Basin, southernmost Brazil. Brazilian Journal of Geology, 49(4). Doi: 10.1590/2317-4889201920190059

Martin, R.E., 2016. Earth's Evolving Systems, The History of Planet Earth, Jones & Bartlett Learning, 2ed. p-328-363. ISBN-10: 1284108295.

Martins, L.L, Schulz, H.M., Ribeiro, H.J.P.S., Nascimento, C.A., Souza, E.S., Cruz, G.F., 2020b. Cadalenes and norcadalenes in organic-rich shales of the Permian Irati Formation (Paraná Basin, Brazil): Tracers for terrestrial input or also indicators of temperature-controlled organic-inorganic interactions?. Organic Geochemistry, 140. https://doi.org/10.1016/j.orggeochem.2019.103962.

Martins, L.L., Schulz, H.M., Ribeiro, H.J.P.S., Nascimento, C.A., Souza, E.S., Cruz, G.F., 2020a. Organic geochemical signals of freshwater dynamics controlling salinity stratification in organic-rich shales in the Lower Permian Irati Formation (Paraná Basin, Brazil), Organic Geochemistry, 40. doi.org/10.1016/j.orggeochem.2019.103958.

Matos, S.A., Warren, L.V., Varejao, F.G., Assine, M.L., Simões, M.G., 2017. Permian endemic bivalves of the ‘‘Irati anoxic event”, Paraná Basin, Brazil: Taphonomical, paleogeographical and evolutionary implications. Palaeogeography, Palaeoclimatology, Palaeoecology 469, p.18–33.

Maziviero, M.V., Vasconcelos, M.A.R., Crósta, A.P., Góes, A.M., Reimold, W.U., Carneiro, C.C., 2013. Geology and impact features of Riachão structure, northern Brazil. Meteoritics and Planetary Science, 48, 2044–2058.

Mendonça-Filho, J.G., Sommer, M.G., Klepzig, M.C., Mendonça, J.O., Silva, T.F., Kern, M.L., Santos, L.G.C., 2013. Permian carbonaceous rocks from the Bonito Coalfield, Santa Catarina, Brazil: Organic facies approaches. International Journal of Coal Geology, 111, 23–36. doi:10.1016/j.coal.2012.07.008.

Meunier, A., 2005. Clays. Berlin: Springer-verlag, 472p.

Miall, A.D., 2016. Stratigraphy: A Modern Synthesis. University of Toronto, Springer. P.311-370. Doi:10.1007/978-3-319-24304-7.

Milani, E.J. and De Wit, M.J., 2008. Correlations between the classic Paraná and Cape-Karoo sequences of South America and southern Africa and their basin infills flanking the Gondwanides: du Toit revisited. Geological Society, London, Special Publications, 294, 319-342. doi:10.1144/SP294.17.

Milani, E.J. and Ramos, V.A., 1998. Orogenias paleozóicas no domínio sul-ocidental do Gondwana e os ciclos de subsidência da Bacia do Paraná. Rev. Bras. Geociencias 28, 473–484. https://doi.org/10.5327/rbg.v28i4.651.

Milani, E.J. and Zalán, P.V., 1999. An outline of the geology and petroleum systems of the Paleozoic interior basins of South America: Episodes, 22, 199-205.

Milani, E.J., 1997. Evolução tectono-estratigráfica da Bacia do Paraná e seu relacionamento com a geodinâmica fanerozóica do Gondwana sul-ocidental. Tese de doutorado, 2v. Universidade Federal do Rio Grande do Sul (UFRGS), Porto Alegre 255p.

Milani, E.J., Melo, J.H.G., Souza, P.A., Fernandes, L.A., França, A.B., 2007. Bacia do Paraná. Boletim de Geociências Petrobras 15, 265–287.

Miller, J., Matzel, J., Miller, C., Burgess, S., Miller, R., 2007. Zircon growth and recycling during the assembly of large, composite arc plutons. Journal of Volcanology and Geothermal Research. 167, p.282–299.

Mohriak, W., Szatmari, P., Anjos, S.M.C., 2008. Sedimentação de evaporitos. In: Mohriak W., Szatmari P., Anjos S. M. C. (Eds.), Sal, Geologia e Tectônica. São Paulo: Beca Edições. p. 65-88.

Montañez, I.P. and Poulsen, C.J., 2013. The late Paleozoic Ice Age: An Evolving Paradigm: Annual Review of Earth and Planetary Sciences, 41, 629–656. https://doi.org/10.1146/annurev.earth.031208.100118.

Montañez, I.P., Tabor, N.J., Niemeier, D., DiMichele, W.A., Frank, T.D., Fielding, C.R., Isbell, J.L., Birgenheier, L.P., Rygel, M.C., 2007. CO2-forced climate and vegetation instability during Late Paleozoic deglaciation. Science 315(5808), 87–91.

Mori, A.L.O., de Souza, P.A., Marques, J.C., Lopes, R.C., 2012. A new U-Pb zircon age dating and palynological data from a Lower Permian section of the southernmost Parana Basin, Brazil: Biochronostratigraphical and geochronological implications for Gondwanan correlations: Gondwana Research, 21(2-3), 654–669. https://doi.org/10.1016/j.gr.2011.05.019.

NACSN (North American Stratigraphic Code), 2005. North American stratigraphic code. American Association of Petroleum Geologists Bulletin, 89, p.1547-1591.

Nascimento, C.A., Souza, E.S., Martins, L.L., Severiano, H.J.P.R., Santos, V.H., Rodrigues, R., 2021. Changes in depositional paleoenvironment of black shales in the Permian Irati Formation (Paraná Basin, Brazil): Geochemical evidence and aromatic biomarkers. Marine and Petroleum Geology, 126. 104917.https://doi.org/10.1016/j.marpetgeo.2021.104917.

Nelson, D.A. and Cottle, J.M., 2019. Tracking voluminous Permian volcanism of the Choiyoi Province into central Antarctica. The Geological Society of America, 11(3), 386–398. doi:10.1130/l1015.1.

Neregato, R., 2005. Estudo Palinológico das Formações Serra Alta, Teresina e Rio do Rasto nos Furos de Sondagem SP-23-PR e SP-58-PR, Centro-Norte Do Paraná (Permiano, Bacia do Paraná). Universidade Estadual Paulista.

Ng, C., Vega, C.S., Maranhão, M.S.A.S., 2019. Mixed carbonate-siliciclastic microfacies from Permian deposits of Western Gondwana: Evidence of gradual marine to continental transition or episodes of marine transgression?. Sedimentary Geology 390, 62–82. https://doi.org/10.1016/j.sedgeo.2019.07.006.

Odin, G.S. and Matter, A., 1981. De glauconiarum origine. Sedimentology, 28, 611-641. https://doi.org/10.1111/j.1365-3091.1981.tb01925.x.

Ogg, J.G., Ogg, G., Gradstein, F.M., 2016. A Concise Geologic Time Scale: 2016. Elsevier, Amsterdam 240 pp.

Orton, G.J., 1996. Volcanic environments. In: Reading H.G. (Ed.), Sedimentary Environments: Processes, Facies and Stratigraphy, 3rd ed, Blackwell Publishing, p.485-567 pp.688.

Pupin, J.P., 1980. Zircon and granite petrology. Contributions to Mineralogy and Petrology**,** 73, 207-220.

Qie, W., Algeo, T.J., Luo, G., Herrmann, A., 2019. Global events of the Late Paleozoic (Early Devonian to Middle Permian): A review. Palaeogeography, Palaeoclimatology, Palaeoecology, 531. https://doi.org/10.1016/j.palaeo.2019.109259

Reiners, P.W., Carlson, R.W., Renne, P.R., Cooper, K.M., Granger, D.E., McLean, N.M., Schoene, B., 2018. Geochronology and Thermochronology. John Wiley & Sons. p. 39-82. ISBN: 978-1-118-45578-4.

Reis, D.E.S., Rodrigues, R., Moldowan, J.M., Jones, C.M., Brito, M., Cavalcante, D.C., Portela, H.A., 2018. Biomarkers stratigraphy of Irati Formation (Lower Permian) in the southern portion of Paraná Basin (Brazil). Marine and Petroleum Geology 95, 110–138. https://doi.org/10.1016/j.marpetgeo.2018.04.007.

Rocha, H.V., Mendes, M., Pereira, Z., Rodrigues, C., Fernandes, P., Lopes, G., Sant'Anna, L.G., Tassinari, C.C.G., Lemos de Sousa, M.J., 2020. New palynostratigraphic data of the Irati (Assistência Member) and the Corumbataí formations, Paraná Basin, Brazil, and correlation with other south American basins. Journal of South American Earth Sciences 102. https://doi.org/10.1016/j.jsames.2020.102631

Rocha-Campos, A.C., Basei, M.A., Nutman, A.P., Kleiman, L.E., Varela, R., Llambias, E., Canile, F.M., da Rosa, O., de, C.R., 2011. 30 million years of Permian volcanism recorded in the Choiyoi igneous province (W Argentina) and their source for younger ash fall deposits in the Paraná Basin: SHRIMP U-Pb zircon geochronology evidence. Gondwana Research. 19, 509–523.

Rocha-Campos, A.C., Basei, M.A.S., Nutman, A.P., Santos, P.R., Passarelli, C.R., Canile, F.M., Rosa, O.C.R., Fernandes, M.T., Santa Ana, H., Veroslavsky, G., 2019. U-Pb Zircon Dating of Ash Fall Deposits from the Paleozoic Paraná Basin of Brazil and Uruguay: A Reevaluation of the Stratigraphic Correlations. The Journal of Geology, The University of Chicago. 127, 167–182.

Rohn, R., 2007. The Passa Dois group (Paraná Basin, permian): investigations in progress. In: Ianuzzi, R., Boardman, D.R. (Eds.), I Workshop - Problems in Western Gondwana Geology, South America - Africa Correlations: Du Toit Revisited. Petrobrás, Gramado, pp.151–157.

Rossignol, C., Hallot, E., Bourquin, S., Poujol, M., Jolivet, M., Pellenard, P., Dabard, M.P., 2019. Using volcaniclastic rocks to constrain sedimentation ages: To what extent are volcanism and sedimentation synchronous? Sedimentary Geology, 381, 46–64. doi:10.1016/j.sedgeo.2018.12.010

Sahney, S., Benton, M.J., Ferry, P.A., 2010. Links between global taxonomic diversity, ecological diversity and the expansion of vertebrates on land. Biology Letters, 6, 544-547.

Santos, R.V., Souza, P.A., de Alvarenga, C.J.S., Dantas, E.L., Pimentel, M.M., de Oliveira, C.G., de Araújo, L.M., 2006. Shrimp U–Pb zircon dating and palynology of bentonitic layers from the Permian Irati Formation, Paraná Basin, Brazil. Gondwana Research 9(4), 456-463.

Sato, A.M., Llambías, E.J. Basei, M.A.S., Castro, C.E., 2015. Three stages in the Late Paleozoic to Triassic magmatism of southwestern Gondwana, and the relationships with the volcanogenic events in coeval basins. Journal of South American Earth Sciences 63, 48-69. http://dx.doi.org/10.1016/j.jsames.2015.07.005

Sato, A.M., Llambías, E.J., 1993. El Grupo Choiyoi, provincia de San Juan: equivalentes efusivos del batolito de Colangüil. In: 12 Congreso Geologico Argentino y 2 Congreso de Exploracion de Hidrocarburos (Mendoza), Actas 4, 156-165.

Schneider, R.L., Mühlmann, H., Tommasi, E., Medeiros, R.A., Daemon, R.F., Nogueira, A.A., 1974. Revisão estratigráfica da Bacia do Paraná. In: Anais do XXVIII Congresso Brasileiro de Geologia, Porto Alegre-RS, v1. Sociedade Brasileira de Geologia, Rio de Janeiro, pp. 41–65.

Schneider, R.R., Schulz, H.D., Hensen, C., 2000. Marine carbonates: their formation and destruction. In: Schulz, H.D., Zabel, M. (Eds.), Marine geochemistry. Berlin: Springer Verlag, 311–337. doi:10.1007/3-540-32144-6_9

Scotese, C., 2014. Atlas of Permo-Carboniferous Paleogeographic Maps (Mollweide Projection), Maps 53 – 64, Volumes 4, The Late Paleozoic, PALEOMAP Atlas for ArcGIS, PALEOMAP Project, Evanston, IL.. 10.13140/2.1.1837.8244.

Sgarbi, G.N.C., Sgarbi, P.B.A., Campos, J.E.G., Dardenne, M.A., Penha, U.C., 2001. Bacia Sanfranciscana: Registro fanerozóico da Bacia do São Francisco. In: Pinto C.P. and Martins-Neto, M.A. (Eds.), Bacia do São Francisco: Geologia e Recursos Naturais. Belo Horizonte, Ed. SBG-MG, 93-138.

Silva, A. F., Dani, N., Remus, M.V.D., Guerra-Sommer, M., Horn, B.L.D., 2017. Bentonitas da Formação Irati no setor sul da Bacia do Paraná. Geologia USP**,** Série Científica**,** v. 17(1), p.75-88.

Silva, A.F., Dani, N., Xavier, P.L.A., Remus, M.V.D., Schultz, C.L., Philipp, R.P., Silva A.L., in press.Pyroclastic fall deposits (PFD) from Irati Formation: characterization and chronostratigraphy reconstruction based on high-resolution geochronology.

Simas, M.W., Guerra-Sommer, M., Cazzulo-Klepzig, M., Menegat, R., Schneider Santos, J.O., Fonseca Ferreira, J.A., and Degani-Schmidt, I., 2012. Geochronological correlation of the main coal interval in Brazilian Lower Permian: Radiometric dating of tonstein and calibration of biostratigraphic framework. Journal of South American Earth Sciences, 39, 1–15, https://doi.org/10.1016/j.jsames.2012.06.001.

Spalletti, L., Limarino, C., 2017. The Choiyoi magmatism in south western Gondwana: implications for the end-permian mass extinction - a review. Andean Geology 44 (3): 328-338. Doi:http://dx.doi.org/10.5027/andgeoV44n3-a05.

Spears, D.A., 2012. The origin of tonsteins, an overview, and links with seatearths, fireclays and fragmental clay rocks. International Journal of Coal Geology, 94,22–31.

Steiger, R.H. and Jager, E., 1977. Subcommission on Geochronology: Convention on the use of decay constants in geochronology and cosmochronology. Earth and Planetary Science Letters. 36, 359–62.

Stephenson, M.H., 2008. A review of the palynostratigraphy of Gondwanan Late Carboniferous to Early Permian glacigene successions. Special Paper 441: Resolving the Late Paleozoic Ice Age in Time and Space, 317–330. doi:10.1130/2008.2441(22)

Stephenson, M.H., 2016. Permian palynostratigraphy: a global overview, in The Permian Timescale, Lucas, S.G., and Shen, S.Z. (eds). The Permian Timescale. Geological Society, London, Special Publications, vol. 450. https://doi.org/10.1144/SP450.2.

Tedesco, J., Cagliari, J., Coitinho, J.R., Lopes, R.C.L., Lavina, E.L.C., 2016. Late Paleozoic paleofjord in the southernmost Parana Basin (Brasil): geomorphology and sedimentary fill. Geomorphology 269, 203–214.

Tomezzoli, R.N. and Cristallini, E.O., 1998. Nuevas evidencias sobre la importancia del fallamiento en la estructura de las Sierras Australes de la Provincia de Buenos Aires. Revista de la Asociación Geológica Argentina 53, 117–129.

Torsvik, T.H. and Cocks, L.R.M., 2017. Earth History and Palaeogeography. Cambridge: Cambridge University Press, pp. 178-194.

TS-Creator 7.4. www.timescalecreator.org acessado em junho de 2020.

Van Achterbergh, E., Ryan, C.G., Jackson, S.E., Griffin, W.L., 2001. Data reduction software for LA-ICP-MS: appendix. In: Sylvester P.J. (Ed.), Laser Ablation-ICPMass Spectrometry in the Earth Sciences: Principles and Applications (vol. 29, 239-243). Ottawa: Mineralog. Assoc. Canada (MAC) Short Course Series.

Vasconcelos, M.A.R., Crósta, A.P., Reimold, W.U., Góes, A.M., Kenkmann, T., Poelchau, M.H., 2013. The Serra da Cangalha impact structure, Brazil: geological, stratigraphic and petrographic aspects of a recently confirmed impact structure. Journal of South American Earth Sciences, 45, 316–330. http://dx.doi.org/10.1016/j.jsames.2013.03.007

Vasconcelos, M.A.R., Wünnemann, K., Crósta, A.P., Molina, E.C., Reimold, W.U., Yokoyama, E., 2012. Insights into the morphology of the Serra da Cangalha impact structure from geophysical modeling. Meteoritics and Planetary Science, 47,1659–1670.

Vavra, G., 1990. On the kinematics of zircon growth and its petrogenetic significance: a cathodoluminescence study. Contributions to Mineralogy and Petrology, 106, 90-99.

Vavra, G., 1993. A guide to quantitative morphology of accessory zircon. Chemical Geology, 110, 15-28.

Vázquez, M.S. and César, S.N., 2017. The Permian palynological Lueckisporites-Weylandites Biozone in the San Rafael Block and its correlation in Western Gondwana. Journal of South American Earth Sciences, 76, 165-181. http://dx.doi.org/10.1016/j.jsames.2017.02.009.

Velde, B., 1992. Introduction to Clay Minerals: Chemistry, origins, uses and environmental significance. Chapman & Hall, Hong Kong, 198 pp, DOI 10.1007/978-94-011-2368-.

Walker, J.D., Geissman, J.W., Bowring, S.A., Babcock, L.E., 2018. Geologic Time Scale v. 5.0: Geological Society of America, https://doi.org/10.1130/2018.CTS005R3C.

Warren, L.V., Assine, M.L., Simões, M.G., Riccomini, C., Anelli, L.E., 2015. A Formação Serra Alta, Permiano, no centro-leste do Estado de São Paulo, Bacia do Paraná, Brazilian Journal of Geology, 45(1), 109-126. https://doi.org/10.1590/23174889201500010008.

Werner, N., 2006. New implications from studies on sediments and altered pyroclastic layers of the Dwyka and Ecca Group (lower Karoo Supergroup) in southern Namibia.Doctorate Thesis. Universität Würzburg, Würzburg. 428 pp.

White, I.C., 1908. Relatório sobre as coal measures e rochas associadas ao sul do Brasil. Rio de Janeiro: Comissão das Minas de Carvão de Pedra do Brasil, 300 p.

Xavier, P.L.A., Silva, A.F., Soares, M.B., Horn, B.L.D., Schultz, C.L., 2018. Sequence stratigraphy control on fossil occurrence and concentration in the epeiric mixed carbonate-siliciclastic ramp of the Early Permian Irati Formation of southern Brazil. Journal of South American Earth Sciences, 88,157–178. https://doi.org/10.1016/j.jsames.2018.08.014.

Zalán, P.V. and Romeiro-Silva, P.C., 2007. Bacia do São Francisco. Boletim de Geociências da Petrobras, 15(2), 561-571.

Zuffa, G.G., 1980. Hybrid arenites: their composition and classification. J. Sediment. Petrol. 50, 21–29. https://doi.org/10.1306/212F7950-2B24-11D7-8648000102C1865D.

Zuffa, G.G., 1985. Optical analyses of arenites: influence of methodology on compositional results. In: Provenance of Arenites. Springer, Dordrecht, p. 165-189.

Zuffa, G.G., 1987. Unravelling Hinterland and Offshore Palaeogeography from Deep-water Arenites. In: Leggett, J. K.; Zuffa, G. G. Marine Clastic Sedimentology: Concepts and case Studies. Dordrecht: Springer, p. 39-61.

Artigos em co-autoria - *Sequence stratigraphy control on fossil occurrence and concentration in the epeiric mixed carbonate-siliciclastic ramp of the Early Permian Irati Formation of southern Brazil*.

Journal of South American Earth Sciences 88 (2018) 157–178

Contents lists available at ScienceDirect

Journal of South American Earth Sciences

journal homepage: www.elsevier.com/locate/jsames

Sequence stratigraphy control on fossil occurrence and concentration in the epeiric mixed carbonate-siliciclastic ramp of the Early Permian Irati Formation of southern Brazil

Pedro L.A. Xavier[a,*], Aurélio F. Silva[a], Marina B. Soares[a,b], Bruno L.D. Horn[c], Cesar L. Schultz[a,b]

[a] Programa de Pós-Graduação em Geociências (PPGGEO), Instituto de Geociências, Universidade Federal do Rio Grande do Sul (UFRGS), Brazil
[b] Departamento de Paleontologia e Estratigrafia, Instituto de Geociências, Universidade Federal do Rio Grande do Sul (UFRGS), 91501-970, Porto Alegre, Brazil
[c] Serviço Geológico do Brasil (CPRM), Brazil

ARTICLE INFO

Keywords:
Irati Formation
Mesosaurid
Pygocephalomorph
Sequence stratigraphy
Taphonomy

ABSTRACT

The Early Permian Irati Formation records sedimentation of a mixed carbonate-siliciclastic, storm-influenced ramp in a shallow and restricted epeiric sea. It is formally divided in the dark grey mudstones of the lower Taquaral Member, and alternating dark grey mudstones, bituminous black shales, and carbonates of the upper Assistência Member. The formation crops out from central to southern Brazil on the eastern border of the intracratonic Paraná Basin. Fossils of mesosaurid reptiles, pygocephalomorph crustaceans, and subordinate paleonisciform fish form dense concentrations within carbonate tempestites, interpreted as mass mortality events caused by storms. The present study describes the Passo do São Borja outcrop and five new locations, along with 11 drill cores of the complete Irati interval in the Rio Grande do Sul state, applying methods of facies analysis and sequence stratigraphy. Three fourth-order sequences within the Irati Formation were recognized, termed sequences 1, 2, and 3 (S1, S2, S3). S1 is broadly coincident with the Taquaral Member, and S2 and S3 with the Assistência Member. The upper two sequences are composed of a lowstand systems tract (LST), a transgressive systems tract (TST), and a highstand systems tract (HST), whereas the lower sequence lacks a LST. Sequence boundary SB2 was interpreted as coincident with a third-order sequence boundary. Mesosaurid and pygocephalomorph concentrations occur only in S3. Fossil occurrences and concentration were found to be strongly controlled by facies and sequence stratigraphy. Paleonisciform fish fossils are considerably more common at the early HST of S2 and S3, resulting from balanced sedimentation to accommodation rates. Pygocephalomorphs compose intraclasts concentrated in grainstone proximal tempestites of the LST in S3. They are the result of mass mortality events and background bioclastic input, enhanced by firmground formation (hiatal concentration) and subsequent storm reworking. Mesosaurids are also concentrated in grainstone tempestites of the LST, but in cores they were mostly found in distal tempestites of the TST, becoming more common towards the maximum transgressive surface (MTS). Their accumulation is also the result of mass mortality and background sedimentation, enhanced by sediment omission (hiatal concentration) of a severely sediment starved TST (culminating in a condensed section near the MTS), and subsequent storm reworking.

Artigos em co-autoria - *Hiperpicnitos (Inunditos) como análogos de reservatórios: um exemplo nos* depósitos Gonduânicos Triássicos do Gráben Arroio Moirão, Rio Grande do Sul.

Hiperpicnitos (Inunditos) como análogos de reservatórios: um exemplo nos depósitos Gonduânicos Triássicos do Gráben Arroio Moirão, Rio Grande do Sul

Hiperpicnites (Inundites) as reservoir analogs: an example in the Triassic Gondwanic deposits of Arroio Moirão Graben, Rio Grande do Sul

Yolanda Caliman Rodrigues[1], Rualdo Menegat[1], Ana Maria Pimentel Mizusaki[1], Aurélio Fagundes Silva[1]
[1]Universidade Federal do Rio Grande do Sul - UFRGS, Instituto de Geociências, Curso de Pós-Graduação em Geociências - IG/CPGG, Avenida Bento Gonçalves, 9.500, Caixa Postal 15.001, CEP 91501-970, Porto Alegre, RS, BR
(yolanda.caliman@ufrgs.br; rualdo.menegat@ufrgs.br; ana.mizusaki@ufrgs.br; aureliofagundes@hotmail.com)

Recebido em 5 de fevereiro de 2018; aceito em 29 de outubro de 2019

Resumo
Os arenitos associados a modelos episódicos de inundação, como os Inunditos provenientes de fluxos hiperpicnais em corpos de água rasa, podem ser reservatórios de hidrocarbonetos. No entanto, há poucos estudos para entender a arquitetura e heterogeneidade desses modelos, o que resulta em dificuldades para exploração e explotação desses reservatórios. O presente trabalho visa à análise de pacotes triássicos da Bacia do Paraná pertencentes à Formação Santa Maria, que ocorrem como fragmentos isolados sobre o Escudo Sul-Rio-Grandense na região do Gráben Arroio Moirão (Rio Grande do Sul). Para tanto, fez-se um estudo comparativo de modelos de inundação e como metodologia de obtenção de dados utilizou-se mapeamento sistemático, análise de heterogeneidade de fácies e estratigrafia de sequências, que incluem levantamento de perfis colunares, identificação de associações e sucessões de fácies e superfícies-chave. Secundariamente, algumas análises petrográficas foram realizadas. Foi possível delimitar os principais depósitos de arenitos, dos quais predominam geometria tabular, grãos mal selecionados e alguma matriz argilosa. Distinguiram-se cinco ciclos deposicionais granodecrescentes ascendentes, limitados na base e no topo por superfícies erosivas, que marcam heterogeneidades recorrentes. As fácies-reservatório são subarcósios, de matriz argilosa com agregados de caulinita, porosidade intergranular e *shrinkage*. Identificaram-se potenciais fácies-reservatório constituídas de arenitos grossos a conglomeráticos, com estratificações cruzada tangencial e plano-paralela. A integração dos dados resultou na elaboração de um modelo de variação lateral e vertical de fácies de hiperpicnitos lacustres, como um potencial modelo análogo de reservatório do tipo compartimentado. Esses resultados possibilitam prospectar outros depósitos arenosos dessa unidade estratigráfica da Bacia do Paraná, para fins de dimensionar regionalmente o análogo de reservatório.

Palavras-chave: Bacia do Paraná; Formação Santa Maria; Sequência Candelária; Turbiditos extrabacinais.

ANEXO I
Título da Dissertação/Tese:
DEPÓSITOS PIROCLÁSTICOS DE QUEDA (PFDs) COMO FERRAMENTA ESTRATIGRÁFICA. PROVENIÊNCIA, GEOCRONOLOGIA E RECONSTRUÇÃO DAS SEQUÊNCIAS DEPOSICIONAIS DA FORMAÇÃO IRATI
Área de Concentração: Estratigrafia
Autor: **Aurélio Fagundes Silva**
Orientador: Prof. Dr. Norberto Dani
Examinador: Prof. Dr. Ernesto Luiz Correa Lavina
Data:
Conceito: A (excelente)
PARECER: A tese envolve tema importante e inédito, qual seja o estudo detalhado dos depósitos piroclásticos de queda existentes nos depósitos da Formação Irati. Apesar da pandemia, o trabalho, apresentado na forma de artigos, está muito bem elaborado, sem omissões ou falhas, compondo o conjunto uma tese de nível excelente. Pequenos ajustes foram indicados diretamente ao doutorando.
Assinatura:  Data: 28 de julho de 2021
Ciente do Orientador: Ciente do Aluno:

ANEXO I

Título da Dissertação:

DEPÓSITOS PIROCLÁSTICOS DE QUEDA (PFDs) COMO FERRAMENTA ESTRATIGRÁFICA. PROVENIÊNCIA, GEOCRONOLOGIA E RECONSTRUÇÃO DAS SEQUÊNCIAS DEPOSICIONAIS DA FORMAÇÃO IRATI

Área de Concentração: Estratigrafia

Autor: **AURÉLIO FAGUNDES SILVA**

Orientador: Dr. Norberto Dani

Examinador: Dr. Edison José Milani

Data: 28/maio/2021

Conceito: A

PARECER:

O doutorando produziu um trabalho notável, multidisciplinar, de amplo valor para as Geociências do Brasil.

Apresentou resultados inéditos em Geocronologia de horizonte em estudo, além de uma caracterização mineralógica-composicional de cinzas modernas e bentonitas paleozoicas que terá certamente ampla utilização por geocientistas interessados no tema.

Suas correlações interregionais das bacias paleozoicas sul-americanas também trazem contribuições à Geologia Regional do continente.

O texto foi bem redigido, porém algumas das figuras pecam por estarem parcialmente ilegíveis (fontes muito reduzidas). Utilizou bibliografia atualizada além de referências históricas.

Apresentou a tese com segurança e respondeu às indagações dos examinadores com propriedade.

Parabéns ao doutorando e aos orientadores.

Assinatura: [signature] Data: 29/julho/21

Ciente do Orientador:

Ciente do Aluno:

ANEXO I

Título da Dissertação/Tese:

DEPÓSITOS PIROCLÁSTICOS DE QUEDA (PFDs) COMO FERRAMENTA ESTRATIGRÁFICA. PROVENIÊNCIA, GEOCRONOLOGIA E RECONSTRUÇÃO DAS SEQUÊNCIAS DEPOSICIONAIS DA FORMAÇÃO IRATI

Área de Concentração: Estratigrafia

Autor: **Aurélio Fagundes Silva**

Orientador: Prof. Dr. Norberto Dani

Examinadora: Profa. Dra. Márcia Elisa Boscato Gomes

Data: 28/05/2021

Conceito: A

PARECER:

O presente estudo constitui uma contribuição científica de grande relevância para o entendimento estratigráfico da Fm Irati, com a produção de dados geocronológicos e de proveniência permitindo a reconstrução paleoambiental. É também uma contribuição importante deste estudo, a abordagem integrada de diferentes técnicas analíticas e a determinação da gênese dos diferentes PFDs. Apresenta uma ampla revisão teórica, trazendo o estado da arte dos temas principais. Um dos pontos altos deste trabalho está nas várias ferramentas analíticas utilizadas, como a descrição faciológica, petrografia, MEV, DRX, IR e FRX, que permitiram a caracterização de detalhe de tefra, esmectita e caolinita, e a interpretação dos processos cristaloquímicos envolvidos na formação destes. Neste sentido, os objetivos foram plenamente atingidos resultando em um trabalho original e de referência na área.

Assinatura: MárciaEBG Data:28/052021

Ciente do Orientador:

Ciente do Aluno: